Growth of Planetesimals and the Formation of Debris Disks

by

Andrew Shannon

A thesis submitted in conformity with the requirements
for the degree of Doctor of Philosophy
Graduate Department of Astronomy and Astrophysics
University of Toronto

Abstract

Growth of Planetesimals and the Formation of Debris Disks

Andrew Shannon

Doctor of Philosophy

Graduate Department of Astronomy and Astrophysics

University of Toronto

2012

At the edge of the Solar System lies the Kuiper Belt, a ring of leftover planetesimals from the era of planet formation. Collisions between the Kuiper Belt Objects produce dust grains, which absorb and re-radiate stellar radiation. The total amount of stellar radiation so absorbed is perhaps one part in ten million. Analogous to this, Sun-like stars at Sun-like ages commonly have dusty debris disks, which absorb and re-radiate as much as one part in ten thousand of the stellar radiation. We set out to understand this difference. In chapter 1, we outline the relevant observations and give a feel for the relevant physics. In chapter 2, we turn to the extrasolar debris disks. Using disks spanning a wide range of ages, we construct a pseudo-evolution sequence for extrasolar debris disks. We apply a straightforward collision model to this sequence, and find that the brightest disks are a hundred to a thousand times as massive as the Kuiper Belt, which causes the difference in dust luminosity. Current theoretical models of planetesimal growth predict very low efficiency in making large planetesimals, such that the Kuiper Belt should be the typical outcome of Minimum Mass Solar Nebula type disks. These models cannot produce the massive disks we find around other stars. We revisit these models in chapter 3, to understand the origin of this low efficiency. We confirm that these models, which begin with kilometer sized planetesimals, cannot produce the observed extrasolar debris disks. Instead, we propose an alternate model where most mass begins in centimeter sized grains, with some kilometer sized seed planetesimals. In this model,

collisional cooling amongst the centimeter grains produces a new growth mode. We show in chapter 4 that this can produce the Kuiper Belt from a belt not much more massive than the Kuiper Belt today. We follow in chapter 5 by showing that this model can also produce the massive planetesimal populations needed to produce extrasolar debris disks.

Dedication

For my wife, Vivian

I know she will appreciate anything that will put her to sleep

Acknowledgements

The most important acknowledge I can make is the debt I owe my thesis advisor, Yanqin Wu. She has been patient when I needed patience, pushed me when I needed to be pushed, and I could not have become the scientist I am today without her guidance. And she has been a valuable collaborator in the development of this thesis.

I also want to acknowledge my collaborator Yoram Lithwick, who contributed not just to this thesis, but was a major contributor to much of the work on which it is based.

I should thank my mother and my father, who lead by example. More than anything else, I think it was the attitude that *it is easier to do something yourself, rather than let someone else do it*, that got me here.

There are too many other teachers, friends, family members, and fellow scholars who have helped me along the way for me to name here. Nonetheless, their influence must be acknowledged.

Contents

List of Tables

List of Figures

Chapter 1

Introduction

1.1 The Solar Nebula

The planets of the solar system lie roughly in a plane. This remarkable fact seems positively pedestrian today, but this collective behaviour was the basis of the revolutionary hypothesis that the planets formed out of a primordial circumsolar nebula (Kant, 1755; Laplace, 1796), which is the beginning of modern planet formation theory. This trend held true with the subsequent discovery of additional planets within the solar system (Herschel & Watson (1781), Galle (1846)). This hypothesis was further strengthened by the discovery of minor planets. The asteroids, the short-period comets, and the Kuiper belt objects all lie roughly in the plane of the planets, with primarily prograde, planar orbits. The small dust grains in the solar system also follow this general pattern. Today, there is no significant challenge to the overall picture that the planets and minor planets of the solar system formed from a circumsolar disk of material. Modern observations of the solar system cover more than 100 000 asteroids (Juric et al., 2007), and more than 1000 Kuiper belt objects (Barucci et al., 2008). Compared to the total solar luminosity $L_\odot$, small dust grains within the solar system have a total luminosity $\sim 10^{-7} L_\odot$ (Pyo et al., 2010), which represents $\sim 10^{30}$ micron sized grains. We have just begun to mine

the wealth of information contained within the minor planets.

The nebular hypothesis dictates that the protosolar nebula was composed of the same materials as the Sun. However, the planets are heavily depleted in hydrogen and helium relative to the solar composition. To infer the mass distribution of the primordial nebula, the planet masses are augmented with hydrogen and helium to match the solar abundances, and that mass is spread into annuli around their orbits. This construct is called the Minimum Mass Solar Nebula (MMSN) (Weidenschilling, 1977b; Hayashi, 1981). The resulting nebula has a surface density Σ that depends on the distance r from the Sun:

$$\Sigma\left(r\right) = \Sigma_0 r^{-\frac{3}{2}} , \tag{1.1}$$

where $\Sigma_0 \sim 10^{23}$ g cm$^{-0.5}$ (or $\Sigma \sim 1700$ g cm^{-2} at 1 AU). The uncertainty in this value is of order unity, as a result of the uncertainties in the planetary compositions. Given the uncertainties about where and how the planets formed, other parameterisations may be preferred (e.g., Desch, 2007).

It must be noted that that the asteroid and Kuiper belts are substantially lower in mass than is anticipated in the MMSN model (by $\gtrsim 10^{-3}$ in both cases). The low mass of the asteroid belt is generally thought to be the result of dynamical clearing by the giant planets (Liou & Malhotra, 1997; Petit et al., 2002; O'Brien et al., 2007). The same is sometimes postulated for the Kuiper Belt region (Hahn & Malhotra, 1999; Charnoz & Morbidelli, 2007; Booth et al., 2009); however, collisional grinding is sometimes suggested as the source of the low mass today (Stern & Colwell, 1997; Kenyon & Bromley, 2004b; Pan & Sari, 2005); and it has also been suggested that the MMSN disk was truncated inside of 40 AU, and the low mass density is the result of an inefficient implantation process (Levison & Morbidelli, 2003). The low mass of the Kuiper belt remains an open problem.

The low density of the Kuiper belt is even more significantly truncated at $\sim$50 AU (Dones, 1997; Trujillo & Brown, 2001). The surface density remains orders of magnitude

below the MMSN to heliocentric distances of hundreds of AU (Bernstein et al., 2004; Fuentes & Holman, 2008; Parker & Kavelaars, 2010b). Such a truncation must occur at some distance; the integrated mass of the MMSN is divergent unless a truncation is applied. It is likely (though far from certain) that the lower densities in the Kuiper belt represent the primordial edge of the disk. Compared to the solar mass $M_\oplus$, a truncation radius of $30 - 50$ AU gives the MMSN a total mass of $\sim 10^{-2}$ $M_\odot$.

1.2 The Kuiper Belt

1.2.1 Prediction and Discovery

Edgeworth (1949) noted that the nebular hypothesis suggested that a number of smaller bodies should inhabit trans-neptunian space. The same analysis dismissed (134340) Pluto as an "escaped satellite", leaving astronomers in the lurch until the subsequent discovery of (15760) 1992 QB$_1$ (Jewitt & Luu, 1993), which ushered in a new era in outer solar system small body discovery. Although Edgeworth's name is sometimes attached, the region is usually known as the 'Kuiper Belt', after the suggestion that such a region would exist by Kuiper (1951). Pluto wasn't officially removed from the planets and placed among the Kuiper belt objects until 2006, and even that seemingly obvious recognition was fraught with emotion and resistance (Williams & Bell, 2006). As of 2011, more than 1200 Kuiper belt objects are observationally well established, and more remain undiscovered. Attempts to debias the detection statistics suggest roughly one-tenth of the mass in the Kuiper belt is in known objects, which gives the total mass of Kuiper Belt objects as $\sim 10^{-1} M_\oplus$ (Vitense et al., 2010).

1.2.2 Focussing on the Cold Classical Kuiper Belt

It is generally recognised that the Kuiper belt is not a single population of bodies (Jewitt & Luu, 1995; Luu et al., 1997; Fraser et al., 2010). The most common divisional

scheme sets them into three dynamical classes: resonant objects, bodies in mean-motion resonances with Neptune; scattered bodies, non-resonant objects with periapse $\lesssim 38 \mathrm{AU}$; and classical bodies, bodies with low eccentricity/inclination orbits between 38 and 50 AU. Bodies periapses above 38AU, but with eccentricity $e \gtrsim 0.2$ are sometimes identified as an "extended-scattered disk", or "detached disk" (Gladman et al., 2002; Brown et al., 2004). The Classical Belt may be further subdivided into a "Cold Classical" and "Hot Classical" belt, typically at $\sim 5°$, as there is a statistical excess of bodies with eccentricity $e < 0.1$ and inclination $i < 5°$ between ~ 42 and ~ 45 AU (Kavelaars et al., 2008) (outlined in figure 1.1).

Amongst the populations of Kuiper Belt objects (KBOs), the Cold Classical Kuiper Belt stands alone. Three important distinctions should be noted. Cold Classical Kuiper Belt objects (CCKBOs) individually have different properties than other Kuiper Belt objects. Cold Classical Kuiper Belt objects have different population properties than other Kuiper Belt objects. Cold Classical Kuiper Belt Objects have a different dynamical history from other Kuiper Belt Objects.

Cold Classical Kuiper Belt object have very red colours, while other KBOs range from very red to grey in colour (Tegler & Romanishin, 2000; Perna et al., 2010; Fraser & Brown, 2011). The Hot Classical Belt, the Scattered Belt, and the Resonant Objects have similar colour distributions to one another, and the colour of individual objects within those populations is not correlated with their orbital properties (Morbidelli & Brown, 2004). The origin of the red surface colour of CCKBOs (and the red and grey surfaces of other KBOs) is not definitely understood. Gradie & Veverka (1980) suggested that outer solar system objects might be expected to have red colours from complex organic molecules, molecules that would be destroyed at higher temperatures. In this case, the colours would reflect primordial composition, set by the temperature the object formed at, relative to the condensation temperature of various ices (Doressoundiram et al., 2008). For instance, Brown et al. (2011b) note that ammonia condenses as ice beyond ~ 35 AU, and a CCKBO
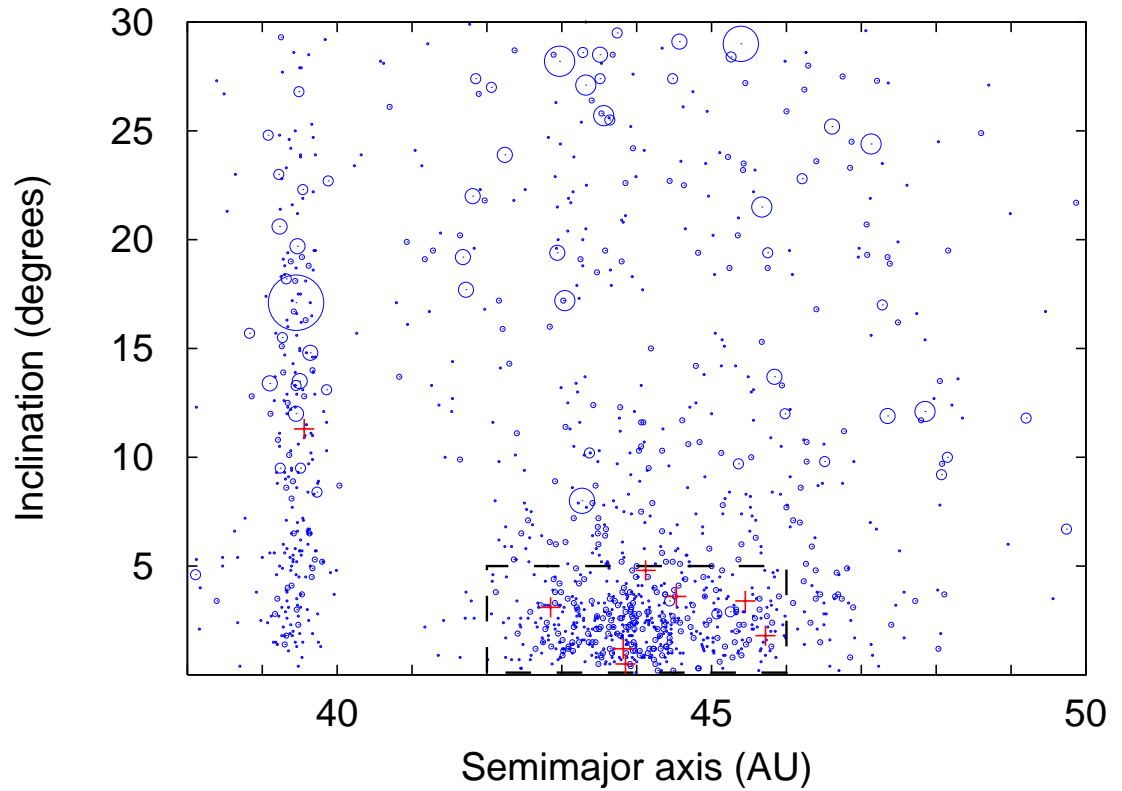
Figure 1.1: Known objects in the Kuiper Belt, plotted in semimajor axis and inclination. The size of the circles corresponds to the size of bodies (where sizes are unmeasured, it assumes an albedo of 0.04). Long period binaries are denoted with red '+'. The approximate region of the Cold Classical Kuiper Belt is enclosed by the black dashed line. Not that surveys preferentially target the ecliptic, so our knowledge is more complete at lower inclinations. The lack of large objects at low inclination is not an artifact of that selection bias. Orbital data and magnitude information for this plot is taken from the Minor Planet Center (2012), as well as Young et al. (2007); Stansberry et al. (2008); Sicardy et al. (2011); Sheppard et al. (2011); Parker et al. (2011); Müller et al. (2010); Elliot et al. (2010); Carry et al. (2011); Brucker et al. (2009); Brown et al. (2011a); Brown (2008)

that formed in situ would retain it, while KBOs that formed closer to the Sun would not (and formation closer to the Sun is expected for the other populations (Malhotra, 1995; Levison et al., 2008)). Alternatively, colours may reflect the evolutionary history, for instance, where the red colour is caused by the polymerization of surface ices by cosmic rays, and the grey colour caused by the excavation of fresh ices in collisions (Luu & Jewitt, 1996; Delsanti et al., 2004). Cold Classical Kuiper Belt objects also have higher albedos than do members of the other populations (as well as the low eccentricity, low inclination objects inside of 42 AU) (Brucker et al., 2009).

The largest CCKBOs are much smaller than the largest KBOs in all other populations (Levison & Stern, 2001; Brown, 2001). For the largest KBOs, their radii are well constrained, at 1163 ± 6 km (Sicardy et al., 2011), and 1173^{+20}_{-10} km (Zalucha et al., 2011), with many additional objects $\gtrsim 500$ km (Stansberry et al., 2008). The largest CCKBOs are ~ 200 km in radius, with a fairly large uncertainty, as these values are obtained in model dependent ways (e.g., Fraser et al., 2010; Müller et al., 2010). Additionally, the size distribution of CCKBOs is steeper than other populations. If we parameterise the size (s) number (n) distribution of KBOs in the form:

$$\frac{dn}{ds} \propto s^{-q} . \tag{1.2}$$

Observations find that CCKBOs have $q = 5.1 \pm 1.2$ (Fraser et al., 2010), $q = 7^{+1}_{-1.5}$ (Petit et al., 2011), at large sizes. At a size ~ 50 km, the power breaks to a shallower form (Bernstein et al., 2004), which is constrained to be $q \lesssim 4$ (Schlichting et al., 2009). Particular care must be paid to where the fitting is done, as fitting a different range of sizes will give a different q (Fuentes & Holman, 2008), as will the criteria used to discern CCKBOs from other KBOs. Scattered objects, in contrast, have $q = 2.8 \pm 1.1$ (Fraser et al., 2010), $q = 2.8 \pm 0.1$ (Vitense et al., 2010) (figure 1.2 contrasts the Cold Classical Kuiper Belt from the total population). Most of the mass in the Cold Classical Kuiper Belt is in ~ 50 km size objects, while most of the mass in hot KBOs is in ~ 1000 km objects. In rough terms, the CCKB is $50 \pm 20\%$ of the classical bodies (Kavelaars et al.,

2009), and the total classical belt has a mass $0.01 \sim 0.05 M_{\oplus}$ (Fuentes & Holman, 2008; Vitense et al., 2010). These mass estimates should be regarded with some suspicion, as they are made with assumed albedos that are probably too low for CCKBOs (Brucker et al., 2009), and thus may overestimate the mass. As an order of magnitude estimate, $\sim 10^{-2} M_{\oplus}$ should be regared as secure.
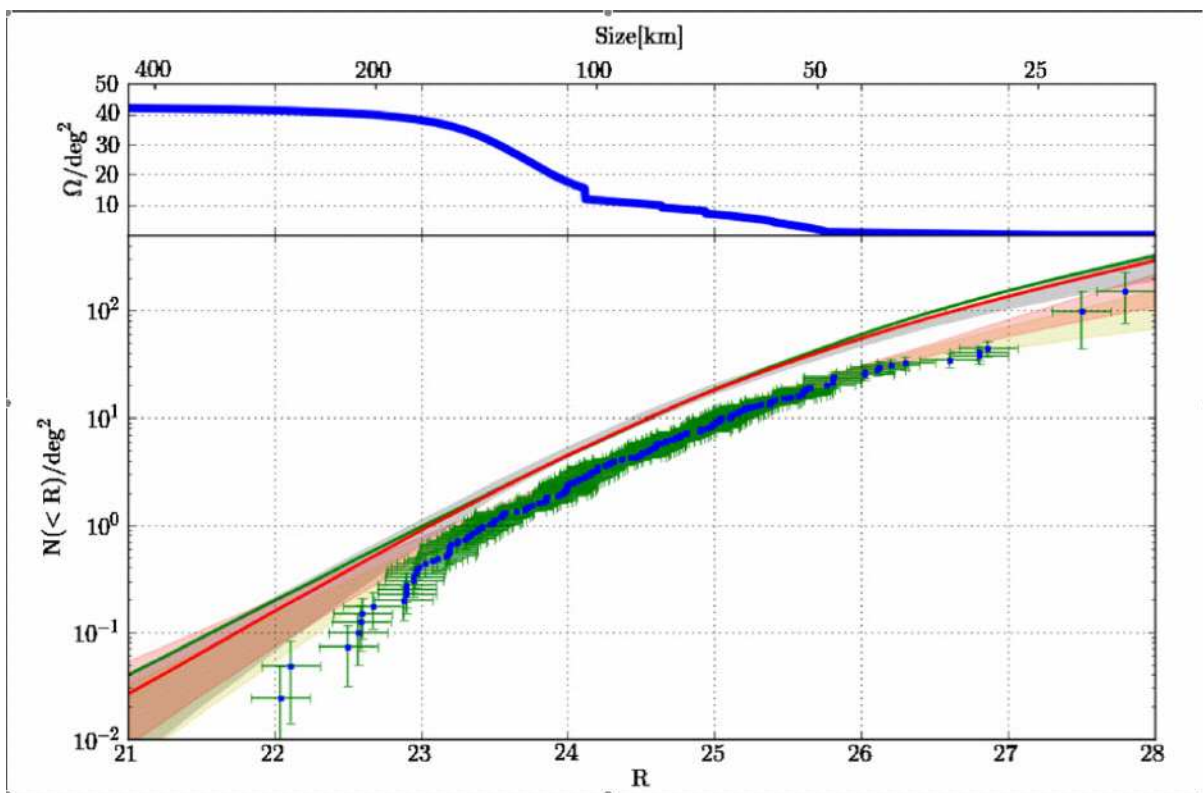
Figure 1.2: Size number distribution of the Cold Kuiper Belt Objects, from Fuentes et al. (2010). The bottom plot shows observed cold ($i < 5°$) bodies from their survey, combined with several others (blue points, with green error bars), as well as the best fit to their survey (green solid line), and all surveys (red solid line). Note that "Size" here refers to the diameter of bodies. The cold bodies with size $\gtrsim$ 75 km do not obey the same size number distribution as the population as a whole. The top plot shows the effective observing area of the combined surveys (Ω) as a function of their sensitivity to bodies of a given size.

The fraction of CCKBOs that are binaries is much higher than the fraction of all KBOs that are binaries. Noll et al. (2008) found that $29^{+7}_{-6}\%$ of objects with inclination less than 5.5° were detectable binaries, while $9.3^{+6.7}_{-4.4}\%$ were binaries. That rate probably understates the true difference, as the brightest KBOs in that sample had many detectable binaries, and were all high inclination. Using on the dimmer bodies (so the two populations are more alike), the fraction fell to $2.9^{+6.5}_{-2.4}\%$. Additionally, all of the known ultra-wide binaries (those with separations $\gtrsim 0.1$ Hill radii) are CCKBOs (Parker et al., 2011). The difference in binary fraction could represent a difference in formation, although it is more often taken to represent a different dynamical history, where primordial binaries in the hot populations were subsequently disrupted. Close encounters with Neptune will disrupt binaries, especially ultra-wide ones (Parker & Kavelaars, 2010a). Current orbits keep most KBOs (apart from scattered objects) far away from Neptune. It is generally accepted, however, that much of the current architecture was produced during an outward migration of Neptune (Fernandez & Ip, 1984), which trapped the resonant populations into their mean-motion resonances Malhotra (1993); Malhotra et al. (2000), scattered, hot classical, and detached objects into their current orbits (Duncan & Levison, 1997). Such an event produces the dynamics of the KBO populations apart from the CCKBOs (Levison et al., 2008), and would naturally explain their low binary fraction and lack of wide binaries. The scattering event can leave a primordial population at the position of the CCKB intact (Batygin et al., 2011), correspondingly with their high binary fraction and wide binaries.

Given all these considerations, we find the Cold Classical Kuiper belt to be of particular interest, and thus expound upon its properties here. The CCKB extends from ~ 42 to ~ 46 AU in semi-major axis. Interior to 42 AU, low inclination orbits are unstable on timescales of $\sim 10^7$ years (Duncan et al., 1995). At 40-42 AU, overlapping secular resonances of Uranus and Neptune produce this orbital instability (Knezevic et al., 1991; Lykawka & Mukai, 2005). An outer edge to the CCKB is detected at $45 \sim 46$ AU

(Dones, 1997; Hahn & Malhotra, 2005; Kavelaars et al., 2009). The origin of the outer edge is not established. The decreased surface density continues for at least ~ 10 AU (Bernstein et al., 2004; Parker & Kavelaars, 2010b). The most obvious explanation is that it is the primordial edge of the solar system, as no evidence of MMSN type results are detected at larger distances. From the overdensity of KBOs at low inclination, the inclination distribution of CCKBOs seems to have a characteristic scale $2 \sim 3°$ (Brown, 2001; Gulbis et al., 2010). This is not very secure, as other results show the presence of a substantial number of CCKB-type objects at inclinations of up to $\sim 10°$ (Peixinho et al., 2008; Fuentes et al., 2011).

1.2.3   Trans-Neptunian Dust

In addition to direct imaging of the large bodies, the Kuiper Belt can also be detected by the presence of small dust grains in the outer solar system. A substantial fraction of these grains are produced in collisions between Kuiper Belt objects (also see Yamamoto & Mukai, 1998). Impacts of dust grains onto the Voyager spacecrafts find small dust grains to ~ 50 AU from the sun (Gurnett et al., 1997). Other probes with instruments more suited to detecting dust grains have detected dust grains inside 20 AU, some of which must originate in the Kuiper belt (Landgraf et al., 2002; Poppe et al., 2010)[1]. The Voyager results give a volume density of dust grain that is $\sim 2 \times 10^{-14}$ cm^{-3} in the ecliptic. Given the uncertainties in dust scale height, the size of the grains, etc., the dust density implies the grains should have a total (thermal + reflected) luminosity at least $\sim 10^{-8} L_\odot$. This is well below the upper limits set by observation of $\sim 10^{-6} L_\odot$ (Teplitz et al., 1999; Ichikawa & Fukugita, 2011). The dust of the outer solar system is confused with similar dust in the inner solar system, produced by asteroids and comets, which has

---

[1] By assuming all grains are the maximum detectable mass from the Pioneer experiments, then placing them at 40 AU.

a total luminosity of $\sim 5 \times 10^{-8} L_\odot$ (Hahn et al., 2002)[2].

1.3   Extrasolar Debris Disks

Observations of young stars have confirmed that they have circumstellar nebulae (Mc-Caughrean & O'Dell, 1996). These nebulae posses comparable sizes and masses to those of the MMSN (with significant dispersion), lending additional weight to the nebular hypothesis (Andrews & Williams, 2005). Such circumstellar disks are ubiquitous around young stars, and the disks disappear within 1-10 Myrs (Zuckerman et al., 1995; Haisch et al., 2001). A similar timescale should be expected to apply to the solar nebula. Although the solar nebula may have been truncated at as little as 30 AU, extrasolar nebulae can extend to hundreds of AU from the central star (Dutrey, 2007).

Dust grains around older stars have been detected in both reflected starlight (Smith & Terrile, 1984) and thermal radiation (Aumann et al., 1984). A host of surveys have followed: Walker & Wolstencroft (1988); Oudmaijer et al. (1992); Su et al. (2006); Bryden et al. (2006); Lestrade et al. (2009); Matthews et al. (2010); Moór et al. (2011). Analogous to the dust in the solar system, these disks must be fed fresh dust by larger parent bodies. Typical surveys can detect extrasolar dust disks as dim as $\sim 10^{-4} L_*$. At present, the Herschel telescope is bringing that limit down to $\sim 10^{-6} L_*$, which means that we should soon have an observational sample of Kuiper belt-like debris disks around other stars (Eiroa et al., 2010). In the interim, we must make do understanding the statistics of those debris disks already detected. With luminosities $10^2 - 10^4$ times that of the sun, it is a puzzle how the sun fits into this picture. Indeed, if one extrapolates from the observed population, the sun is unusually faint, among the dimmest 10% of solar-type stars (Greaves & Wyatt, 2010).

In the sample of known disks, at fractional luminosities of $10^{-4} L_*$ or higher, debris

---

[2]The possibly dimmer inner solar system is able to obscure the outer solar system because these observations are all taken near the Earth.
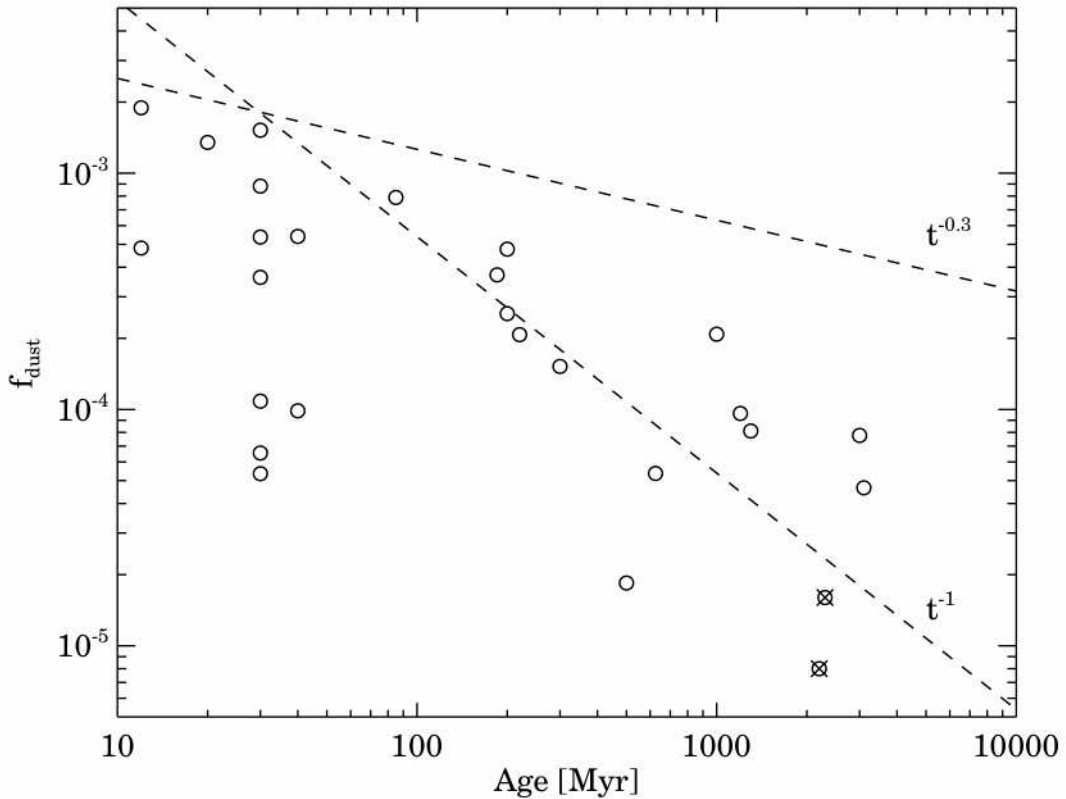
Figure 1.3: Fractional luminosity against stellar age for debris disks observed around nearby F stars, from Moór et al. (2011). The $t^{-0.3}$ line represents the predicted luminosity evolution from Löhne et al. (2008), and the t^{-1} represents the predicted luminosity evolution from Wyatt et al. (2007b). Both are steady state collisional cascade debris disk models. The decay is comparable to what is expected from steady state collisional cascade models. Disks show a slow decay in fractional luminosity, from a maximum of $\sim 10^{-3}$ at $\sim 10^8$ years to a maximum of $\sim 10^{-4}$ at $\sim 10^{10}$ years.

disks with 70 μm excess are found around $\sim 15\%$ of solar type stars, a fraction which decays little with age (Trilling et al., 2008) (figure 1.4). While the total population of detectable debris disks remains roughly constant with age, the brightest disks decay in luminosity - the occurence of bright disks ($> 5 \times 10^{-4}$) decays sharply with age, with few detectable around stars more than 100 Myrs old (Moór et al., 2006). Assuming a

11

blackbody spectrum, $70\mu m$ emission corresponds to dust at 10 - 100 AU. The luminosity evolution of the population is consistent with the slow grind down of massive kuiper belt analogues in a steady state cascade (e.g., Moór et al., 2011). Some models of the origin of the solar systems' low luminosity disk rely on sharp transition in brightness associated with dynamical clearing of the primordial population (e.g., Booth et al., 2009). If that is the case for the solar system, however, it would appear to make it an outlier.
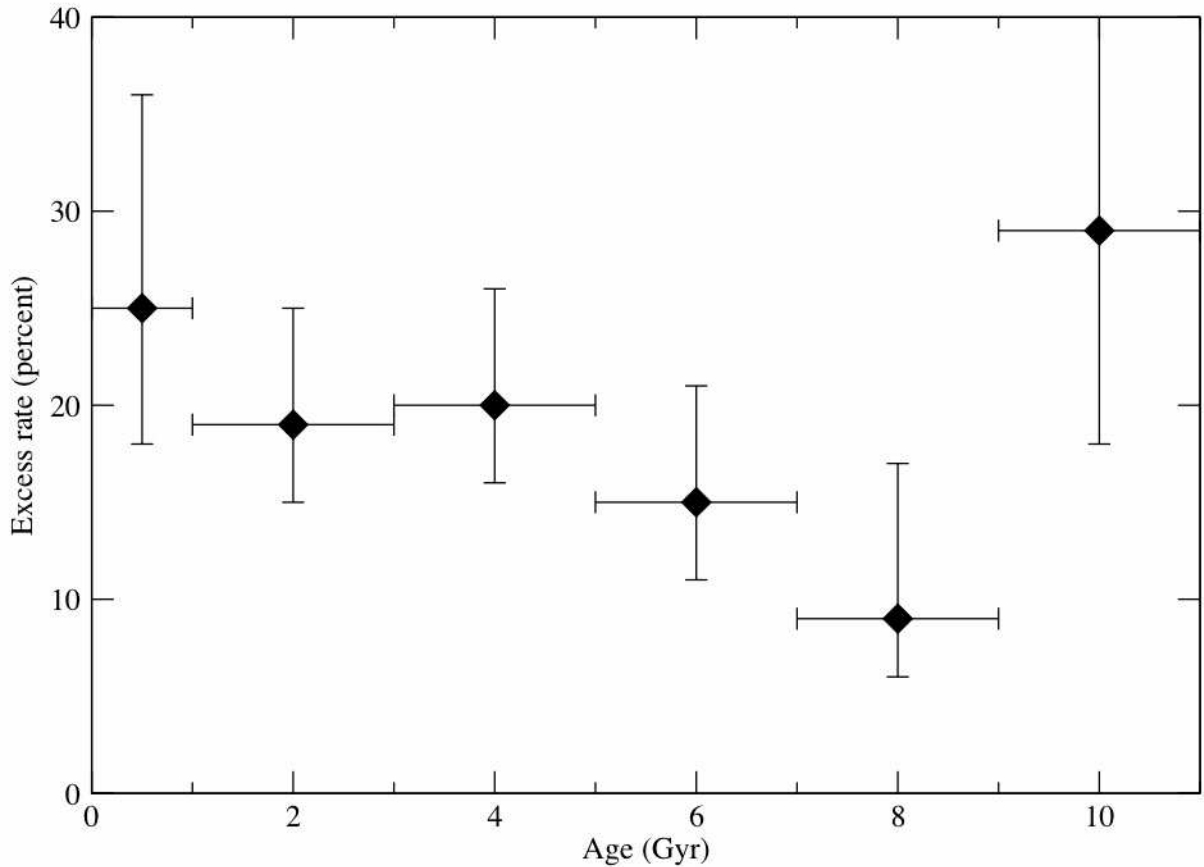
Figure 1.4: Fraction of FGK stars with detectable debris disks as a function of the stellar age, from Trilling et al. (2008). The survey was done with 24 μm and 70 μm data from the Spitzer Space Telescope. The detection threshold was relative to the noise in the observations of the particular star, but detections were typically at fractional luminosities of $10^{-5} \sim 10^{-4}$.

At shorter wavelength (which measures hotter dust located closer to the host star) the fraction of the stellar population with detectable debris disks is much smaller (e.g. at 24 μm, corresponding to 1-10 AU for blackbodies, the detection rate is $\sim 4\%$ of solar type stars at ages of $10^8 \sim 10^{10}$ years (Trilling et al., 2008), while it is $\sim 10\%$ before 10^8 years (Meyer et al., 2008). Many of the older systems with warm dust (within a few AU) must be transient events (Wyatt et al., 2007a; Smith et al., 2008), in contrast to the cold dust systems, which can all be steady state cascades. Most known warm disks are around young ($\lesssim 100$ Myrs) (Moór et al., 2009, and references therein), but this may be a selection bias in surveys for warm dust disks. Although in the MMSN surface density (and thus, dust luminosity) peaks at the star, this distance dependence is not surprising. Steady state debris disk models predict that evolution proceeds inside out (chapter 2). At distances of 10s of AU, the decay time becomes comparable to stellar ages (Gyrs), while closer to the star, the disks are more evolved, and thus dimmer.

1.4 Physics of Debris Disks

1.4.1 Radiative Blowout

A spherical dust grain orbiting a star intercepts the stellar radiation, which provides an outward momentum (Kepler, 1619; Maxwell, 1873; Lebedev, 1901). Outgoing radiation with energy E has momentum $p = E/c$, (where c is the speed of light), and consequently a dust grain of radius s, orbiting the star with luminosity L_* at a distance a intercepts outgoing momentum at a rate:

$$\frac{dp}{dt} = F_{\text{rad}} = \pi s^2 \frac{L_*}{4\pi a^2 c} \; . \tag{1.3}$$

This force can be compared with the gravity from the star $F_g = \left(4\pi\rho s^3\right)/3 \times \left(GM_*\right)/\left(a^2\right)$, (where M_* is the star's mass, and ρ is the mass density of the grain) to yield the ratio of

Physical constant	Symbol
Speed of light	$c \equiv 29979245800$ cm s^{-1}
Gravitational constant	$G \approx 6.67 \times 10^{-8}$cm^{3}g^{-2}s^{-1}
Mass of the Earth	$M_\oplus \approx 6 \times 10^{27}$g

Properties of the central star	Symbol
Mass	M_*
Radius	R_*
Luminosity	L_*
Angular size	α

Properties of orbiting bodies.	In some cases, we divide bodies into two groups; in this case, the symbols for small and large bodies are listed in parentheses $(small, large)$
Mass density	ρ
Radius	s, (s, R)
Mass	$m = \frac{4\pi}{3}\rho s^3$
Specific energy for catastrophic disruption	Q^*
Escape velocity	$v_{\text{esc}} = \sqrt{\frac{2Gm}{R}} \sim \sqrt{G\rho}R$
Semimajor axis	a
Planetesimal belt radial width	Δa
Orbital eccentricity	e
Orbital inclination	i
Orbital period	$P = \sqrt{\frac{4\pi^2}{GM_*}a^3}$
Orbital frequency	$\Omega = \sqrt{\frac{GM_*}{a^3}}$
Keplerian velocity	$v_{\text{kep}} = \frac{2\pi a}{P} = \Omega a = \sqrt{\frac{GM_*}{a}}$
Hill radius	$R_{\text{H}} = a\sqrt[3]{\frac{m}{3M_*}} \sim \frac{R}{\alpha}$
Hill velocity	$v_{\text{H}} = \Omega R_{\text{H}} \sim \alpha^{-\frac{1}{2}}v_{\text{esc}}$
Velocity dispersion	$v \sim \sqrt{e^2 + i^2}v_{\text{kep}}$, (u, v)

Table 1.1: Symbolic notation commonly used in this work.

the two forces:

$$\beta \equiv \frac{F_{\text{rad}}}{F_{\text{g}}} = \frac{L_*}{GM_*} \frac{3}{16\pi\rho c} s^{-1}. \tag{1.4}$$

Alone, a particle for which $\beta = 1$ would be necessarily unbound from the system, with no net force to hold it. Around sun-like stars, this means that particles smaller than $s \sim 10^{-4}$ cm are unbound. When a grain is released from a much larger body on a circular Keplerian orbit, if $\beta \geq 0.5$ the grain will escape. Given the uncertainties based on grain shape, density, etc, this should not be taken as more than an order of magnitude estimate for grain size in a real disk anyhow. So we write:

$$s_{\text{blow}-\text{out}} \sim \frac{L_*}{GM_*} \frac{3}{8\pi\rho c}. \tag{1.5}$$

In practice, this will not form a perfectly sharp cut-off, but we can approximate the disk as having no particles below $s_{\text{blow}-\text{out}}$ for most purposes (Löhne et al., 2008). When particles with $\beta \gtrsim 0.5$ are produced, they leave the system on hyperbolic orbits. The outgoing grains can cause avalanching collisional cascades in particularly dusty disks (Grigorieva et al., 2007), but in most cases it can be treated as instantaneously removed.

1.4.2   Poynting Robertson Drag

A body orbiting a star will experience a drag from the radiation pressure. Photons streaming outwards are encountered as a headwind by the moving bodies, which consequences experiences a drag force, called the Poynting-Robertson (PR) drag (Poynting, 1904; Robertson, 1937). The resulting force has the form (Burns et al., 1979):

$$\vec{F} \approx \frac{SA}{c} Q_{\text{pr}} \left[\left(1 - \frac{\dot{r}}{c} \right) \hat{S} - \frac{\vec{v}}{c} \right] \tag{1.6}$$

Where S is the total flux density of outgoing radiation, A is the cross-section of the grain $(A \sim \pi s^2)$, r is the distance from the sun, $\hat{S}$ is the unit radial vector, and Q_{pr} is a quality factor that accounts for how the incident radiation is absorbed, reflected, and re-emitted. A perfect absorber has $Q_{\text{pr}} = 1$, and the Sun has $S \approx 1.36 \times 10^6$ erg/s/cm^2 $\left(\left(1 \text{ AU}^2 \right) / \left(a^2 \right) \right)$.

A particle on a circular orbit has $\dot{r} \approx 0$. In that case, starting from a semimajor axis a_0, the force can be integrated to solve for the evolution of the circular orbit's semimajor axis, which obeys:

$$a \sim a_0 e^{-\frac{S}{c^2 \rho s t}}. \tag{1.7}$$

So the grains fall towards the star with a timescale $\tau_{\mathrm{pr}} \sim c^2 \rho s a^2 L_*^{-1}$. For cm sized grains at 1 AU, this is of order one million years. Micron sized grains at the earth's position will spiral into the sun within a few hundred orbits, but live $\sim 10^7$ orbits before a catastrophic collision. At 40AU, these numbers of $\sim 10^3$ and $\gtrsim 10^6$ respectively. The solar debris disk loses mass primarily by PR drag. For extrasolar debris disks, however, the collision times in the outer disk are much shorter, typically $\sim 10^2 - 10^4$ orbits for those disks which have so far been detected (§1.3). In this case, we might expect that radiation blow-out might be expected to compete with PR drag as the dominant dust removal mechanism, and a more detailed analysis shows that collisional destruction with radiative blow-out is the dominant mass removal mechanism in extrasolar disks (Wyatt, 2005).

1.4.3 Disruption of Bodies

In a debris disk, bodies evolve by primarily catastrophic disruption. A collision is defined to be catastrophically disruptive if the body loses at least 50% of its original mass. An ideal strengthless body can be disrupted if enough energy is imparted in a collision to move half the mass to infinitety. A shell a distance s from the body's center, with mass $dm = 4\pi \rho s^2 ds$ can be lifted from a body of mass $s = 4\pi/3\rho s^3$ to infinity with energy dU, where:

$$dU = -\frac{16\pi^2}{3} \frac{G\rho^2 s^5}{s} ds, \tag{1.8}$$

this means for a body of uniform density, and size s_0, a total energy of $U = \int_{2^{-(1/3)} s_0}^{s_0} dU = (16/15) \pi^2 G \rho^2 s_0^5$ is needed for catastrophic disruption. The usual convention measures the specific energy of catastrophic disruption, $Q^* = U/m$, so an ideal strengthless body

has

$$Q^* = \frac{4\pi}{5} G\rho s^2. \tag{1.9}$$

Non-ideal bodies will require more energy, in a fashion that may be radius or impact velocity dependent. Simulations, laboratory experiments, and theoretical arguments favour $Q^* \propto s^\beta$ with $1.2 \lesssim \beta \lesssim 2$ (Benz & Asphaug, 1999; Pan & Sari, 2005; Stewart & Leinhardt, 2009, and references therein) for large bodies where gravitational self binding is the primary source of cohesion.

In smaller bodies, the need to fragment the body is what sets the threshold for disruption. Once fragmented, the pieces are dispersed rather easily, the opposite of the large body case just discussed. For a naive physical picture, we can imagine a catastrophic disruption breaks a body of mass m_0 into fragments of masses 0 to $m_{\max}$, which obey a single, cumulative power law $N\,(> m) = \xi m^{-l}$, where ξ, l are material constants. By requiring $N\,(m_{\max}) = 1$, we get $\xi = m_{\max}^l$, and from mass conservation we get $l = (1 + m_{\max}/m_0)^{-1}$, where m_0 is the mass of the disrupted body (Greenberg et al., 1978). A minimally catastrophic collision will have $m_{\max} = 0.5m_0$ (from the definition of catastrophically disruptive), and a maximally catastrophic collision (no large fragments at all) will have $m_{\max} << m_0$; these two cases have $l = 2/3$ and $l = 1$ respectively. The newly created bodies have total surface area:

$$A = \int_{m_{\min}}^{m_{\max}} -4\pi\xi\frac{l}{l+1}m^{-(1+l)} \left(\frac{3}{4\pi\rho}\right)^{\frac{2}{3}} m^{\frac{2}{3}} \tag{1.10}$$

The final surface area thus obeys $A \propto m_0^l$. If we assume that the energy required to create the new surfaces is proportional to their area, then $Q_{\mathrm{crit}} \propto m_0^l$, and we have

$$Q^* \propto s^{3(1-l)}, \tag{1.11}$$

with $2/3 \leq l \leq 1$. Q^* should decrease with size for small bodies. This approach follows Farinella et al. (1982), and is meant only to be illustrative of how one might think about disruption of small bodies. For instance, Housen & Holsapple (1990) develop a model

in which disruption of small asteroids is accomplished by the joining of pre-existing cracks in the material, which is more accurate. Many subsequent models (e.g., Benz & Asphaug, 1999; Jutzi et al., 2008; Stewart & Leinhardt, 2009) better characterise catastrophic disruption, and should be employed in any investigation (as we do, later, in our numerical investigations).

Thus we turn to the numerous numerical, analytic, and even experimental approaches which have been used to estimate the criterion for catastrophic disruption of a body. The current canonical approach is that of Benz & Asphaug (1999). The employ a critical specific energy for catastrophic disruption for a body of size R:

$$Q^* = Q_0 \left(\frac{R}{1 \text{ cm}} \right)^a + B\rho \left(\frac{R}{1 \text{ cm}} \right)^b. \tag{1.12}$$

A body of mass M is catastrophically disrupted by a body of mass m in a collision if the impact velocity u exceeds:

$$\frac{1}{2}mu^2 \geq Q^*M. \tag{1.13}$$

The specific values of the material constants Q_0, a, B, b that Benz & Asphaug (1999) vary with the material of the parent body, and the speed of impact. In particular, they report values of Q^* as shown in table 1.2. Although the formulation considers only energy, that

Table 1.2: Coefficients of the critical specific energy for catastrophic disruption in Benz & Asphaug (1999)

material	v(km/s)	Q_0(erg/g)	B(erg cm^3/g^2)	a	b
basalt	5	9.0×10^7	0.5	-0.36	1.36
basalt	3	3.5×10^7	0.3	-0.38	1.36
ice	3	1.6×10^7	1.2	-0.39	1.26
ice	0.5	7.0×10^7	2.1	-0.45	1.19

the values of Q_0, B, a, and b depend on the velocity implies that momentum is a factor.

Nevertheless, note that because $a < 0$ and $b > 0$ the $Q_0 \left(R/1 \text{ cm}\right)^a$ term is dominant at small sizes, and the $B\rho \left(R/1 \text{ cm}\right)^b$ term is dominant at large sizes. Effectively, Q^* can be thought of as having two regimes, one at small sizes where bodies are held together by molecular cohesion and van der waals forces, and one at large sizes, where bodies are held together by self-gravity. The transition size is typically expected to be $\sim 10^4$ cm. We can then separate equation 1.12 into two parts:

$$Q^* = \begin{cases} Q_0 \left(\frac{R}{1 \text{ cm}}\right)^a & R \lesssim 10^4 \text{ cm,} \\ B\rho \left(\frac{R}{1 \text{ cm}}\right)^b & R \gtrsim 10^4 \text{cm.} \end{cases} \tag{1.14}$$

Bodies experience two regimes of disruption. Bodies smaller than ~ 100 m are held together by intermolecular forces, and bodies larger than ~ 100 m are held together primarily by their self-gravity.

1.4.4 A Size-Number Distribution for Bodies

In general, we express the relationship between the number of bodies n, and their size s in a differential power law with the form:

$$\frac{dn}{ds} = n_k s^{-q}. \tag{1.15}$$

Here n_k and q are parameterisations that depend on the population. Dohnanyi (1969) noted that if bodies are being broken apart in a scaleless way, $q = 3.5$ is the equilibrium solution. The arises from the fairly straightforward consideration that in an infinite scaleless collisional cascade, the mass flux must be constant. In this case, consider the mass flux at size s, broken up by particles of size ks, and the bodies broken up by the bodies of size s, having themselves a size $k^{-1}s$. Individual bodies of size s break up at a rate $\pi s^2 n \left(ks\right)^{-q} \Delta \left(ks\right)$, which means the total ns^{-q} should produce a total mass flux of:

$$\left. \frac{d\mathcal{M}}{dt} \right|_s \propto \pi s^2 n \left(ks\right)^{-q} \Delta \left(ks\right) n \frac{4\pi\rho}{3} s^3 \Delta s. \tag{1.16}$$

19

Compare this to the production at some other size, R. Then

$$\left.\frac{d\mathcal{M}}{dt}\right|_R \propto \pi R^2 n\, (kR)^{-q}\, \Delta\,(kR)\, n\frac{4\pi\rho}{3}R^3\Delta R.$$

At equilibrium, the mass flux at all sizes must be constant, i.e. $d\mathcal{M}/dt|_s = d\mathcal{M}/dt|_R$, so when we divide the two equations we find:

$$\left(\frac{s}{R}\right)^{7-2q} = 1, \tag{1.17}$$

which yields the solution $q = 3.5$. The same approach yields

$$q = \frac{6+\eta}{1+\eta}, \tag{1.18}$$

if a scale is introduced into the problem by having bodies of size s broken up by bodies of size ks^η (see e.g., Wyatt et al., 2011). Such a scale is expected from material properties, although it may also be introduced by a size dependent velocity (e.g., Pan & Schlichting, 2012). This is a more realistic case, and so we ask "What values of q do we expect in the size-number distribution, and where?"

We discussed realistic disruption criteria in section 1.4.3. Using those criteria, and assuming velocity dispersions do not depend on size in a debris disk, we find that during a collisional cascade, we expect bodies to obey two different power laws, joined at $\sim 10^4$ cm. From equation 1.13, we get that $\eta \approx 1 + a/3$ for small bodies, and $\eta \approx 1 + b/3$ for large bodies. For the values in table 1.2, equation 1.18 means that small bodies in collisional equilibrium will obey $-3.66 \gtrsim q_1 \gtrsim -3.70$, across the various impact velocities and possible material compositions. Likewise, large bodies in collisional equilibrium will obey $3.09 \gtrsim q_2 \gtrsim 3.04$.

1.5 Physics of Coagulation

1.5.1 Dynamical Fricton

A planetesimal moving through a swarm of other planetesimals will scatter off them due to gravity. The phenomena is not unique to planetesimal disks, and does not depend on the Keplerian potential; indeed, it was first identified in stellar clusters (Chandrasekhar, 1943). Such kicks occur in random directions, and sum in the first order to zero if the planetesimal is moving with the bulk flow. If the planetesimal is not moving with the bulk flow, it will preferentially receive kicks that tend to align it with the bulk flow. This movement against the bulk flow provides a retarding term. The planetesimal (represented with a subscript 1) moves at speed v through the sea of bodies (represented here with the subscript 2) moving at speed u, encountering them in face-on collisions at a rate:

$$f_c = \frac{n_2}{V} \pi b^2 \left(v + u \right), \tag{1.19}$$

where n_2/V is the volume density of other bodies, and πb^2 is the cross section for an interaction which changes the velocity of body two by $\sim u$ (this equation and much of this derivation is from Goldreich et al., 2004b). Each such encounter imparts a momentum kick of size $\Delta \vec{p} \sim m_2 \left(v + u \right) \times -\vec{v}/ |\vec{v}|$. This combines with the tail-on collisions (which occur at a frequency proportional to $v - u$ and impart a momentum kick proportional to $(v - u)$ to produce a velocity loss of

$$\frac{1}{v} \frac{dv}{dt} \bigg|_{\parallel} \approx -\frac{m_2}{m_1} \frac{n_2}{V} u b^2. \tag{1.20}$$

In addition to that term which operates parallel to body 1's velocity, a second order term operates orthogonal to body 1's velocity (as body 2 generically has a parallel and an orthogonal velocity component). These kicks have a magnitude $v_{\text{kick}} \sim \left(m_2/m_1 \right) u_{\perp}$, and for isotropic u we can assume $u_{\perp} \sim u$. Because they are randomly oriented, the first order term vanishes, as a kick and its opposite are equally likely. The second order terms

over $\mathcal{N}$ interactions add up $\sum v_{\text{kick}}^2 \sim \mathcal{N} (m_2/m_1)^2 u^2$. These kicks add, and the body m_1 sees its velocity double once $\langle \sum v_{\text{kick}}^2 \rangle^{0.5} \sim v$. Thus we can write:

$$\frac{1}{v}\frac{dv}{dt}\bigg|_{\perp} \approx \frac{n_2 \pi v b^2}{V \mathcal{N}} \approx \frac{n_2}{V}\pi v b^2 \left(\frac{m_2 u}{m_1 v}\right)^2 \approx -\frac{m_2 u^2}{m_1 v^2}\frac{1}{v}\frac{dv}{dt}\bigg|_{\parallel}. \tag{1.21}$$

We can combine these terms to form a full dynamical friction equation:

$$\frac{1}{v}\frac{dv}{dt}\bigg|_{\parallel} \approx -\frac{m_2}{m_1}\frac{n_2}{V}ub^2 \left(1 - \frac{m_2 u^2}{m_1 v^2}\right). \tag{1.22}$$

Note that the right hand side is zero when $m_1 v^2 = m_2 u^2$. So in the presence of dynamical friction and the absence of anything else, the bodies will come to an equilibrium of $m_1 v^2 \sim m_2 u^2$ for any sizes $1, 2$, which is the equipartition of kinetic energy. With other forces present, dynamical friction will work towards equipartitioning kinetic energy. In debris disks, equations for dynamical friction are necessarily more complicated, the presence of the central star distorts the geometry (a factor we've entirely neglected here).

The interaction radius b has two regimes. When the encounter velocity is dominated by the random velocities of the bodies (i.e., $u > v_{\text{H}}$), an encounter at separation b will spin u through a large angle if the force of gravity between the bodies $Gm_1 m_2/b^2$ is comparable to the centrifugal force for a circular path $m_2 u^2/b$ of that radius. In that case, we have $b \sim Gm_1/u^2 \sim R (v_{\text{esc}}/u)^2$. Then the dynamical friction term is:

$$\frac{1}{v}\frac{dv}{dt} \sim -\frac{\sigma \Omega}{\rho R}\left(\frac{v_{\text{esc}}}{u}\right)^4 \left(1 - \frac{m_2 u^2}{m_1 v^2}\right), \tag{1.23}$$

where $\sigma \sim m_2 n_2 / (2\pi a \Delta a)$ is the surface mass density of the small bodies we labelled with the subscript 2, and we substituted $V \sim 2\pi a \Delta a h$, where h is the scale height of bodies, with $h \sim (u/v_{\text{kep}}) a \sim u/\Omega$ so that our expression for the rate is the same as Goldreich et al. (2004b). If the encounter velocity is dominated by the Keplerian shear, the encounter distance is typically the Hill radius R_{H}, and the encounter velocity is the Hill velocity v_{H}. In that case, the kick received is $v_{\text{kick}} \sim (m_2/m_1) v_{\text{H}}$, and the dynamical friction is

$$\frac{1}{v}\frac{dv}{dt} \sim -\frac{\sigma \Omega}{\rho R}\alpha^{-2} \left(1 - \frac{m_2 v_{\text{H}}^2}{m_1 v^2}\right). \tag{1.24}$$

In most applications viscous stirring will serve to keep the large bodies much hotter than equipartition, and the left bracket in equations 1.23 and 1.24 is very close to unity, and can be ignored.

1.5.2 Viscous Stirring

Unique to disks orbiting in a central potential is viscous stirring. This process takes potential energy out of the central potential and converts it into random motions. It can be qualitatively understood as follows (Safronov, 1969; Goldreich et al., 2004b). Consider a body of mass m, on an eccentric orbit (with random velocity u_{random}), encountering much larger bodies on circular orbits. Because their interactions conserve both energy and momentum, velocity vectors are rotated randomly in the center of mass frame. In the orbital plane, the vectors are rotated an average of $\pi/2$. If an encounter occurs at apoapse or periapse, the random velocity vector is rotated from being in line with the keplerian velocity vector to being orthogonal to it, changing the total velocity from $u_{\text{kepler}} + u$ to $\sqrt{u_{\text{kepler}}^2 + u^2} \approx u_{\text{kepler}} + 0.5u$ (here I have assumed $u_{\text{kepler}} >> u$). Thus the random velocity is halved. If the encounter occurs at quadrature, the process is reversed, and the random velocity is doubled. Then the average kinetic energy in an encounter is changed from $mu^2 \rightarrow 0.5m\left(0.5u\right)^2 + 0.5m\left(2u\right)^2 = 17/8mu^2$. The numeric coefficient is wrong, of course, but the underlying mechanism is elucidated.

The encounter rate is the same as in section 1.5.1, so we can write a stirring equation of the form:

$$\frac{1}{u}\frac{du}{dt} \sim \frac{n_2}{V}u\pi b^2,\tag{1.25}$$

and as in section 1.5.1, when smaller bodies stir bigger bodies (those with mass M and random velocity v), so we need multiple collisions to achieve a turn of $\pi/2$. The same random walk principle as we used to derive equation 1.21 applies, and we get:

$$\frac{1}{v}\frac{dv}{dt} \sim \frac{n_1}{V} u \pi b^2 \left(\frac{Mv}{mu}\right)^2. \tag{1.26}$$

Here we use V defined by the larger velocity (presumably u). It is notable that the form of b here is different from section 1.5.5. There, gravitational focussing must be sufficient to bring bodies into contact, here it needs only to be sufficient for the bodies to be rotated through an angle of $\pi/2$. This happens for an impact parameter b where the kinetic energy mu^2 of the incoming particle is equal to the work done on it (roughly $GmM/b^2 \times b$), or $b \sim Gm/u^2 \sim R\left(v_{\rm esc}/u\right)^2$. Then the stirring is

$$\frac{1}{u}\frac{du}{dt} \sim \frac{n_2}{V} u \pi R^2 \left(\frac{v_{\rm esc}}{u}\right)^4 \sim \frac{\Sigma\Omega}{\rho R}\left(\frac{v_{\rm esc}}{u}\right)^4. \tag{1.27}$$

This form applies only to dispersion dominated encounters. Shear dominated encounters proceed differently. Then all bodies entering the Hill sphere (which they do with frequency $f \sim \left(n_2/V\right) u R_{\rm H}^2$) acquire a velocity dispersion of roughly the Hill velocity. Since they begin with much less velocity, they gain energy of roughly $m v_{\rm H}^2$. So they have an effective $b \sim R_{\rm H}\sqrt{v_{\rm escape}/u}$. In that case, the viscous stirring rate is

$$\frac{1}{u}\frac{du}{dt} \sim \frac{n_2}{V} u \pi R_{\rm H}^2 \left(\sqrt{\frac{v_{\rm esc}}{u}}\right)^2 \sim \frac{\Sigma\Omega}{\rho R}\alpha^{-2}\left(\frac{v_{\rm H}}{u}\right). \tag{1.28}$$

Detailed equations appropriate for keplerian disks have been developed by various authors (Safronov, 1969; Stewart & Kaula, 1980; Hornung et al., 1985; Stewart & Wetherill, 1988; Ida et al., 1993; Stewart & Ida, 2000; Ohtsuki et al., 2002). Typically this is done in conjunction with dynamical friction, as is the case with most of the references listed.

1.5.3 Sticking of Small Grains

Stars form from the gas in giant molecular clouds, with is embedded with dust particles less than a micron in size. As the cloud collapses, the amount of angular momentum present results in a disk forming around the central protostar with $\sim 10^{-1} - 10^{-2}$ of the

total mass. As the densities increase, dust grains begin to frequently collide, and small dust grains stick to one another by van der Waals forces in low velocity collisions.

1.5.4 The First Planetesimals

Micron sized grains are strongly coupled to the gas. As the grains grow larger, they become partially decoupled from the gas. The decoupling raises the grains' random velocities as the gaseous disk rotates more slowly than a particle disk, due to gas pressure support (Adachi et al., 1976). The partially decoupled grains move at intermediate speeds, so their relative velocities become too high for effective sticking (Blum, 2010). Compounding that problem, Weidenschilling (1977a) showed that while very small particles are well-coupled to the gas, following sub-keplerian orbits, and large bodies effectively decouple from the gas, losing only a small amount of energy to the gas disk over the system life, intermediate sized bodies experience a strong drag and migrate quickly towards the central star. At 1 AU, they find a lifetime of $\sim 10^2$ years for meter-sized bodies, growing only to $\sim 10^4$ years at Kuiper belt distances. The theoretical difficulties in growing meter-sized particles are known as the "meter size problem". Subsequent estimates have re-iterated this problem (Klahr & Bodenheimer, 2006).

In order to solve the meter size problem, theorists have eschewed meter sized bodies for more cooperative sizes. Safronov (1969), and independently Goldreich & Ward (1973) showed that if centimeter sized bodies could settle to the mid-plane of the protostellar disk, they could collapse under self-gravity to form kilometer sized objects. Without de-coupling of the gas and dust (which can be incomplete), the gas, with $\sim 10^2$ times as much mass as the dust, is dominant in the collapse. Collapse of gas produces Jovian (or larger) bodies at large radii, it cannot be the source of smaller bodies, such as asteroids or Kuiper belt objects (Kratter et al., 2010). Small dust grains will remain bound to the gas, however, as grains become larger, they will begin to settle out of the nebula towards the mid-plane. If the density of the small grains exceeds the Roche density, they will

be bound and may collapse. Historically, it was believed that the interface between the gas rich and dust rich layers would become unstable, and excite turbulence that would prevent them from becoming sufficiently thin for collapse (Weidenschilling, 1980, 1995).

Despite the difficulty in concentrating the small grains, direct collapse has continued to be favoured as the most promising way to form the first planetesimals. The question of how to achieve the densities necessary for gravitational collapse has seen significant progress in the last decade. Youdin & Shu (2002) showed that the mechanism of Goldreich & Ward (1973) would operate if there were local variations in the dust-to-gas ratio that lead to patches of enhanced dust density. Numerical simulations have demonstrated that the process can be effective (Fromang & Nelson, 2005; Johansen et al., 2007; Cuzzi et al., 2008) These simulations are necessarily highly simplified, and rely on uncertain (and different) mechanisms to produce the needed overdensities. Consequently, the initial size of planetesimals, the fraction of small bodies converted into planetesimals, and similar questions, remain open.

1.5.5 Planetesimal Coagulation

However the first planetesimals form, they are large enough that they are strongly decoupled from the gas, and growth proceeds in a straightforward way. These bodies grow by accreting other bodies which stick due to the mutual gravity. For this problem, Safronov (1969) pioneered the "particle in a box" approach to the problem, where individual planetesimals are treated in the approximation where they move randomly about the swarm of planetesimals with a random velocity u related to their eccentricity e by $u \sim e v_{\text{kepler}}$. N bodies in a volume V with an impact cross section of πb^2 collide with a frequency

$$f_c = \frac{N}{V} \pi b^2 u. \tag{1.29}$$

This approach is necessary for a computational analysis as the Minimum Mass Solar Nebula has enough heavy elements to produce $\sim 10^{14}$ one kilometer sized bodies, far too

many to be tracked for the $10^5 - 10^7$ dynamical times (orbits) that would be necessary to perform an N-body simulation of planet formation.

If the mutual gravity between bodies is small, we can neglect it, and consider the interaction between two bodies being a collision with a cross section for interaction for bodies of size s and R to simply the geometric cross section between the two bodies:

$$\pi b^2 = \pi \left(R + s \right)^2. \tag{1.30}$$

In the limit that $R >> s$, we can find the mass doubling time for the larger bodies, with mass M, by accreting the smaller bodies, with mass m, by applying $(1/M)\,(dM/dt) \sim f_c\,(m/M)$. The bodies orbit in a volume $V \sim 2\pi a\Delta ah$, where h is the scale height of bodies, with $h \sim (u/v_{\mathrm{kep}})\,a$. The bodies double grow like:

$$\frac{1}{M}\frac{dM}{dt} \sim \frac{Nm}{2\pi a\Delta a\frac{u}{v_k}a}\pi R^2\frac{1}{M}u \sim \frac{\sigma\Omega}{\rho R}. \tag{1.31}$$

Note the constants have been dropped. The important point is that the mass doubling time scales as $\tau_{\mathrm{growth}} \propto R$. Larger bodies take longer to grow than smaller bodies, and thus the distribution remains tightly clustered. Bodies that fall behind catch up due to the enhanced growth rate, bodies that get ahead are slowed until the pack catches up. This results in the name "orderly growth".

Eventually, a few bodies will get far enough ahead of the pack that gravitational focussing will become important. As noted earlier, a population of bodies at a single size will have a velocity dispersion roughly their own escape velocity; bodies that are substantially bigger than the average will accrete other bodies with significant gravitational focussing. Consequently, they have a cross section:

$$\pi b^2 = \pi \left(s + R \right)^2 \left(1 + \left(\frac{v_{\mathrm{esc}}}{u} \right)^2 \right) \sim \pi \left(R \right)^2 \left(\frac{v_{\mathrm{esc}}}{u} \right)^2, \tag{1.32}$$

with $v_{\mathrm{esc}} = \sqrt{2GM/R} \sim \sqrt{8G\rho R^2}$, we the form of the mass double time changes to:

$$\tau_{\mathrm{growth}} \sim \frac{\rho u^2}{\sigma\Omega GR}. \tag{1.33}$$

Here, the qualitative nature of the growth changes. Larger bodies have shorter growth times, and consequently run away from the group; this leads to the name "runaway growth". Runaway growth produces a few large bodies, while growth of smaller bodies is inhibited as the velocity dispersion goes up.

Runaway growth cannot continue forever. Eventually the large bodies have enough mass that they excite the orbits of the remaining planetesimals through viscous stirring (Ida & Makino, 1993), and enough planetesimals are accreted that their surface density decreases (Lissauer, 1987), which ends the runaway growth regime. Runaway growth begins to slow when $\Sigma M > \sigma m$ (Ida & Makino, 1993), at this time most of the mass is still in the smaller planetesimals.

A change occurs when the large bodies begin to dominate the stirring of their own zone. These bodies, called oligarchs, are locally in runaway, but oligarchs in different zones do not run away from one another. Oligarchy begins when bodies reach a size:

$$R_{\text{oligarch}} \sim \left(\frac{\rho_\odot^{\frac{1}{3}}}{\rho^{\frac{7}{3}}} \frac{\sigma m}{a^2} \right)^{\frac{1}{7}}. \tag{1.34}$$

Numerical simulations find that bodies are a factor of a few larger than this size before the onset of oligarchic growth due to corrections to the two-size approximation used here (Ormel et al., 2010). This is somewhat more unwieldy, as the uncertainty in m is significant in the astrophysically interesting cases. Oligarchs remain well separated from one another, as Kokubo & Ida (1998) found they typically remain several Hill radii apart.

Oligarchic growth continues until the bodies contain most of the mass in their zone, at which point they are called isolated. Bodies become isolated when they reach an isolation size R_{iso}:

$$\frac{4\pi}{3}\rho R_{\text{iso}}^3 \approx 2\pi\sigma a R_{\text{H}} \tag{1.35}$$

$$R_{\text{iso}} \sim \left(\frac{a^2 \sigma}{\rho^{2/3}\rho_\odot^{1/3} R_\odot} \right)^{\frac{1}{2}}.$$

Once the isolated bodies have sufficiently depleted the remaining planetesimals, their

long-range interactions will stir each other into crossing orbits. At this point, growth is dominated by giant impact mergers (Chambers, 2001). The giant impacts end when the planets are on sufficiently distant orbits that they are stable over the age of the star.

The picture outlined previously is the usual model of planet formation. The collisional cross sections above were derived assuming the sun's gravitational role was negligible. When the relative velocity between the two bodies is dominated by the keplerian shear, rather than the eccentricity and inclination, the cross section modified (Goldreich et al., 2004b). In the case, the assumption that the large body is moving through an infinite sea of small bodies in equation 1.29 is no longer valid. Instead, we note the small bodies have a scale height less than the Hill radius, and thus the Hill sphere intercepts a sheet with surface density σ to a distance $R_{\rm H}$ which moves by at a shearing speed of $\Omega R_{\rm H}$. Thus small bodies enter the Hill sphere of the large body is $\sim (\sigma/m) R_{\rm H}^2 \Omega$. Once inside the Hill sphere, the small bodies motion relative to the new standard of rest (i.e. in the large body frame rather than the stellar frame) has random velocity of roughly the Hill velocity (as that was the shearing speed on entry). The large body intercepts an area $\pi R^2 (v_{\rm esc}^2) / (v_{\rm H}^2)$ of the total area $(u/\Omega) R_{\rm H}$ of the incoming bodies. The large body then accretes mass at a rate $\Omega \sigma R^2 \alpha^{-1} (v_{rmH}/u)$. Here the α is from (Goldreich et al., 2004b), who define:

$$\alpha \equiv \left(\frac{\rho_\odot}{\rho} \right)^{\frac{1}{3}} \frac{R_\odot}{a}. \tag{1.36}$$

In this case the growth time is:

$$\tau_{\rm growth} \sim \frac{\rho u \alpha^2}{\Omega^2 \sigma}. \tag{1.37}$$

This has a limit, however. When $(u/\Omega) < \alpha^{-0.5} R$ the large body intercepts all the bodies vertically, and the focussing is capped by the scale height of the disk. In that case $(R v_{\rm esc}) / (v_{\rm H} R_{\rm H})$ of the bodies entering the Hill sphere, resulting in a growth time

$$\tau_{\rm growth} \sim \frac{\rho R}{\sigma \Omega} \alpha^{\frac{1}{2}} \tag{1.38}$$

. Note that in the former (thin) case, the growth time is independent of size. All bodies

29

grow together in a uniform fashion. In the latter case (superthin), the growth time is linear with size. With larger bodies taking longer to grow, the growth reverts to the orderly fashion.

1.6   Previous Conglomeration Simulations

Under special conditions, analytic solutions can be found for growing planetesimals. For instance, Makino et al. (1998) find that an infinite sequence of bodies obeying energy equipartition and undergoing runaway growth have a stationary solution at $dn/ds \propto s^{-6}$. In other restrictive cases, other steady-state solutions may be found. Schlichting & Sari (2011) use the "two-groups" approximation to derive a size-number distribution and velocity dispersion during planetesimal growth with $dn/ds \propto s^{-4}$ during runaway growth. We show in section 3, however, that the solution is not robust to the inclusion of necessary physics. While analytic solutions would be preferable, numerical investigations are often used as they allow progress with more of the necessary physics.

Modern planetesimal growth simulations fall into two general categories; N-body simulations, in which individual particles are tracked, and statistical simulations, in which all bodies with similar properties are binned together. N-body simulations are limited in the number of bodies they can track (with current computing power, simulations use up to a few thousand particles (e.g., Ogihara & Ida, 2009; Morishima et al., 2010). Consequently, they are restricted to late times when bodies are quite large ($\sim 10^3$ km). Statistical simulations can cover the early times, but cannot address later phases such as oligarchy. Hybrid schemes (e.g., Bromley & Kenyon, 2006; Ormel et al., 2010) attempt to combine the two approaches to draw on the strengths and cover the weaknesses of each. They still must sacrifice some physics so they can be computed in a reasonable time, however.

Planetesimal growth simulations have tended to follow the general approach of Green-

berg et al. (1978). Inspired by Safronov (1969) and Goldreich & Ward (1973), they begin with kilometer sized planetesimals. The planetesimals experience viscous stirring and dynamical friction, and evolve by mutual collisions that may be either conglomerative or destructive. They evolve bodies at 2.7 AU (i.e., with the asteroid belt in mind) until the largest bodies are ~ 500 km in size. Their results set up the general outcome of future simulations; they find that most of the mass remains in the km bodies, they find that the km bodies do not reach reach the escape speed of the large bodies, but remain quite sub-escape throughout the growth. The velocity distribution had most bodies super-Hill and sub-escape to the large bodies, with the largest bodies substantially colder. All of these results went against the prevailing model of the day, that of Safronov (1969), which had found a top heavy mass distribution (and consequently that most bodies were roughly the escape speed of the large bodies).

Subsequent investigations have refined the approach, with better approximations to the coagulation physics and increased computing power. The macroscopic conclusions have not substantially changed, however. Wetherill & Stewart (1989) show that the conclusions depend on the dynamical friction cooling of large bodies, and the enhancement of cross sections due to gravitational focussing. Both are necessary to generate the conditions for runaway growth. These conditions were also found by Spaute et al. (1991). All of these simulations focussed on the terrestrial zone.

Models for the inner terrestrial zone (i.e., the formation of Mercury, Venus, Earth, and Mars), show eventually the largest bodies isolate themselves, forming "Oligarchs", which grow slowly, until most of the mass is in oligarchs (Kokubo & Ida, 1998). As the damping from the small bodies ends (because they've been accreted), the giant impact phase begins (Lecar & Aarseth, 1986; Chambers & Wetherill, 1998). In this phase, all of the mass is swept up into a few planets. Such a result matches the overall character of the terrestrial planets, although not the asteroid belt. The failure to produce planets in the asteroid belt region is generally ascribed to the action of Jupiter interrupting the

growth process before the giant impact and cleanup stage (Wetherill, 1992; Petit et al., 2002).

With the discovery of the Kuiper belt in the early 1990s, similar investigations were launched into coagulation at Kuiper belt distances. The lower surface densities and longer orbital periods at greater distances from the central star change the problem in a quantitative way. Because the relevant timescale may be the age of the Sun, or the time until the gas disk dissipates, we might expect qualitatively different outcomes. Perhaps the most canonical "growth of the Kuiper belt" simulation is that of Kenyon & Luu (1998). Beginning with large bodies of a single size, they found quite similar outcomes to the runaway growth simulations of the inner solar system. Only a small fraction of the initial mass, typically of order 10^{-3}, ended up in large (100+ km) bodies. For Minimum Mass Solar Nebula like initial conditions, there should be $\sim 10 M_\oplus$ in the Kuiper Belt region, so this efficiency produces at $\sim 10^{-2} M_\oplus$ present day Kuiper belt. Mass at large sizes was distributed roughly equally at all logarithmic sizes. The largest bodies are typically 10^3 km in size; the final turnover to planet formation does not occur at Kuiper belt distances, as the lower surface densities and longer orbital periods extend the timescale of planet formation beyond the age of the solar system. Subsequent simulations (Kenyon & Bromley, 2008; Ormel et al., 2010; Schlichting & Sari, 2011) have reiterated these conclusions.

These conditions match the general character of the trans-Neptunian region today, and the model was hailed as a great success. The large size end looks like the observed bodies, and the small bodies are expected to have been removed by collisional processing (Kenyon & Bromley, 2004b; Pan & Sari, 2005). A loose thread remained in the evidence that the Cold Classical Kuiper Belt had formed in situ (section 1.2.2), while models of Neptune's migration posited an end to the Minimum Mass Solar Nebula at ~ 30 AU to stop Neptune's migration at its current orbit (Gomes et al., 2004; Levison et al., 2008). Another challenge was raised from the long period binaries, which should have been

disrupted by the kilometer bodies (Parker & Kavelaars, 2012), had they existed. We pose a significant challenge in chapter 2, where we show that the bright extrasolar debris disks cannot be produced by this coagulation model.

1.7 This Work

Extrasolar debris disks around sun-like stars at sun-like ages have as much as $\sim 10^3$ times the mass in dust as is found in the solar system. Taken alone, it is an interesting question to ask "Why are these systems so much dustier than the Sun?" The debris disk of the Sun contains only $\sim 10^{-1} M_\oplus$ in parent planetesimals, which suggests a natural explanation in more massive debris disks. The question becomes much more urgent in the light of planetesimal growth models, however, which naturally predict Kuiper Belt like debris disks should arise from typical protostellar nebulae.

To address this question, we apply a collisional evolution model of debris disks to a sample of well characterised extrasolar debris disks in chapter 2. By constructing a pseudo-evolution sequence of massive debris disks using observations of disks at different ages, we are able to constrain the properties of the parent planetesimal populations. We find that that these bright extrasolar debris disks are scaled up versions of the Kuiper Belt, with MMSN like surface densities in parent planetesimals of size $10 \sim 100$ km. This present a serious challenge to the standard coagulation model, which did not predict such disks.

Previous to chapter 2, little was known about the properties of the parent planetesimal populations in debris disks, apart from the Kuiper belt, where the parent bodies could be observed directly. While coagulation models did not predict the existence of debris disks with $\sim 10 M_\oplus$ in 10 to 100 km objects, expectations had been strongly guided by the observations of the Kuiper Belt. With our new results in hand, we develop a code for conducting simulations of coagulation, which we describe in chapter 3. We employ

this code to simulate the growth of planetesimals in the standard case of kilometer sized planetesimals. Our model finds similar conclusions to previous models. Coagulation of large planetesimals at ~ 40 AU is inefficient, with $<< 1\%$ of the total mass ending up in large bodies, for a variety of possible initial conditions. We provide a physical explanation for the resultant $q \sim 4$ power spectrum, and the low efficiency $\sim \alpha$.

The fundamental root of the low efficiency is runaway growth. Runaway growth only occurs when accretion is in the sub-escape but super-Hill regime. Given this, we investigate whether accretion in the sub-Hill regime could produce the Kuiper Belt from a much lower starting mass in chapter 4. The key modification in this model is that most of the mass begins in centimeter sized grains, which are dynamically cooled in mutual collisions. We include a seed population of kilometer sized planetesimals, which accrete the centimeter sized grains. In this growth mode, growth is orderly. In this case, growth can be efficient, and we demonstrated that the Kuiper Belt could have been formed from a primordial belt with $2 \sim 3$ times the present day mass of the Kuiper Belt. We follow that up in chapter 5 by applying the same model to extrasolar debris disks. We show that the same "kilometer plus centimeter" model can produce the parent population of planetesimals needed to explain the properties of extrasolar debris disks we found in chapter 2.

Chapter 2

Planetesimals in the debris disks of Sun-like Stars

2.1   Background

Dusty disks made up of rocky and icy debris have been observed around other stars, both in reflected optical light (Smith & Terrile, 1984) and in long wavelength thermal radiation (Aumann et al., 1984). Multiple surveys have reported that a significant fraction of main-sequence stars harbor detectable infrared excesses: $\sim 15\%$ solar-type stars (Trilling et al., 2008; Lawler et al., 2009), and $\sim 30\%$ for A-stars (Su et al., 2006). The infrared luminosity, when compared to the luminosity of the central star, ranges from $\sim 10^{-5}$ to $\sim 10^{-3}$. In contrast, the fractional dust luminosity from the Kuiper belt is estimated to be $\sim 10^{-7}$ (Teplitz et al., 1999) and remains undetected. The observed excess luminosities arise primarily from small ($\sim \mu m - mm$) dust grains. Due to their short survival time

(Artymowicz & Clampin, 1997), these grains are believed to be continuously produced by collisions between large parent bodies ('planetesimals'). These planetesimals, analogous to the Kuiper belt objects in our own system, are in turn left-overs from the epoch of planet formation.

In this chapter, we describe how we can use debris disks to test theories of planetesimal formation. We first focus our attention on the primordial size spectrum of planetesimals, often characterized by a single power-law, $dn/ds \propto s^{-q}$, where s is the size. In the following, we briefly summarize theoretical understandings and observational evidences for the value of q.

The conventional picture of planetesimal formation is composed of a number of steps. The formation of the first generation planetesimals is not yet well-understood and is an area of active research (see, e. g. Youdin & Shu, 2002; Dominik et al., 2007; Johansen et al., 2007; Garaud, 2007). If these are sufficiently massive, gravity dominates their subsequent growth (Weidenschilling et al., 1997). At first, objects grow in an orderly fashion, where collisions and conglomerations occur at rates that are proportional to their geometric cross sections. But when these bodies become so massive that the effect of gravitational focusing becomes significant, run-away growth commences where the largest bodies accrete small planetesimals at the highest rate and quickly distance themselves from their former peers (Wetherill & Stewart, 1989; Kokubo & Ida, 1996). The run-away phase is succeeded by the oligarchic phase where individual large bodies are responsible for stirring the small bodies that they accrete (Kokubo & Ida, 1995, 1998). At the end of these steps, an entire size spectrum of planetesimals are produced. This is the 'primordial spectrum'.

During the run-away phase, N-body simulations have typically produced a slope of $q \sim 6$ (Kokubo & Ida, 1996; Morishima et al., 2008). This slope is naturally explained if there is energy equi-partition among planetesimals of different sizes (Makino et al., 1998). Moreover, one expects that the distribution becomes shallower (smaller q) if

36

larger planetesimals have higher kinetic energies. This indeed occurs during the oligarchic phase when all small and intermediate-sized planetesimals are stirred to the same velocity dispersion. The value of q is then reduced to ≈ 4 (Morishima et al., 2008).

Using particles-in-a-box simulations and later hybrid simulations, Kenyon & Luu (1999a); Kenyon & Bromley (2004b, 2008) followed the growth of planetesimals. They also found that q decreases with time after the run-away phase, finishing up with $3.75 \leq q \leq 4.5$ for planetesimals of sizes between 10 and 1000 kms. Recently, Schlichting & Sari (2011) argued analytically that a $q = 4$ spectrum is the natural outcome of conglomeration.

Observational constraints on the value of q currently come exclusively from counting large Kuiper belt objects. Kuiper belt objects larger than about $30 - 50$ kms are commonly believed to be primordial. Collision timescales for these bodies well exceed that of the Solar system age (Davis & Farinella, 1997; Bianco et al., 2010). The size distribution for these bodies can be probed by present-day surveys. Published values for q are scattered: $q = 4.0^{+0.5}_{-0.6}$ (Trujillo et al., 2001), $q = 4.25 \pm 0.25$ (Fraser et al., 2008), $q = 4.5 \pm 0.4$ (Fraser & Kavelaars, 2009) and $q = 4.5^{+1.0}_{-0.5}$ (Fuentes & Holman, 2008). This scatter may be intrinsic and reflect both the different size ranges and the different dynamical populations emphasized by various surveys (Bernstein et al., 2004; Donnison, 2006; Fraser et al., 2010). For bodies smaller than ~ 30 kms, the size distribution adopts a shallower power-law (Bernstein et al., 2004; Fuentes & Holman, 2008; Schlichting et al., 2009). This break in the power-law index has been argued to be due to collisional erosion (Pan & Sari, 2005), but a different opinion has surfaced (Charnoz & Morbidelli, 2006).

So at least for the value of q, current coagulation models appear to be vindicated by the observations. These models enjoy a further success. In the Kuiper belt region, the solid mass of the so-called Minimum Mass Solar Nebula is $\sim 10\ M_\oplus$ (Hayashi, 1981; Weidenschilling, 1977b), while the mass in large Kuiper belt objects is estimated to be $\lesssim 0.1 M_\oplus$ (see, e.g. Gladman et al., 2001; Bernstein et al., 2004). This large difference,

however, is explained by current models where the formation of large planetesimals has a very low efficiency (Bromley & Kenyon, 2006; Schlichting & Sari, 2011).

With these two remarkable concordances, one wonders if debris disks will ever tell us anything new and unexpected. Furthermore, every debris disk likely has a different initial condition and evolves in a different dynamical environment. For instance, dynamical interactions with Neptune or other planets may have qualitatively affected the evolution of the Kuiper belt (Levison et al., 2008). It seems difficult, therefore, to extract any universal truth about the formation process from these disparate objects.

However, based only on a modest sample of debris disks, we argue in this paper that there is already a serious issue in current coagulation models.

To achieve this, we first construct a simple collisional model (§2.2) to compare against the set of debris disks reported in Hillenbrand et al. (2008). Our collisional model does not differ in essence from previous works (Krivov et al., 2005; Wyatt et al., 2007b; Löhne et al., 2008), but we interpret the observations in a new way. This allows us to measure the value of q as well as the initial masses of planetesimal belts (§2.4). The latter result challenges the current models of planetesimal formation (2.5). We summarize in §2.6.

2.2 Model: Luminosity Evolution of a Debris Disk

The debris phase commences when eccentricities of the primordial planetesimals are further increased so that they no longer coalesce at encounter, but are instead broken into fragments.[1] In this phase, the smallest primordial planetesimals enter into a collisional cascade first, followed by progressively larger bodies. During the collisional cascade, a primordial body is broken down into smaller and smaller fragments until all its mass ends up in small grains. The small grains may spiral in towards the star due to Poynting-Robertson drag, as happens in the Solar system, or, be ground down by frequent collisions

---

[1]Kenyon & Bromley (2008) find that fragmentation begins once Pluto-sized bodies form.

to sizes so small that they are promptly removed by radiation pressure, as happens in bright debris disks (Wyatt, 2005).

2.2.1 Debris Rings

We model the debris disk as a single, azimuthally smooth ring composed of planetesimals of different sizes. The ring is centered at a semi-major axis a with a full radial width of Δa and a constant surface density. We take $\Delta a/a = 0.1 \ll 1$ as our standard input. This is motivated by the following observations. Spatially resolved debris disks often appear as narrow rings. Examples are, $\Delta a/a \sim 0.1$ for AU Microscopii (Fitzgerald et al., 2007), ~ 0.5 for HD 10647 (Liseau et al., 2010), ~ 0.3 for HD 92945 (Golimowski et al., 2007), ~ 0.3 for HD 139664 (Kalas et al., 2006), ~ 0.2 for HD 207129, (Krist et al., 2010), ~ 0.5 for ϵ Eridani (Dent et al., 2000), ~ 0.1 for Fomalhaut (Kalas et al., 2005), ~ 0.2 for Vega (Su et al., 2005). Similarly, unresolved disks often exhibit spectral energy distribution that is well fit by a single temperature blackbody (Hillenbrand et al., 2008; Nilsson et al., 2010; Moór et al., 2011). This ring-like topology (see Thébault & Wu, 2008, for an extensive review) also show up in our own Solar system, hence the name the asteroid "belt" and the Kuiper "belt".

2.2.2 Initial Size Distribution of the Planetesimals

We adopt the following power-law forms for the initial size distributions,

$$
\left.\frac{dn}{ds}\right|_{t=0} \propto
\begin{cases}
s^{-q_3} & s_{\mathrm{small}} < s < s_{\mathrm{big}}, \\[2ex]
s^{-q_1} & s_{\mathrm{min}} < s < s_{\mathrm{small}}.
\end{cases}
\tag{2.1}
$$

The index q_3 is the primordial size index for large bodies, like one that arises out of conglomeration models. Previous studies of collisional debris disks have taken this value to be a given, in fact it is commonly set to be the power law one expects from collisional equilibrium (Krivov et al., 2005, 2006; Wyatt et al., 2007b; Löhne et al., 2008). In

contrast, in this contribution we use the observed sample to measure this value.

In equation 2.1, s_{big} is the size of the biggest planetesimals, s_{min} the smallest. The intermediate size s_{small} is introduced for the purpose of mass accounting (see below): the original mass counts only those between s_{small} and s_{big},

$$M_0 = \int_{s_{\mathrm{small}}}^{s_{\mathrm{big}}} \frac{4\pi}{3} \rho s^3 \, n_3 s^{-q_3} \, ds. \tag{2.2}$$

While s_{min} is naturally taken to be the size at which radiation pressure unbinds dust grains from the star ($\sim \mu m$ for a Sun-like star), we discuss our choice for s_{big} and s_{small} below.

Motivated by the observational and numerical results discussed in §2.1, we investigate values of q_3 between 3.5 and 5. The value $q_3 = 4$ has the special property that mass is distributed equally among all logarithmic size ranges, while masses in systems with $q_3 > 4$ diverge toward the small end. The intermediate size s_{small} is introduced, partly to avoid dealing with this divergence. For sizes below s_{small}, we assume that collisions have set up an equilibrium power law with index q_1 ($q_1 = 3.6$ for the hard-strength law, see Appendix). So sizes below s_{small} contributes little to the total mass. The intermediate size s_{small} can also be interpreted as the collisional break size at time zero. We set $s_{\mathrm{small}} = 100$ m. For our typical disks, collisional equilibrium is established within a few million years for bodies up to a size ~ 1 km. So the choice of s_{small} is not important for late time evolution.

The choice of size for the largest bodies, s_{big}, deserves some discussion, as it affects the qualitative character of the evolution. As a collisional cascade progresses, bodies of larger and larger sizes come into collisional equilibrium, opening up fresh mass reserve to produce the small particles. Once the largest bodies enter into collisional equilibrium, the dust production rate decays with time as $L_{\mathrm{IR}} \propto t^{-1}$ (Wyatt et al., 2007a). Two previous studies (Wyatt et al., 2007b; Löhne et al., 2008) have adopted sizes for the largest bodies of $s_{\mathrm{big}} = 30$ and 74 km, respectively. For some of their disks, the largest bodies can enter collision equilibrium during the lifetime of the system.

Both Kuiper belt observations and numerical studies of coagulation favor a largest size of ~ 1000 km. The largest object yet found in the Kuiper Belt, (136199) Eris, has a radius of 1200 ± 50 km (Brown et al., 2006). In the simulations of Kenyon & Bromley (2004a), coagulation of planetesimals at 30 - 150 AU produces bodies as large as 1000 - 3000 km. When the largest bodies reach this size, self-stirring increases the velocity dispersion and collisions become destructive rather than conglomerating.

Therefore, we adopt a maximum body size of 1000 km in our study. Our quoted masses reflect this choice of s_{big}. Our largest bodies never enter into collisional equilibrium. If this assumption turns out to be erroneous, namely, s_{big} is much smaller and enters into collisional cascade within system lifetime, our model would underestimate the initial masses for old disks. As a result, we would overestimate the value for q_3.

2.2.3 Collisions

We only consider collisions that are catastrophically destructive. A catastrophic collision is defined as one that removes at least 50% of the mass of the primary body. In so doing, we have implicitly assumed that both cratering collisions and conglomerating collisions are unimportant. When a destructive collision occurs, the total mass (bullet plus target) is redistributed to all smaller sizes according to $dn/ds \propto s^{-4}$. This choice is somewhat arbitrary and we have confirmed that modifying it (within reasonable bounds) does not change our results.

We do not model evolution of the orbital dynamics as bodies collide. This is justified by the discussions in §2.5.2.

Let the frequency of collisions between two bodies of sizes s and s' be,

$$f_{\mathrm{collision}} = \frac{\pi \left(s + s' \right)^2}{2\pi a \Delta a\, t_{\mathrm{orb}}}.$$

(2.3)

Here, $2\pi a \Delta a$ is the surface area spanned by the debris ring in the orbital plane, and t_{orb} is the orbital period. Gravitational focusing is negligible for the high random velocities

we consider here. The typical encounter velocity, for particles with eccentricity e and inclination i, is (Wetherill & Stewart, 1993)

$$v_{\text{col}} = \sqrt{1.25e^2 + i^2}\, v_{\text{kep}}, \tag{2.4}$$

where v_{kep} is the local Keplerian velocity. We adopt $i \approx e/2$ so $v_{\text{col}} \approx 1.32\, e\, v_{\text{kep}}$. As argued in §2.5.2, it is reasonable to assume a constant eccentricity (and inclination) for all bodies. We take a value of $e = 0.1$ as the standard input and discuss this assumption in §2.5.

We denote the specific impact energy required to catastrophically disrupt a body (target) as Q^*. The scaling of Q^* with the size of the target depends on whether its strength is dominated by material cohesion or self-gravity. We adopt the following form (Benz & Asphaug, 1999),

$$Q^* = A\left(\frac{s}{1\text{ cm}}\right)^{\alpha} + B\rho\left(\frac{s}{1\text{ cm}}\right)^{\beta}, \tag{2.5}$$

where ρ is the bulk density which we take to be 2.5g/cm^3. The first term on the right-hand-side describes the internal strength limit, important for small bodies, while the second term the self-gravity limit, important for larger bodies.

The strength law sets the size of the smallest bullets required to destroy a target. Since these are also the most numerous, they determine the downward conversion rate of mass during a collisional cascade. As such, the power indexes in the strength law directly determine the size spectrum at collisional equilibrium. For a strength law of the form $Q^* \propto s^c$, the equilibrium size spectrum is $dn/ds \propto s^{-q}$, with (Durda & Dermott, 1997):

$$q = (21 + c)/(6 + c). \tag{2.6}$$

The famous Dohnanyi-law (Dohnanyi, 1969), $dn/ds \propto s^{-3.5}$, obtains from $c = 0$.

The value and form for Q^* are notoriously difficult to assess. It depends on, among other factors, material composition, porosity and impact velocity. A number of computations and compilations have appeared in the literature. We select three representative formulations for our study (Fig. 2.1).

Based on a variety of experimental data and SPH simulations, Krivov et al. (2005); Löhne et al. (2008) advocated the following choices, $A = 2 \times 10^7 \text{erg/g}$, $\alpha = -0.3$, $B = 0.158$, $\beta = 1.5$. We call this the 'hard' strength law. In this case, the collision spectrum satisfies $q \approx 3.6$ and 3.0, in the strength and gravity regimes respectively.

Based on energy conservation, Pan & Sari (2005) calculated a destruction threshold for bodies that have zero internal strength and obtained $B = 3.3 \times 10^{-8}$, $\beta = 2$. So bodies at 100km is weaker by a factor ~ 1000 than their counterparts in the Krivov et al. (2005) formulation. We refer to this as the 'soft' strength law. A softer strength implies smaller bullets and therefore more frequent destruction of the targets. Pan & Sari (2005) did not consider smaller bodies that are strength bound. We adopt $A = 2 \times 10^7 \text{erg/g}$ and $\alpha = -0.3$ in this range to complete the soft prescription.

Stewart & Leinhardt (2009) proposed a strength law that depends on impact velocity,

$$Q^* = \left(500 \, s^{-0.33} + 10^{-4} \, s^{1.2}\right) v_{\text{col}}^{0.8}. \tag{2.7}$$

For a typical velocity $v_{\text{col}} = 500 \text{m/s}$ and for bodies greater than 1km, this gives rise to a strength law that falls in-between that of the hard and the soft case. We call this the medium strength law.[2] Note that this strength law is much weaker than the other two for small bodies.

For the strength laws we consider, transitions from material strength domination to self-gravity domination occur at size $s \approx s_1$, with s_1 ranging between 100 m (the hard and the medium laws) and 10 km (the soft law).

2.2.4 Luminosity Evolution

The planetesimal disk, starting from an initial disk mass of M_0, and an initial size spectrum (eq. 2.1), is numerically collided and ground down. We divide the particles between

---

[2]We thank P. Thebault for pointing out that the definition of critical energy in that work differs slightly from our use here, but the difference disappears when the impactor is much smaller than the target.
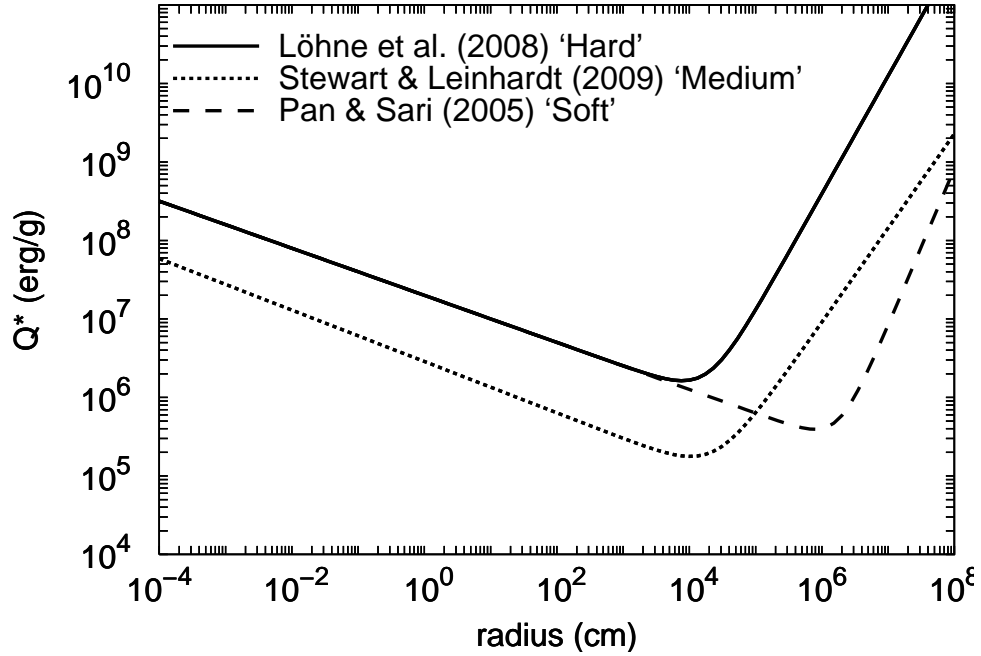
Figure 2.1: Prescriptions for specific strength from Löhne et al. (2008), Pan & Sari (2005) and Stewart & Leinhardt (2009), plotted here as functions of target sizes. We insert an impact velocity of 500m/s to evaluate the last prescription. Strength of small bodies are dominated by material cohesion, while that of larger bodies by self-gravity. Transitions between the two limits occur around 100 m (the hard and the medium laws) or around 10 km (the soft law). Strength for bodies smaller than 1cm are extrapolations as both laboratory and numerical experiments only concern bodies of larger sizes.

s_{small} and s_{big} into 500 equal logarithmic size bins. The time-step for the simulations is adaptively set so that over one time-step, the maximum mass gain (from larger bodies) or loss (to smaller bodies) per bin falls below 5%. The net mass change is substantially smaller than this due to the cancellation between gain and loss.

We calculate the fractional brightness of the dust disk, L_{IR}/L_*, by integrating the geometrical cross section over all grains. This assumes that grains are perfect absorbers at the optical and can emit efficiently in the infrared.
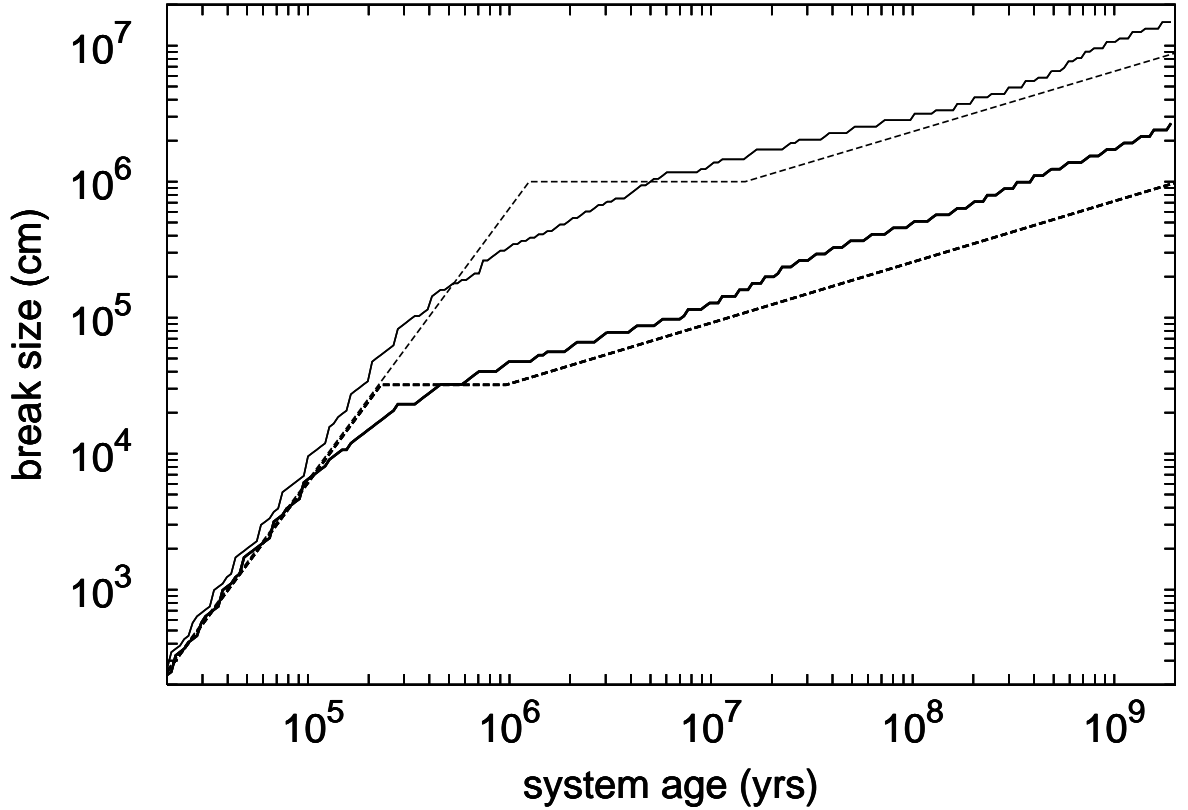
Figure 2.2: Time evolution of the break-size in a model system, with $M_0 = 12.4 M_\oplus$, $q_3 = 4.0$, $e = 0.1$, $a = 31$AU, and $\Delta a/a = 0.1$. Here, break-size is defined as the size at which all bodies initially at that size have encountered of order one destructive collision. Break size increases with time monotonically as larger bodies enter into collisional cascade. The numerical results are shown as solid curves, while the analytical scaling relations (see Appendix) are plotted as dashed lines. The bends in the curves occur at $s \approx s_1$, where s_1 is the size for which material cohesion and gravity binding are equal. The set of thick curves are for the case of hard material strength, while the thin lines for soft strength.

An example of such a calculation is reported in Figs. 2.2 & 2.3. To understand these results, a simple analytical model (see Appendix) is introduced. Scaling relations obtained using this analytical model compares well with our numerical results.

45
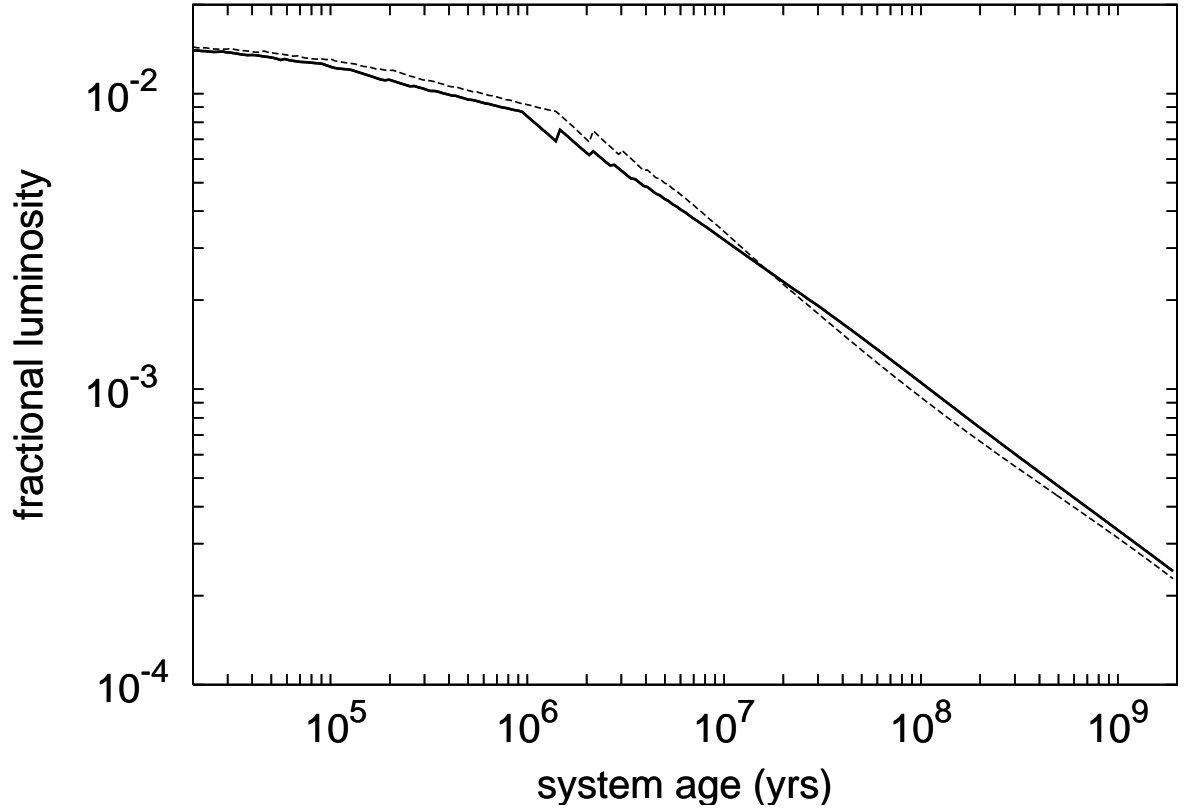
Figure 2.3: Evolution of fractional luminosity, L_{IR}/L_*, for the system in Fig. 2.2. The solid line is obtained using the hard strength law, and the dashed line the soft one. The evolution proceeds in two stages: the flatter early stage when collisional cascade only involves small bodies that are bound by material cohesion; and a steeper later stage where bodies bound by self-gravity enter the cascade. At late times, fractional luminosity decays as $t^{-0.5}$ (eq. 7.9, also see Fig. 7 of Löhne et al., 2008). While break-sizes differ for the two adopted strength laws (Fig. 2.2), this appears to have little influence on the overall luminosity. The dotted curve presents results using the hard strength law, but with the collisional debris distributed as $dn/ds \sim s^{-2}$, as opposed to our usual -4 case. The luminosity evolution is similar, aside from a constant offset. Also see figure 2.7, panel 1.

Fig. 2.2 shows that, with time, larger and larger planetesimals enter into collisional cascade. Within a million years or so, the cascade has advanced to size of order one kilometer. Beyond this time, bodies bound by self-gravity can be gradually eroded. By 1 Gyrs, bodies with sizes $10 - 100$ kms may be affected. The exact value depends on the strength law. The dust luminosity is related to the dust mass, which is in turn related to the dust production rate. The dust production rate, on the other hand, is roughly the primordial mass stored around the break-size divided by the system age. If the primordial spectrum is such that a large amount of mass is initially piled at the large end, debris disks would not exhibit significant fading even up to a few billion years.

Fig. 2.3 shows that dust luminosity $L_{\rm IR}/L_* \propto t^{-0.5}$ for $q_3 = 4$, consistent with equation 7.11. This result has previously been obtained, both numerically and analytically, by Löhne et al. (2008). That same equation also demonstrates that the value of B, strength constant for bodies bound by self-gravity, affects the luminosity only minorly. This is born out by results shown in Fig. 2.3.

An important result on which we base our later analysis is shown in Fig. 2.4. Luminosity evolution for disks with the same initial mass but different q_3 are depicted. As eq. 7.9 predicts, $L \propto t^{(q_3-3)/(2-q_3)}$ (also see Löhne et al., 2008). If q_3 is shallow (e.g. $q_3 \leq 4$), most of the initial mass is deposited at the largest planetesimals. This mass reservoir is harder to reach by collision and allows the disk to remain brighter at later times. In comparison, disks with a steeper q_3 decay faster.

If one observes a collection of debris disks all at the same age, intrinsic scatter in, e.g., initial masses, makes it impossible to differentiate between models of different q_3. However, a collection of disks with a large age spread can be used to constrain q_3. This we proceed to demonstrate.
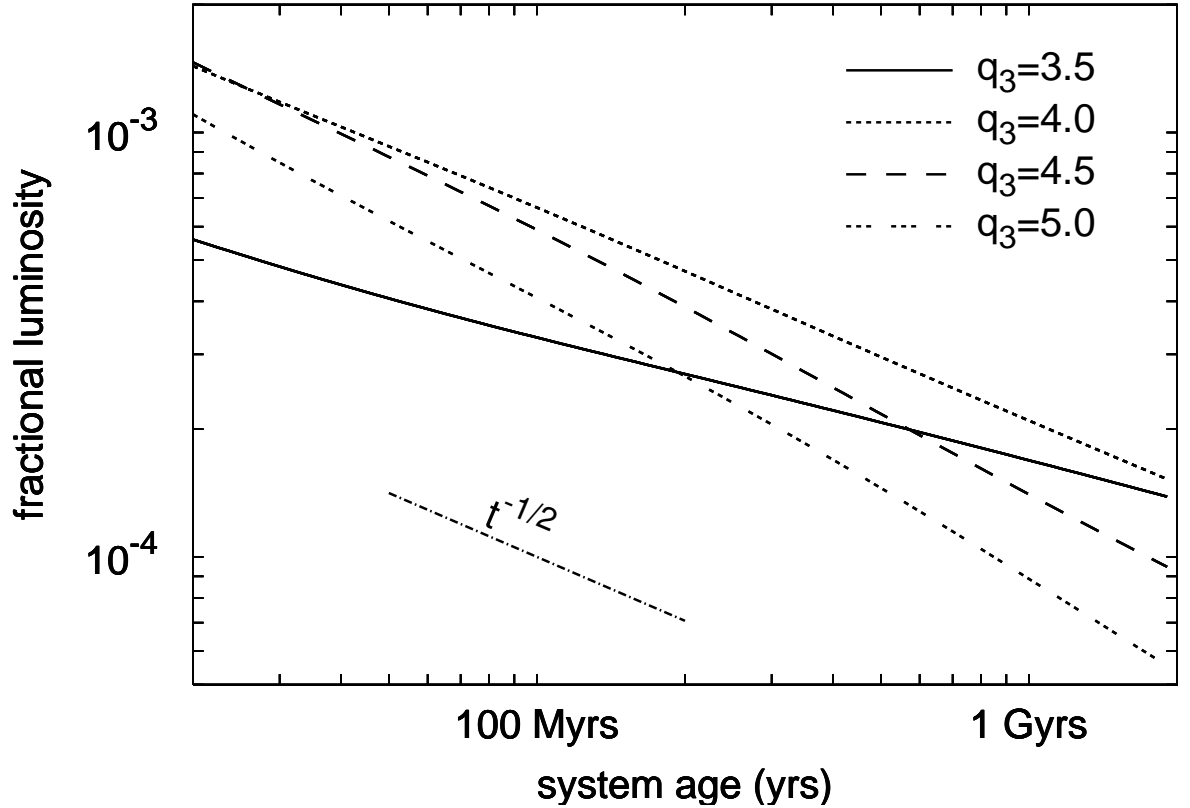
Figure 2.4: Luminosity evolution for disks with different q_3 but the same initial mass $(8M_\oplus)$. Systems with a steeper primordial size spectrum (larger q_3) exhibit a more pronounced decline of luminosity with time, since at a given time, a bigger fraction of their mass reservoir has been depleted. Systems with shallower q_3 (e.g., $q_3 = 3.5$), on the other hand, are initially dimmer due to the relative shortage of smaller rocks, but eventually outshine the higher q_3 disks as they can hold on to their mass reservoir for longer. The luminosity decay of observed disks that span a large range of ages can thus be used to infer the value of q_3. All other parameters here are similar to those used in Fig. 2.3 and we adopt the hard strength law.

2.3 Observed Ensemble

Several debris disks surveys have been carried out (see, e.g. Su et al., 2006; Trilling et al., 2008; Lawler et al., 2009; Moór et al., 2011). The sample of most interest to us is that

reported in Hillenbrand et al. (2008). Together with updates in Carpenter et al. (2009), Hillenbrand et al. (2008) presented a collection of debris disks around F/G/K type stars, obtained as part of the Spitzer program on Formation and Evolution of Planetary Systems (FEPS). This sample is unique in that both the stellar age and the radial distance of the dust ring are determined: isochrone fitting provides the age for the host stars (spanning from $\sim 10^7$ years to a few 10^9 years),[3] while multi-band photometry and spectral energy fitting yield the semi-major axis of the dust ring. Together with fractional luminosity of the dust belt, these provide the most important constraints to infer the primordial properties of parent planetesimals.

To obtain the blow-out size (s_{min}) for each system, we take luminosity values for the central stars as given in (Hillenbrand et al., 2008), and we assign stellar masses by assuming that $M_* \propto L_*^{1/3}$, as appropriate for solar type main-sequence stars.

Out of the 31 disks listed in Hillenbrand et al. (2008), we focus only on a sub-sample of 13 disks that appear radially unextended and are around main-sequence stars. In Hillenbrand et al. (2008), emission from each disk is initially fitted with a single temperature blackbody (a ring). If agreement between the 24μm/33μm fit and the 33μm/70μm fit is poor, they argue that the disk is likely radially extended and fit the data instead with two radial components. Since our numerical model is a one-zone model, we find that including the extended sources into our analysis causes significant scatter in the results. This leads us to discard them for the current analysis. We have excluded HD 191089 from our sample. Its fluxes in 13 μm and 33 μm are not measured, and cannot be reliably identified as an unextended source. In all, we are left with 13 sources.

It is interesting to note that most of the extended sources are relatively young, all younger than a few hundred million years. In contrast, the unextended sources have a larger age spread, lasting till a few billion years (Fig. 2.5). All systems may be born

---

[3]In this work, we assume that the duration of the debris phase in every system is the same as the stellar age. We return to justify this assumption in §2.5.4.

System	Age (yr)	$\log \frac{L_*}{L_\odot}$	$\log \frac{L_{\mathrm{IR}}}{L_*}$	a (AU)
HD 6963	10^9	-0.26	-4.0	18
HD 8907	$10^{8.5}$	0.32	-3.6	49
HD 25457	$10^{8.0}$	0.32	-4.0	23
HD 31392	$10^{9.0}$	-0.26	-3.6	24
HD 35850	$10^{7.5}$	0.25	-4.5	15
HD 72905	$10^{8.0}$	-0.04	-4.7	7
HD104860	$10^{7.6}$	0.12	-3.2	42
HD 122652	$10^{9.3}$	0.18	-3.9	31
HD 145229	$10^{8.8}$	-0.02	-3.9	26
HD 150706	$10^{8.8}$	-0.02	-4.3	23
HD 187897	$10^{9.1}$	0.10	-4.0	43
HD 201219	$10^{9.0}$	-0.16	-3.9	23
HD 209253	$10^{8.0}$	0.21	-4.1	20

Table 2.1: Debris disks selected from Hillenbrand et al. (2008) for our analysis. Semimajor axes are calculated assuming small grains are blackbody radiators. A more realistic model of grain emission would find the disks reside at larger semimajor axes; however, the qualitative conclusions of this investigation should remain robust to a uniformly outward shift in semimajor axes.

with more than one debris rings, but after a sufficiently long time, only the outermost ring, which has the longest erosion timescale, remains shining. The extended system are also brighter than the average, likely related to their relative youth.
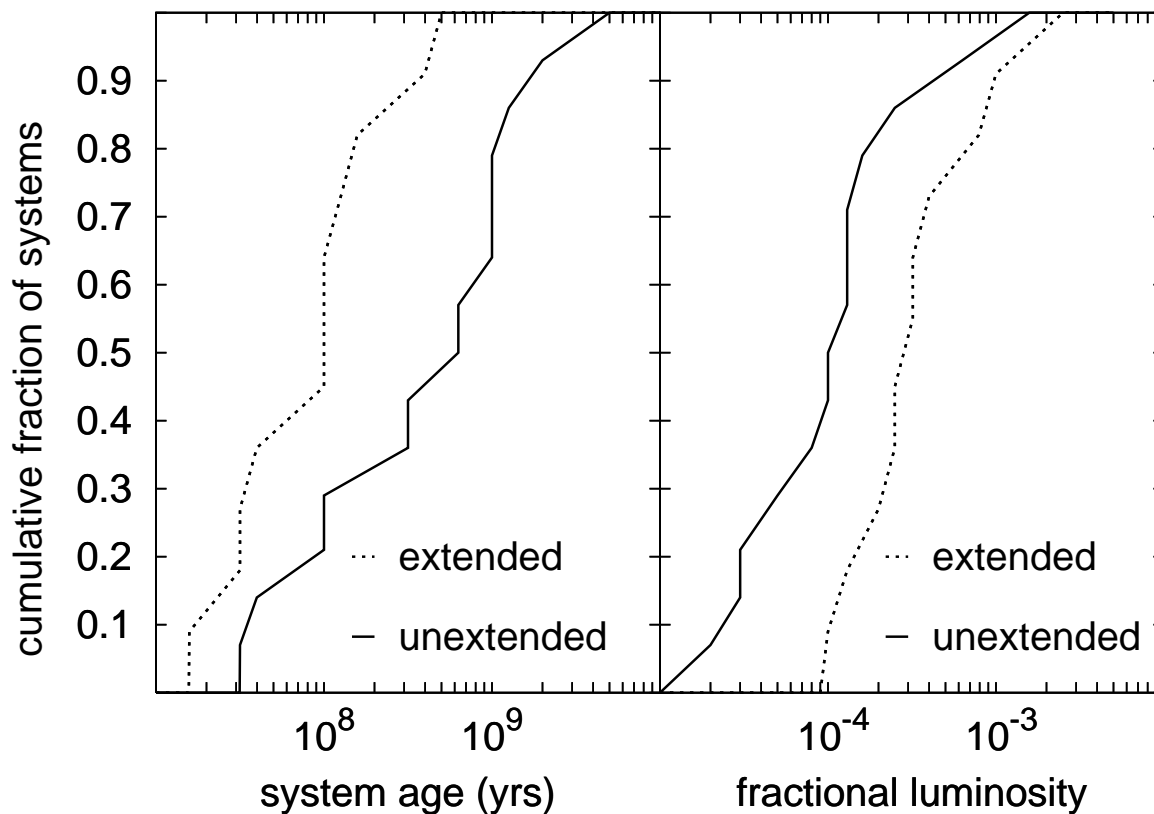
Figure 2.5: Cumulative distribution of stellar age (left panel) and dust luminosity (right panel) for the Hillenbrand et al. (2008) sample. The extended systems (solid curve) tend to be younger and brighter than the unextended systems (dashed curves).

2.4 The Primordial Size Spectrum Revealed

We have a simple strategy. Knowing the luminosity, the age and the semi-major axis of each debris ring, we use our collisional model to infer its initial mass of planetesimals by searching for the initial mass that produces the observed luminosity at the current age. These initial masses, when plotted against system ages, should show a spread. A
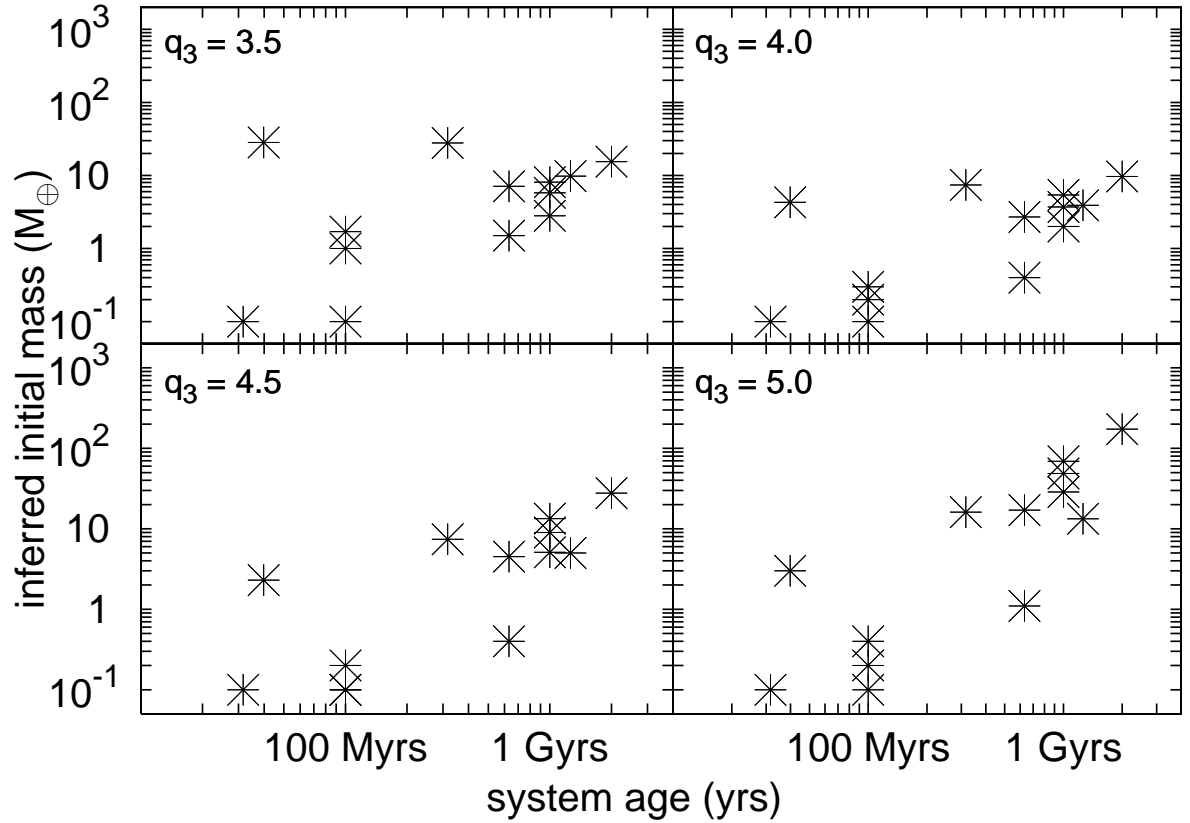
Figure 2.6: Inferred disk initial masses, plotted against system ages, for the unextended systems in Hillenbrand et al. (2008). The four panels present four different choices of q_3. The other parameters chosen are $e = 0.1$, $s_{\mathrm{small}} = 10^4$cm, and $\Delta a/a = 0.1$. A value of $q_3 \in [3.5, 4.0]$ is preferred: the upper envelopes for the disk mass remain constant at all ages in the two top plots. Models with higher q_3 are excluded as they require a rising upper envelope. In addition, the $q_3 = 5$ model requires unphysically large disk masses for very old disks.
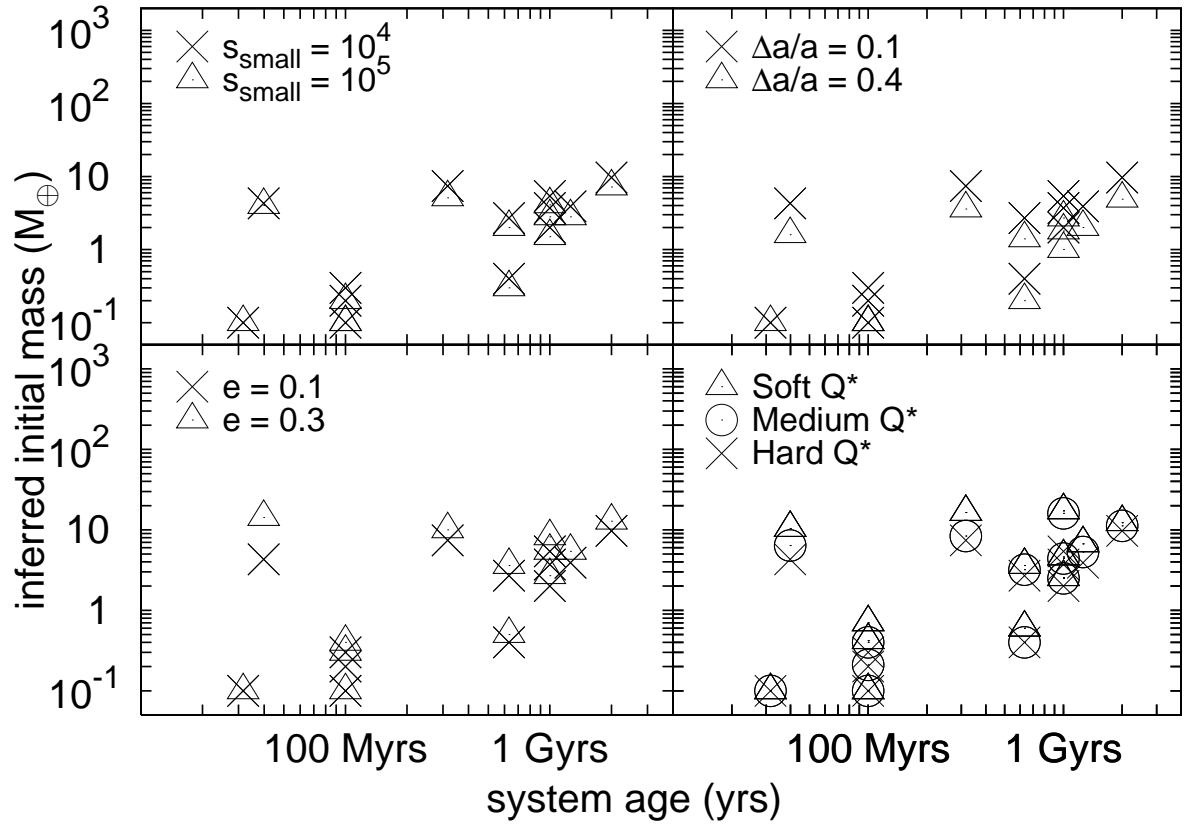
Figure 2.7: Similar to Fig. 2.6 except q_3 is fixed at 4 and a number of parameters are varied to test how the inferred initial masses depend on them. Specific values for the inferred mass may change, when the redistribution pattern for the collisional debris ($dn/ds \sim s^{-q_d}$, top-left), the eccentricity of particles (bottom-left), the fractional width of the debris ring (top-right), and the adopted strength law (bottom-right) are varied for all systems. These changes are mostly described by equation 7.11. However, the important indicator for our study, the upper envelope of the masses as a function of system age, remains flat. So the conclusion that $q_3 \sim 4$ is insensitive to the choice of these parameters.

spread in initial mass is expected as these disks have intrinsically different formation environment and history. However, the spread should be invariant with regard to stellar age, as disks formed at different cosmic times likely have the same initial distribution of disk properties. This simple assumption underpins our work.

We will be using this invariance to identify the correct model. However, using the spread itself is difficult due to selection effects. For instance, low mass disks may become too dim at late times to be observable. So we propose instead to study the upper envelope of this spread. If the spread is uniform across time, its upper envelope should also be flat with age for the correct model. In the following, we show that the model parameter most affecting the slant of the upper envelope is q_3, the power-law index in the primordial size spectrum.

The central figure of this chapter is Fig. 2.6 where we plot the inferred initial disk masses as functions of stellar age. Focusing only on the most massive systems, their inferred masses appear to slope differently with time for different q_3, the power-law index in the primordial size spectrum. Models with $q_3 = 4.5$ or greater have upward rising upper envelopes and are therefore excluded by the data. Models with q_3 smaller than 3.5 lead to a decreasing initial mass with system age and are excluded as well. Only models with q_3 between 3.5 and 4 survive the test.

Our model employs a number of other parameters, such as the radial position and extent of the debris ring, the dynamical excitation and break-up strength of the particles. We have studied the robustness of our results when these parameters take different values. (Fig. 2.7). Changes in the inferred initial masses are largely explained by equation 7.11. The important message is that, as long as the values for these parameters remain constant over age, their exact values do not affect our conclusion on q_3. The assumption that the dynamical excitation is constant over age is suspicious, in light of results from coagulation models showing that stirring by large plantesemals increases gradually eccentricities of the disk particles. This is discussed in §2.5.

There is significant uncertainty in our conclusion due to the small sample size. However, we argue that a larger sample may still not favor models with, e.g., $q_3 = 5$. If $q_3 = 5$ (lower-right panel in Fig. 2.4), the system that remains easily detectable at 2 Gyrs of age requires an initial solid mass of $\sim 200 M_\oplus \sim 1 M_J$ in the planetesimal belt. The initial gas mass in such a belt will be higher than the total disk mass of a typical T-Tauri star ($0.01 M_\odot$).

By focusing on dust luminosities, we are sensitive only to bodies that lie below the break-size. As seen in Fig. 2.2, break-size marches up to few tens to a hundred kilometers by the end of a few billion years, if the disk has a mass of $M_0 = 12.4 M_\oplus$.

2.5 Discussions

2.5.1 Coagulation Models vs. Debris Disks

In our exercise, we have assumed a simple initial size distribution (eq. 2.1), with all bodies larger than a few hundred meters described by a single power law index q_3. We relax this assumption here.

Simulations of planetesimal coagulation produce typically more complicated size distributions. For example, Kenyon & Bromley (2008) started their simulations with all bodies at ≤ 1 km. After tens of millions of years of growth, most of the mass still remains at or below 1 km, with only $\sim 8\%$ of the mass being accreted into bodies 10 km or larger, $\sim 6\%$ into bodies 100 kms or larger, and $\sim 3\%$ into bodies of order 1000 kms.[4] We use a broken power-law to replicate this kind of primordial spectrum. We set $q_3 = 5.5$ from 1 km to 10 km, and $q_3 = 4$ from 10 km to 1000 km. Motivated by Schlichting & Sari (2011), we also consider a slightly different initial distribution with $q_3 = 7$ from 1 km to 10 km, and $q_3 = 4$ from 10 km to 1000 km. Both sets of size spectrum deposit mass

---

[4]Even at 10 Gyr, the same model predicts that no more than a few percent of the initial mass wind up in large planetesimals.
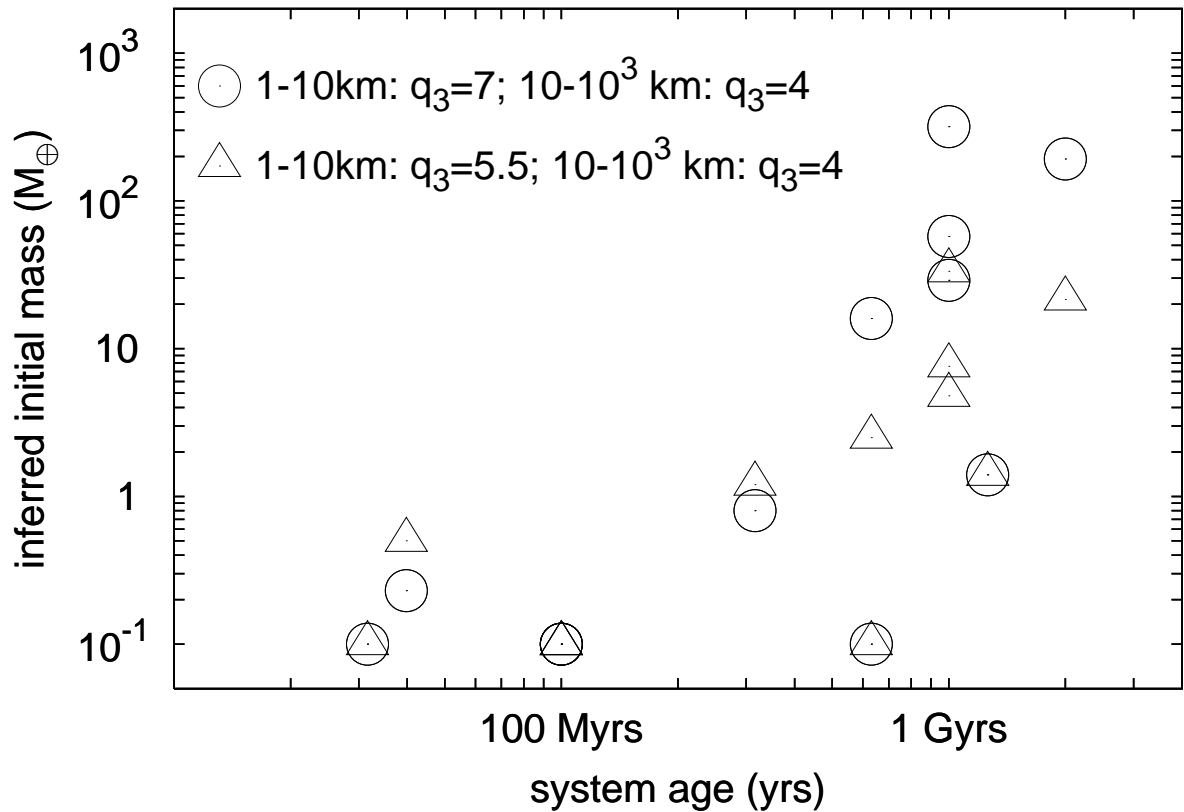
Figure 2.8: Inferred initial masses for a broken power-law size-distribution. We investigate two particular forms, motivated by coagulation simulations by Kenyon & Bromley (2008) and Schlichting & Sari (2011), respectively. Other parameters adopted are $e = 0.1$, $\Delta a/a = 0.1$, and the hard strength law. The inferred disk mass rises sharply with system age. Moreover, to make old and bright systems, we require disk masses that approach the mass of Jupiter.

mostly at the low end (≤ 1 km) and little at the large sizes. As expected, when initial masses are determined for different systems (Fig. 2.8), we find that young systems require exceedingly low initial masses, while old systems require unphysically large initial masses.

If we follow the luminosity evolution of such a disk, we will see that the disk flares brightly in the first tens of millions of years, due to the large mass reservoir at the 1 km-

range. Then the luminosity decays as $t^{-1/2}$ (as expected of a $q_3 = 4$ spectrum) but with a low normalization – most of the disk mass has been ground down in the early stage and we are now left with but a scrap remnant of the original. Conglomeration simulations typically find that only a small fraction of the mass can be accreted to make large bodies, before viscous stirring effectively stalls the growth. Schlichting & Sari (2011) showed that the fraction in large bodies can only be of order 10^{-3} in Kuiper-belt-like environments.

Does results in Fig. 2.8 allow us to exclude current conglomeration models? One possible caveat in our analysis is the eccentricity. We discuss this below.

2.5.2 Eccentricity

We assume a static, high eccentricity ($e = 0.1$) for all systems at all times and ignore eccentricity evolution due to collisional cooling and dynamical excitations. In realistic systems, eccentricities may be functions of time and particle size. How does this impact our conclusions?

One possible cause of eccentricity evolution is collisional cooling. Collisions dissipate energy, so collisional products have in average lower velocity dispersion than their parent bodies. In a single collision, two bodies with masses m_1 and m_1' (assume $m_1 \gg m_1'$) impact with typical random velocities

$$v_1 \sim v_1' \sim e_1 \, v_{\text{kep}}, \tag{2.8}$$

where the subscript 1 indicates that this is a first generation collision in our counting. Assuming maximum collisional cooling where all collision debris fly away from the collision site with the velocity of the center-of-mass, i.e., all relative velocities in the center-of-mass frame is dissipated during the collision, dispersion velocity in the debris is now reduced to

$$v_2 \sim \frac{\sqrt{m_1^2 v_1^2 + m_1'^2 v_1'^2}}{m_1 + m_1'} \sim v_1 \left(1 - \frac{m_1'}{2m_1}\right). \tag{2.9}$$

So the closer in mass the two colliding bodies are, the more cooling their debris experiences. The ratio of the two masses depends on the material strength as well as the impact velocity (eq. 7.2). For $e = 0.1$ and the hard strength law, this mass ratio is evaluated to be 0.006 for meter-sized boulders and 0.025 for cm-sized grains, respectively. Collisional cooling is negligible until near the blowout size.

Integrating the collisional cooling suffered by sucessive generations (mostly contributed by the small end), we find that collisional cascade can proceed all the way to blowout size as long as the initial eccentricity $e \geq 0.13$ for the hard strength law (or $e \geq 0.02$ for the medium strength law). We confirm this using a code which explictly includes collisional damping. In other words, for the $e = 0.1$ case we study, one can ignore collisional cooling.

This conclusion is further strengthened when one considers viscous stirring by large planetesimals. For the massive disks we consider here, the stirring can typically resupply eccentricity faster than collision can remove it. Eccentricity evolution is dominated by viscous stirring and eccentricity is largely size-independent. [5]

Over time, stirring gradually raises the eccentricity of all bodies as $e \propto t^{1/4}$ (c.f. Goldreich et al., 2004b). In the simulations of Kenyon & Bromley (2008), planetesimals, stirred by Pluto-like bodies, reach $e \sim 0.1$ at about a Gyr.[6]

Our inferred large body masses are orders of magnitude greater than that in their simulations so an eccentricity of 0.1 can be reached much earlier. Fig 2.9 shows that, even for a slowly rising eccentricity of the form $e = 0.1(t/1 \text{ Gyr})^{1/4}$, our estimates for disk masses remain largely unchanged.

In conclusion, we believe that collisional cooling is not important during the debris phase, and that we are justified in adopting a constant, high value of $e = 0.1$.

---

[5]Moreover, the condition for a successful collisional cascade is now reduced to $e \geq 0.05$ for the hard strength law (and $e \geq 0.01$ for the medium strength law). These constraints correspond to the minimum random motion necessary to break up the hardest grains (the smallest ones). They can be reduced by a factor of unity when radiation pressure on small grains are considered (Thébault, 2009).

[6]An eccentricity of $e \sim 0.3$ at 40 AU corresponds to the surface escape velocity of Pluto. Planetesimals have to have a near-surface encounter before they can reach such a high eccentricity.
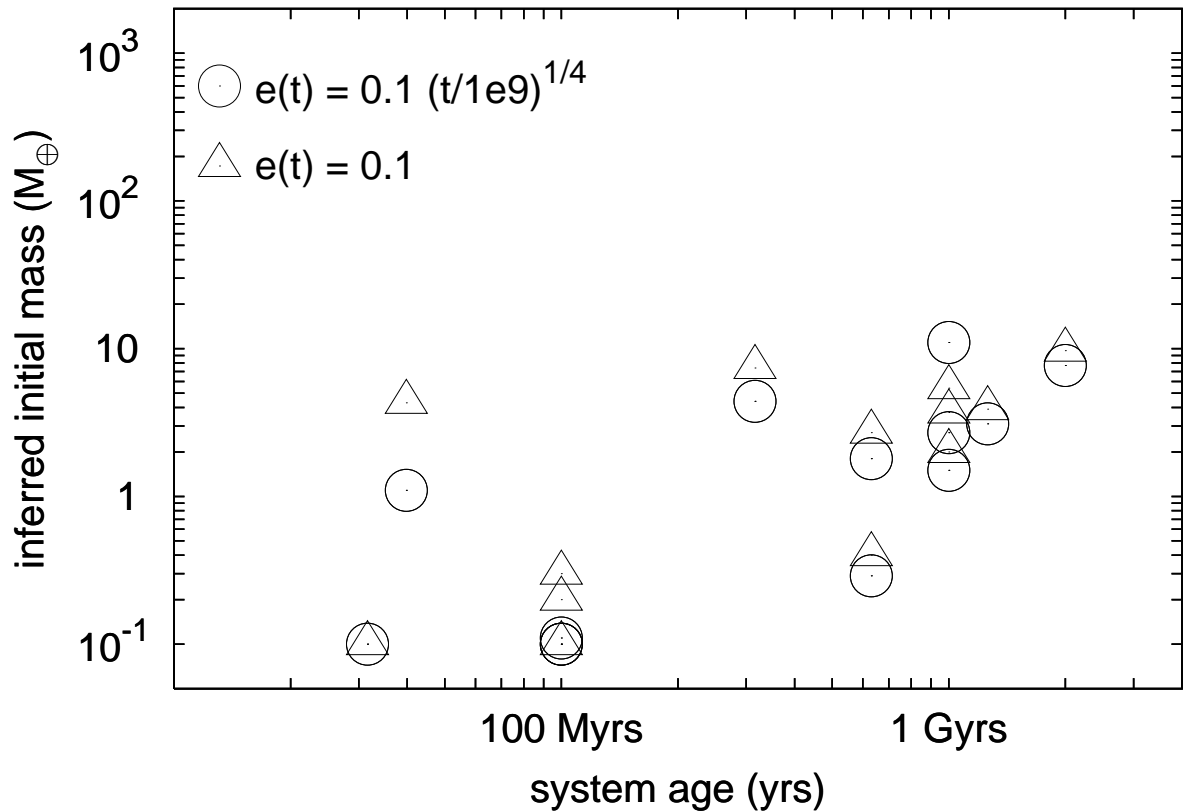
Figure 2.9: Same as the top-right panel in Fig. 2.6 but instead of a constant eccentricity ($e = 0.1$), here we assume that the eccentricity rises as $e(t) \approx 0.1(t/10^9\text{yrs})^{1/4}$. There is little difference to the inferred mass, and if anything, the data seems to argue that a $q_3 = 4$ model slightly overestimate the value of q_3. So our conclusion that $q_3 \in [3.5, 4]$ remains unchanged even considering eccentricity growth.

2.5.3 Radial Optical Depth

During the review process, the refreee pointed out that a debris disk with a radial optical depth greater than unity can sustain a large infrared luminosity over longer times. This may then invalidate much of the conclusions drawn here.

Here we have studied disks with an eccentricity (and inclination) of order 0.1. For these disks to be radially optically thick, the fractional optical/IR dust luminosity will be of order 0.1, about 100 times brighter than the brightest systems known. Conversely,

if the radial optical depth is indeed unity or greater, the true eccentricity/inclination will have to be about 100 times lower than our assumed values. With such a low excitation, collisions may well be conglomerative as opposed to destructive (see Fig. 2.1). In particular, it will be difficult to destroy micron-sized grains. And even if this issue is overcome, there are theoretical problems with optically thick disks: continuous grind-down without a mass exit will lead to rise of the optical depth with time; collisional cooling will be increasingly effective; and small bodies will be accreted by large rocks can as opposed to being ground down. We therefore suggest that a debris disk with a larger-than-unity radial optical depth may not exist.

2.5.4   Age of the debris disk = Age of the star?

As pointed out by our referee, our results in this paper relies critically on our implicit assumption that the duration of the debris disk phase is the same as the age of the star. There are at least two reasons to question this assumption. First, conglomeration models (Kenyon & Luu, 1999a; Kenyon & Bromley, 2001) typically require a few 10^7 years to produce Pluto-like bodies in Kuiper-belt-like environment, with the timescale increasing as one moves away from the star.[7] This will delay the onset of the debris phase. Second, some models associate the onset of debris disks with "Delayed Stirring" (Dominik & Decin, 2003; Mustill & Wyatt, 2009), and associate their disappearance with dynamical clearing (Fernandez & Ip, 1984; Habing et al., 1999; Raymond et al., 2011), thereby suggesting that debris disks may be a transient phenomena.

However, both of these theoretical arguments rub against current observations.

The youngest debris disks we observe are at a few Myrs old (Hernández et al., 2006). The disks peak in brightness around 10-15 Myrs, and decay slowly after that (Currie et al., 2008). Whether self-stirring or external stirring is responsible for the onset of debris disks, this occurs soon after the stars are born. One possibility is that small planetesimals

---

[7]We note, however, that none of our systems is younger than 30 Myrs.

enter the debris disk phase well before the largest bodies have finished forming (Kenyon & Bromley, 2008). The other possibility, as we will argue below using an independent line of evidence, is that the standard conglomeration theory today requires significant modification.

Dynamical instability of giant planets may excite the velocity dispersion of planetesimals and jump start the debris phase. If the debris phase lasts of order the stellar lifetime, our conclusion remains unchanged. But what if the debris phase lasts only a small fraction of the stellar lifetime and we happen to detect them when they are turned on? The fraction of stars that harbor bright disks at any age should then be of order the disk duration divided by the stellar age, in contradiction with the observations that the fraction of detectable disks is $\sim 15\%$ for stars of all ages (Trilling et al., 2008). Dynamical ejection of the plantesimals by planets, on the other hand, can explain why some stars are so dust poor.

2.6   Summary

Using an ensemble of bright debris disks around Sun-like stars, we have inferred the size spectrum of their embedded planetesimals. We parametrize the size spectrum as $dn/ds \propto s^{-q_3}$ and find $q_3 \approx 3.5 - 4$, where $q_3 = 4$ corresponds to equal mass per logarithmic decade. The planetesimal sizes our technique probes lie between a couple kms to ~ 100km.

While this size spectrum is consistent with the size spectrum of large planetesimals arising from coagulation simulations ($q_3 \sim 4$), there are two lines of evidence that suggest problems in current coagulation models.

The first line of evidence is related to the inferred disk mass. The inferred initial masses for these bright disks are surprisingly high. We find total masses reaching as

high as $10M_\oplus$.[8] This is comparable to the total solid mass in the Kuiper belt region of Minimum Mass Solar Nebula model, and about a factor of 100 higher than the mass in large Kuiper belt objects. Current coagulation models require an MMSN-like total mass to produce the observed density of large Kuiper belt objects. If the same inefficiency persists for our disks, one would require a total disk mass of $\sim$ 100 MMSN to produce those embedded planetesimals. This is difficult to imagine.

The second line of evidence regards the luminosity evolution. Current coagulation models are highly inefficient in making large planetesimals. So most of the mass remains at where they started, presumably $\sim$ 1 km. This leads to debris disks that are too bright at early times, reaching larger than unity radial optical depth, and that are too dim by a couple orders of magnitude at late times.

We do not believe these discrepancies can be resolved by relaxing some of our model assumptions. In particular, we argue that our estimate for q_3 is unchanged even taking into account the fact that disk eccentricity may rise with time.

Our results are also insensitive to the width of the debris ring, to the strength of bodies, and to the assumed upper and lower sizes.

Because we restrict our attention to the upper envelope of inferred masses, our result is dominated by a handful of systems. Our analysis may be vulnerable to errors. However, the presence of bright debris disks even at a few billion years is firmly established by current observations. This alone dictates that there ought to be a significant amount of mass stored in large (10-100 kms) planetesimals. We address how this is accomplished by revisiting coagulation model in chapters 4 and 5.

---

[8]This is for $q_3 = 4$, and even higher values are required if $q_3 = 3.5$.

Chapter 3

Collisionally Undamped Conglomeration

This chapter is a modified version of a draft publication. The research was done in conjunction with Dr. Yanqin Wu, and Dr. Yoram Lithwick, and the preparation of the chapter was done in conjunction with Dr. Yanqin Wu. It is reproduced here with their permission.

3.1   Background

We now know that solid bodies, ranging from a few kilometers to a couple thousand kilometers, roam in the outskirts of both the solar and many extrasolar systems. In the case of the solar system, Pluto, Sedna and other large Kuiper belt objects are directly detected (Slipher & Tombaugh, 1930; Jewitt & Luu, 1993; Brown et al., 2004; Schlichting et al., 2009); and in the case of extrasolar ones, these bodies are inferred from the dust grains that are produced during their mutual collisions. Even a small amount of dust can intercept enough star light to become detectable as debris disks (Smith & Terrile, 1984; Wyatt, 2008). Surprisingly, $\sim 20\%$ of solar analogs harbor dust disks that are brighter than ours by more than three orders of magnitude (Meyer et al., 2007).

How do these bodies form? Are they an intermediate step in the formation route for planets? Why are they not incorporated into Earth or even Neptune-like planets? Why are many exo-debris disks so bright yet ours so anemic? These are the questions we set out to answer.

The conventional picture for the formation of (our own) Kuiper belt (Kenyon & Luu, 1998; Ormel et al., 2010; Schlichting & Sari, 2011) postulates that there were ~ 10 Earth masses of primordial rock and ice ($\sim$ solid mass in the Minimum Mass Solar Nebulae), and only $\sim 10^{-3}$ of this mass conglomerated into the large Kuiper belt bodies we see today. The rest was somehow removed. This extremely low efficiency occurs because, theorists argue, as bodies like Pluto grow, they stir the orderly orbital motion of the seed material to such an extent that the latter can no longer be accreted quickly into large bodies: Plutos starve themselves.

However, there is a serious issue with this paradigm: the exo-debris disks are too bright. The total mass in their large Kuiper belt bodies must be ~ 1000 times that in our own system (chapter 2). According to the conventional picture of Kuiper belt formation, this would have required $\sim 10^4$ Earth masses of primordial solid, some 100 times more than the value expected in a minimum mass solar nebula. The low efficiency problem is further exacerbated if many Pluto-like large bodies were scattered away by giant planets, as some theories of Neptune migration maintain (Stern, 1991; Levison et al., 2008).

Instead, we start exploring along a different route, stimulated by the theoretical proposal of Goldreich et al. (2004b) (hereafter GLS). Different from all previous works (e.g., Safronov, 1969; Greenberg et al., 1978; Wetherill & Stewart, 1989; Kenyon & Luu, 1998; Kenyon & Bromley, 2008; Ormel et al., 2010; Schlichting & Sari, 2011), we model the plantesimals as being so small that their mutual collisions are dynamically important. In this picture, as seed materials are stirred up their destructive collisions grind them down to smaller debris. Smaller seeds collide much more frequently than larger ones and their

64

relative velocities remain low. This collisional cooling continuously guarantees efficient accretion by large bodies, until almost all mass has been converted to large bodies. Such a picture will allow the *in situ* formation of the cold classical Kuiper belt (chapter 4), and explain the high mass in the bright exo-debris disks (chapter 5).

In this chapter, however, we restrict ourselves to the conventional case of no collisional cooling. There are three purposes to this chapter. One is to document our numerical algorithm and certify its various components against theoretical expectations. This code already contains collisional break-down and cooling but these are unimportant here since we adopt large initial sizes for the planetesimals (~ 1 km). The second purpose is to compare the results from our code against previous works. In particular, Schlichting & Sari (2011, hereafter, SS11) have recently proposed a simple explanation for the size distribution of Kuiper belt bodies, in the case of collisionless conglomeration. We examine this claim critically. Lastly, our results here highlight one serious plight of all collisionless conglomeration models: extreme inefficiency. Starting with a plantesimal disk of a mass of $\sim 10 M_\oplus$ (similar to that expected in a MMSN disk extrapolated to the Kuiper belt distance, Weidenschilling (1977b); Hayashi (1981)), only $\sim 10^{-3}$ of the mass can be incorporated into large bodies that one observes today.

3.2   The Conglomeration Code: Component Testing

We adopt a particle-in-a-box approach (Safronov, 1969) to study the interactions of plantesimals and their growth. The range of body sizes we track runs from $\sim$ km to $\sim 10^3$ km (and even larger when we consider grains as small as 1μm in the future). The total number of particles active in our simulations can exceed 10^{15} or more. We typically simulate the system for up to 10^6 dynamical times. These factors necessitate a statistical approach where particles with similar properties (mass, eccentricity, inclination, semi-major axis) are grouped into the same bin. We do not yet have the capability of coupling

N-body integrators with the statistical code, as was done by Bromley & Kenyon (2006); Kenyon & Bromley (2008); Glaschke (2006). As such, we fail to capture the evolution correctly when only a few large bodies dominate the dynamics.

3.2.1 Particles and Bins

A total of six parameters are needed to specify an orbit, the semi-major axis a, the eccentricity e, the inclination i, the argument of periapse ω, the longitude of the ascending node Ω, and the mean anomaly M. Together with mass, each particle should be described by seven parameters. This is computationally prohibitive and approximations are in order. In the following we explain the simplifying assumptions we make in this code.

We adopt a single-value of semi-major axis ($a = 45\text{AU}$) for all particles, spread to a width $\Delta a \sim 0.13a \sim 6$ AU. Our single zone approach limits us to study systems where the eccentricities are small ($e < \Delta a/a$). The particles are assumed to be distributed uniformly in ω, Ω, and M. We assume that the random kinetic energy of particles is equipartitioned between eccentricity and inclination, so $i = 0.5e$ (Hornung et al., 1985). So velocity anisotropy, important when particles are very cold (Ida & Makino, 1992; Rafikov, 2003), is not treated properly here.

These simplifications allow us to describe particles only by their masses and eccentricities. We track particle flow across both the mass bins and the eccentricity bins, as is done in Krivov et al. (2005). This differs from the approach of, e.g., Kenyon & Luu (1998), where particles carry with them floating mass values. The eccentricity bins have values from $e = 10^{-7}$ to $e = 1$ and are equally spaced in logarithmic space with typically four bins per decade ($\Delta e = 10^{0.25}e$). The mass bins are also spaced in logarithmic space, with six bins covering a decade of mass (i.e., $\Delta m \approx 1.47m$). Particles of all masses are assigned the same bulk density, $\rho = 1.5\text{g/cm}^3$.

The dispersion velocity of a particle is (Wetherill & Stewart, 1993),

$$v = v_{\text{kep}} \sqrt{\frac{5}{8}e^2 + \frac{1}{2}i^2} \tag{3.1}$$

where $v_{\text{kep}} = \Omega a$ with Ω being the orbital angular frequency.

We use a second-order Runge-Kutta integrator to advance the simulation in time, as the dynamical processes detailed below lead to mass and eccentricity evolution. There are two subtleties in the actual implementation. First, when the outcome of an interaction results in a new mass/eccentricity that falls in between two adjacent bins, we split the particles into the two logarithmic bins conserving total mass and mass-weighted eccentricity (in the case of eccentricity), and total mass and total number (in the case of mass). Moreover, our integration has a fixed time step, typically set to be 100 years. In the case where dynamical evolution leads to undershooting (negative number of particles) in a bin at the end of a timestep, we reduce the strength of the dynamical interaction such that the bin empties to zero. This is necessary when bodies are strongly affected by processes like viscous stirring and collisional cooling.

3.2.2   Dynamical Friction & Viscous Stirring

Mutual gravitational interactions lead to equipartition of random kinetic energies between bodies. This is called dynamical friction (Chandrasekhar, 1943). Additionally, in a keplerian disk, gravitational interactions between bodies convert their orbital energy into random kinetic energy. This is called viscous stirring (Safronov, 1969).

To model dynamical friction and viscous stirring, we adopt the prescription of Ohtsuki et al. (2002), who provide semi-analytic formula for the rates at which eccentricity and inclination evolve through gravitational scatterings, calibrated by N-body simulations.
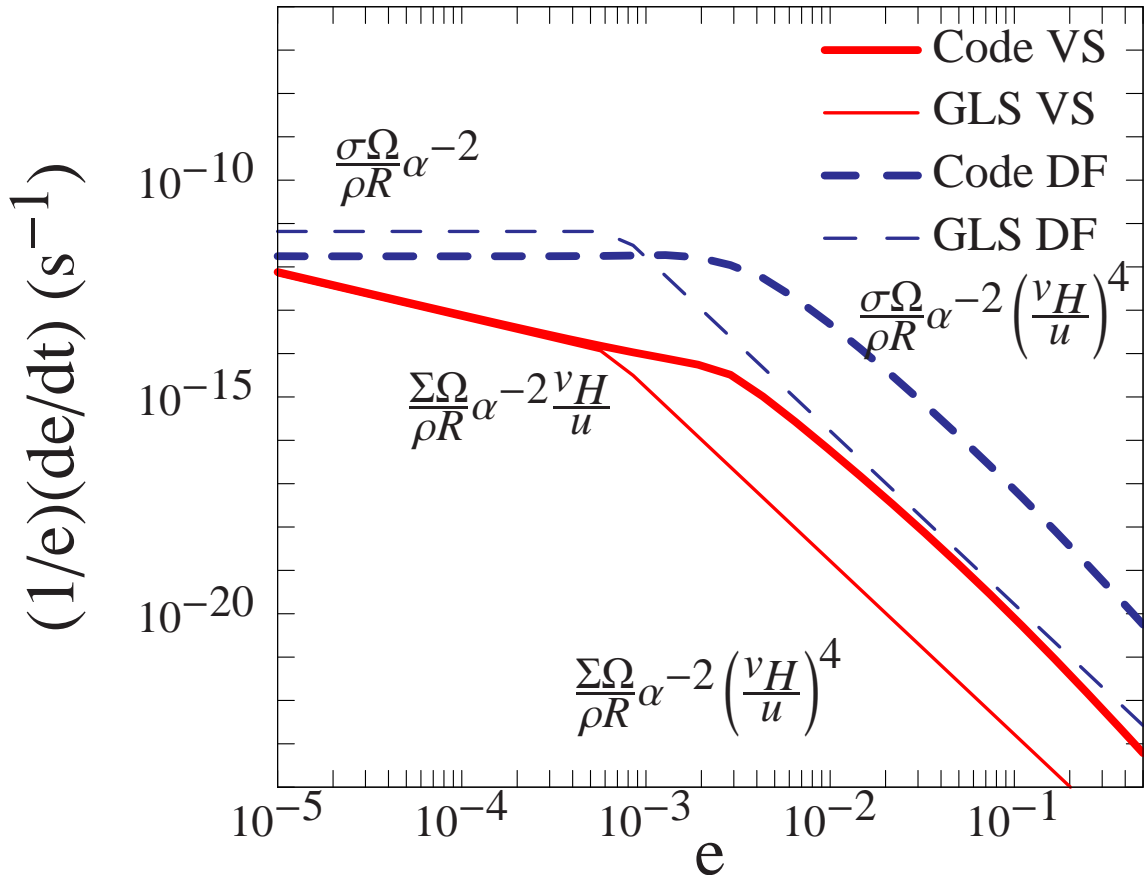
Figure 3.1: The magnitudes of viscous stirring and dynamical friction (negative in sign) used in our code (continuous lines), as compared to the order-of-magnitude estimates (broken lines) of GLS, plotted here as functions of eccentricities. Their expressions are explicitly labelled here. These rates are calculated for a population of $s = 1$ cm small bodies and $R = 1000$ km big bodies interacting with small bodies at 45 AU. The surface densities are $\Sigma \sim 10^{-4}$ g/cm^3 and $\sigma \sim 0.1$g/cm^3, and the velocities are set to be $u = v$. The rate of dynamical friction applies to the big bodies only. The big body have Hill velocity $v_H = e_H v_{\text{kep}}$ with $e_H \sim 10^{-3}$. The GLS rates are similar to our numerical rates if one replaces their v_H by $2.5 v_H$, as also suggested by N-body experiments (Nishida, 1983; Greenberg et al., 1991).

They provide the expression:

$$\frac{d\langle e_1^2\rangle}{dt} = a^2\Omega \sum_{j=1,2}\left[\frac{h_{1j}^4\sigma_j}{(m_1+m_j)^2}\right.$$

$$\left.\times \left(m_j\langle P_{VS}\rangle_{1j} + \frac{m_j\langle e_j^2\rangle - m_1\langle e_1^2\rangle}{\langle e_1^2\rangle + \langle e_j^2\rangle}\langle P_{DF}\rangle_{1j}\right)\right]. \tag{3.2}$$

Here:

$$P_{VS} = c_1 P_{VS}^{\text{low}} + P_{VS}^{\text{high}},$$

$$c_1 = \ln\left(\frac{10\Lambda^2}{\tilde{e}^2}+1\right),$$

$$\Lambda = \frac{1}{12}\left(\tilde{e}^2+\tilde{i}^2\right)\sqrt{\tilde{i}^2},$$

$$P_{VS}^{\text{low}} = 73,$$

$$P_{VS}^{\text{high}} = P_{VS}'\ln\left(\Lambda^2+1\right),$$

$$P_{VS}' = \frac{72 I_{PVS}(\beta)}{\pi\langle e^2\rangle^{\frac{1}{2}}\langle i^2\rangle^{\frac{1}{2}}},$$

$$I_{PVS}(\beta) = \int_0^1 \frac{5K_\lambda - \frac{12(1-\lambda^2)}{1+3\lambda^2}E_\lambda}{\beta+(\beta^{-1}-\beta)\lambda^2}d\lambda,$$

$$\beta = \frac{\langle i^2\rangle^{\frac{1}{2}}}{\langle e^2\rangle^{\frac{1}{2}}},$$

with $K_\lambda = K\left([3(1-\lambda^2)]^{0.5}\div 2\right)$, and $E_\lambda = E\left([3(1-\lambda^2)]^{0.5}\div 2\right)$ being the complete elliptic integrals of the first and second kind respectively. But when the mutual velocity of two bodies are below their mutual Hill velocity (sub-Hill), we instead adopt the viscous heating prescription in eq. (13) of Collins et al. (2007), calibrated by the numerical simulations of Collins & Sari (2006). They provide the expression

$$\frac{de}{dt} = 2.4\frac{\Sigma\Omega}{\rho R}\frac{1}{\alpha^2}e_{\text{Hill}}. \tag{3.3}$$

To compare our adopted prescriptions against analytical scalings in GLS, we integrate a disk that is composed of two uniform groups of particles (Wetherill & Stewart, 1989, GLS). One group is the smaller bodies with size s, surface density σ and velocity

dispersion u; the other group is the large bodies with radius R, surface density Σ and velocity dispersion v. We denote v_H to be the Hill velocity of the large bodies,

$$v_H = v_{\text{kep}} \left(\frac{M_{\text{big}}}{3 M_\odot} \right)^{1/3} \approx 3^{-1/3} \alpha^{-1} \Omega R \,, \tag{3.4}$$

where the big body mass $M_{\text{big}} = 4\pi/3 \rho R^3$ with ρ being the bulk density. We set ρ to be the mean density of the Sun, and use α to denote the angular size of the Sun, viewed by the bodies, $\alpha = R_\odot/a$. For the Kuiper belt, $\alpha \sim 10^{-4}$.

GLS give explicit formulae for the rate of viscous stirring and dynamical friction, depending on whether the velocities are sub- or super-Hill (also called shear- or dispersion-dominated). The two most relevant expressions are viscous stirring of small bodies by the big ones, and dynamical friction of the big bodies by the small bodies. Assuming $u > v$, these are

$$\frac{1}{u} \frac{du}{dt} \bigg|_{vs} \sim \frac{\Sigma \Omega}{\rho R} \alpha^{-2} \begin{cases} \left(\frac{v_H}{u} \right)^4 & u > v_H, \\ \left(\frac{v_H}{u} \right) & u < v_H. \end{cases} \tag{3.5}$$

$$\frac{1}{v} \frac{dv}{dt} \bigg|_{df} \sim -\frac{\sigma \Omega}{\rho R} \alpha^{-2} \begin{cases} \left(\frac{v_H}{u} \right)^4 & u > v_H, \\ 1 & u < v_H. \end{cases} \tag{3.6}$$

Viscous stirring of large bodies by themselves can be found by substituting v for u in equation 3.5. As Fig. 3.1 shows, our adopted prescriptions agree with the above estimates well, especially if v_H in these estimates are substituted by $2.5 v_H$. We will henceforth adopt the GLS rates for analytical derivations.

3.2.3 Collisions: Cooling and Cascade

In the particle in a box method, the frequency of collision for a particle is $f_c = n\pi b^2 v$. Here, n is the number density of other particles, πb^2 the cross section for collision, and v the relative velocity. The relative velocity between two particles is simply set to be $v = \sqrt{(v_1^2 + v_2^2)}$ where v_i is as defined in equation (3.1).

Under our assumption of evenly distributed orbital angles, particles in an (a, e) bin occupy a torus that has a physical volumn (see, e.g. Krivov et al., 2005),

$$V(e) = \frac{4\pi}{3} a^3 \left[(1+e)^3 - (1-e)^3 \right] \sin i \,. \tag{3.7}$$

Their number density is then obtained by $n = N/V$ where N is the particle number. Between two groups of particles with different e's (e_1, e_2, but the same a), their overlapping volume is determined by the group with the smaller e (let it be e_1), and the collision frequency should be reduced by a ratio of $V(e_1)/V(e_2)$ to take account of the reduced residence time group 2 particles spend inside $V(e_1)$.

The cross section for interaction, between particles of size s_1 and s_2, has a three-piece form (Greenberg et al., 1991; Dones & Tremaine, 1993, GLS),

$$\pi b^2 = \begin{cases} \pi \left(s_1 + s_2\right)^2 \left(1 + \frac{v_{\mathrm{esc}}^2}{v^2}\right) & v_{\mathrm{H}} < v, \\ \pi \left(s_1 + s_2\right)^2 \left(\sqrt{6}\alpha^{-\frac{1}{2}} \frac{v_{\mathrm{H}}}{v}\right) & \alpha^{\frac{1}{2}} v_{\mathrm{H}} < v < v_{\mathrm{H}}, \\ \pi \left(s_1 + s_2\right)^2 \left(\sqrt{6}\alpha^{-\frac{3}{2}}\right) & v < \alpha^{\frac{1}{2}} v_{\mathrm{H}} \,. \end{cases} \tag{3.8}$$

These are the thick, thin, and superthin cases, respectively. Moreover, these expressions apply when the velocity dispersion is isotropic ($i \sim e$).

Collisions can change both velocity and mass for the particles concerned.

In terms of velocity evolution, we set the orbits of the post-collision particles to follow the motion of the center of mass. This is equivalent to assuming a complete dissipative collision, or that the coefficient of restitution is zero. Let the two bodies have initially masses m_1, m_2 ($m_c = m_1 + m_2$), dispersion velocities v_1, v_2, the constraints of mass and momentum conservation lead to the following expressions for the new orbital elements, (a_f, e_f) (Krivov et al., 2005):

$$\frac{m_c}{2a_f} = \frac{m_1}{m_c}\frac{m_1}{2a_1} + \frac{m_2}{m_c}\frac{m_2}{2a_2}$$
$$- \frac{m_1 m_2}{m_c} \left(\frac{\mathbf{v_1} \cdot \mathbf{v_2}}{GM_\odot} - \frac{2}{r} \right),$$
$$m_c a_f \sqrt{1 - e_f^2} = m_1 a_1 \sqrt{1 - e_1^2} + m_2 a_2 \sqrt{1 - e_2^2}, \tag{3.9}$$

71

where r is the position of the collision. For our single zone calculation, we keep $a_f = a$ but adopt the new e_f.

An order-of-magnitude estimate for the rate of collisional cooling among small bodies is (GLS)

$$\frac{1}{u}\frac{du}{dt} = -\frac{\sigma\Omega}{\rho s} \, . \tag{3.10}$$

We confirm that our code produces a quantitatively similar behaviour (figure 3.2).
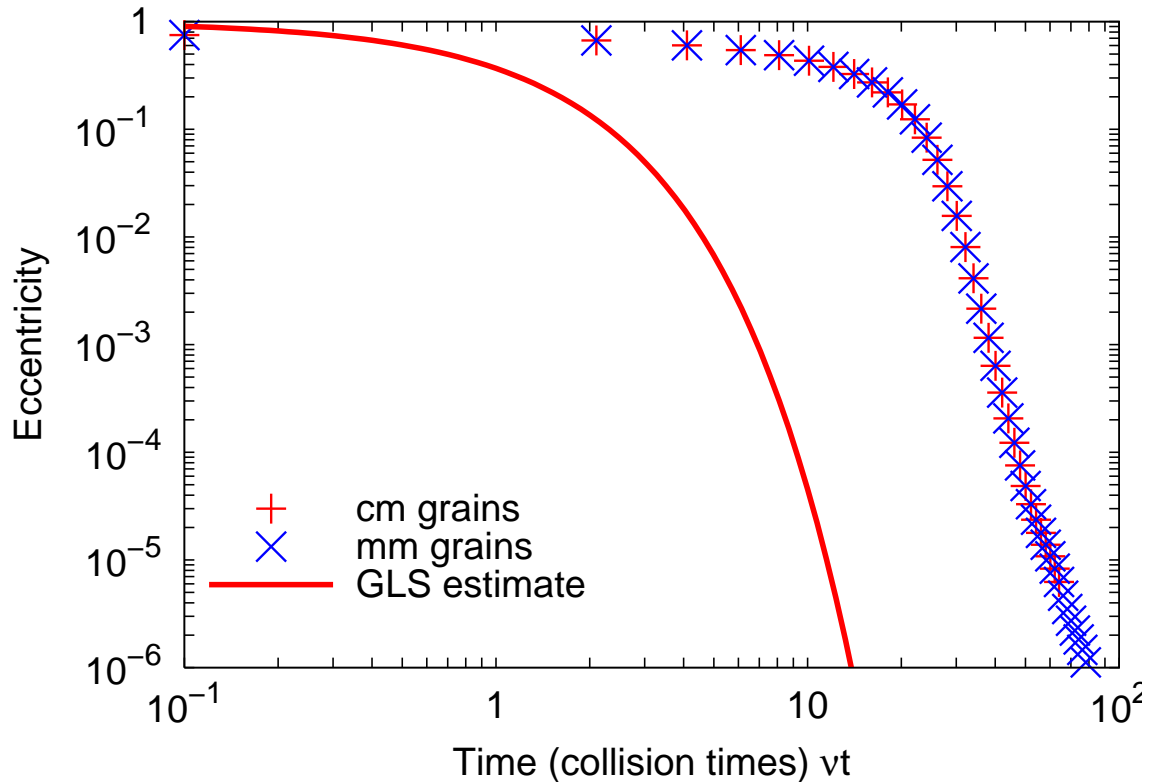
Figure 3.2: Numerical simulations of collisional cooling, when the particles are of sizes cm (red dots and curves) and mm (blue ones). The time axis is rescaled as νt where ν is the collisional frequency (eq. 3.15). The order-of-magnitude expressions from GLS are plotted as thin curves. Numerical results and analytical estimates agree to within order of unity.

In terms of mass evolution, collisions can lead to collisional destruction, (inelastic)

rebound, or conglomeration. Catastrophic collision is defined where the primary body loses $\geq 50\%$ of its mass. We specify this to happen if the specific kinetic energy in the impact, $0.5 \, (m_1 m_2) / (m_1 + m_2)^2 \, v^2$, exceeds the disruption threshold Q^* (Stewart & Leinhardt, 2009),

$$Q^* \approx 500 \left(s_1^3 + s_2^3\right)^{-1/9} v^{0.8} + 10^{-4} \left(s_1^3 + s_2^3\right)^{0.4} v^{0.8}, \tag{3.11}$$

with all numbers in cgs units. This is the scaling for weak aggregates, and should be appropriate for Kuiper belt bodies. For km-sized bodies, $Q^* \sim 10^4$ g cm^{-3}, or a disruption velocity with $v \sim 100$ cm/s, or $e \approx 10^{-3.5}$ at 40 AU. When bodies are catastrophically disrupted, we distribute their masses to all smaller sizes with a number distribution that is power-law in size, $dn/ds \propto s^{-q}$ with s for $s = s_i/10^{1/18}$ and 0. We typically take $q = 3.5$. This means the size of the biggest fragments is close to the primary mass. In the future, it may be useful to implement the dependence of the largest fragment mass on the impact energy (Stewart & Leinhardt, 2009).

To verify the collisional mass evolution, we test our code against the standard case of collisional equilibrium for which an analytical solution is known. For a material strength $Q^* \propto s^p$, collisional cascade will carry a constant mass flux downward in particle size and build up an equilibrium size distribution of (Dohnanyi, 1969),

$$\frac{dn}{ds} \propto s^{-q}, \tag{3.12}$$

with $q = (21 + p)/(6 + p)$. The well-known Dohnanyi law is a special case: $q = 3.5$ when $p = 0$. In the numerical experiment shown in Fig. 3.3, we adopt a constant strength of $Q^* = 10^8$ ergs/g, and initialize the particle size distribution with $dn/ds \propto s^{-4}$. We ignore collisional cooling here by using only one eccentricity bin ($e = 0.15$). Irrespective of the power-law we choose for the debris redistribution, we find that small bodies in the system settles into the expected $q = 3.5$ form and larger bodies gradually enter into collisional equilibrium as time goes on (figure 3.3).
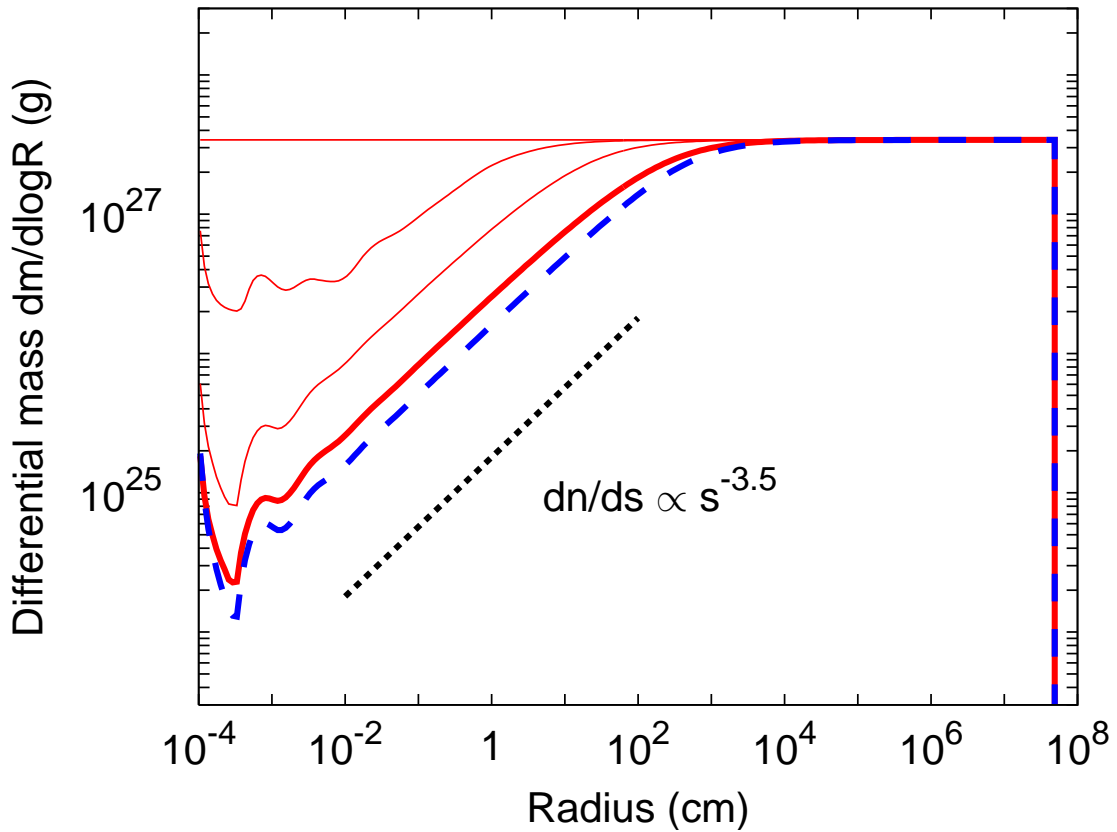
Figure 3.3: Evolution in the differential mass distribution during a collisional cascade, plotted at $t = 0, 10^4, 10^5, 10^6$ yrs (red curves). Collisional strength is taken to be a constant and bodies that are in collisional equilibrium satisfy $dn/dR \propto R^{-3.5}$ (Dohnanyi, 1969). Initial surface density $\sigma = 0.1 \mathrm{g/cm^2}$, and mass of the catastrophically disrupted bodies are distributed to smaller sizes as $dn/dR \propto R^{-q}$ with $q = 4$. For comparison, the blue dashed curve shows the size distribution at 10^6 yr if the redistribution instead proceeds as $q = 2$. We assume all particles smaller than 1μ m are instantly blow away by radiation pressure, this leads to the wavy pattern near the cut-off size, as described in Thébault et al. (2003).

If the collision energy is too low to cause destruction, we separate the outcomes into two further categories: rebound or conglomeration. In our code, conglomeration occurs

74

when the relative velocity is less than 10 times the mutual escape velocity. This disfavors conglomeration of small bodies: kilometer-sized bodies only accrete each other when $e \lesssim 10^{-3}$. When this is not satisfied, the bodies rebound, moving away from the collision site at the velocity of the center-of-mass. We do not model either cratering collision or sticking by chemical forces. In the following, we discuss in more detail the accretion process.

3.2.4 Details on Accretion

Given the collisional cross section in eq. (3.8), we find the following rate for accretional growth (GLS),

$$\frac{1}{R}\frac{dR}{dt} \sim \frac{\sigma\Omega}{\rho R}\alpha^{-1}\begin{cases}\left(\frac{v_{\rm H}}{u}\right)^2, & v_{\rm H} < u < v_{\rm esc}, \\ \left(\frac{v_{\rm H}}{u}\right), & \alpha^{\frac{1}{2}}v_{\rm H} < u < v_{\rm H}, \\ \left(\alpha^{-\frac{1}{2}}\right), & u < \alpha^{\frac{1}{2}}v_{\rm H}.\end{cases} \tag{3.13}$$

Small bodies here (σ and u) refer to all bodies $\leq R$ that contribute to the accretional growth. Our numerical algorithm does reproduce the above relations. But we have to discuss a subtlty here. These expressions are based on an isotropic velocity dispersion, or $i \approx e$. However, when $u < v_H$, small body inclinations are stirred by bodies R at a lower rate than their eccentricities while both quantities are damped by dynamical friction at comparable rates. If only bodies R are responsible for stirring, we should find small bodies with $i \ll e$ and the accretion rate should take on the super-thin formula (GLS). In practice, the stirring is contributed by all bodies, and especially in the sub-Hill regime, contribution from bodies other than the largest sizes are more important. Short of tracking the inclination evolution[1], it is difficult to ascertain the accretion geometry. Moreover, the enhancement in accretion rate due to the super-thin treatment is a factor of $\alpha^{-1/2}(u/v_{\rm H})$ over the sub-Hill accretion rate. This is a significant enhancement for

---

[1]This is computationally prohibitive

bodies that have $u \approx v_{\mathrm{H}}$, but insignificant for bodies with $u \ll v_{\mathrm{H}}$. Fig. 3.4 shows that these are objects that are much smaller than R_{max} at any given time. In this chapter, we simply assume an isotropic velocity dispersion even though it carries mistakes when dealing with, esp., accretion among big bodies. See section 7.2 for a comparison of the isotropic and superthin limits in the collisionless case.

We discuss a numerical detail that concerns the growth of the largest bodies. When two bodies (m_1, m_2, with $m_1 < m_2$) merge, the combined mass in the new body typically falls between m_2 and the next mass bin (m_3). We deposit a fractional body in the m_2 bin and the remainding fraction in the m_3 bin, conserving total mass. This causes no major concern except where the fractional body in m_3 is the largest body in the system and it accretes much more quickly than other bodies. We would then have a fractional body running away from the pack. To avoid this unphysical outcome, we record the number of bodies in m_3 when the bin is first occupied, let this be f. We then refrain from promoting the body in size until the bin has grown in total mass (Δm) through accretion onto the bodies of mass m_3, by an amount of

$$\Delta m \geq (m_4 - m_3) \times f \,, \tag{3.14}$$

where m_4 is the next mass bin. Until that time, the extra mass is stored in bodies of size m_3. Once Δm meets condition 3.14, bodies are promoted from m_3 to m_4 in a fashion that retroactively conserves total number. We call this "large body gating" and we believe it best captures the nature of large body growth in our numerical scheme.

3.3   Conglomeration: Results and Analytics

For the purpose of validating our conglomeration code, we adopt an initial set-up of the planetesimal disk that is similar to previous works (Greenberg et al., 1978; Wetherill & Stewart, 1989; Kenyon & Luu, 1998; Kenyon & Bromley, 2008; Ormel et al., 2010; Schlichting & Sari, 2011). Our disk is made up of 1 km planetesimals with a surface
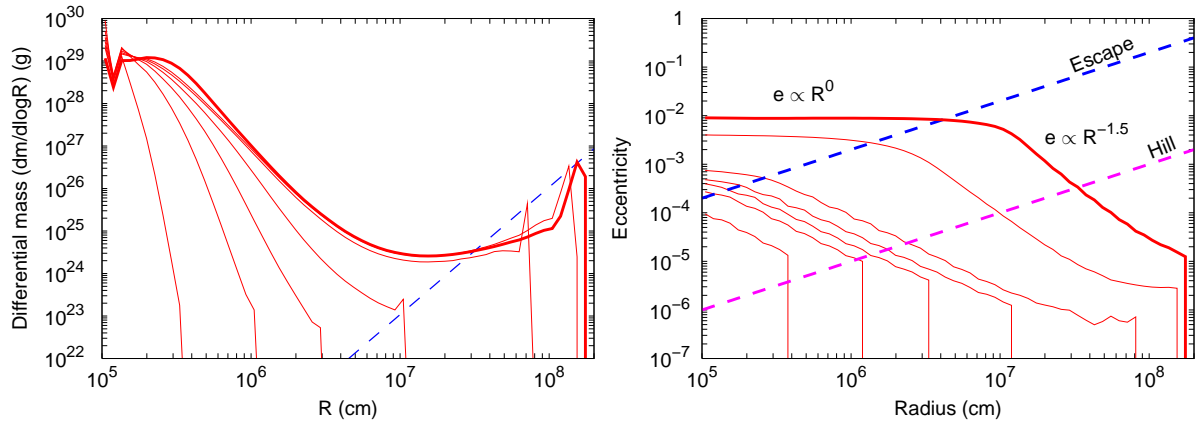
Figure 3.4: Results of conglomeration simulations, starting from a disk of 1km bodies with a surface density $\sigma \sim 0.1\text{g/cm}^2$ (solid density for MMSN at 40 AU, a total mass of $10M_\oplus$ in simulation) and an initial eccentricity 10^{-7}. The left panel shows the evolution of differential mass and the right panel that of eccentricity, plotted as functions of body sizes. Data is plotted at 250 kyrs, 4 Myrs, 8 Myrs, 12 Myrs, 16 Myrs, 20 Myrs (thin lines), and 40 Myrs (thick line). In the left panel, the dashed blue line indicate 1 body per mass bin (18 bodies per size decade), and the upturn in differential mass at the largest size bin is an artefact of our 'large-body-gating' procedure (see §3.2.4). At 40 Myrs, the number distribution of large bodies (100-1000km) can be roughly described as a power-law, $dn/ds \propto s^{-q}$ with $q \sim 3.5$ (although a power law fit may not be preferred). The efficiency of conglomeration, defined here as the mass fraction above 100 km, is 10^{-3}. On the right panel, the two thin dashed lines correspond to the surface escape velocity and Hill velocity for different size bodies. At 40 Myrs, small bodies are uniformly stirred by the largest bodies ($e \propto s^0$), while larger bodies experience dynamical friction from the seed planetesimals, so $e \propto s^{-1/2}$, roughly consistent with equipartition of kinetic energies. These behavior agree with the analytical expectations in Rafikov (2003), and is found in simulations by Kenyon & Bromley (2008); Ormel et al. (2010)
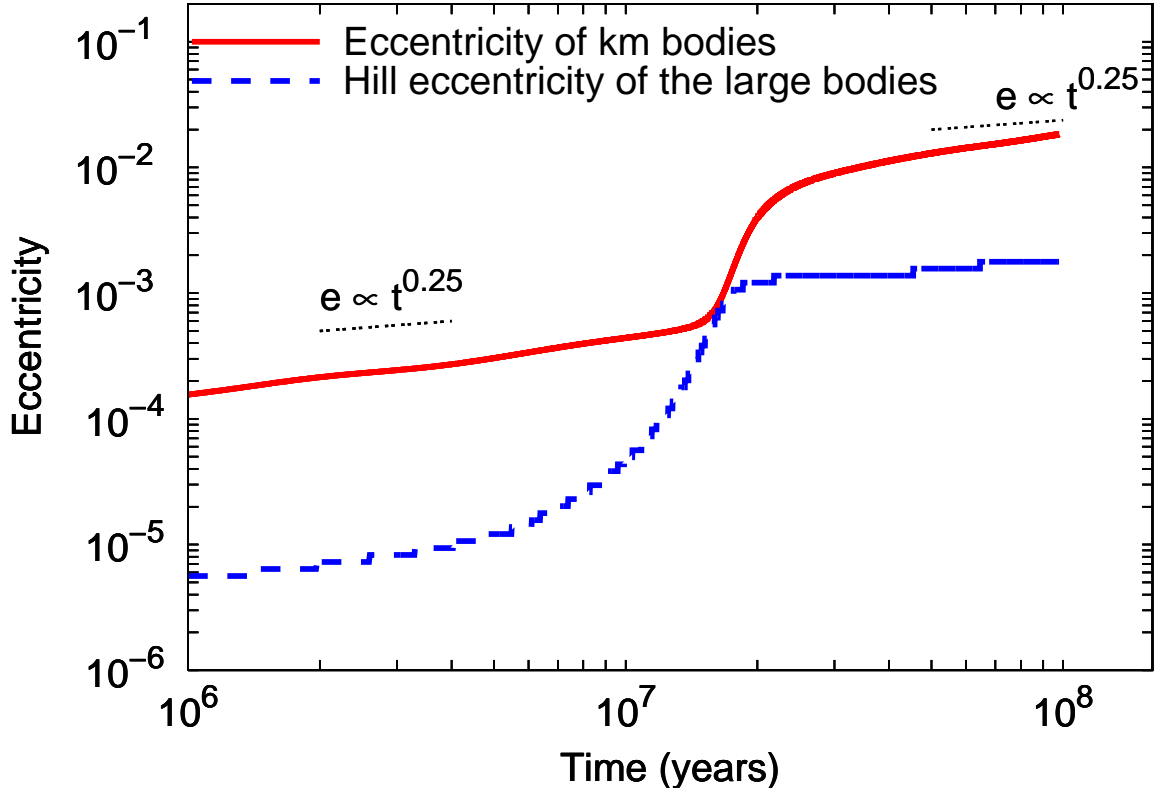
Figure 3.5: Time evolution of small body eccentricities for the simulation in Fig. 3.4 is plotted as a solid red curve, and that of the Hill eccentricity of the largest bodies plotted as blue dashed curve, $e_{\mathrm{H}}(R_{\mathrm{max}}) \sim 10^{-3}(R_{\mathrm{max}}/1000~\mathrm{km})$. Initially, eccentricities of small bodies grow $\propto t^{1/4}$, as their self-stirring ... then eccentricity growth follows $e \propto t$; afterwards, $e \propto t^{1/4}$ again. The small bodies stir each other up to $\sim 1/3$ of their escape velocities after a few Myrs. This is followed by a rapid (flat e) and slow (rising e) run-away phase. See text for details. In the slow phase, the dispersion velocity of the seed materials scales with the largest body size as in equation (3.22).

density of $\sigma = 0.1~\mathrm{g/cm^2}$, spread over a radial width of $\Delta a/a = 0.13$ at $a = 45$ AU. This corresponds to a total mass of $10 M_{\oplus}$. These bodies ($\sim 10^{13}$ of them) are initially placed on dynamically cold orbits with $e = 10^{-7}$. There is not a strong rationale for these initial conditions, and we will revisit the subject in chapters 4 and 5. We argued in chapter

2 that current observations are inconsistent with conglomeration simulations where the seed planetesimals are as large as a kilometer, however, given the body of previous works, it is a sensible starting case.

Our simulations results are shown in Fig. 3.4, with Figs. 3.5 & 3.7 providing diagnostic details. The growth of the largest bodies is mainly due to accretion of kilometer seeds, at all times. So we focus on the eccentricity of the seed materials. The following scalings for the Kuiper belt region are useful: $e_{esc} \sim 10^{-1}(R/10^8 \text{ cm})$, and $e_H \sim \alpha^{1/2}e_{esc} \sim 10^{-3}(R/10^8 \text{ cm})$. We also interchangably use two size distributions: the number distribution and the mass distribution. If the number distribution $dn/dR \propto R^{-q}$, then the mass distribution $dm/d\log R \propto R^{4-q}$.

The seeds have a mean collision frequency

$$\nu = \frac{\sigma\Omega}{\rho s} \sim 10^{-7} \text{ yr}^{-1} . \tag{3.15}$$

This is the natural timescale in the problem of interest. So from now on, we express time always in the unit of $t\nu$. So after $\sim 10^6$ yrs, or $t\nu = 0.1$, they stir each other up to $\sim 1/2$ of their escape velocities (eq. 3.5).[2] Or, $e \sim 10^{-4}$, this is about the Hill velocity of a 100 km body. Run-away accretion (eq. 3.13) proceeds with the largest bodies pulling away from the rest of the pack but carrying little total mass (left panel of Fig. 3.4). These largest bodies dominate the heating process but they are able to grow faster than they stir. This fast growth proceeds for a few million years until the largest bodies have reached ~ 500km. By now their stirring effects begin to interfere with their feeding. This is a precursor to the 'oligarchic phase' (Kokubo & Ida, 1998) in which individual large bodies dominates the stirring in its own feeding zone. The run-away growth proceeds much more slowly from this point on, so we term it the 'slow run-away'.

We can understand these growth processes quantitatively, using the analytical scalings from GLS, as collected in §3.2.2 and 3.2.4. To do so, we separate the growth into three

---

[2]The actual value is closer to v_{esc} as we have shown that numerical expressions are best approximated by the GLS scalings if we replace v_H by $2.5v_H$. We ignore the difference here.

phases.

3.3.1 Geometric Accretion

The very early growth is dominated by pair-wise conglomeration among equal-sized bodies (size s). Assume collisions occur with geometric cross-section. At time $t \ll 1/\nu$, the average collision probability for each of the 10^{13} km-sized bodies is $(t\nu)$, but the probability of a single body having experienced N collisions is $(t\nu)^N$. So the size distribution is a steep function of N,

$$\frac{dn}{dR} \propto (t\nu)^N R^2 , \tag{3.16}$$

where $R = N^{1/3}s$. The largest body expected at time t is determined by $(t\nu)^N 10^{13} = 1$, or at a radius of

$$R_{1000}(t\nu) \approx \frac{s}{10^8} \left[\frac{-\log(10^{13})}{\log(t\nu)} \right]^{1/3} , \tag{3.17}$$

where we have scaled R by the approximate size of Pluto, $R_{1000} = R/10^8$ cm. We have ignored the evolution of u and the gravitational focussing during this process. These two effects complicates the discussion without affecting the conclusion much.

3.3.2 Rapid Run-away

During this stage of growth, we consider the seeds have been self-stirred to a constant value of $e \sim 10^{-4}$ (or $u \sim u_{\rm esc}$). The growth rate of large bodies is controlled by the super-Hill accretion (eq. 3.13),

$$\frac{1}{R_{1000}} \frac{dR_{1000}}{d(t\nu)} \sim \frac{s}{R} \alpha^{-1} \left(\frac{v_H}{u} \right)^2 \sim 10^8 s^{-1} R_{1000}. \tag{3.18}$$

From time $t\nu$ to $t\nu + \Delta$, large bodies have grown to

$$R_{1000}(t\nu + \Delta) = \frac{1}{R_{1000}^{-1}(t\nu) - 10^8 s^{-1} \Delta} . \tag{3.19}$$

Obviously, most of the time is spent at growing bodies near the starting size, $R_{1000}(t\nu)$. The value of this size critically impacts the duration of runaway growth. Setting this value

to that in equation (3.17), taking the limit of $R_{1000}(t\nu + \Delta) \to \infty$, and approximating $\Delta \sim t\nu$, we find the time to commence the run-away growth is (for $s = 1$ km)

$$(t\nu)_{\text{run}-\text{away}} \sim 0.33 . \tag{3.20}$$

At this time, the biggest body present is $R \approx 3$ km. We consider this the time before a "successful run-away": if u is maintained at the value of 10^{-4}, by $(t\nu)_{\text{run}-\text{away}}$, geometric accretion have produced large enough seeds (3 km) that can grow to infinity within a similar amount of time. This explains why the simulations have already produced bodies almost as large as Pluto in a few Myrs.

During this runaway stage, it is possible to deduce the shape of the size spectrum. Consider an initial size spectrum, dn_0/dR_0, over a narrow range of R_0 (say, $R_0 = 2$ km to 3 km). Each body grows according to equation (3.19). Conservation of the body number yields,

$$\frac{dn}{dR} = \frac{dn_0}{dR_0}\frac{dR_0}{dR} \propto \frac{dn_0}{dR_0}\left(\frac{R_0}{R}\right)^2 . \tag{3.21}$$

The results of this simple analytical model are illustrated in Fig. 3.6. The size spectrum, $dn/dR \propto R^{-q}$, starting with an initial $q \gg 1$, transitions to $q \approx 4$ when v_{H} reaches u. By this time, the largest bodies manage to dominate the viscous stirring. And their stirring rate becomes comparable to their growth rate, or,

$$\frac{\Sigma}{\sigma}\alpha^{-1}\left(\frac{v_{\text{H}}}{u}\right)^2 \approx 1 . \tag{3.22}$$

For our simulation, this occurs at $R \sim 100$ km, with $e \sim 10^{-4}$, and $\Sigma/\sigma \sim \alpha \sim 10^{-4}$, at a time of $t \sim 12$ Myrs. Beyond this point, the assumption that u remains constant breaks down.

This transition point is affected by our treatment of 'large body gating'. If one employs a more stringent advance criterion than that in equation (3.14), for instance, the mass density Σ at a given size will be greater as the run-away (which thins out the number) is more restrained. So the transition would occur at a smaller R.

This transition point is also affected by the value of u. If initial $e = 10^{-3}$, e.g., the transition would occur at $R = 10^3$ km with again $\Sigma/\sigma = 10^{-4}$.

Lastly, this transition point is affected by the initial size spectrum, which we have taken to be that in equation (3.17). If we take a less steep fall-off, the minimum in the mass spectrum (where $q = 4$) occurs at a smaller size.

3.3.3 Slow Run-away

The rapid run-away stage, discussed above, ends when the large bodies become powerful stirrers. It is then followed by a slower growth during which the rate of stirring by large bodies remain comparable to their growth rate. The evolution beyond this point is a slow run-away as the rising u slows down the growth. Assuming a power-law size spectrum $dn/dR \propto R^{-q}$, the size for the largest body and the small body dispersion scales with time as

$$R_{\mathrm{max}} \propto (t\nu)^{1/(5-q)}, \quad u(t) \propto (t\nu)^{\frac{6-q}{2(5-q)}} \propto R_{\mathrm{max}}^{(6-q)/2},$$

(3.23)

respectively. But, what is the value of q?

From our simulations, we find q fluctuates with time but centers around $q \approx 4$. This is similar to results of Kenyon & Luu (1998); Schlichting & Sari (2011). An explanation for $q \approx 4$ is given in SS11 (see §3.4.2). However, here, we present a different interpretation.

Let us define a class of trans-Hill bodies $(R_{\mathrm{trans}}(t))$ that satisfy $v_{\mathrm{H}} \approx u(t)$. These bodies are ~ 100 km at the end of the rapid run-away. We argue below that at later timers, the trans-Hill bodies remain effectively the largest bodies in the system, or, $R_{\mathrm{max}} \approx R_{\mathrm{trans}}$, and equivalently, $u \sim v_{\mathrm{H}}(R_{\mathrm{max}})$. According to equation (3.23), this gives rise to $q = 4$.

Let us consider growth of bodies above and below $R_{\mathrm{trans}}(t)$. Growth of bodies with $R < R_{\mathrm{trans}}$ is a run-away processs. Rescale their growth by that of R_{trans} (eq. 3.13), we

obtain

$$\frac{1}{R}\frac{dR}{d(t\nu)} \approx \frac{s}{R_{\text{trans}}}\alpha^{-1}\left(\frac{R}{R_{\text{trans}}}\right), \tag{3.24}$$

which, with a suitable transformation of the time-coordinate, is identical to equation (3.18). The growth of smaller bodies will be negligible compared to that of R_{trans} and their size spectrum remains largely frozen.

Growth of bodies with $R > R_{\text{trans}}$ is orderly. Their size spectrum remains invariant with time. Since $R_{\text{trans}} = R_{\text{max}}$, or the trans-Hill bodies are practically the largest bodies at the end of rapid run-away (i.e., not much mass above it), they would also remain the largest bodies at later times.

As a result of these two considerations, $u \approx v_{\text{Hill}}(R_{\text{max}}) \propto t$ during the slow run-away, and the size spectrum extends to larger and larger sizes with $\Sigma \sim$ const, or $q \approx 4$.

Adopting $u \sim v_{\text{H}}$ and using equation (3.13), one finds that it takes a time $\sim (s^{-1}\alpha\,10^8\text{ cm})t\nu \sim 0.1t\nu$ to reach $R = 1000$ km, consistent with the results shown in Fig. 3.4. The mass distribution shown in Fig. 3.4 shows an upturn near $R \sim 1000$ km, or the large bodies grow above the $q = 4$ spectrum. This is the result of our 'large body gating', that we insist on the presence of an integer body in the largest bin. The requirement that Σ have at least one body slows down the run-away and allows a higher mass density to accumulate in these largest bins. This also explains the upward thrust of u/v_{H} in Fig. 3.5 at the very end.

3.3.4 End of Growth

The efficiency of formation, defined here as the mass fraction above 100 km, rises from $\sim 10^{-4}$ to $\sim 10^{-3}$ during the slow run-away. The largest bodies formed has a size of ~ 1000 km, roughly Pluto-sized. We argue below that the growth effectively stops when these values are reached. In other words, collisionless conglomeration produces large bodies but at a very low efficiency.

During the slow run-away, equation (3.22) is continuously satisfied, yielding $\Sigma/\sigma \sim \alpha$.

So the largest size bodies that can form, insisting on at least a single body, is at ~ 1000km (see the single-body line in Fig. 3.7). With $R_{\mathrm{max}} \approx 1000$ km, our definition of formation efficiency is then

$$\epsilon = \int_{100\mathrm{km}}^{R_{\mathrm{max}}} \Sigma\, d\log R \approx \mathrm{a\ few}\ \ \alpha^{-1} \sim 10^{-3}\,. \tag{3.25}$$

Once the single large body reaches 1000km, its growth is stunted by the lack of materials, $R \sim$ const and $\Sigma \sim$ const. Meanwhile, it continuously stirs small bodies to super-Hill velocites, this produces the $u \sim t^{1/4}$ scaling that we observe in the simulations (figure 3.5). This process only stops when $u \sim v_{\mathrm{esc}}$ beyond which the growth of the big bodies proceeds as geometrical accretion. Pluto has a geometrical optical depth of $(1000\ \mathrm{km}/40\ \mathrm{AU})^2 \sim 10^{-14}$. With a Pluto providing $\Sigma/\sigma \sim 10^{-4}$, it will take $\sim 10^{10}$ orbits ($\sim 10^{12}$ years) to double its mass. Thus growth is effectively over at that point. If the efficiency of formation is small at the end of the slow run-away, it will always remain low over the life-time of the Solar System.

Two important remarks are in order here. As the stirring of km seeds continue, they approach their mutual destruction speed at $e \sim 10^{-3}$ (eq. 3.11). Their mutual collisions beyond this point should be destructive and will produce many small debris. At that time collisional cooling may become important.

Second, we have assumed isotropic velocity dispersion for all bodies. This should break down, to a varying degree, for large bodies which stir each other in the sub-Hill range. As a result, accretion among large bodies should proceed at a greater rate than adopted here. While formation gives rise to $q = 4$ along the sizes, bodies that are formed earlier may be significantly depleted by later larger bodies, and the actual q value can be reduced.

3.4 Discussions

3.4.1 Varying Initial Conditions

Our above understanding of the conglomeration process allows us to explain the following dependences when initial conditions in the simulation are altered. In all cases, we find a similar size spectrum as that obtained above.

- **Initial eccentricity** Compare the growth of bodies with initial eccentricities ranging from 10^{-7} to 10^{-3}, with all other properties held constant. The escape velocity of km bodies is at $e \sim 10^{-4}$. We find that simulations with initial velocity dispersion smaller than this quickly converge to our standard case; while those with velocity dispersion above this value first undergo orderly growth and produce a more significant mass intermediate class bodies. In all case, the final efficiency of making 100+ km bodies is $\epsilon \approx 10^{-3}$.

- **Initial surface density** We vary the initial surface density of solids from 10^{-3} times to 10 times the MMSN values (our standard case being 1 MMSN), with an initial eccentricity of $e = 10^{-7}$. We observe that the growth time scales inversely linearly with the surface density (Fig. 3.9). This is because the natural timescale in the problem is the small body collision time (eq. 3.15). This result has also been reported reported by Kenyon & Luu (1998). We also find that higher mass disks can harbor larger $R_{\max}$ – the final size of the largest body scales roughly as $\sigma^{1/3}$, a result of us insisting that the largest bin has at least one whole body. Lastly, the efficiency of formation only depends logarithmically on the initial σ.

- **Initial planetesimal sizes** We perform a suite of simulations with different planetesimal sizes ranging from 10 m to 10 km. Since the mean collision time (eq. (3.15)) scales inversely with the starting size s, and the entire evolution takes place within a few collision time, we expect that a smaller starting size leads to quicker

growth, and vice versa. This is observed in Fig. 3.10 where the growth time scales roughly as $\nu^{-1} \sim 10^7 (s/1 \text{ km})$ yrs.[3] The size of the largest bodies that form and the size spectrum are comparable in all simulations. More importantly, the efficiency of formation (ϵ) remains similarly low in all cases.

- **Value of α** Changes in surface density, starting size primarily affect the simulation through their effect on the mean collision frequency (eq. 3.15). This quantity is also affected by the value of α. We explore a range of α from 10^{-2} to 10^{-5}, this corresponds to a heliocentric distance between 4 to 400 AU. At constant surface density σ_0, the typical growth timescale scales as $\alpha^{-1.5}$, as expected (a realistic solar nebula would employ $\sigma_0 \propto a^{-1} \sim \sigma_0 \propto a^{-1.5}$ (Weidenschilling, 1977b; Hayashi, 1981; Desch, 2007)). Moreover, we find that the efficiency of formation scales as α^{-1} (Fig. 3.11), confirming equation (3.25). This dependency is slightly stronger than that found in SS11 ($\epsilon \propto \alpha^{-3/4}$) but the numerical range of concern here is limited.

3.4.2   Comparison with Previous Works

3.4.3   Schlichting & Sari (2011)

While earlier works (Greenberg et al., 1978; Wetherill & Stewart, 1989; Kenyon & Luu, 1998; Kenyon & Bromley, 2008; Ormel et al., 2010) have presented exhaustive studies of the conglomeration process, SS11 is the first work to present simple analytical arguments for the numerical results. As such, their work form the most appropriate basis for comparison.

SS11 aims to explain the $q = 4$ spectrum, obtained by all works, as a result of equal accretion: the largest bodies grow by accreting each other and small seeds at equal rates.

---

[3]This is steeper than the relation of $s^{1/3}$ found by Kenyon & Luu (1998). This is because their initial conditions use super-escape velocity dispersions. See figure 3.8.

They also argued, based on the above logic, that the efficiency of large body formation is $\epsilon \sim \alpha^{-3/4}$. These claims appear to be backed up by their simple but elegant numerical experiments.

We disagree with both of their interpretations. We show that the $q = 4$ spectrum arises is due to the fact that the largest bodies at any given time are trans-Hill relative to the small seeds. Accretion among large bodies are not important in the growth. We also argue that the efficiency of growth is $\sim \alpha^{-1}$ (see Fig. 3.11). Although given that the difference between ours and their scaling only depends weakly on α, and that there are uncertain order-of-unity constants[4], it is difficult to differentiate the two claims numerically.

The first difference is more significant. We have given a logical argument to our trans-Hill criterion in §3.3.3. And we study the relative accretion rates in figure 3.12, showing that big body accretion is never significant. Unfortunately, a similar study was not presented in SS11 and their argument for the causal connection between equal accretion and the power spectrum seems somewhat stretched.

Our simulations have the caveat that we insist on isotropic velocity dispersion and therefore may have underestimated the accretion between big bodies that are sub-Hill to each other. We argued earlier that this is a significant mistake only for bodies much smaller than R_{max} and in general it does not cause much changes in the size spectrum. However, even with this caveat, which yields unequal accretion rates, our simulations produces $q \approx 4$. This argues that the equal accretion is not an essential piece in the theory, rather, it is the result of $u \approx v_{\mathrm{H}}(R_{\mathrm{max}})$, our trans-Hill criterion.

Lastly, our trans-Hill criterion necessarily yields that the ratio of big body accretion to small body accretion remains a constant during the growth, a fact we observe in Fig. 3.12.

---

[4]In particular, σ occurs at a single size, while Σ occurs across a range of sizes. Since Σ can reasonably be defined per factor 2, e, 10 in either size or mass, there is a lot of freedom to choose the absolute normalisation.

Our numerical results differ from that in SS11 in a number of ways. So for a better comparison, we repeat their simulations by adopting their parameters and their equations. Different from our standard case in Fig. 3.4, the disk is now more massive and closer-in. It is comprised of $40M_{\oplus}$ in 1km objects orbiting at $35-45$AU. The initial velocity dispersion is set at $e = 3 \times 10^{-6}$. The rates are GLS rates (see equations 3.5-3.6, 3.13) which are order of magnitude estimates. SS11 used the so-called two-group approximation where big bodies feel dynamical friction from smaller bodies, and bodies are viscously stirred only by bodies greater than themselves. The results of our simulations are compared with that of SS11 in Fig. 3.13. The agreement is good. We obtain the same normalization and the same size spectrum.

The timescale for growth in our simulation is drastically faster than that in SS11, by almost a factor of 100. The mean collision frequency in this system is now $\nu \sim 1/2 \times 10^6 \, \mathrm{yr}^{-1}$. But the simplified rates formula causes relatively less stirring per growth timescale; this may explain why our growth time is $1/(4\nu)$, as opposed to a few $1/\nu$. Moreover, we find that if one includes viscous stirring on a particle by bodies of all sizes (instead of only by bodies greater than the particle), as one should in the case of sub-Hill stirring and $q = 4$ spectrum, the results will be changed. In particular, the intermediate bodies are now substantially hotter and they are less likely to be accreted by the largest bodies. This causes the size spectrum to be slightly more bottom-heavy than the $q = 4$ case. But we suppress these disagreements and focus on the issue of equal accretion. This is shown in Fig. 3.14. Even in simulations that are tuned to close match that of SS11, and that reproduce largely the results of SS11, we still find accretion of small bodies dominate the growth. We do observe that accretion of big bodies stay at a constant fraction of the total growth ($\sim 10\%$), as is necessary when $v \sim v_{\mathrm{Hill}}$.

3.4.4   Kenyon & Luu (1998)

We conduct a second comparison, to the simulations of Kenyon & Luu (1998). We choose this paper for comparison over subsequent ones from the same group because simulations in this paper experiences negligible influence from the gas dynamics and has initial conditions that are the closest to our set-up. They begin with bodies of a single size (we will compare here to their 800 m case), with a total mass of $10M_\oplus$ in an annulus from 32 to 38 AU and an eccentricity of $e = 10^{-3}$. This corresponds to velocities that are the escape velocity of 10 km-sized bodies. So the early accretion (before 10km) proceeds slowly without the benefit of gravitational focussing. Results for $R_{\max}(t)$ are plotted in figure 3.15. The growth time in our simulations agree within $\sim 30\%$ from those in Kenyon & Luu (1998).

One significant difference appears when we compare the size distributions. Kenyon & Luu (1998) report a quantity r_5 (defined by the cumulative number $n(> r_5) = 10^5$) of 51 km, while we find $r_5 = 31$ km. Similarly, our formation efficiency ϵ is a factor of a few lower. We believe their higher efficiency is related to the pseudo-multizone treatment in their simulations where big bodies are intentionally seperated from each other to suppress the rate their mutual accretion. Ormel et al. (2010) achieve the same result by employing a multi-zone treatment of semimajor axis. We experiment by imposing a minimum eccentricity floor of $e = 10^{-4}$ (standard value 10^{-7}). This keeps the big bodies artificially hot and results in a larger surface density in the big bodies. We now have $r_5 = 53$ km. The growth of the largest body proceeds at the same rate, as growth is dominated by accretion of small bodies. The formation efficiency remains low, in line the experiments of Kenyon & Luu (1998) and Ormel et al. (2010).

3.5 Conclusions

In this chapter, we focus on the efficiency of forming large bodies by conglomeration. Starting from a sea of equal-sized plantesimals, we find, concuring with previous studies, that the formation efficiency is $\sim$ a few $\times \alpha^{-1}$, or $\sim 10^{-3}$ at the distance of Kuiper belt.

We achieve this result numerically by constructing a conglomeration code that incorporates physical processes such as viscous stirring, dynamical friction and accretion. This code also has the capability of dealing with catastrophic disruption but we do not employ that ability in this chapter. Collisional cooling is not significant for planetesimal seeds of $\sim$ 1km in size. And here we insist that these seeds can not be broken down to smaller particles.

We also achieve an analytical understanding of the formation efficiency. We find that in collisionless environments, growth passes through several stages but is essentially finished within a few collision times of the starting planetesimals. During these, large bodies grow primarily by accreting the small bodies (and not by accreting each other). Growth is a run-away process when small bodies are super-Hill and an orderly process when small bodies are sub-Hill. Consequently, the biggest body at any given time sits at trans-Hill, or $u \sim v_{\mathrm{H}}(R_{\mathrm{max}})$. This trans-Hill criterion then yields the size spectrum $q = 4$ and a formation efficiency of $\epsilon \sim \alpha^{-1}$.

To be confident of our numerical procedure, we have tested individual components in the code against the order-of-magnitude formula in GLS. We have also performed detailed comparisons with previous simulations. These include SS11, Kenyon & Luu (1998) and Ormel et al. (2010). All previous works yield the same low formation efficiency, and a similar size spectrum ($q \approx 4$) as we do here. But some detailed differences exist. We are able to reproduce the exact size distribution (both in normalization and in slope) of SS11 when we follow them in adopting the order-of-magnitude rate formula from GLS and in ignoring viscous stirring contributed by small bodies. However, we demonstrate that the key assumption they base their analytical understanding on, that big bodies grow equally

by accreting small bodies and by accreting other big bodies, does not hold. Comparison against Kenyon & Luu (1998) show that we reproduce their growth timescale but under-predicts the number of intermediate size bodies. This is likely related to their treatment of separating big bodies to prevent mutual accretion. We have also found that our main results stand even when initial conditions are varied over large numerical ranges.

We further argue that it is impossible to raise the formation efficiency to order unity ($\Sigma \sim \sigma$) during the oligarchic accretion phase, when individual big bodies are well separated and dominate the stirring in their respective feeding zones.

Surface densities in large bodies in the Kuiper belt have been measured to be $\sim 10^{-3}$ of that of the MMSN. This has traditionally been viewed as a success of the collisionless coagulation theory. However, recent discoveries of bright extra-solar debris disks call this into question. Their dust luminosities reveal that they likely harbor large bodies that are a factor of 100 or more in mass than that in our Kuiper belt (chapter 2), comparable to the total mass in a MMSN disk in these outer regions. This conflicts with the low formation efficiency, generic to collisionless conglomeration scenarios.

In our simulations, km-size seeds reach such high velocity dispersion towards the end, that their mutual encounter should cause fragmentation. This is also observed in Kenyon & Luu (1999a); Kenyon & Bromley (2008); Ormel et al. (2010). Even if planetesimal seeds start as large as 1 km, collisional evolution appears unavoidable. An evolutionary path that is qualitatively different from that described here may ensue. Previous simulations have used very approximate treatments to describe small grains that may have missed important dynamics.

To resolve the issue of long formation timescale for Uranus and Neptune, Goldreich et al. (2004a) have proposed that conglomeration can proceed in a collisional environment, where small bodies are cooled by their frequent collisions. In chapters 4 and 5, we follow this path and demonstrate that collisional conglomeration would also be able to raise the efficiency of formation to of order unity, thereby uniting within one paradigm the

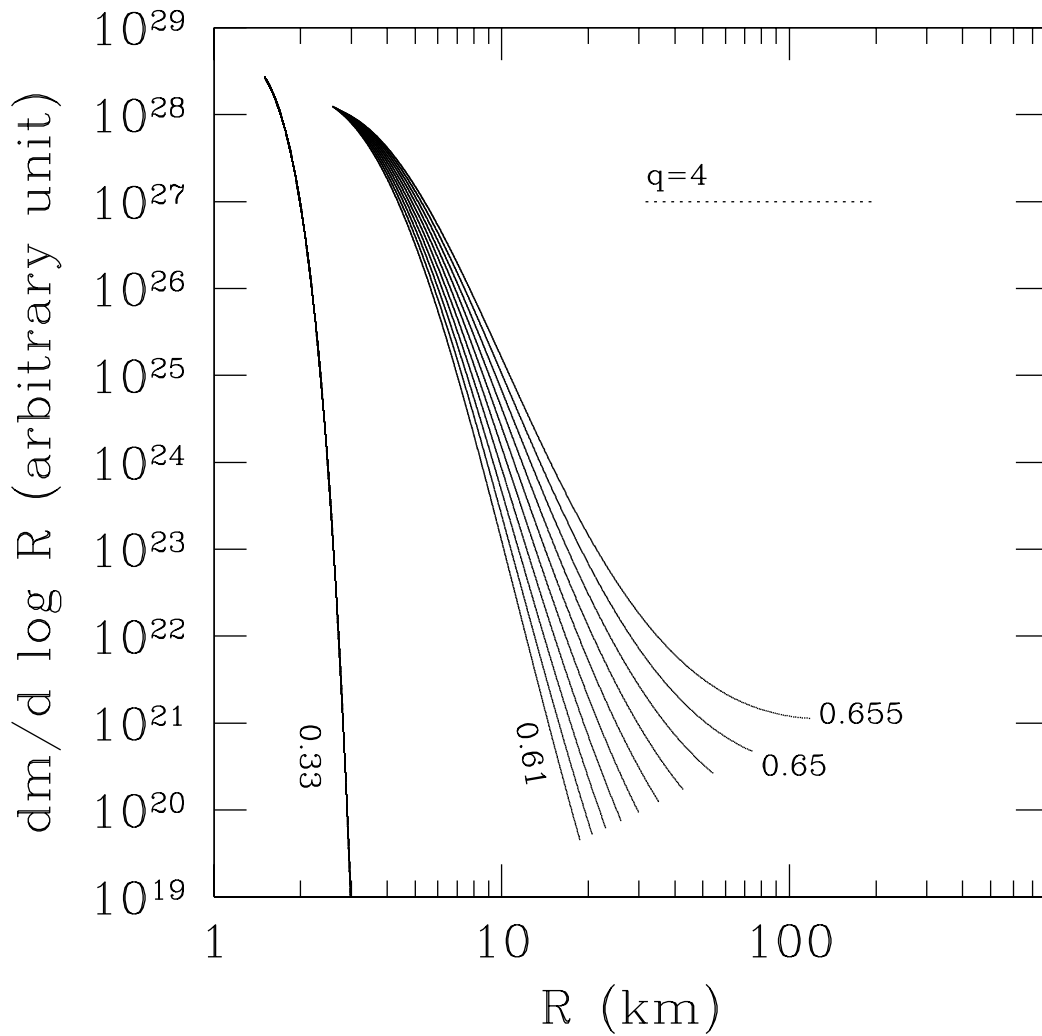formation of the Kuiper belt and the extra-solar debris disks.

Figure 3.6: Simple analytical model for the evolution of the mass spectrum during the phase of rapid runaway. The numbers next to the lines mark the time in unit of $t\nu$. Particles with initial sizes between 2 and 3 km, and an initial mass spectrum (at $t\nu = 0.33$) as described by equation (3.17), accrete from a sea of 1 km bodies with $e = 10^{-4}$, comparable to the Hill velocity for 100 km bodies. Assuming u remains unchanged during this epoch, the mass spectrum evolves quickly towards $q = 2$ at $R \geq 100$km. However, the assumption of a constant u breaks down when the rate of large body stirring becomes comparable to their growth rate. These results pertain to a steep initial size spectrum like that in equation (3.17). Comparing with the numerical results in Fig. 3.4, we find that the procedure of 'large body gating' in our numerical algorithm prevents the largest bodies from growing as fast as in this analytical model.
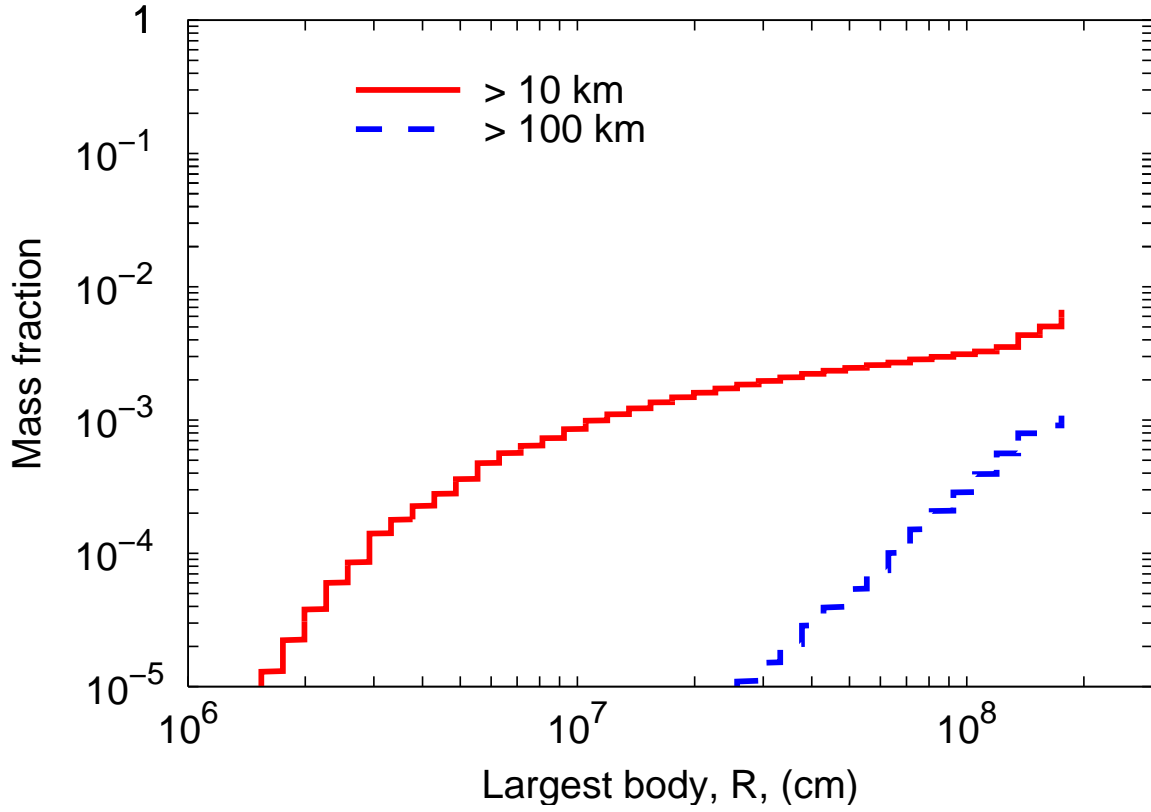
Figure 3.7: Fractions of initial mass that are incorporated into large bodies, as functions of largest body sizes. In the text we adopt the mass fraction above 100 km to be the efficiency of formation, and it reaches $\sim 10^{-3}$ towards the end of the simulation.
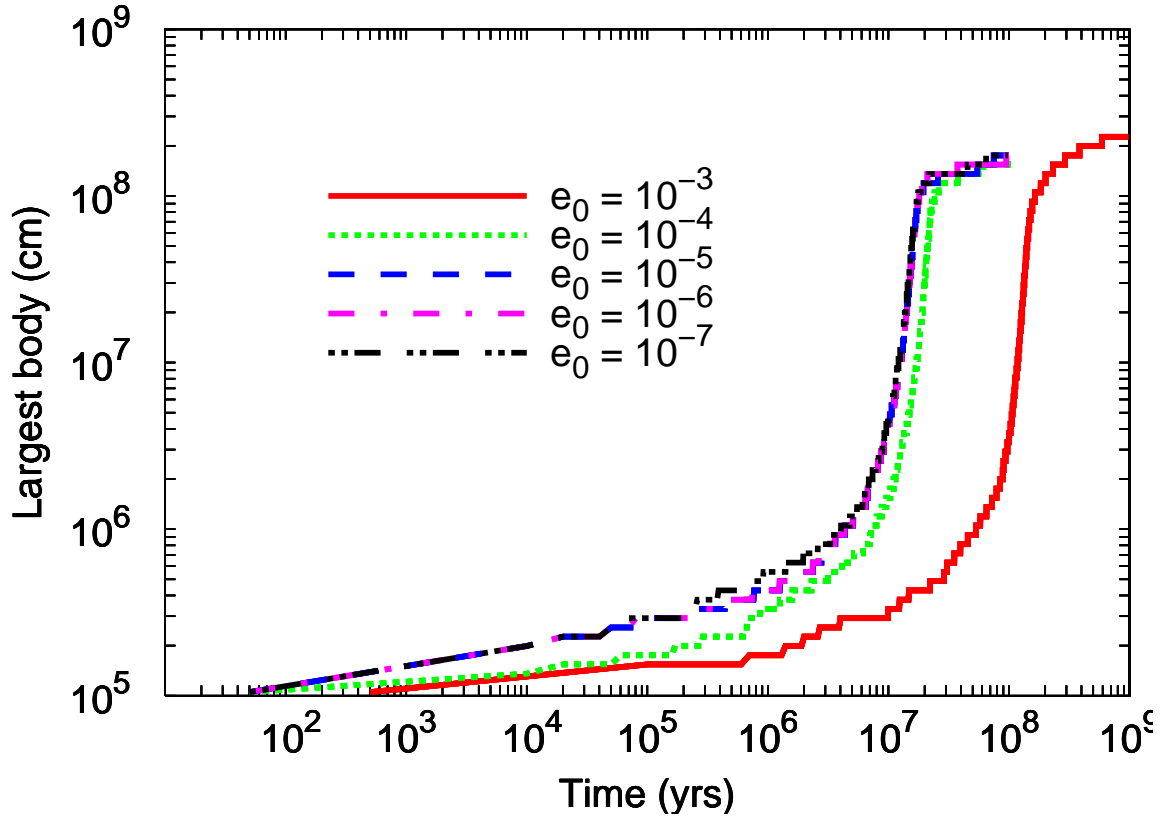
Figure 3.8: The size of the largest body in growth from kilometer sized bodies, comparing cases with initial eccentricity $e_0 = 10^{-3}$, 10^{-4}, 10^{-5}, 10^{-6}, and 10^{-7}. The escape velocity of 1 km bodies corresponds to $e \sim 10^{-4}$. We see that if the bodies begin subescape, the evolution quickly converges. The size mass distributions also converge in that case. Bodies that start superescape grow initially in an orderly regime, until there are bodies that are subhill to the starting eccentricity, then growth proceeds from that size (e.g., the $e_0 = 10^{-3}$ run here is similar to run starting cold with ~ 10 km objects, as 10^{-3} corresponds to $v_{\rm esc}$ for 10 km objects.
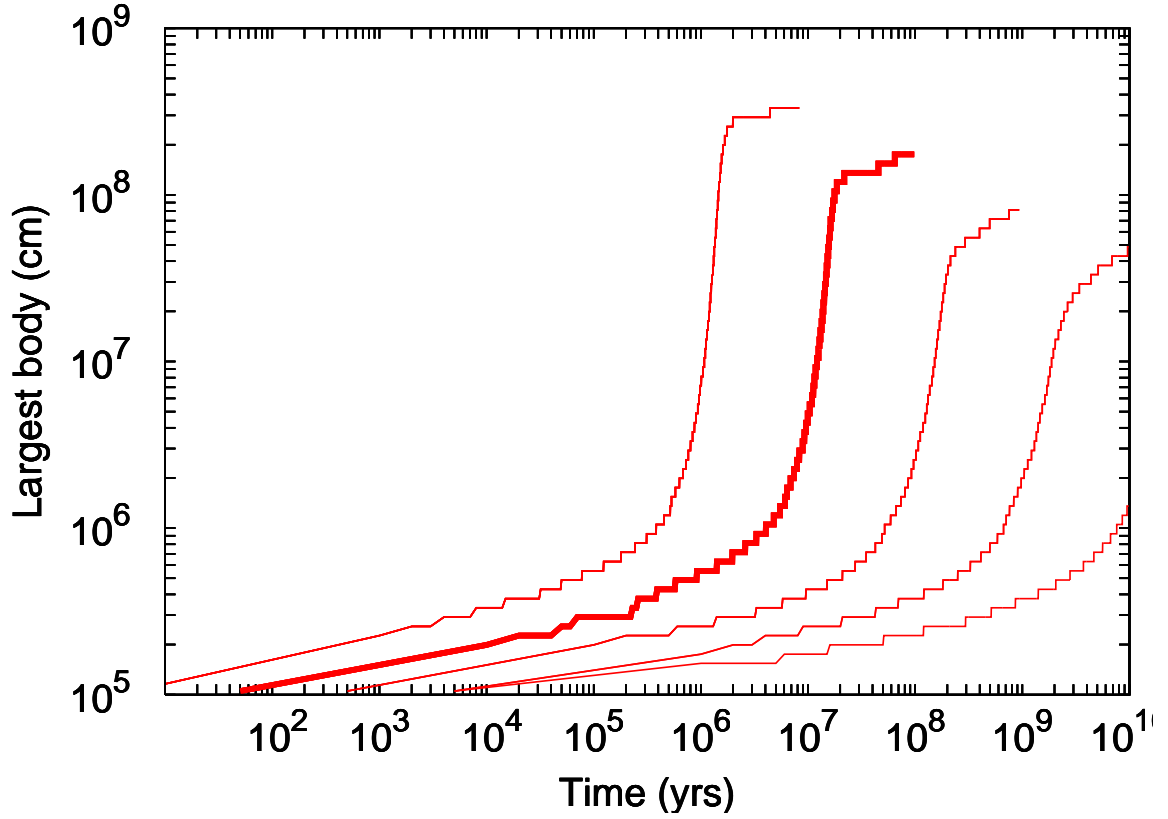
Figure 3.9: Growth of the largest body as functions of time, for disks with different surface densities. The total mass spans from 10^{-3} MMSN (bottom-most curve) to 10^{-2}, 10^{-1}, 1 and 10 MMSN (top-most curve), with the thick red curve being our fiducial case. We find the timescale of runaway growth obeys $t \propto \sigma^{-1}$. All growth follow the pattern of a rapid run-away, followed by a slow run-away, and ending when a single body exceeds the expected Σ.
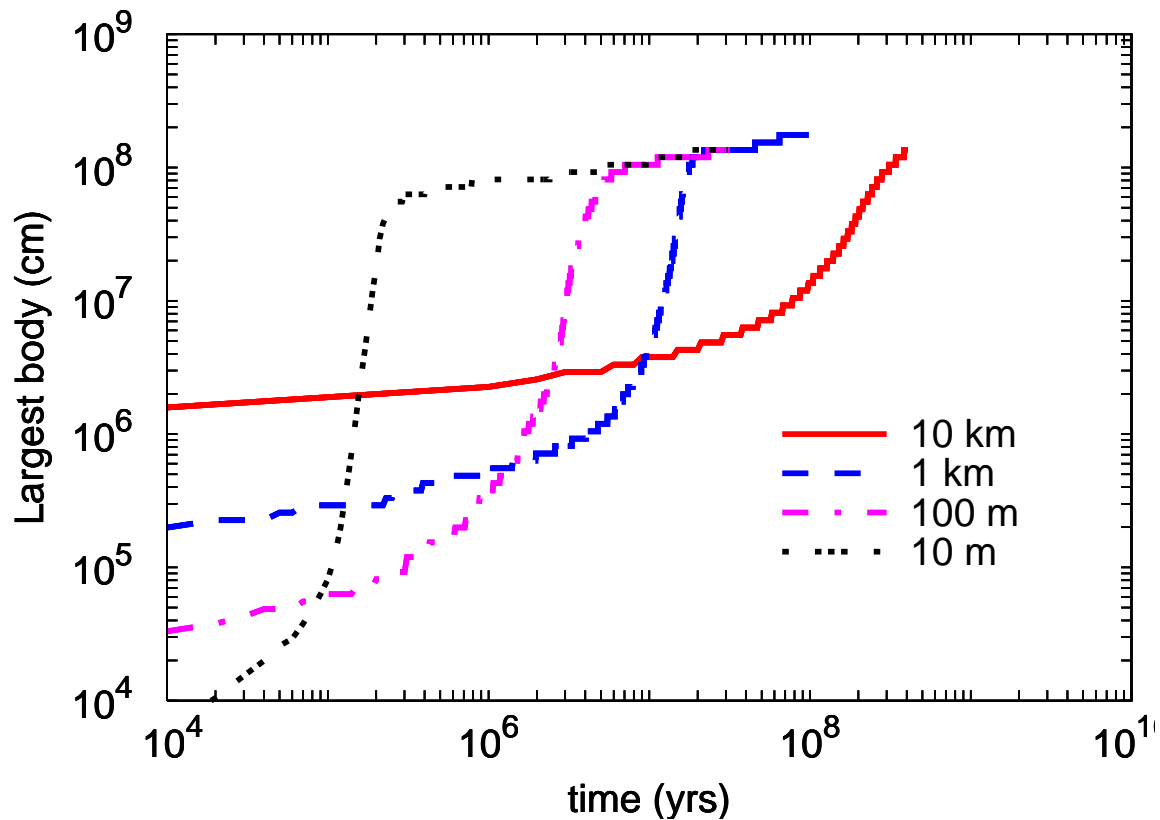
Figure 3.10: Growth of the largest body in simulations with different starting sizes, $s = 10$ m, 100 m, 1 km, and 10 km. Bodies grow slowly at first, while the velocity dispersion is set by the escape velocity of the starting size. Eventually a few bodies run away, when they are sufficiently large. The timescale of runaway increases linearly with starting size, as the collision time varies inversely with the starting size (equation 3.15).
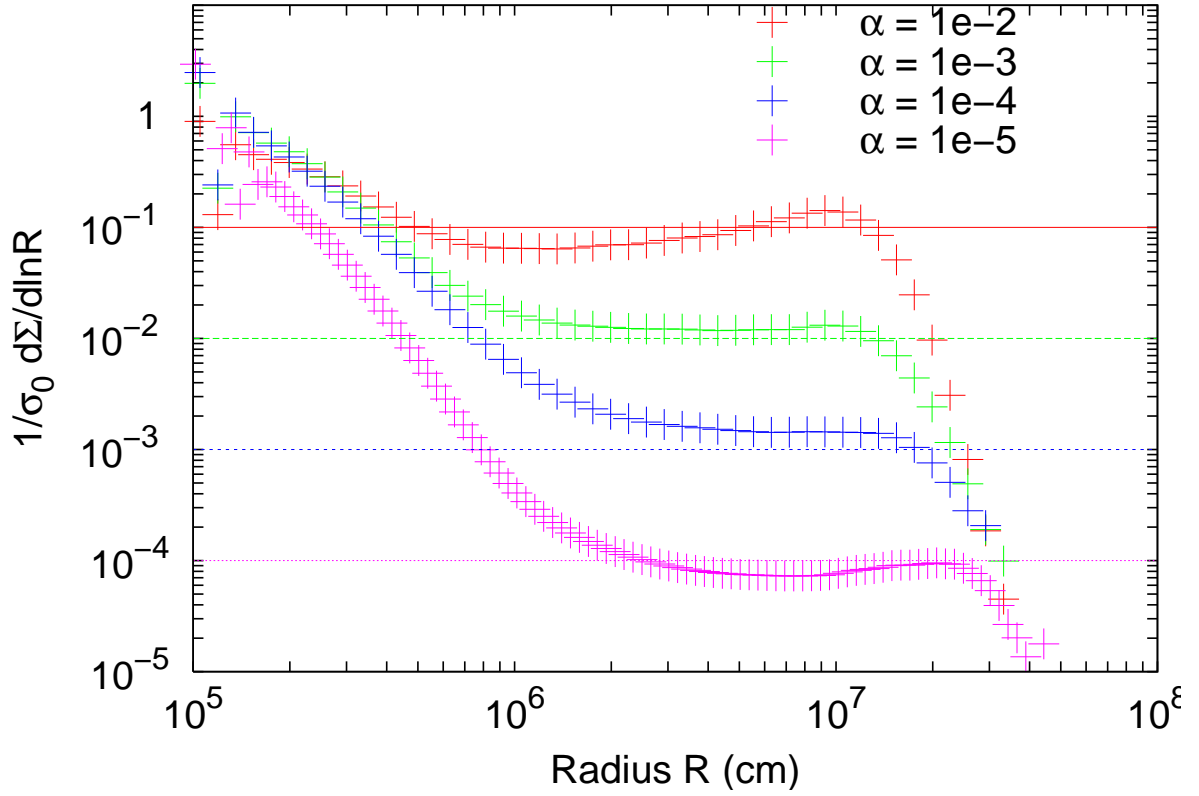
Figure 3.11: Differential mass spectrum for different values of α, where $\alpha = 10^{-4}(40\text{AU}/a)$. We find that at constant surface density σ_0, the formation timescale varies with α roughly as $\alpha^{-1.5}$, as the mean collision time is longer at larger distances. Moreover, as shown here, we find that the efficiency of formation scales roughly as α^{-1}, as predicted by equation (3.25). This is steeper than the prediction of $\alpha^{-3/4}$ in SS11.
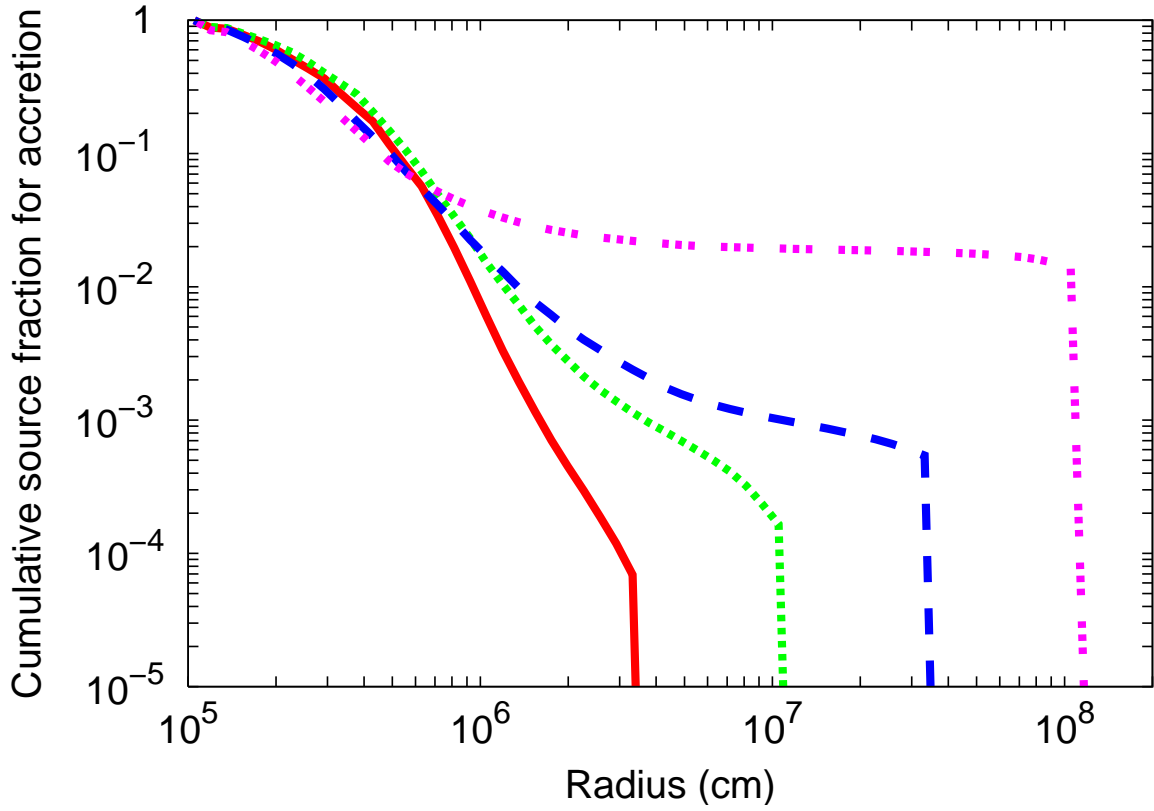
Figure 3.12: Relative contribution in accretional growth from different size bodies, plotted here as cumulative source to growth vs body sizes, for when $R_{\mathrm{max}} = 30,\ 100,\ 300$ and 1000 km. These are obtained for the model as shown in Fig. 3.4. We insist on isotropic velocity dispersion in these simulations, which may underestimate the accretion between large bodies that are sub-Hill to each other.
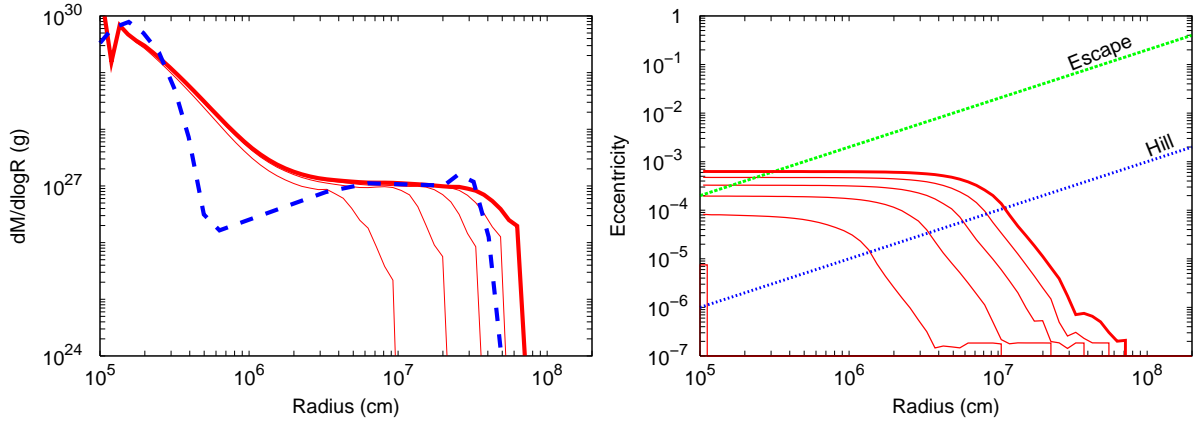
Figure 3.13: The red solid curves show the differential mass distribution from our simulations (plotted every 10^5 yrs, ending at 5×10^5 yrs) that are tuned to match that of SS11 (blue dashed curve). The resulting mass distributions of large bodies agree both in normalization and in shape with that in SS11. The timescales of growth, however, differ substantially. The SS11 results are recorded at the end of 50 Myrs.
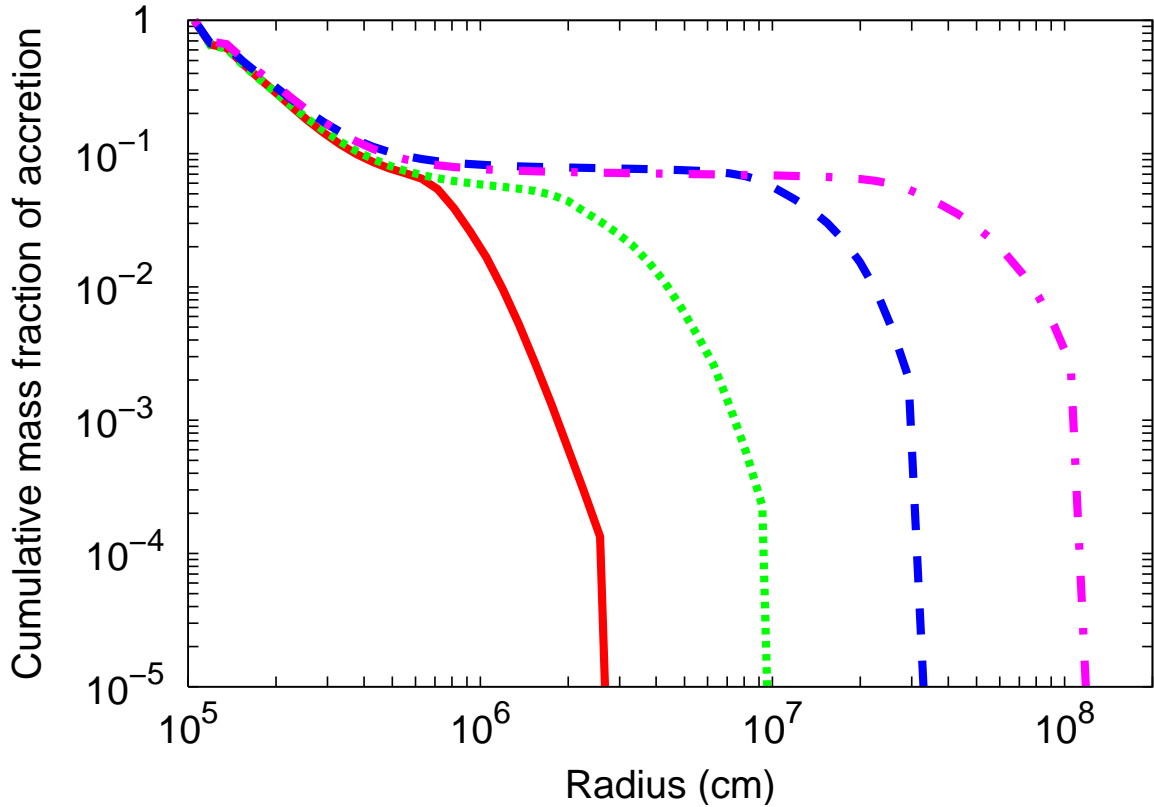
Figure 3.14: Same as Fig. 3.12, but for the simplified simulations that are tuned to match that of SS11 (see text). Instead of equal accretion of big and small bodies expected by Schlichting & Sari (2011), we observe that accretion from small seeds dominates at all times, with accretion from large bodies staying at a constant fraction of the total growth, $\sim 10\%$. The upturn in mass density observed in Fig. 3.4 at the large size end is due to the requirement of a single-body in a given bin. This effect would occur in this simulation as well. But it occurs at a size $> 10^3$ km due to the higher mass normalization and formation efficiency here.
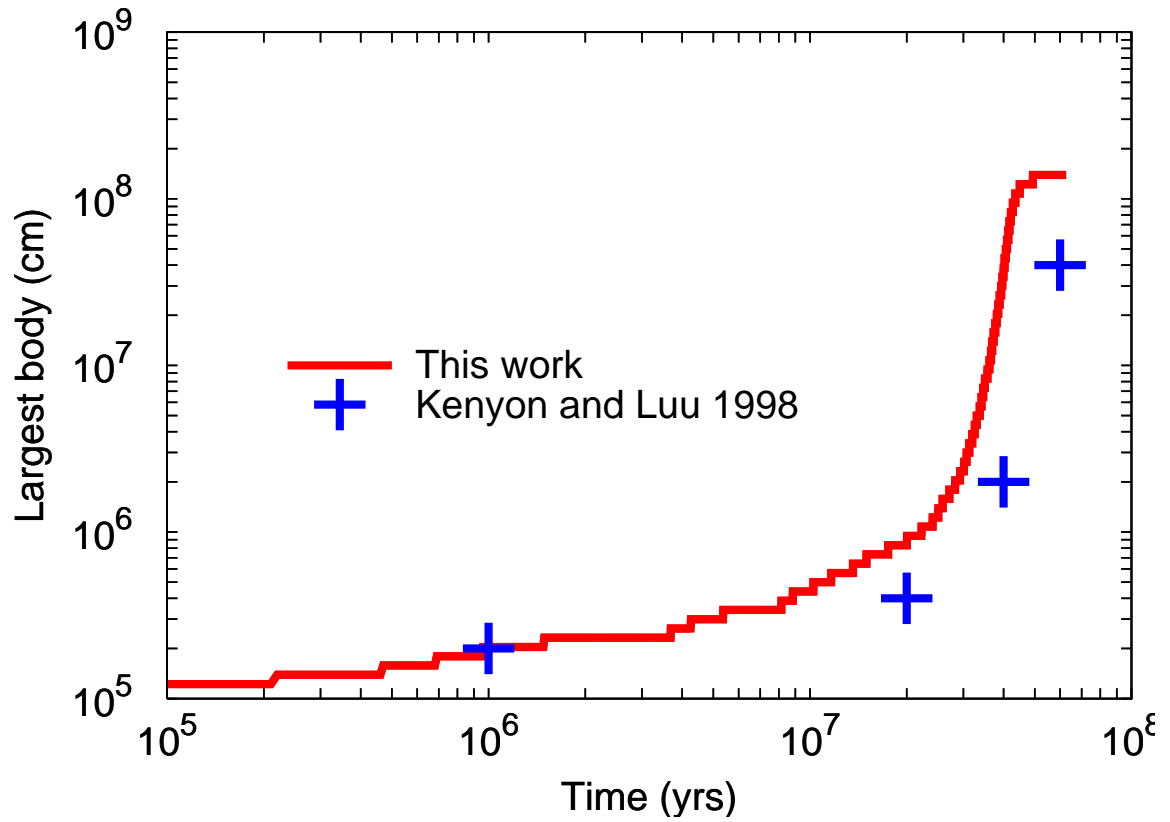
Figure 3.15: The size of the largest body as a function of time, for our simulation (red curve) and that of Kenyon & Luu (1998) (blue crosses). The growth rates agree qualitatively, although ours is faster by $\sim 30\%$.

Chapter 4

Collisionally Damped Conglomeration in the Cold Classical Kuiper Belt

This chapter is a modified version of a draft publication. The research was done in conjunction with Dr. Yanqin Wu, and Dr. Yoram Lithwick, and the preparation of the chapter was done in conjunction with Dr. Yoram Lithwick. It is reproduced here with their permission.

4.1 Background

Edgeworth (1949) and Kuiper (1951) noted that if the protosolar nebula extended beyond Neptune, we should expect to find a comet belt beyond 30 AU. Although that belt had been discovered twenty years previous (Slipher & Tombaugh, 1930), it was not recognised as such until the 1990s, with the discovery of additional members (starting with Jewitt & Luu, 1993). The Kuiper Belt has multiple populations with different formation and dynamical histories. In this section we focus on the Cold Classical Kuiper Belt. While

evidence is suggestive that the other populations formed closer to the Sun (Malhotra, 1993, 1995; Levison et al., 2008), the properties of the Cold Classical Kuiper Belt suggest that it formed in situ.

There is an overabundance of objects with inclinations less than $\sim 5°$ which only exists between ~ 42 and ~ 46 AU (Brown, 2001; Kavelaars et al., 2008; Petit et al., 2011). Other studies that look for correlations among Kuiper Belt objects generally do not distinguish between the dynamical classes, and look for correlations with inclination[1]

Several properties of the Cold Classical Belt are relevant to our analysis. The largest bodies are ~ 200 km (Levison & Stern, 2001; Fraser et al., 2010). At sizes of ~ 200 km down to ~ 50 km, the size number distribution can be fit by a power law $dn/ds \propto s^{-q}$ with index $q = 5.1 \pm 1.2$ (Fraser et al., 2010), $q = 7^{+1}_{-1.5}$ (Petit et al., 2011). The power law breaks at ~ 50 km to a shallower value with $q \lesssim 4$ (Bernstein et al., 2004; Schlichting et al., 2009). This means that most of the $\sim 10^{-2} M_\oplus \sim 10^{-1} M_\oplus$ (Fuentes & Holman, 2008; Fraser & Kavelaars, 2009; Vitense et al., 2010) is in bodies with ~ 50 km radii[2].

Historical models of the growth of the Kuiper Belt planetesimals begin with $\sim$km sized objects, following the planetesimal formation model of Safronov (1969); Goldreich & Ward (1973). These models find that stirring by large bodies is faster than the growth of large bodies, and that in the resulting super-Hill, sub-escape accretion regime, large bodies grow faster than small ones, leaving the small ones behind. The result is a small number of bodies growing, accreting at relatively slow rates, and the efficiency of forming large bodies is $\sim 10^{-3}$, with roughly equal mass per size decade (Greenberg et al., 1978; Wetherill & Stewart, 1989; Kenyon & Luu, 1998; Kenyon & Bromley, 2008; Ormel et al., 2010; Schlichting & Sari, 2011, also see chapter 3). At the distance of the Kuiper Belt, growth in these models proceeds until the largest bodies are $\sim 10^3$ kilometers - with

---

[1]The biggest stumbling block in sorting out Cold Classical Kuiper Belt Objects is that identifying resonant objects in higher order resonances requires a comparatively long baseline of observations that is not always available.

[2]The dynamically cold bodies have higher albedos than hot bodies, so the true mass should be expected to tend towards the lower end of mass estimates (Brucker et al., 2009)

the systems being in oligarchic growth at the present day (Kenyon & Luu, 1999b). At ~ 1 AU, formation of planets takes $\sim 10^8$ years (Wetherill & Stewart, 1989), and scaling by the collision time predicts this should take $\sim 10^{12}$ years at ~ 40 AU. The mass of the Kuiper Belt today is $\sim 10^{-2} \sim 10^{-3}$ times lower than is predicted from an extrapolation of the mass density interior to the Kuiper Belt (Weidenschilling, 1977b; Hayashi, 1981), and the largest objects are $\sim 10^3$ km (Young et al., 2007; Sicardy et al., 2011). In total mass, size number distribution, and largest body size, the region is in rough agreement with the models.

Recently, a number of significant challenges have appeared to the model. While the properties of the Kuiper Belt as a whole are in rough agreement with the model, most objects are believed to have formed closer to the Sun, and been pushed outward during the outward migration of Neptune (Fernandez & Ip, 1984; Levison & Morbidelli, 2003; Hahn & Malhotra, 2005). The Cold Classical Kuiper Belt could have remained in situ during this event (Batygin et al., 2011), but its properties do not match the conglomeration models. The standard formation model would require $10 M_\oplus \sim 100 M_\oplus$ to form the Kuiper Belt in situ, but migration models of Neptune require a much lower mass to prevent Neptune from migrating into the Kuiper Belt (Gomes et al., 2004). If there had been $\sim 10 M_\oplus$ in kilometer sized bodies in the Kuiper Belt, we should expect long period binaries to have been disrupted (Parker & Kavelaars, 2012), which is observed not to be the case (Parker et al., 2011). Furthermore, if the Kuiper Belt requires $\sim 10 M_\oplus$ to form, it may be impossible to form observed extrasolar debris disks (chapter 2). In this chapter, we explore a new model of formation, which begins with mostly centimeter sized grains, along with some kilometer sized seed planetesimals. Collisional cooling among the centimeter sized grains fundamentally alters the growth dynamics, and high efficiency ($\gtrsim 50\%$) can be achieved, allowing in situ formation of the Cold Classical Kuiper Belt from $\sim 10^{-1} M_\oplus$.

4.2 Collisionally-cooled growth: Theory

4.2.1 Initial Conditions

We are necessarily agnostic towards the origin of the initial conditions. It may be that after the gaseous protoplanetary nebula dissipates, solid bodies of a characteristic radius s remain behind. These bodies collide with one another on the timescale $t_{\rm col} \sim (\rho s)/(\sigma \Omega)$, where ρ is their material density, σ is the surface density of their circumsolar disk, and Ω is the orbital angular speed. On timescale $t_{\rm col}$ runaway growth is initiated, and a few bodies grow much larger than the others (Goldreich et al., 2004b). If the small grains are small enough (or break down quickly), and $\sim 10^{-3}$ of the mass in large bodies (Schlichting & Sari, 2011), this could produce an effective two groups conditions (although see appendix 7.3). Alternatively, planetesimal formation models go from small bodies directly to large ones (Safronov, 1969; Goldreich & Ward, 1973; Youdin & Shu, 2002; Johansen et al., 2007), a process that should not necessarily be expected to have $\sim 100\%$ efficiency (Johansen et al., 2009).

In the following subsections, we work out how collisional accretion proceeds, and derive the efficiency for converting small bodies into large. Since the small bodies' size s is unkown (both initially, as well as its subsequent collisional evolution), we treat it here as a free parameter. In our estimates for the various interaction rates between groups of bodies (accretion, viscous stirring, inelastic collisions, etc.), we use the formulae as summarized by Goldreich et al. (2004b), with similar notation: big bodies have radius R, velocity dispersion v, and surface density Σ; small bodies have radius s, velocity dispersion u, and surface density σ; and all bodies have material density ρ, as does the Sun. The formulae can be found in section 5.2. The big bodies' Hill velocity is

$$v_{\rm H} \sim \Omega a (R/R_\odot) \sim \sqrt{G \rho \alpha} R \qquad (4.1)$$

where a is the semimajor axis, $R_\odot$ is the sun's radius, and

$$\alpha \sim R_\odot/a . \tag{4.2}$$

Their Hill radius is

$$R_H \sim R\alpha^{-1} . \tag{4.3}$$

We assume

$$v \quad < \quad v_H \tag{4.4}$$

$$\alpha^{1/2} v_H < u \quad < \quad v_H , \tag{4.5}$$

and check for self-consistency in Section 4.2.7. Note that the escape speed from the surface of big bodies is $v_{esc} \sim \alpha^{-1/2} v_H$.

4.2.2 Early Times: Accretion of Small Bodies

At early times, big bodies grow primarily by accreting small bodies at the rate

$$\frac{1}{R}\frac{dR}{dt}\Big|_{small} \sim \frac{\sigma\Omega}{\rho R}\alpha^{-1}\frac{v_H}{u} . \tag{4.6}$$

Small bodies are viscously heated by big bodies, which increases u, and hence decreases the rate at which big bodies accrete them. We assume that viscous heating is balanced by inelastic collisions amongst small bodies. Otherwise, accretion is collisionless. Then

$$\frac{1}{u}dudt \sim \frac{\Sigma\Omega}{\rho R}\alpha^{-2}\frac{v_H}{u} - \frac{\sigma\Omega}{\rho s} = 0 , \tag{4.7}$$

and hence

$$\frac{u}{v_H} \sim \frac{\Sigma}{\sigma}\frac{s}{R}\alpha^{-2} . \tag{4.8}$$

Therefore big bodies grow by accreting small ones at the rate

$$\frac{1}{R}\frac{dR}{dt}\Big|_{small} \sim \frac{\sigma^2\Omega}{\Sigma\rho s}\alpha . \tag{4.9}$$

When s is small, growth is fast: a smaller s implies more frequent inelastic collisions and hence a smaller u, which enhances gravitational focusing onto big bodies, making them grow faster.

107

4.2.3 Numerical Estimates for the Kuiper Belt

For a numerical estimate, we are interested in the time when accretion is $\sim 100\%$ efficient, i.e. we assume $\Sigma \sim \sigma$ when the KBO's form. In that case, accretion is sub-Hill if $s < s_*$, where is

$$s_* \sim R\alpha^2 \ , \tag{4.10}$$

and the time it takes the observed KBO's to grow by accreting small bodies is

$$t_{\text{grow}} \quad \sim \quad \frac{\rho s}{\sigma \Omega \alpha} \ , \ \text{for } s < s_* \ . \tag{4.11}$$

We take the present Kuiper belt's mass to be $\sim 0.1 M_\oplus$, spread between 42 and 48AU, and hence $\sigma \approx 0.0016$ g/cm^2. Other numerical values are $\rho \sim 1$ g/cm^3, $a \sim 45$ AU, $\Omega \sim 0.02$/yr, and $\alpha \sim 10^{-4}$.

With these values, the Hill velocity is

$$v_{\text{H}} \sim 30 R_{100} \ \text{cm/s} \ , \tag{4.12}$$

where $R_{100} = R/100$ km, and the collision time is

$$t_{\text{col}} \sim \frac{\rho s}{\sigma \Omega} \sim 0.03 s_{\text{cm}} \text{Myr} \ , \tag{4.13}$$

where $s_{\text{cm}} \equiv s/$cm. The critical s for trans-Hill accretion is

$$s_* \sim 0.1 R_{100} \text{cm} \ , \tag{4.14}$$

and the growth time is

$$t_{\text{grow}} \sim 300 s_{\text{cm}} \ \text{Myr}, \quad \text{for } s < s_* \sim 0.1 R_{100} \text{cm} \tag{4.15}$$

where $s_{\text{cm}} \equiv s/$cm. Therefore big bodies in the Kuiper belt of size ~ 100 km could have formed with $\sim 100\%$ efficiency in less than 30 Myr if $s \lesssim 0.1$ cm. We discuss below plausible values of s. However, we have ignored the accretion of big bodies. We consider that in Section 4.2.5

4.2.4 Early Times:Mass in Big Bodies

It is unclear how much mass should begin in large bodies. If the total mass is small, the velocities will be sub-Hill, which is the case we consider in section 4.2.5. The total mass of large bodies is sufficient that $u > v_{\mathrm{H}}$, if

$$\Sigma > \frac{R}{s}\alpha^2\sigma \ . \tag{4.16}$$

In that case, growth is runaway until R is sufficiently large and/or Σ is sufficiently small until equation 4.16 is violated. At that point, $u < v_{\mathrm{H}}$, and the sub-Hill growth begins with

$$\Sigma = \frac{R}{s}\alpha^2\sigma \ . \tag{4.17}$$

4.2.5 Late Times: Equal Accretion of Big and Small Bodies

Big bodies grow by accreting one another at the rate

$$\frac{1}{R}\frac{dR}{dt}\Big|_{\mathrm{big}} \sim \frac{\Sigma\Omega}{\rho R}\alpha^{-3/2} \ . \tag{4.18}$$

Note that this rate is independent of v, whereas Equation (4.6) is $\propto 1/u$. The rates differ because sub-Hill big bodies lie in a flat disk, whereas small ones have an isotropic velocity dispersion due to collisions (Rafikov, 2003; Goldreich et al., 2004b).

Comparing Equations (4.9) and (4.18) when Σ is given by Equation (4.17) shows that the assumption that growth occurs only by accreting small bodies breaks down when

$$R \gtrsim s\alpha^{-3/2} \ . \tag{4.19}$$

After the largest R exceeds this value, big bodies must grow by accreting other big bodies at least as fast as they grow by accreting small bodies. In other words, defining

$$f \equiv \frac{d\ln R/dt|_{\mathrm{small}}}{d\ln R/dt|_{\mathrm{big}}} \ , \tag{4.20}$$

we have shown that if $f \gg 1$, then f will decrease towards unity (once Equation (4.19) is satisfied). We now consider what happens if $f \ll 1$, i.e. if big bodies grow only

by accreting each other. In that case, the growth rate is inversely proportional to R (Equation (4.18)), hence growth is orderly (Goldreich et al., 2004b), and Σ=constant as R grows. As that happens, the ratio of small body to big body accretion,

$$f \sim \frac{\sigma^2}{\Sigma^2} \alpha^{5/2} \frac{R}{s} \ , \tag{4.21}$$

increases with increasing R. We conclude that

$$f \to 1 \tag{4.22}$$

at late times, which we call "equal accretion." As a result, the mass in big bodies increases with R as

$$\Sigma \sim \sigma \sqrt{\frac{R}{s}} \alpha^{5/4} \ . \tag{4.23}$$

Equal accretion was first discussed by Schlichting & Sari (2011), who considered the collisionless case. Here we have shown that it applies to the collisional case.

4.2.6 Efficiency

Equation (4.23) implies that collisional accretion reaches completion (i.e. 100% efficiency or $\Sigma \sim \sigma$) when

$$R_{\text{comp}} \sim s\alpha^{-5/2} \ . \tag{4.24}$$

In the cold classical Kuiper belt, where the bulk of the mass is in bodies of size ~ 100 km, order-unity efficiency could have been achieved if $s \sim 10^{-10} R = 10^{-3} R_{100}$cm at the time the big bodies formed. The timescale to form these bodies assuming s was constant throughout the accretion process is very short, $t_{\text{grow}} \sim 0.3$ Myr (Equation (4.15). However, it seems unlikely that s was so small throughout the accretion process. We discuss plausible scenarios for s below.

4.2.7 Verifying Assumptions

We verify some assumptions during equal accretion.

- Small bodies' speed: From Equations (4.23) and (4.8),

$$\frac{u}{v_{\mathrm{H}}} \sim \sqrt{\frac{s\alpha^{-3/2}}{R}} \ . \tag{4.25}$$

Therefore, $u/v_{\mathrm{H}} \sim 1$ when equal accretion begins, and it falls to $u/v_{\mathrm{H}} \sim \sqrt{\alpha}$ at completion, consistent with inequality (4.5). Over the course of equal accretion, u itself increases (assuming s is constant), reaching $u \sim 0.3R_{100}$ cm/s at completion for Kuiper belt parameters.

- Big bodies' speed: Big bodies are stirred by viscous stirring due to other big bodies, and damped by dynamical friction with small bodies:

$$\frac{1}{v}\frac{dv}{dt} \sim \frac{\Omega}{\rho R}\alpha^{-2}\left(\Sigma v_{\mathrm{H}}v - \sigma\right) \sim 0 \ . \tag{4.26}$$

Hence,

$$\frac{v}{v_{\mathrm{H}}} \sim \frac{\Sigma}{\sigma} \ , \tag{4.27}$$

consistent with inequality (4.4).

- Isolation mass: Bodies that accrete sub-Hill small bodies cannot exceed the isolation mass, which is the mass of a body that sweeps up everything within an annulus of width R_{H} (Goldreich et al., 2004b). A body with the isolation mass has radius

$$R_{\mathrm{iso}} \sim \sqrt{\frac{\sigma a}{\rho \alpha}} \ . \tag{4.28}$$

For Kuiper belt parameters, $R_{\mathrm{iso}} \sim 1000$ km, using the current σ. Hence the bulk of mass in the Kuiper belt is safely below the isolation mass.

- Oligarchy: We have implicitly assumed that $\Delta a \lesssim R_{\mathrm{H}}$, where Δa is the radial spacing between adjacent big bodies. Otherwise, big bodies will have difficulty accreting material that is separated by more than R_{H}. Now, the radial spacing satisfies $2\pi\Sigma a\Delta a = (4\pi/3)\rho R^3$, or

$$\frac{\Delta a}{R_{\mathrm{H}}} \sim \frac{2}{3}\frac{\rho}{\Sigma a}R^2\alpha \sim 0.006\frac{\sigma}{\Sigma}R_{100}^2 \ . \tag{4.29}$$

111

Inserting Equation (4.23) yields

$$\frac{\Delta a}{R_{\mathrm{H}}} \sim \frac{2}{3}\frac{\rho}{\sigma a}R^{3/2}\alpha^{-1/4}s^{1/2} \ . \tag{4.30}$$

Inserting Kuiper belt parameters,

$$\frac{\Delta a}{R_{\mathrm{H}}} \sim 0.2 R_{100}^{3/2}s_{\mathrm{cm}}^{1/2}. \tag{4.31}$$

4.3 Collisionally-Cooled Growth: Simulation

We simulate collisional accretion in order to verify the theory presented in Section 4.2. Our code is a statistical particle in box code, and is described in depth in chapter 3. We consider only a single radial zone. Eccentricity is the only dynamical variable. Random velocities are assumed isotropic, except when the flat disk accretion formula (Equation (4.18)) is applicable. Following Krivov et al. (2005), eccentricity and mass evolution are decoupled. Eccentricities evolve under viscous stirring, dynamical friction, and collisions (with prescriptions from Ohtsuki et al., 2002; Collins & Sari, 2006). Colliding bodies undergo either conglomeration, inelastic rebound, or fragmentation, depending on the collision speed. For the simulation we show here, collision speeds remain sufficiently small that there is little fragmentation given the strength law we use, which is described in Stewart & Leinhardt (2009).

We begin with 1% of the mass in 1 km bodies, and 99% in 1 cm bodies. The total mass is $0.1M_{\oplus}$, assumed to be spread evenly between 42 and 48AU. Bodies begin with $e = 10^{-6}$. All bodies have mass density $\rho = 1.5$ g cm^{-3}. Note that Equation (4.19) predicts that equal accretion begins when $R \gtrsim 10$ km, or shortly after the beginning of the simulation.

The evolution is plotted in Figures 4.1–4.3. The top right panel of Figure 4.1 shows the evolution of the mass spectrum of all the bodies, and the top left panel shows a zoom-in of the big bodies. As time progresses, the peak in the big bodies' mass spectrum

112

moves to larger R and Σ. The relation between the values of R and Σ at the peak agrees with the equal accretion prediction (Equation (4.23)). With $s \sim 1$ cm, the big bodies should reach 10^5 km at completion (Equation (4.24)). However, this simulation does not reach completion because of the code's requirement that there be ≥ 1 largest body, which prevents growth beyond ~ 2000 km for this simulation.

The bottom panels of Figure 4.1 show the eccentricities of all bodies in the simulation. Figure 4.2 shows the eccentricity of just the small (1 cm) and big bodies over the course of the simulation, plotted versus the big body size. For the purposes of the plot, big bodies are taken to be of size R_{stir}, where we define R_{stir} to be the size of the bodies that contribute the most stirring (per logarithmic bin); it lies very close to the peak of the mass spectrum at large sizes. In accordance with Equations (4.25) and (4.27), throughout equal accretion both small and big bodies are sub-Hill with respect to the big ones. As a result, growth due to small bodies is determined by Equation (4.6), and growth due to big bodies is determined by Equation (4.18). In fact, from Figure 4.1, the big bodies that lie within a decade or so in R of R_{stir} are all sub-Hill with respect to the R_{stir} bodies, and hence all accrete at the fast flat disk rate of Equation (4.18). The valley to the left of the big body peak in the top panels of Figure 4.1 is due to the efficient accretion of these intermediate-sized bodies onto the bodies at the peak.

Figure 4.3 shows the ratio of small body ($<$cm) to big body accretion onto bodies of size R_{stir}. As R_{stir} grows over the course of the simulation, this ratio remains nearly unity (Equation (4.22)), hence confirming equal accretion.

4.4   Discussion

In Section 4.2 we presented our model for collisionally cooled growth (CCG), and in Section 4.3 we verified the model with a simulation. Here we address whether the model can explain the Kuiper belt. We first list the model's two primary shortcomings.

- Size of small bodies, s: Our main result is that collisional growth produces bodies of size $R \sim s\alpha^{-5/2}$ with order-unity efficiency (Section 4.2.6). Hence the classical KBO's could have formed out of a "minimum mass Kuiper belt disk" (i.e. σ smaller than the minimum mass solar nebula value by a factor of $10^2 \sim 10^3$) if $s \sim 10^{-3}$ cm. More generally, if one demands an efficiency $\epsilon < 1$, one requires that $s \sim 10^{-3}\epsilon^{-2}$ cm (Equation (4.24)). Although the timescale for formation of KBO's from such small bodies is reasonable (Equation (4.15)), it may not be case that small bodies were always cm-sized or smaller. Rather, bodies might have formed larger[3] and then been continually ground down to smaller sizes by disruptive collisions. For the CCG model to apply, it is only required that s was small when the current Kuiper belt bodies achieved their last doubling in size. Collision speeds at completion are ~ 0.3 cm/s for $\epsilon \sim 1$ (Section 4.2.7). While such speeds might seem too small to break down bodies, there are around $\alpha^{-1} \sim 10^4$ collisions in the last doubling time of bodies of size R_{comp} (Equations 4.13 and 4.15). Cratering disruption may be important.

- Size spectrum: The size spectrum that our model produces is highly peaked at large sizes (Figure 4.1). This is in contrast to observations of the cold classical belt which suggest that, while the bulk of the mass is in objects of size ~ 100 km, for sizes larger than that

$$d\Sigma/d\ln R \propto R^n, \text{where } n \sim -1 \tag{4.32}$$

(e.g., Fraser et al., 2010).

We argue here that despite the above shortcomings, the CCG model is likely preferable to the collisionless growth model (Kenyon & Luu, 1998; Schlichting & Sari, 2011). In collisionless growth, big bodies form with an efficiency $\sim 10^{-3}$. In that model, the initial

---

[3]For example, in the model of Goldreich & Ward (1973), bodies form with size $s \sim \alpha^{-3/2}\sigma/\rho \sim 10$ m in a minimum mass Kuiper belt; see also Appendix C of Goldreich et al. (2004b).

surface density in the Kuiper belt must have been $\gtrsim 100$ times what it is today, all in small bodies of size $s \gtrsim 1$ km. The presence of these bodies has shown to be in conflict with models of Neptune's migration (Gomes et al., 2004), and survival of long period binaries (Parker & Kavelaars, 2012). Furthermore, even the most optimistic collisional destruction models have difficulty removing all the small bodies (Pan & Sari, 2005).

How can the CCG model be made more consistent with the observed properties of the Kuiper belt? One possibility is that u was excited by nearby planets more than it was by Kuiper belt objects, since it has been suggested that the planets underwent violent orbital instabilities in the early solar system (e.g., Thommes et al., 1999; Goldreich et al., 2004b; Levison et al., 2008). That could have been responsible for smaller sizes s. Support for this conjecture is provided by the fact that at the end of accretion v must have been much smaller than it is today (either in the CCG model or the collisionless model). The only plausible mechanism to stir up v is by some form of external stirring, either by planets or planetary embryos that have since been lost. That stirring might have stirred u, and hence broken down s to very small sizes. Such stirring might break the superthin condition, and in chapter 5, we show this reduces the size at which $\Sigma \sim \sigma$ to $R \sim \alpha^{-2}s$, thus requiring only nice millimeter sized, chondrule like small bodies (Mason, 1960; Weisberg et al., 2006) to produce ~ 100 km large bodies. However, we leave serious consideration of planet stirring to future work. As for the size spectrum, it is possible that processes that we have not considered, such as binary formation, could play a role in altering the size spectrum. An alternative possibility for resolving the discrepancy between CCG and observations is that some of the rates we have used for growth or viscous stirring, for example, might be incorrect. We have relied on expressions in the sub-Hill regime, which have not been thoroughly tested by numerical simulations. For example, semicollisional accretion (Schlichting & Sari, 2007) might play a role, or the flat disk formula of Equation (4.18) might not apply if external planets stir up the big bodies. Of course, these details will alter our quantitative conclusions, and each should be explored in turn. Nonetheless,

we suspect that our qualitative conclusion will remain—that Kuiper belt objects were formed with order-unity efficiency.
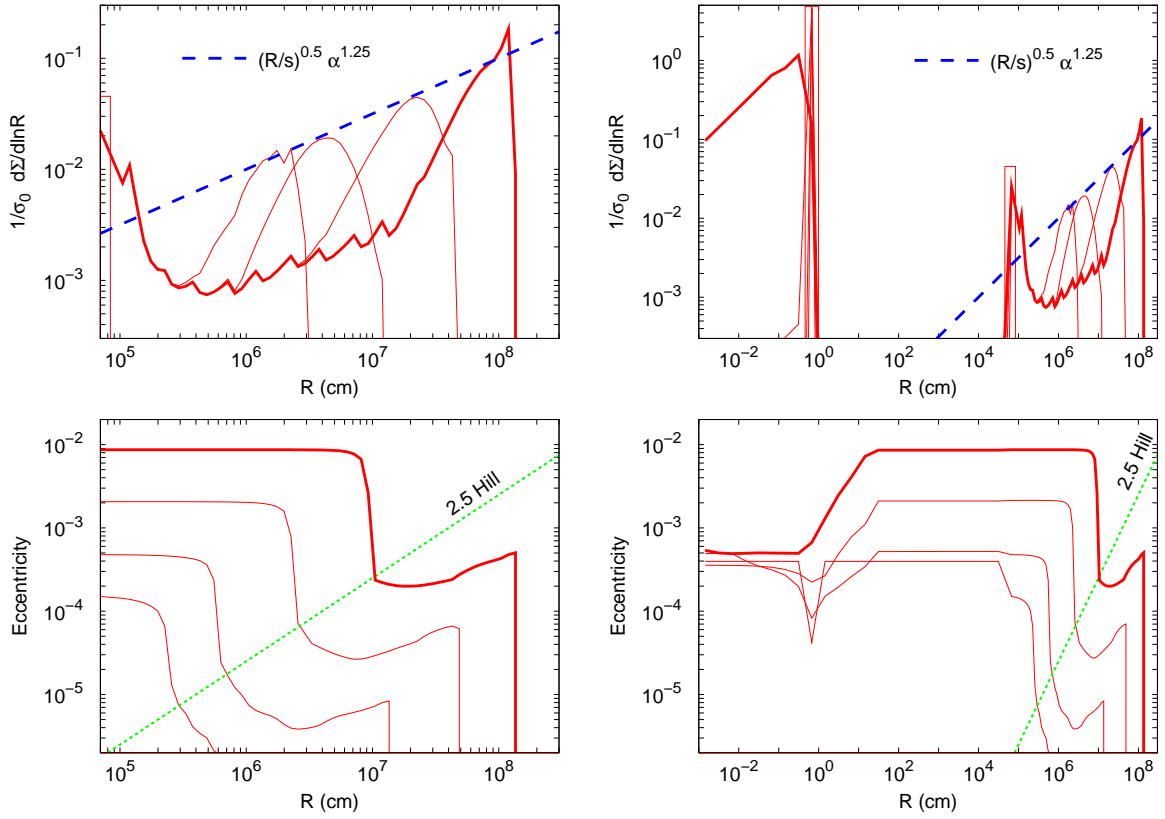
Figure 4.1: The evolution simulation, plotted as mass distribution (top two panels) and eccentricity (bottom). The red lines are plotted at 10, 20, 40, and 80 Myr, where the last line is thick. The left panels are the same as the right, but zoomed in to the big bodies. The peak of the mass distribution nearly obeys Equation (4.23), plotted as a dashed blue line. The surface density Σ (which here includes all bodies, big and small) is normalized by the total surface density $\sigma_0 \equiv 0.0016$ g/cm^2. At around 80 Myr, when the largest body is ~ 1000 km, a numerical artifact appears as the largest mass bin is required to have 1 body (hence the localized spike). In the bottom eccentricity plots, the green line shows the eccentricity corresponding to 2.5 v_H, which is approximately where the formulae that we use in our code (from Ohtsuki et al., 2002) transition from sub-Hill to super-Hill accretion. Both small bodies ($<$cm) and big ones are sub-Hill with respect to the bodies near the peak of the mass spectrum. Small bodies are accreted onto those bodies near the peak according to Equation (4.6); most of the big bodies that fall below the 2.5 Hill line are accreted according to Equation (4.18), because they satisfy the thin disk requirement.
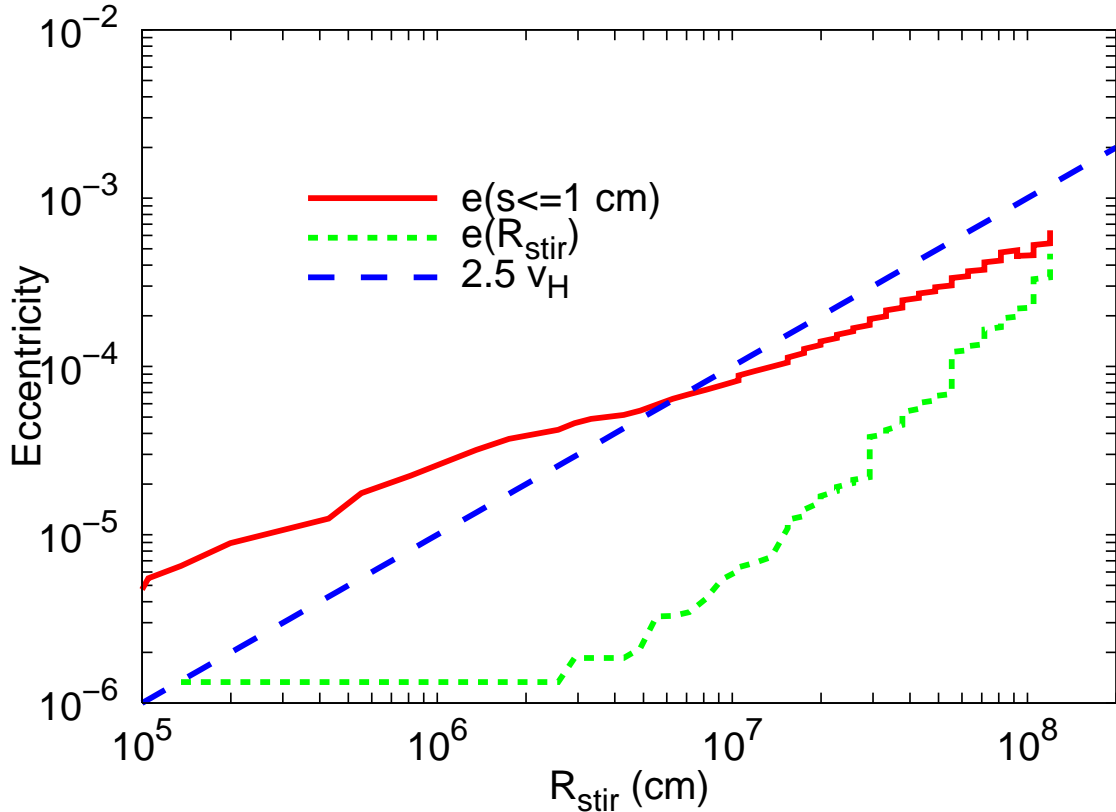
117

Figure 4.2: The eccentricities of small cm bodies (red line) and big R_{stir} bodies (green line) over the course of the simulation, plotted versus R_{stir}. Here, R_{stir} is the radius of the bodies that contribute the most to the stirring, and lies near the peak of the mass spectrum. The blue dotted line line shows the trans-Hill eccentricity relative to bodies of size R_{stir}. During equal accretion, both big and bodies are sub-Hill, with the small bodies becoming increasingly sub-Hill as time—and R_{stir}—proceed (Equation (4.25), and the big bodies becoming less sub-Hill (Equation 4.23). The spike at the end ($R_{stir} \sim 2000$km) occurs because the biggest body is prevented from growing by the requirement that there be at least 1 biggest body (chapter 3).

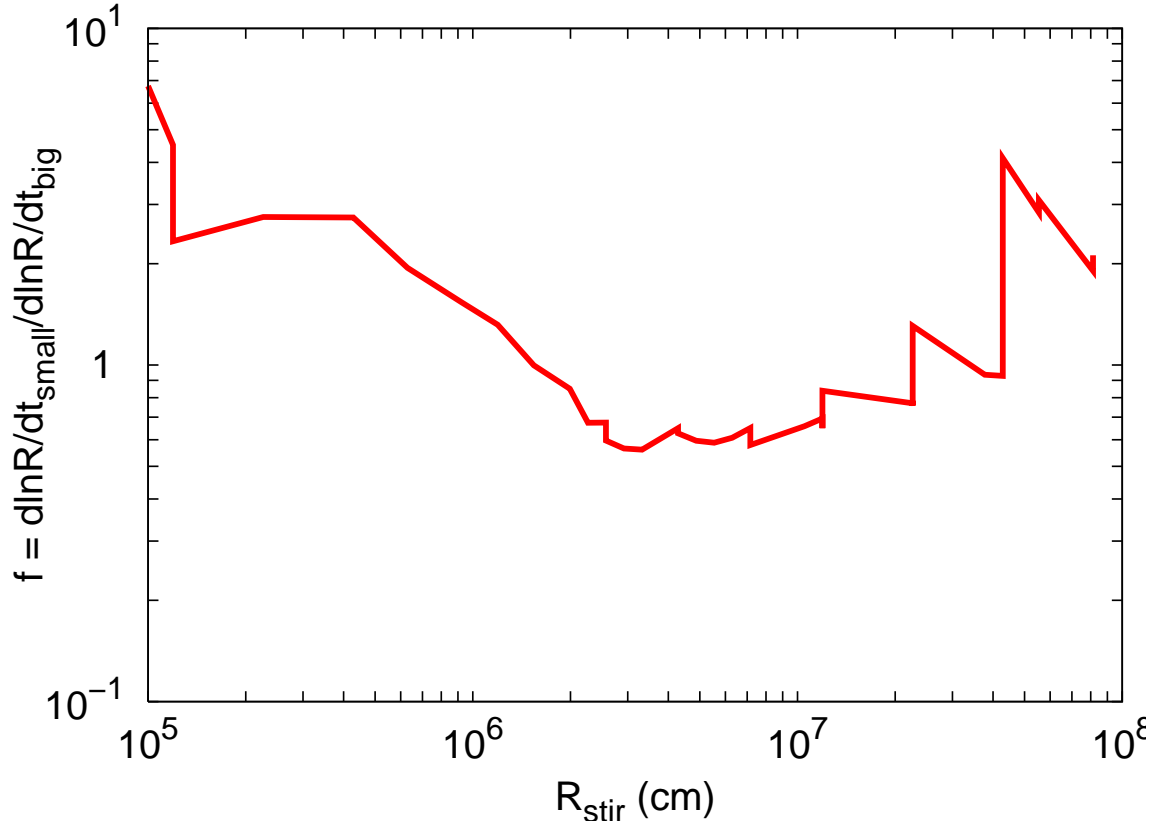Figure 4.3: Equal Accretion: Ratio of small body to big body accretion onto bodies of size $R_{\rm stir}$, where $R_{\rm stir}$ is the body size that dominates stirring. The system quickly moves to the $f \sim 1$ equilibrium, confirming equal accretion.

Chapter 5

Generalised Collisionally Damped Conglomeration

This chapter is a modified version of a draft publication. The research was done in conjunction with Dr. Yanqin Wu, and Dr. Yoram Lithwick. It is reproduced here with their permission.

5.1 Background

Dust in the protostellar nebula grows from 10^{-15} gram interstellar grains to terrestrial planets (or gas giant cores) of up to 10^{28} grams. Across such a large dynamic range of masses, many physical processes are important to the growth. There is not yet a good understanding of how these processes operate, or even necessarily what these processes are.

Small dust grains stick efficiently. While dust grains are small enough to be tightly coupled to the protostellar gas, they encounter other dust grains at low impact velocity. At low impact velocities, grains adhere by intermolecular forces, and grow.

Growing grains begin to decouple from the gas. Due to pressure support, gas orbits at a lower velocity than solids. Partially coupled bodies orbit at a velocity that depends

on the degree of coupling - this means that impact velocities are necessarily high unless the grains are quite similar in size. Other interactions between the gas and dust (such as sedimentation) may exacerbate or mitigate this effect (e.g., Brauer et al., 2007, 2008). Gas drag causes bodies to spiral into the central star on short timescales. The poor sticking combined with the short lifespan is known as the "meter size problem", as it occurs at roughly meter scales in a typical disk.

Solutions to the meter size problem rely on bringing together large numbers of sub-meter sized particles so they can collapse into a single body by mutual gravity (when the bodies are still far too small for pairwise sticking by gravity to be effective). Pioneering models of such processes concentrated particles towards the midplane of the disk, hoping the gas could be ignored once $\Sigma_{dust}/\Sigma_{gas} \gg 1$ (Safronov, 1969; Goldreich & Ward, 1973). Although subsequent results showed the dust could not become sufficiently concentrated in this way (Weidenschilling, 1980), the general form of direct collapse from centimeters or less to kilometers or more by concentration of bodies remains favoured. More recently models have used the interplay between dust and gas to concentrate the dust (Youdin & Shu, 2002; Cuzzi et al., 2008), which has been shown to planetesimals in simplified numerical experiments (Johansen et al., 2007).

The size of these primordial planetesimals is not well constrained. Early linearized analytic estimates tended towards kilometer scales. More recently, numerical simulations have produced objects of ~ 100 kilometer scale. In both cases, it is unclear how much stock should be placed in the quantitative results. Johansen et al. (2011) for instance, produce bodies of 10^{23} $\sim 10^{25}$ grams. They are unable to resolve bodies below $\sim 10^{22}$ grams due to the gravitational softening length, however. Other simplifications may also impact the qualitative results (e.g., the small particles are 40-80 cm in size).

After formation, planetesimals are believed to grow by pairwise collisions. This was simulated by Greenberg et al. (1978). They found that growth was inefficient, with most of the mass remaining at the starting size of one kilometer. Many subsequent

simulations have refined the physics (Wetherill & Stewart, 1993; Kenyon & Luu, 1998; Bromley & Kenyon, 2006; Ormel et al., 2010; Schlichting & Sari, 2011), however, the essential conclusions have not changed substantially during these refinements. Results diverge between the inner and outer solar system at this point. In the outer solar system, growth sputters out once the largest body is $\sim 10^3$ kilometers. In the inner solar system, the mass surface density is $\sim 10^3$ times that of the outer solar system, and the orbital time is 10^{-2} that of the outer solar system, and growth proceeds to terrestrial planets in $\sim 10^8$ years. In the outer solar system, the largest body tends to be $1 - 3 \times 10^3$ km at 10^{10} years (Kenyon & Bromley, 2008).

For a long time, the coagulation models matched the observations well. The largest trans-Neptunian objects are 10^3 km, and the total mass is 10^{-3} MMSN. Recently, however, serious challenges have appeared that question that model. In this chapter, we discuss how to address the challenge posed in chapter 2, where we showed that extrasolar disks have $MMSN$ type surface densities in $10 \sim 100$ km sized bodies, a result not predicted from the pairwise coagulation model (chapter 3).

5.2   Analytics

In our analysis, we use the order of magnitude expressions and symbols of Goldreich et al. (2004b). We repeat them here for reference. They consider bodies of two sizes, small and large. Small bodies have size s, velocity dispersion u, and surface density σ. Large bodies have size R, velocity dispersion v, and surface density Σ. All bodies have mass density ρ, and size dependant specific energy for catastrophic disruption Q^* (we use the Q^* of Stewart & Leinhardt, 2009). Large bodies grow by accreting small bodies at that

rate:

$$\frac{1}{R}\frac{dR}{dt} \sim \frac{\sigma\Omega}{\rho R}\alpha^{-1}\begin{cases}(\alpha) & u > \alpha^{-\frac{1}{2}}, v_{\mathrm{H}} \\[2mm] \left(\frac{v_{\mathrm{H}}}{u}\right)^2 & \alpha^{-\frac{1}{2}}v_{\mathrm{H}} > u > v_{\mathrm{H}} , \\[2mm] \left(\frac{v_{\mathrm{H}}}{u}\right) & v_{\mathrm{H}} > u > \alpha^{\frac{1}{2}}v_{\mathrm{H}} , \\[2mm] \alpha^{-\frac{1}{2}} & \alpha^{\frac{1}{2}}v_{\mathrm{H}} > u .\end{cases} \tag{5.1}$$

Large bodies grow by accreting large bodies at the rate:

$$\frac{1}{R}\frac{dR}{dt} \sim \frac{\Sigma\Omega}{\rho R}\alpha^{-1}\begin{cases}(\alpha) & v > \alpha^{-\frac{1}{2}}v_{\mathrm{H}} , \\[2mm] \left(\frac{v_{\mathrm{H}}}{v}\right)^2 & \alpha^{-\frac{1}{2}}v_{\mathrm{H}} > v > v_{\mathrm{H}} , \\[2mm] \alpha^{-\frac{1}{2}} & v_{\mathrm{H}} > v .\end{cases} \tag{5.2}$$

Note that in this case, we've assumed the limit where large bodies become superthin when sub-Hill to each other (Ida & Makino, 1992). We also discuss the limit where large bodies remain isotropic, in that case the growth equation is the same as for small bodies (i.e., equation 5.1). Large bodies evolve in velocity by viscous stirring from other large bodies, this has the form:

$$\frac{1}{v}\frac{dv}{dt} \sim \frac{\Sigma\Omega}{\rho R}\alpha^{-2}\begin{cases}\left(\frac{v_{\mathrm{H}}}{v}\right)^4 & v > v_{\mathrm{H}} , \\[2mm] \left(\frac{v_{\mathrm{H}}}{v}\right) & v_{\mathrm{H}} > v ,\end{cases} \tag{5.3}$$

and they are cooled by dynamical friction from small bodies:

$$\frac{1}{v}\frac{dv}{dt} \sim -\frac{\sigma\Omega}{\rho R}\alpha^{-2}\begin{cases}\left(\frac{v_{\mathrm{H}}}{u}\right)^4 & u > v_{\mathrm{H}} , \\[2mm] (1) & v_{\mathrm{H}} > u .\end{cases} \tag{5.4}$$

The small bodies, meanwhile, are heated by viscous stirring

$$\frac{1}{u}\frac{du}{dt} \sim \frac{\Sigma\Omega}{\rho R}\alpha^{-2}\begin{cases}\left(\frac{v_{\mathrm{H}}}{u}\right)^4 & u > v_{\mathrm{H}} , \\[2mm] \left(\frac{v_{\mathrm{H}}}{u}\right) & v_{\mathrm{H}} > u .\end{cases} \tag{5.5}$$

and they are cooled by mutual collisions

$$\frac{1}{u}\frac{du}{dt} \sim -\frac{\Omega\sigma}{\rho s} . \tag{5.6}$$

Note that all of these are presented as rate equations. We may refer to the time scale of a process, τ, which is the inverse of the above rate.

5.3 Collisional Physics

There are two main observations we hope to address here. First, we know that the brightest extrasolar debris disks (with fractional luminosity $\sim 10^{-3} \sim 10^{-4}$) have $1 \sim 10 M_\oplus$ in $\sim 10 \sim 100$ km objects (chapter 2). Secondly, such disks are common, $\sim 15\%$ of solar type stars have bright disks (Trilling et al., 2008). Thus any model of conglomeration of planetesimals should produce $\sim 1 \sim 10 M_\oplus$ in $\sim 10 \sim 100$ km objects in massive (but commonplace) disks. Less secure, but still of interest, is that the size distribution in this regime seems to follow a power law with a differential index of $3 < q \lesssim 4$ (again, see chapter 2).

To produce a disk with $\sim 10 M_\oplus$ in $\sim 10 \sim 100$km bodies (at distances of 30-100 AU), coagulation needs to proceed with fairly high efficiency. MMSN-type disks typically have a comparable amount of mass to that in metals at the relevant distances (10-100 AU); Disks may be more massive, by as much as a factor of 10. So, coagulation needs to be $\gtrsim 10\%$ efficient in producing 10+ km bodies. Debris disks typically "turn on" at $3 \sim 15$ Myrs (Currie et al., 2008). Whatever process heats the planetesimals sufficiently that they begin a collisional cascade, bodies of a few hundred kilometers must be in place by then.

Why is growth so inefficient? The answer lies in the collisional cross section at speeds that are below the escape speed, but above the Hill speed. In that case, the cross section for interaction is

$$\pi b^2 = \pi \left(s_1 + s_2\right)^2 \left(1 + \frac{v_{\mathrm{esc}}^2}{u_{\mathrm{rel}}^2}\right) \,, \tag{5.7}$$

where v_{esc} is the mutual escape velocity, and u_{rel} is the relative velocity. One can find this derived in Binney & Tremaine (1987). An orbiting bodies traverses a box of length $2\pi a$,

of width Δa and of height h, at a speed u_{rand}. We can then write $n_m = N_m / (2\pi a \Delta a h)$. We can reasonable assume the scale height is set by the velocity dispersion, i.e., $h \sim u_{\mathrm{rand}} / u_{\mathrm{kepler}} \times a$, and rearrange the frequency of collision equation, $f_c = n\pi b^2 u$ into the Goldreich et al. (2004b) formulation:

$$\frac{1}{M}\frac{dM}{dt} \sim \frac{\sigma\Omega}{\rho R}\left(\frac{v_{\mathrm{esc}}^2}{u^2}\right) . \tag{5.8}$$

For bodies growing by accreting much smaller bodies, u is typically set by the random velocities of the small bodies, and the mass doubling time obeys

$$\tau_{double} \propto s^{-1} . \tag{5.9}$$

This is the fundamental root of runaway growth (Greenberg et al., 1978). Larger bodies grow faster than smaller ones. The larger bodies provide viscous stirring, inhibiting the growth of smaller bodies. Bodies move apart in mass space, and fewer and fewer (eventually only one) grow. If that body can accrete most of the mass, growth may be efficient, but efficiently producing 10 or 100 km bodies is impossible. One proposed solution has been to begin with all of the mass in bodies of that size (Morbidelli et al., 2009), which is certainly effective at reproducing the size distributions observed for small body populations. It is likely to produce difficulties for planet formation, however, as the larger the initial size of planetesimals, the longer it takes to produce planets (Kenyon & Luu, 1998, also see chapter 3)

If we can't get to high efficiency by going through runaway growth, we will have to go around it. Runaway growth only takes place when $v_{\mathrm{esc}} > u > v_{\mathrm{Hill}}$. When $\alpha^{0.5} < u < v_{\mathrm{Hill}}$, bodies grow like (Goldreich et al., 2004b):

$$\frac{1}{M}\frac{dM}{dt} \sim \frac{\Sigma_m\Omega}{\rho s}\alpha^{-1/2}\left(\frac{v_{esc}}{u}\right) . \tag{5.10}$$

In this case, $\tau_{\mathrm{double}} \propto s^0$. Bodies grow together, and many bodies can grow to large sizes in a reasonable time, which can result in high efficiency. Such a scenario can arise when bodies grow primarily by accreting small bodies which undergo significant collisional

damping (Goldreich et al., 2004a). We explore variations on that theme using the code described in chapter 3.

5.4 Simulations

What initial conditions are appropriate for conglomeration is quite speculative. Many meteorites (and hence many asteroids) are composed of primitive millimeter sized grains (chondrules) (Mason, 1960; Weisberg et al., 2006). Dust growth experiments and simulations suggest that dust grains might grow to centimeter scales before impacts become erosive rather than conglomerative (Blum, 2010). Early analytic estimates of planetesimal formation size placed them at ~ 100 m ~ 1km (Safronov, 1969; Goldreich & Ward, 1973). More recent estimates have produced larger ($10 \sim 1000$ km) planetesimals (Cuzzi et al., 2008; Johansen et al., 2011). Solar system observations suggest that post coagulation primordial (i.e., not collisionally produced fragments) exist to sizes at least as small as ~ 50 km (Bottke et al., 2005; Sheppard & Trujillo, 2010) - and without primordial bodies well under 100 km, luminous debris disks wouldn't be produced at the few million year ages we see them (see chapter 2). In rough terms, we might expect small bodies to be $10^{-2} \sim 10^2$ cm, and large bodies to be $10^{-1} \sim 10^3$ km, most likely with some distribution.

5.4.1 Superthin Limit

With these considerations, we begin with a standard case, which we will call "km + cm". We begin with $10 M_\oplus$ in 1 cm and 1 km bodies, with $\sigma_{cm}/\Sigma_{km} = 10$. The bodies are spread evenly between 42 and 48 AU. Bodies begin with $e = 10^{-6}$. All bodies have mass density $\rho = 1.5$ g cm^{-3}. If a collision is catastrophically destructive, the resultant bodies are redistributed to all smaller size bins with $q = 3.5$, and a fraction of the mass is lost equal to the mass that would be distributed to sizes smaller than the smallest size bin if

the redistribution continued to $s = 0$. The evolution is plotted in figure 5.1.
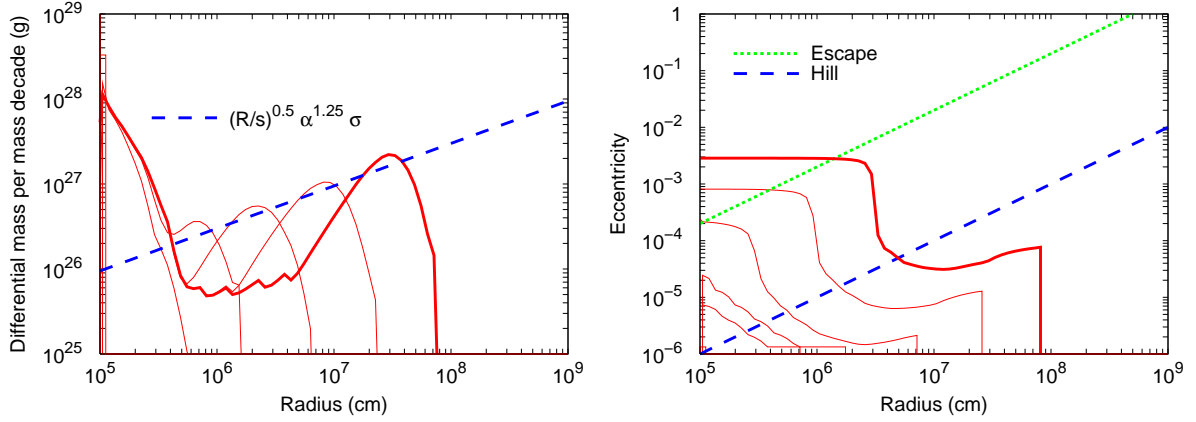

Figure 5.1: The evolution of a standard system, plotted in size mass distribution (left) and eccentricity (right). This standard system begin with $9M_\oplus$ in cm sized grains, and $1M_\oplus$ in kilometer sized seed planetesimals, distributed in a ring from 42 to 48 AU. All bodies begin with $e = 10^{-6}$. Thin red lines are plotted at 40, 80, 160, and 320 kyrs, the thick red line is 640 kyrs. The peak of the mass distribution obeys equation 5.18. The final mass distribution is not the $q \sim 3.5$ of the peak, but obeys $q \sim 2$.

At early times, the velocity dispersion of the small bodies is set by the balance of viscous stirring of the km bodies and collisional cooling amongst the cm bodies. Then balancing equation 5.5 and 5.6 gives:

$$u \sim \left(\frac{\Sigma_{\mathrm{km}}}{\sigma}\right)^{\frac{1}{4}} \left(\frac{s}{R_{\mathrm{km}}}\right)^{\frac{1}{4}} v_{\mathrm{esc,km}} \ . \tag{5.11}$$

For our particular choice of Σ, σ, s, and R_{km}, the small grains quickly reach $u \sim 5v_{\mathrm{H}}$. With $u > v_{\mathrm{H}}$, $v > v_{\mathrm{H}}$, small bodies will have a pseudo-equilibrium velocity where collisional damping (equation 5.6) balances super-Hill viscous stirring (equation 5.5):

$$\frac{u}{v_{\mathrm{H}}} \sim \left(\frac{\Sigma s}{\sigma R} \alpha^{-2}\right)^{\frac{1}{4}} , \tag{5.12}$$

while the large body velocity equilibrium is the balance of super-Hill viscous stirring

127

(equation 5.3) and super-Hill dynamical friction (equation 5.4):

$$\frac{v}{v_{\mathrm{H}}} \sim \left(\frac{u}{v_{\mathrm{H}}}\right)\left(\frac{\Sigma}{\sigma}\right)^{\frac{1}{4}} \sim \left(\frac{\Sigma^2 s}{\sigma^2 R}\alpha^{-2}\right)^{\frac{1}{4}} . \tag{5.13}$$

Then large bodies grow by accreting small bodies and large bodies in the ratio:

$$
\begin{aligned}
f_{\mathrm{superhill}} &\sim \frac{\frac{\sigma\Omega}{\rho R}\alpha^{-1}\left(\frac{v_{\mathrm{H}}}{u}\right)^2}{\frac{\Sigma\Omega}{\rho R}\alpha^{-1}\left(\frac{v_{\mathrm{H}}}{v}\right)^2} \\
&\sim \sqrt{\frac{\sigma}{\Sigma}} \tag{5.14}
\end{aligned}
$$

At early times, we should expect that growth from accreting small bodies is $\sim 3\times$ as important as that from accreting large bodies, roughly what we observe (figure 5.1).

Before long, the system enters a $u < v_{\mathrm{H}}$, $v < v_{\mathrm{H}}$ phase. Then, small bodies have a pseudo-equilibrium velocity were collisional damping (equation 5.6) balances sub-Hill viscous stirring (equation 5.5):

$$\frac{u}{v_{\mathrm{H}}} \sim \left(\frac{\Sigma s}{\sigma R}\alpha^{-2}\right) , \tag{5.15}$$

and large body velocity equilibrium is the balance of sub-Hill viscous stirring (equation 5.3) and sub-Hill dynamical friction (equation 5.4):

$$\frac{v}{v_{\mathrm{H}}} \sim \frac{\Sigma}{\sigma} . \tag{5.16}$$

The large bodies grow by accreting small bodies and large bodies in the ratio:

$$
\begin{aligned}
f_{\mathrm{subhill}} &\sim \frac{\frac{\sigma\Omega}{\rho R}\alpha^{-1}\left(\frac{v_{\mathrm{H}}}{u}\right)}{\frac{\Sigma\Omega}{\rho R}\alpha^{-\frac{3}{2}}} \\
&\sim \left(\frac{\Sigma^2}{\sigma^2}\frac{s}{R}\alpha^{-\frac{5}{2}}\right)^{-1} \tag{5.17}
\end{aligned}
$$

Let N be the number of large bodies. We consider two limits: If the large bodies grow primarily by accreting small bodies, then $\Sigma = NR^3$ as they grow, and Σ^2/R increases (as R^5). Substituting that into equation 5.17, we find f_{subhill} decreases, and accretion of large bodies becomes more important. In the second limit, the large bodies grow primarily by

accreting each other, so $\Sigma \sim \Sigma_0$ is constant, and Σ^2/R decreases with R. Substituting into equation 5.17, we find f_{subhill} increases, and accretion of small bodies becomes more important.

Thus $f_{\text{subhill}} \sim 1$ is a stable point, and the system quickly moves to it (physically, it represents equal accretion of small bodies and large bodies, also found in Schlichting & Sari, 2011). We find excellent agreement to equal accretion in the simulation (figure 5.2). At early times, we can approximate s, σ, and α as constants, and we obtain:

$$\Sigma \sim \sqrt{\frac{R}{s}} \alpha^{\frac{5}{4}} \sigma \ . \tag{5.18}$$

This does not predict power law size number distribution $dn/dR \propto R^{-q}$ with $q \sim 3.5$. Instead, the mass peak obeys this relation. In the orderly growth regime, the smaller large bodies grow faster, and keep up with the peak. The leeside of the distribution has $q \sim 2$ (figure 5.1).

Intermediate sized bodies exhibit a dichotomous eccentricity distribution. Bodies at size $R' < R$, which are cooled in the sub-Hill regime have a velocity equilibrium $v' = \Sigma/\sigma \times R'/R \times v_{\text{H}}$. Considering large bodies of different sizes results in a Σ that is poorly defined, but velocity inversion (larger bodies dynamically hotter than smaller bodies) is observed in the sub-Hill large bodies (figure 5.1). In the super-Hill regime, smaller bodies do not have a velocity equilibrium if $R' < \sqrt[3]{\Sigma/\sigma} R$, and rise freely in eccentricity, such that at any time, their stirring time is equal to the system age. These bodies for a plateau in eccentricity.

In the following subsections, we explore variations on the initial s, R, Σ/σ, and σ.

Variations on s

We consider s of 1 cm, 1 mm, and 100 μm. If we substitute equation 5.18 into equation 5.15, we predict that during growth, the small body velocity dispersion should obey

$$u \sim \sqrt{\frac{s}{R}} \alpha^{-\frac{3}{4}} v_{\text{H}} \ . \tag{5.19}$$
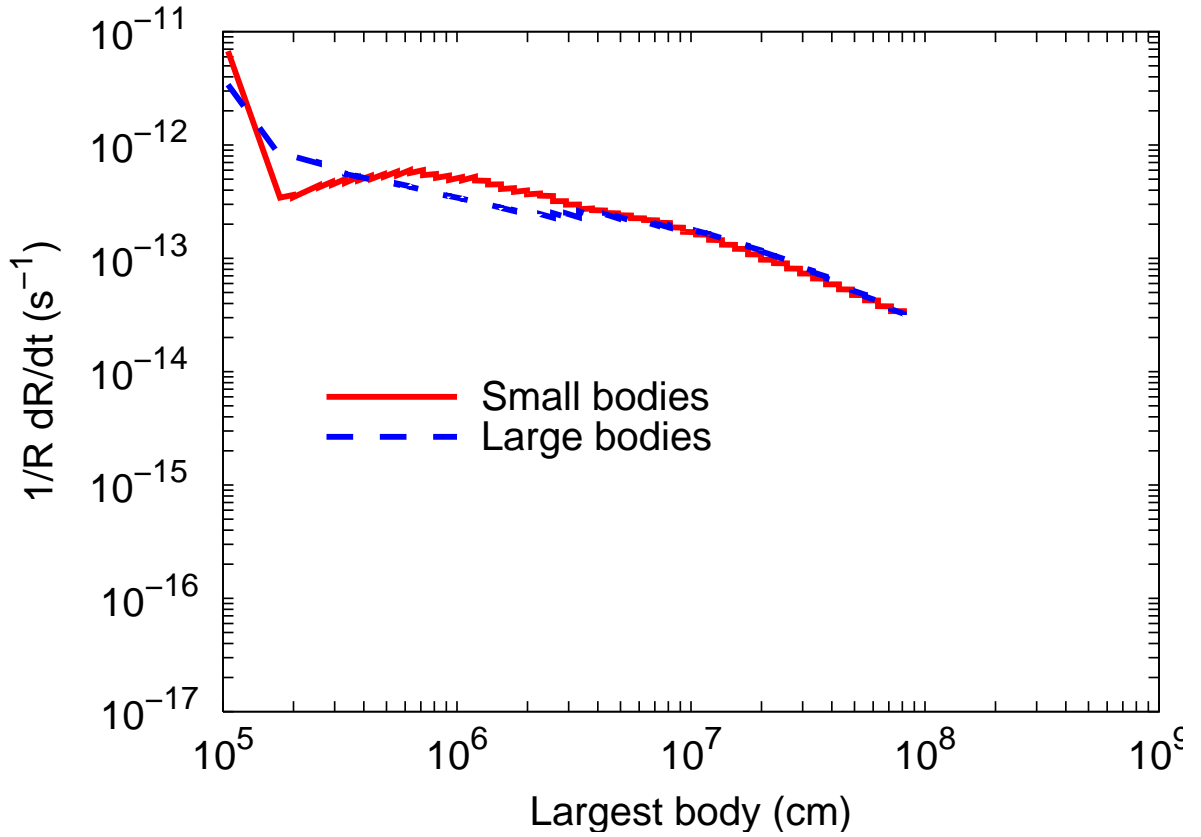
Figure 5.2: Growth rate of the largest body in the simulation plotted in figure 5.1, showing the contribution from accretion small bodies (solid red line), and from accreting other large bodies (dashed blue lines). Our initial conditions begin with growth mainly from accreting small bodies, but the system quickly moves to the $f \sim 1$ equilibrium (equation 5.17).

This relation is observed in simulations 5.3.

The size distributions obey the scaling implied by equation 5.18, namely that at a given R, $\Sigma \propto s^{-0.5}$ (figure 5.4). During sub-Hill accretion, the accretion rate of small bodies is proportional to v_{H}/u, and substituting in equation 5.19, proportional to $s^{-0.5}$, as observed in the simulation (figure 5.4 is plotted when the largest body is $\sim 10^3$ km, which is ~ 500 kyrs with $s = 1$ cm, and ~ 200 kyrs when $s = 1$ mm).

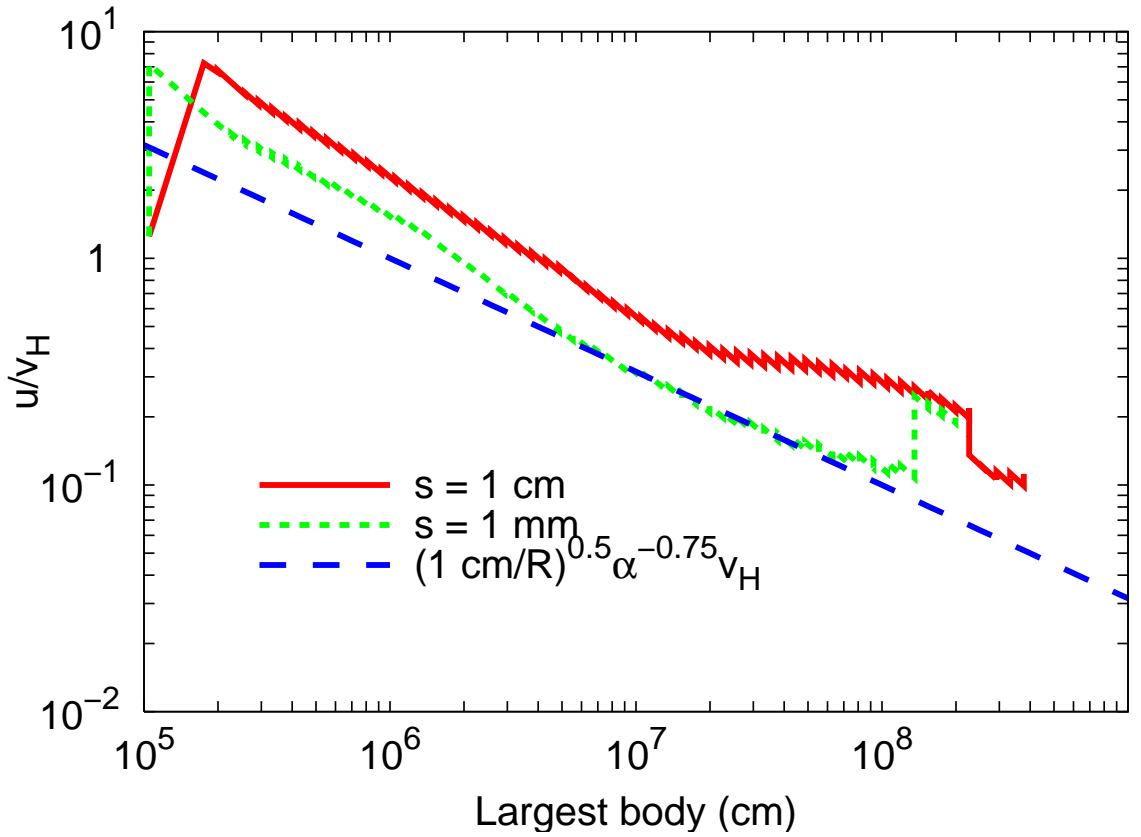Figure 5.3: u/v_{H} in the simulation plotted in figure 5.1, compared to a variate where the starting size of small bodies is 1 mm. During growth, the small grain velocity dispersion scales with R as predicted by equation 5.19, with a numerical constant of ~ 3. During the evolution u rises slower than v_{H}, and growth remains quick.

Variations on R

Here we consider different starting sizes for large bodies, namely $R = 100$ m, 1 km, and 10km. The equilibrium solution does not depend on the starting size of large bodies, and once the growth has proceeded far enough from R_0, the mass distribution is the same for different starting R (figure 5.5). Numerically, we find convergence to be slow, with simulations converging when the largest body is $\sim 10^{1.5}\times$ the starting size R_0.
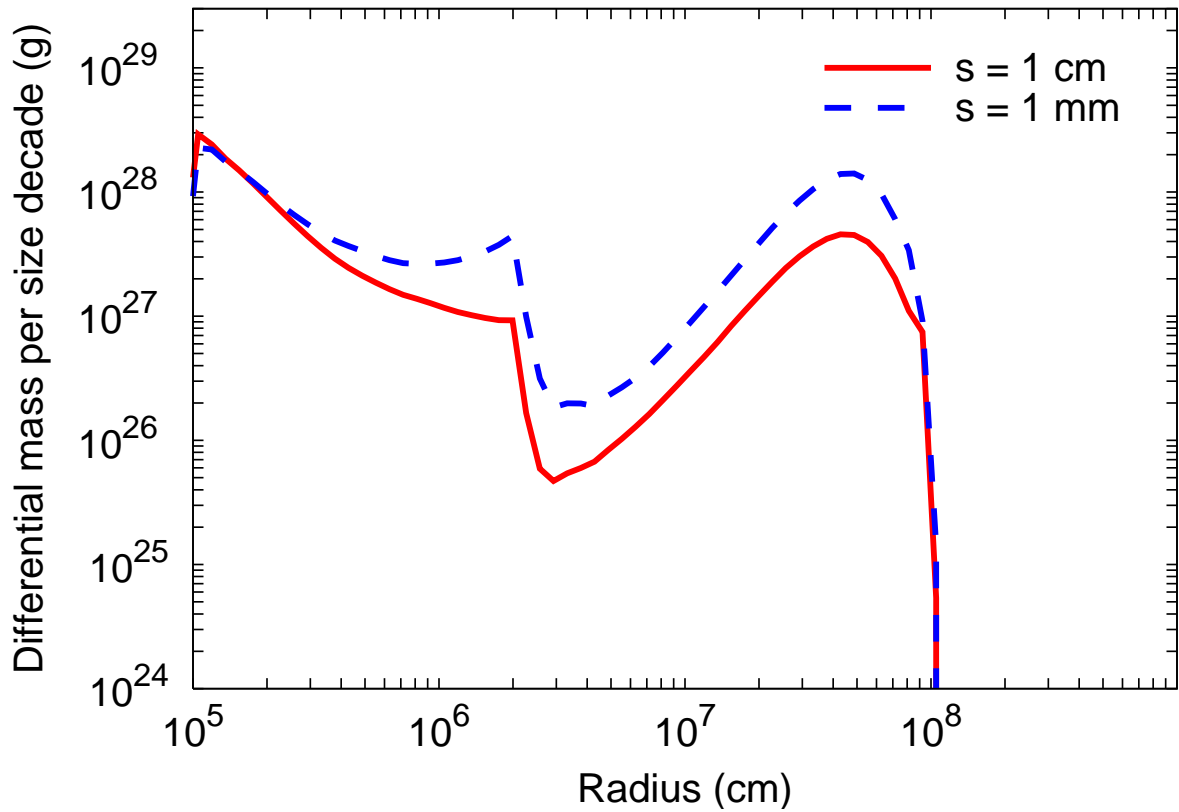
Figure 5.4: The size mass distribution for the standard case plotted in figure 5.1, and the variant where small bodies are initially $s_0 = 1$ mm in size, plotted when the largest body is $R = 1000$ km. The largest body reaches 1000 km after 500 kyrs in the cm case, and takes 200 kyrs in the 1 mm case. The mass of large bodies scales like $s_0^{-0.5}$, as predicted by equation 5.18.

Variations of Σ/σ

We consider starting conditions with $\Sigma/\sigma \sim 0.01, 0.1$, and 0.5. The equilibrium solution does not depend on Σ/σ, however, since total mass is kept constant, small variations show up due to the slight variations in σ_0. The simulations confirm that the outcome depends only slightly on the initial Σ/σ (figure 5.6).
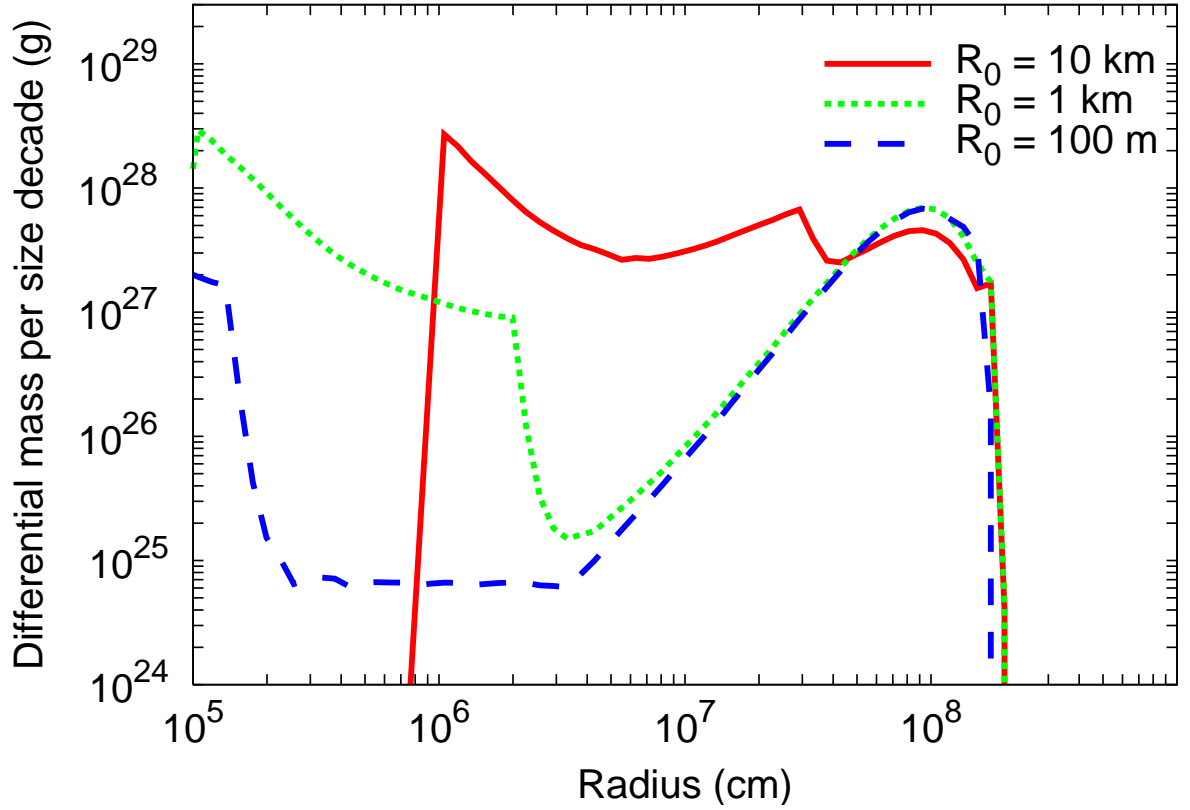
Figure 5.5: The size mass distribution for the standard case plotted in figure 5.1, and two cases where the initial size of the large seed planetesimals are 100 m, and 10 km, plotted when the largest body is $R = 2000$ km, for initial large bodies sizes $R_0 = 100$ m, 1km, and 10km. The largest body reaches 2000 km after 680 kyrs in the 100 m and 1 km cases, but takes 1.18 Myrs in the 10 km case. The mass distributions do converge once $R >> R_0$, here we find this occurs around $R \sim 10^2 R_0$.

Variations on σ

The equilibrium solution is invariant in Σ/σ, and thus variations in σ result in a linear response in Σ. Growth rates are linear in σ (equations 5.1 and 5.2), and thus growth times are inversely proportional to sigma. This dependence is observed in simulations (figure 5.13).
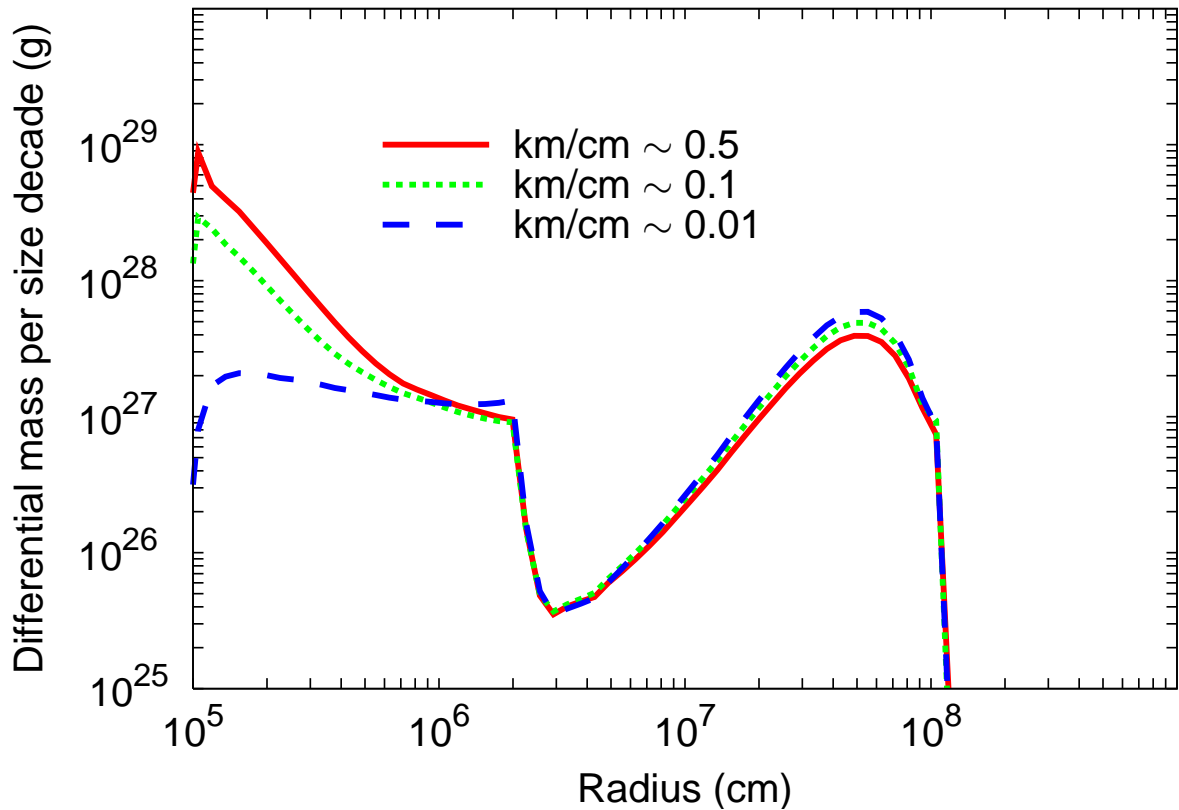
Figure 5.6: The size mass distribution for the standard case plotted in figure 5.1 (dotted green line), and two cases where the starting mass ratio of kilometer bodies to centimeter bodies is ~ 0.5 (solid red line) and ~ 0.01 (dashed blue line), plotted when the largest body is $R = 1000$ km. The simulations are plotted at 680 kyrs, 530 kyrs, and 500 kyrs, respectively, to account for the slower growth time in simulations with lower starting σ. The final result is very similar mass distributions.

5.4.2 Isotropic Limit

In section 5.4.1, we assumed that large bodies at sub-Hill velocity dispersions always accrete each other in the superthin limit. The other limit worth considering is the isotropic limit. In this case, large bodies accrete one another with the same cross section they accrete small bodies with (i.e., equation 5.1). The new collisional cross section changes
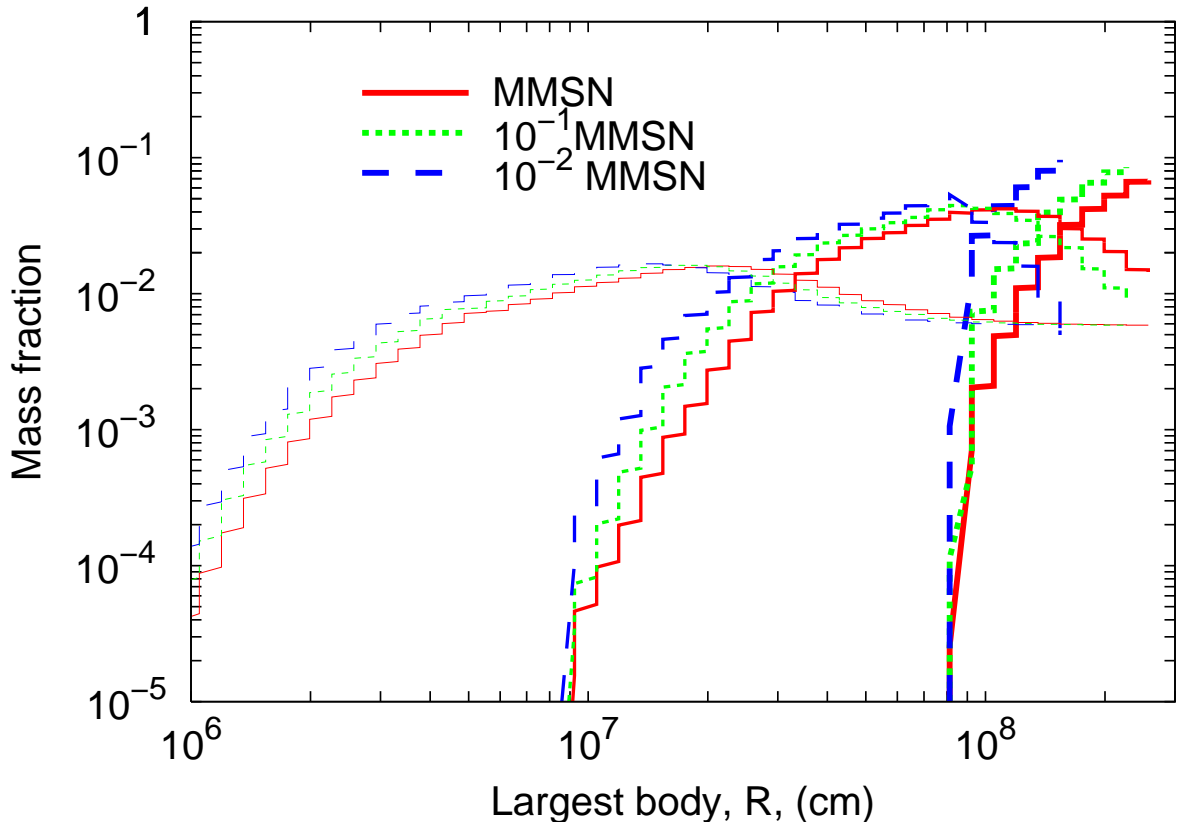
Figure 5.7: The efficiency of growth in the standard case plotted in figure 5.1 (solid red lines), compared to a case which begins with $0.9M_\oplus$ in cm grains and $0.1M_\oplus$ in km bodies (dotted green lines), and a case which begins with $0.09M_\oplus$ in cm grains and $0.01M_\oplus$ in kilometer seeds. Plotted are the fraction of the total mass between 10 and 100 km (thin lines), between 100 km and 1000 km (medium lines), and at sizes larger than 1000 km (thick lines). Because they are scaled by Σ/σ, the three simulations are very similar.

equation 5.17 to

$$f_{\text{subhill}} \sim \left(\frac{\Sigma}{\sigma}\frac{s}{R}\alpha^{-2}\right)^{-1}. \tag{5.20}$$

The rest of the analysis remains qualitatively unchanged. Accretion of mostly small bodies causes Σ/R to rise, and accretion of big bodies becomes more important. Accretion of mostly big bodies causes Σ/R to fall, and accretion of small bodies becomes more important. This factor was Σ^2/R in the previous section, but the principle is the same.

The system is again at equilibrium when $f_{\text{subhill}} \sim 1$. The surface density of large bodies now obeys:

$$\Sigma \sim \alpha^2 \frac{R}{s} \sigma \ . \tag{5.21}$$

The size mass distribution is different at well. The most important contrast with the superthin limit is that in the superthin limit, large bodies experience orderly growth, where their growth time τ is linearly proportionate to their size, $\tau \propto R^1$ (see equation 5.2). In that case, the smaller large bodies grow faster than the large ones, and they all tend towards the same size. During growth, their mass peak moves forward, with very few bodies left at intermediate sizes (refer to figure 5.1). In contrast, in the isotropic case, large bodies grow uniformly, with $\tau \propto R^0$ (equation 5.1 now applies to accreting other large bodies), and large bodies all grow at the same rate. This makes it much easier for small ones to fall behind, and thus the final size distribution is close to the differential power law with $q \sim 3$ that the mass peak follows during growth (figure 5.8).

The isotropic case often achives $\Sigma \sim \sigma$, as this happens at $R \sim \alpha^{-2}s$, a factor of $\sim 10^2$ earlier in size. At that point, $v \sim u$, and subsequently $v > u$. In this case, equation 5.17 changes to use $\alpha^{-1} \left(v_{\text{H}}/v \right)^2$ as the focussing factor in both accretion from small grains, and accretion from large bodies. With $f \sim \sigma/\Sigma$, the equilibrium solution becomes

$$\Sigma \sim \sigma \ . \tag{5.22}$$

This continues until the small grains are depleted or removed. Although not plotted in figure 5.8, the result can be seen in figure 5.10, for the $s < 1$ cm cases.

In the following subsections, we explore variations on the initial s, R, Σ/σ, and σ.

Variations on s

The most interesting variation is probably in s, since s appears in the equilibrium solution. Once bodies reach the equilibrium solution, substituting equation 5.21 into equation
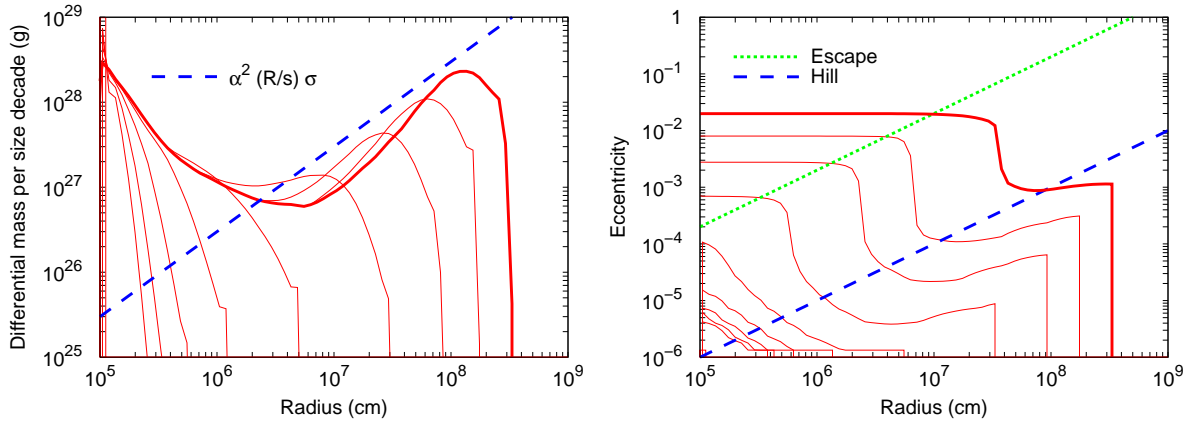
Figure 5.8: The evolution of a standard system, plotted in size mass distribution (left) and eccentricity (right). This standard system begin with $9M_\oplus$ in cm sized grains, and $1M_\oplus$ in kilometer sized seed planetesimals, distributed in a ring from 42 to 48 AU. All bodies begin with $e = 10^{-6}$. This system differs from the one presented in figure 5.1 in the behaviour of large bodies, which are assumed to be isotropic, rather than superthin. Thin red lines are plotted at 10, 20, 40, 80, 160, 320, 640, and 1280 kyrs, the thick red line is 2.56 Myrs. The peak of the mass distribution obeys equation 5.21. Unlike the superthin case, the final mass distribution remains close to the $q \sim 3$ implied by equation 5.21.

5.15 predicts that small bodies should obey

$$u \sim v_H \ . \tag{5.23}$$

This behaviour is observed in simulations (figure 5.9), for $s \le 1$ cm. At larger starting s, the collisional destruction of the small grains begins before the equilibrium is reached.

The simulations produce roughly the equilibrium size distribution where u obeys equation 5.23 (figure 5.10).

Once the simulations reach $R \sim \alpha^{-2}s$, equation 5.23 no longer holds, and the equilibrium solution can no longer be followed. As predicted by equation 5.22, we find $v > u$, and the size spectrum breaks to a $q \sim 4$ power law, which is observed in the $s \sim 100$ μm,
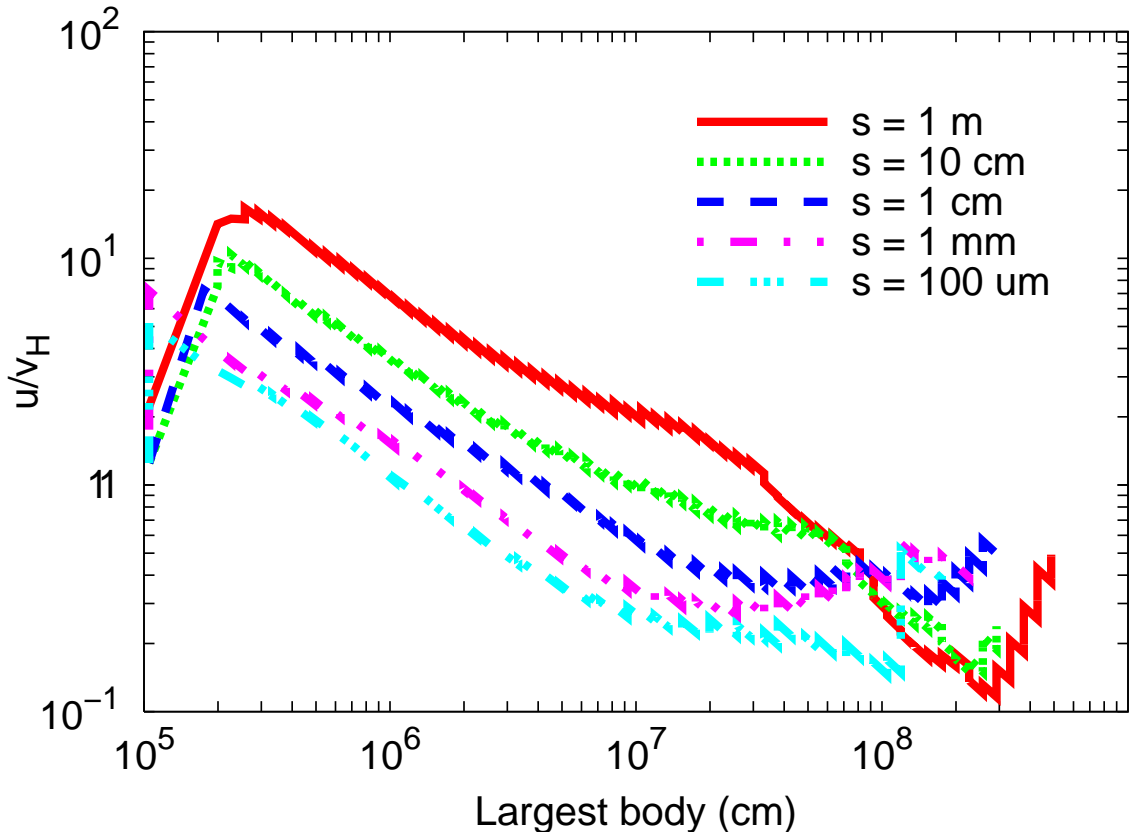
Figure 5.9: u/v_{H} in the standard case plotted in figure 5.8, as well as cases where the small bodies begin with size $s_0 = 1$ m, 10 cm, 1 mm, and 100μm. During growth, u/v_{H} reaches an equilibrum of ~ 0.5 in the cm, mm, and 100 μm, cases, as predicted in equation 5.23. In the 10 cm and 1 m cases, collisional destruction of small grains onsets early, and the equilibrium is not reached.

and mm simulations.

Variations on R

Our equilibrium solution does not depend on the starting size of large bodies. Thus we expect the size number distribution at large sizes will not depend on the initial size of large bodies. We find this to be the case in simulation (figure 5.11), as long as the starting size R_0 is much smaller than size in consideration. Notably, the only significant
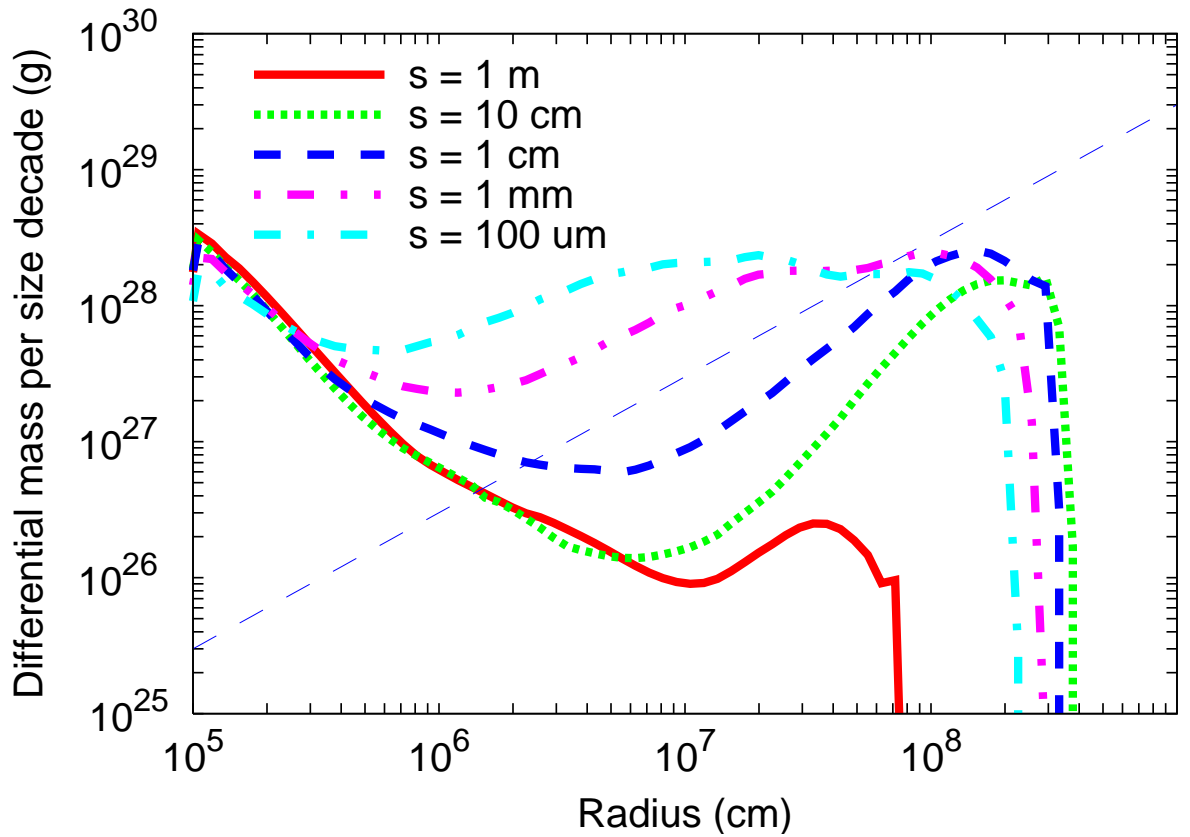
Figure 5.10: Differential mass distribution ($dM/ds\Delta s$) the standard case plotted in figure 5.8, as well as cases where the small bodies begin with size $s_0 = 1$ m, 10 cm, 1 mm, and 100 μm, all plotted after 3 Myrs. The thin blue dashed line shows the equilibrium solution for the $s_0 = 1$ cm case. The m and 10 cm cases do not make a good match to predictions, owing to insufficient time in the former case, and breakdown of small grains in the latter. Bodies reach $\Sigma \sim \sigma$ at approximately $R \sim \alpha^{-2}s$. At larger sizes, equation 5.22 applies, and bodies produce that size mas spectrum in the $s_0 = 100$ μm, and $s_0 = 1$ mm cases.

variation is that the $R_0 = 10$ km simulation has much more mass in 10 - 100 km objects. Thus we conclude that simulations converge before $10R_0$.
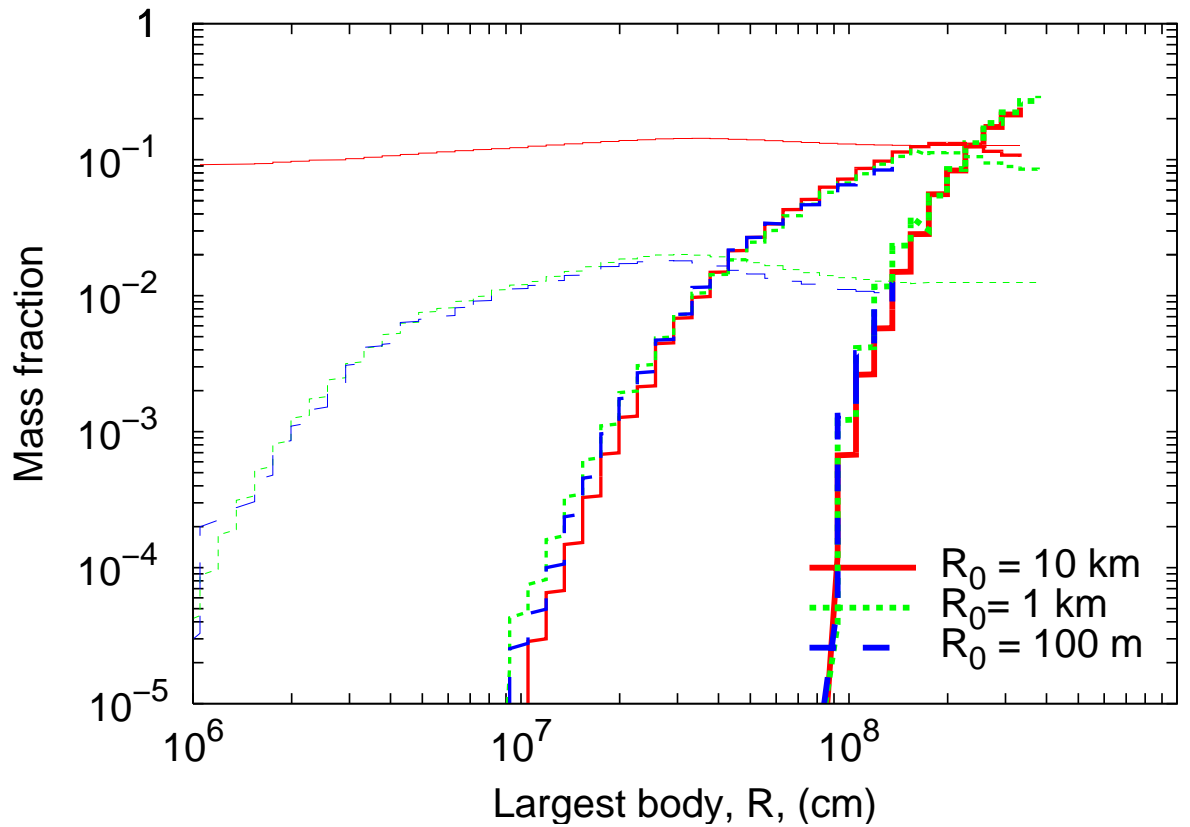
Figure 5.11: Mass fraction in 1000+ km (thick lines), 100 km - 1000 km bodies (medium lines), and 10 km - 100 km (thin lines), for the standard case plotted in figure 5.8 (dotted green lines), as well as cases where the large bodies begin at size $R_0 = 10$ km (solid red lines), and at $R_0 = 100$ m (dashed blue lines) The lines lie atop one another for the different R_0, apart from the $R_0 = 10$ km, mass fraction in 10 km - 100 km bodies, where initial conditions persist. The large end size distribution follows the equilibrium solution (equation 5.18), and is independent of R_0.

Variations on Σ/σ

The equilibrium solution does not depend on the primordial Σ/σ. Simulations move towards the equilibrium solution, and the final results depend only very weakly on the initial conditions (figure 5.12).
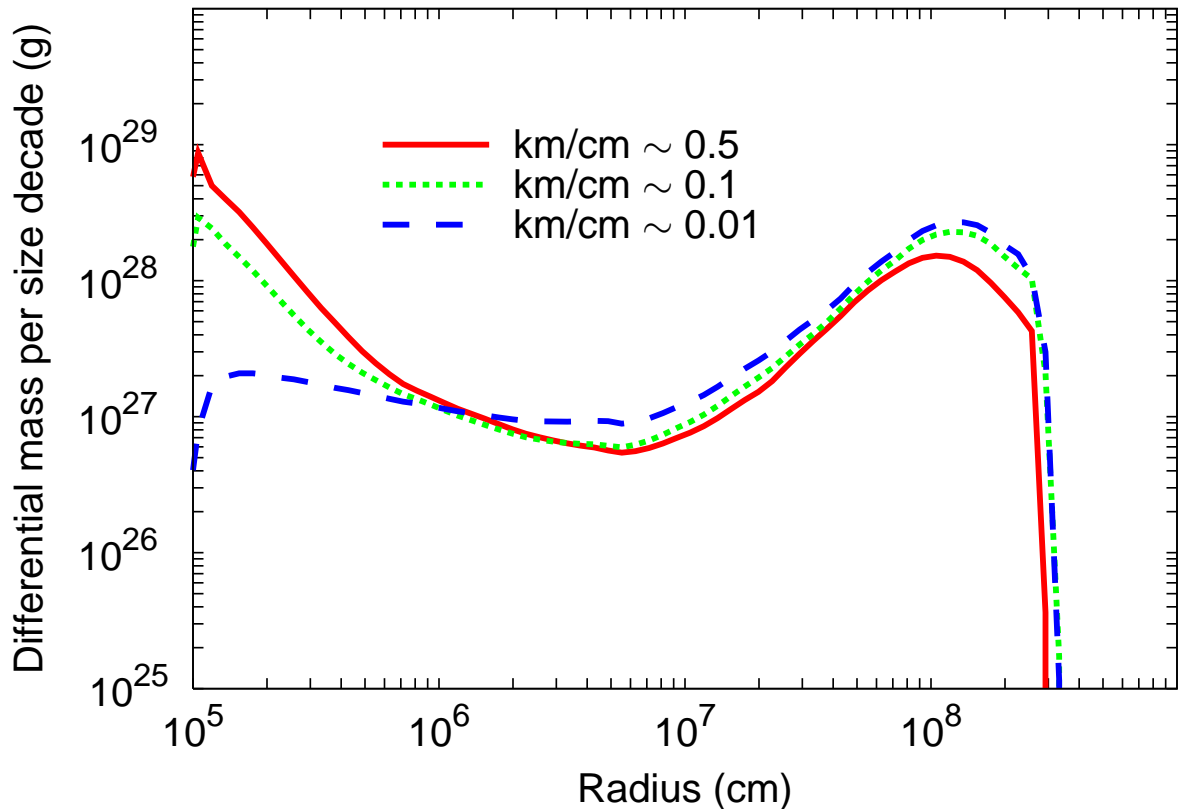
Figure 5.12: Differential size mass distribution for the standard case plotted in figure 5.8 (dotted green line), a case which begins with $7M_\oplus$ in cm grains and $3M_\oplus$ in kilometer seeds (solid red line), and a case which begins with $9.9M_\oplus$ in cm grains and $0.1M_\oplus$ in km seeds (dashed blue line), plotted at 2.5 Myrs. This is the approximate time when $\Sigma \sim \sigma$, and $R \sim \alpha^{-2}s$, for these simulations. The initial Σ/σ has a negligible effect on the the size distribution and growth time.

We employ constant total mass in the simulations, so different Σ/σ have slightly different σ to start. This results in small differences in the evolution and final state.

Variations on σ

The equilibrium solution is invariant in Σ/σ, and thus variations in σ result in a linear response in Σ. Growth rates are linear in σ (equations 5.1 and 5.2), and thus growth

times are inversely proportional to sigma. This dependence is observed in simulations (figure 5.13).
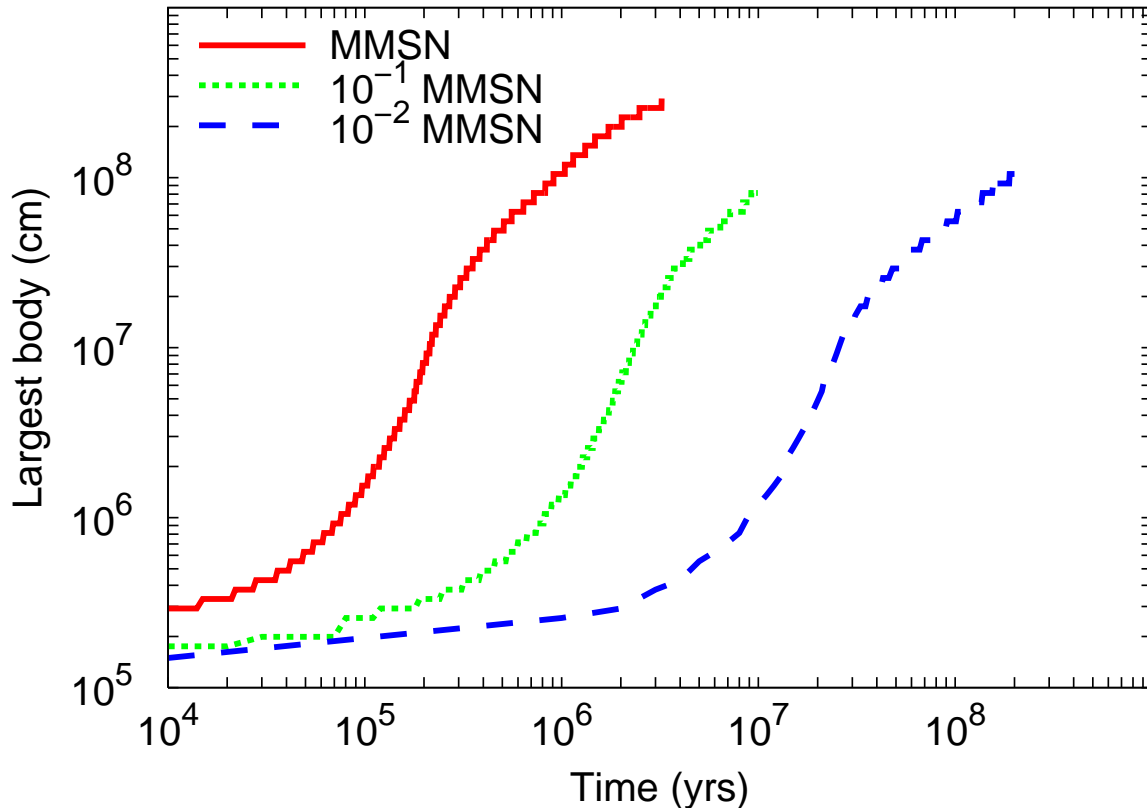
Figure 5.13: Growth of the largest body in the standard case plotted in figure 5.8 (solid red line), as well as cases that begin with $0.9M_\oplus$ in cm grains and $0.1M_\oplus$ in km seeds (dotted green line), and with $0.09M_\oplus$ in cm grains and $0.01M_\oplus$ in km seeds (dashed blue line). The growth is linearly faster with σ, as is expected from the rate equations (equations 5.1 & 5.2).

Despite the different timescales, the final size number distribution is approximately the same in the three runs (figure 5.14). A slight offset appears, and becomes large in the 1% MMSN simulation when $R \sim 10^3$ km, as the surface density in the largest bodies becomes close to one body per bin (or 18 bodies per size decade).

142
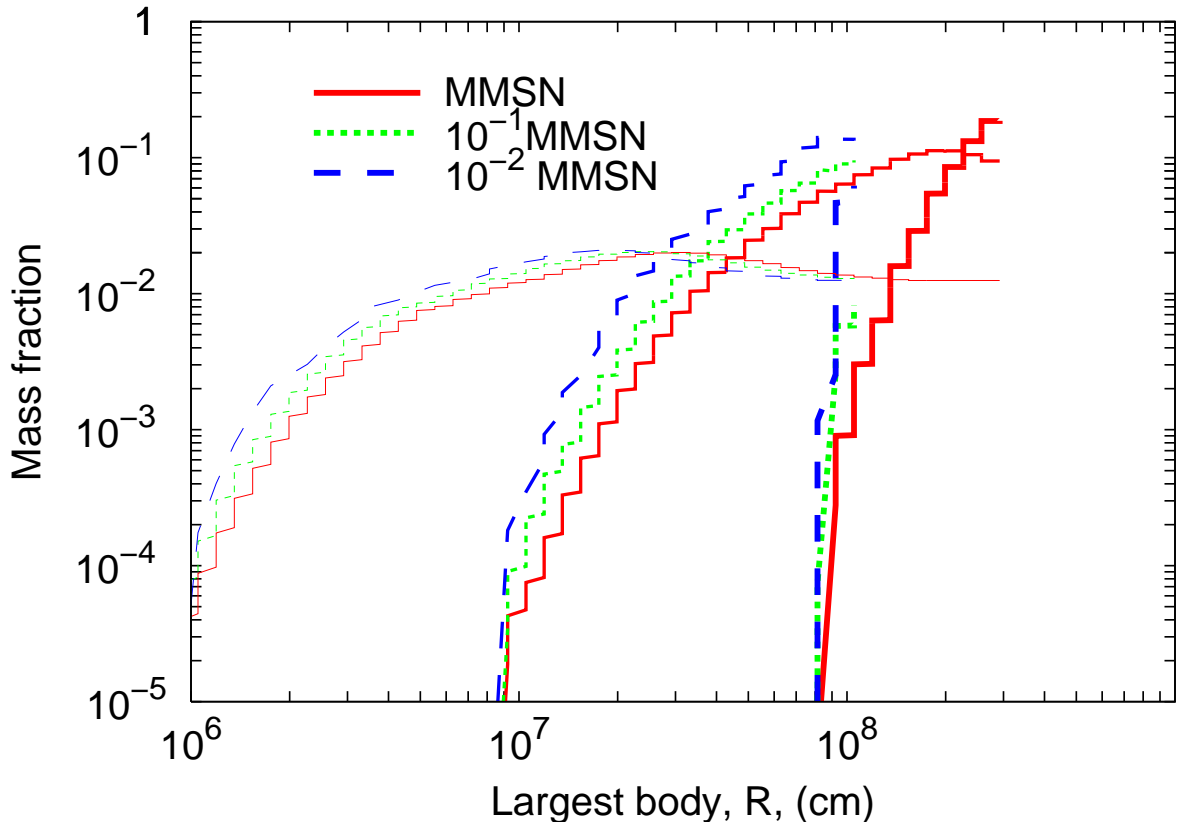
Figure 5.14: Mass fraction in 1000+ km (thick lines), 100 km - 1000 km bodies (medium lines), and 10 km - 100 km (thin lines), for the standard case plotted in figure 5.8 (solid red lines), as well as cases that begin with $0.9M_\oplus$ in cm grains and $0.1M_\oplus$ in km seeds (dotted green lines), and with $0.09M_\oplus$ in cm grains and $0.01M_\oplus$ in km seeds (dashed blue lines). The final size number distributions are substantially similar, scaled by the total mass.

5.5   The End of Growth

Growth cannot continue to obey the equilibrium solution forever. Barring other processes, the system reaches $\Sigma \sim \sigma$. At that point $v \sim u \sim v_{\mathrm{H}}$, and growth switches to a runaway mode. The presence of collisionally cooled grains means growth is still different from collisionless approaches. The simulations find $v \gtrsim u$, and v sets the encounter velocity

and gravitational focussing factors. While $\Sigma \sim \sigma$, the two groups approximation does not make a prediction for v, as the cooling and heating terms are comparable. Only full numerical integrations can solve for v (and through it, u).

In integrations, we find that v and u both rise (with $v > u$), until small bodies destroy each other in collisions. When bodies with masses m_1 and m_2 collide at a speed v, they are catastrophically disrupted if the specific kinetic energy $Q = (m_1 m_2) / (m_1 + m_2)^2 v^2$ exceeds a threshold specific energy Q^*. Thus small bodies have:

$$u \propto \sqrt{Q^*} , \tag{5.24}$$

which we observe in simulations (figure 5.15). Problematically, this allows small grains to break down to the blow-out size ($\sim \mu$m for a sunlike star), while the radial optical depth through the disk greatly exceeds value (typical values are $\sim 10^2$). Thus radiation blow out should be prevented by the shadowing of other grains. Our treatment of these small grains in this case is problematic. If the small grains are $\sim \mu$m sized, and still contain $10 + \%$ of their primordial mass, they collide $\gtrsim 10^2$ times per orbit. With eccentricity $e \sim 10^{-3}$, they should dissipate a total amount of energy equal to the orbital energy in a few orbits - the single zone, constant a treatment should fail, due to viscous spreading. Such viscous spreading might be sufficient to remove the small grains.

Poynting-Robertson drag is also significantly compromised as a dust removal mechanism due to shadowing. It would operate effectively on the first optical depth of grains. On long timescales it might clear dust grains, but even at $\sim \mu$m sizes, the time to remove the grains would be $\gtrsim 10^8$ years. Thus it cannot be regarded as a viable option.

Goldreich et al. (2004b) suggested that once large bodies were hot, small grains might recool, allowing them to form a second generation of planetesimals. We did not observe recooling in any simulations. This is because the small grains follow a pseudo-equilbrium $u \sim \sqrt{Q^*}$. To achieve recooling, grains must be small enough that cooling is more important than heating. With the pseudo-equilibrium, this does not occur. If grains were heated to a u such that they were catastrophically destroyed to a size smaller than
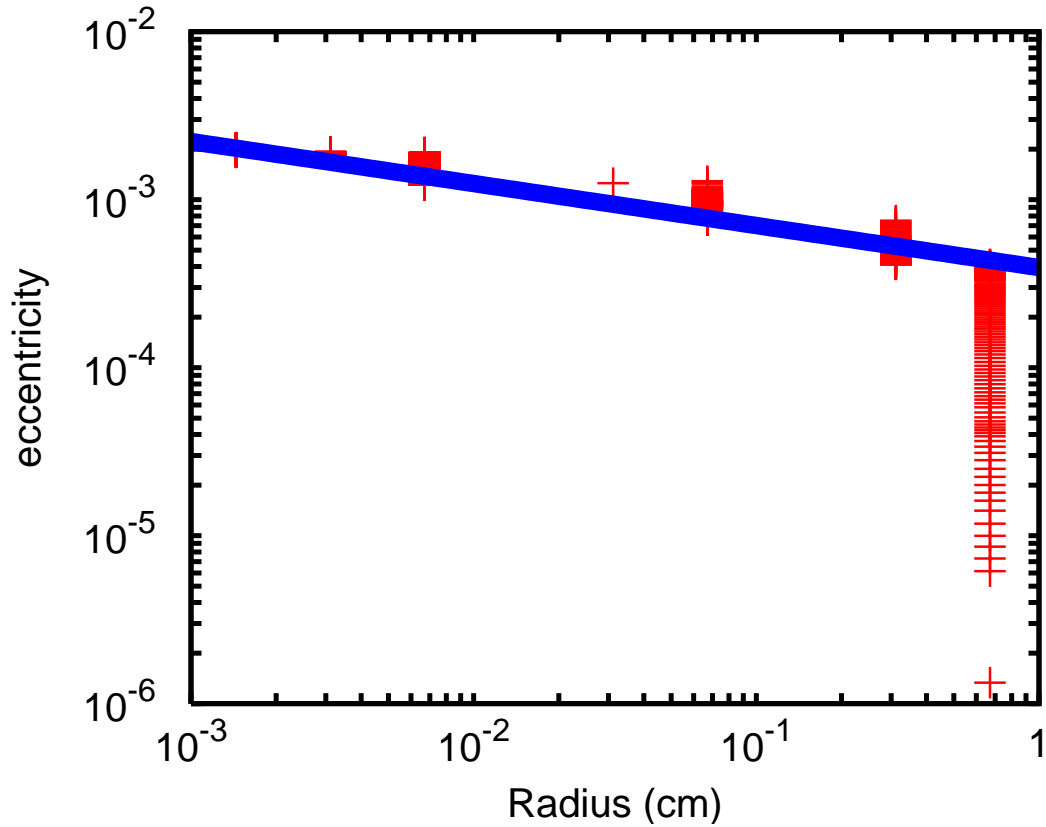
Figure 5.15: Eccentricity of the small bodies as a function of their size, in the 10^{-2} MMSN simulation discussed in section 5.4.2. Bodies begin at 1 cm and $e = 10^{-6}$. As the large bodies grow, the small grains are heated until their collisions are destructive, this occurs when the largest body is $\sim 10^3$ km. At smaller sizes, cooling is increased, but once large bodies have grown enough, the small grains are again hot enough to be destroyed in collisions. This continues until the small bodies are removed from the simulation. In 10^{-2} MMSN simulations, such removal may be caused by radiation pressure. At higher mass densities, the radial optical depth of dust grains exceeds one, and blow out should be ineffectitive.

the pseudo-equilibrium size before $u \sim \sqrt{Q^*}$, recooling should occur. This requires the collision time of small grains to be longer than their heating time (so u rises rapidly between individual collisions), and thus would require $s >> (\sigma/\Sigma)\,\alpha\,(u/v_H)$. To achieve

recooling when $\Sigma \sim \sigma$, and thus $u \sim v_{\mathrm{H}}$, the simulation would require $s > \alpha R$, In practice, we find such simulations unviable as when $s >> 1$ cm, collisional cooling is insufficient to enter the sub-Hill regime (figure 5.9).

Given these considerations, removal of the small dust grains remains an open problem. The size and mass spectrum of debris disks at the $1 \sim 1000$ km sizes relevant to debris disk evolution is set before dust grain removal takes place.

5.6   Discussion

We present a model of planetesimal formation, which we confirm with simulations. In contrast to previous models, which begin entirely with large ($\sim$ km) planetesimals, we begin primarily with small grains, with a small contingent of seed planetesimals. The inclusion of small grains results in dynamically important collisional cooling, and qualitatively different outcomes. While previous models had found that large planetesimals are made with low $\sim 10^{-3}$ efficiency, this model is able to produce large planetesimals with efficiencies of $\gtrsim 50\%$.

The higher efficiency comes from two changes in the growth. In the standard model, the large bodies accrete small bodies at sub-escape but super-Hill velocities. In this case, larger bodies grow faster than small bodies, and quickly run away from the group. Consequently, the number of growing bodies is small, and growth is inefficient. With collisional cooling, the velocities are sub-Hill, and large bodies all grow at the same rate. With many more accreting bodies, growth is more efficient. In addition, the cross section for accretion is larger at sub-Hill velocities than super-Hill velocities, and each large body accretes more rapidly.

In this model, growth is substantially faster than in the standard kilometer planetesimal model. In those models, producing 10^3 km bodies takes $10^7 - 10^8$ years at $30 \sim 50$ AU (see, e.g., chapter 3 Kenyon & Luu, 1998; Kenyon & Bromley, 2008; Ormel

et al., 2010). In this model, $\sim 10^3$ km bodies arise in roughly 10^6 years. This model can be adapted towards the formation of giant planet cores to address those giant planets already discovered at $>> 10$ AU (Marois et al., 2008; Kalas et al., 2008).

In chapter 2, we found that extrasolar debris disks have $3 < q \lesssim 4$, and total mass $\sim 10 M_\oplus$ in 1 - 100 km size objects. There, we interpreted this as reflecting a single population of massive disks with individual size number distributions of the form $3 < q \lesssim 4$. To fit the superthin simulation results to the extrasolar debris disk results, we must reinterpret the extrasolar debris disk results. The analysis in chapter 2 measured the size mass distribution at the point where bodies are entering collisional equilibrium. It is thus compatible with a situation where the brightest disks at a given age are not a constant population, but different populations of disks are brightest at different ages if the brightest disks at any given age obey $3 < q \lesssim 4$ in an average way when they are the brightest disks. The superthin results thus can fit the data if growth ends at different R in different systems, reflecting either a distribution in effective s, or if an external an external process is responsible for ending growth. Similar considerations may also apply to the isotropic case, but the disagreement between the isotropic accretion growth model and the extrasolar debris disks results is marginal.

Chapter 6

Summary

6.1 The Road Behind Us

The ultimate goal of this work has been to connect what we know about the Kuiper belt to what we know of extrasolar debris disks. Around roughly one in six stars of comparable age and mass to the Sun, bright debris disks have been detected. This disks are $\sim 10^3 \times$ brighter than our own debris disk, the Kuiper Belt. How the Sun fits into the full range of sun-like stars will not be known until more sensitive instruments can detect the full range of debris disks that exist in nature. In the interim, it is interesting to ask: "What sets these bright debris disks apart from the Sun?"

To this end, we have investigated the size number distribution of planetesimals in extrasolar debris disks (chapter 1). Using a sample of observed extrasolar debris disks, we constructed a pseudo-evolution sequence of the disks, which we fit to an analytic model. Using the model, we we able to infer some parameters of the large ($10 \sim 100$ km) planetesimals that are the parents of the dusty debris. We found that extrasolar debris disks have surface densities in $10 \sim 100$ km bodies comparable to the Minimum Mass Solar Nebula, with roughly equal mass per size decade.

The brightest extrasolar debris disks have $\sim 10^3$ times the mass of the Kuiper belt.

That the most massive extrasolar debris disks have masses comparable to that of the Minimum Mass Solar Nebula may seem like a natural situation, but planetesimal growth models have predicted that the efficiency of growing the large planetesimals needed is very low, $\sim 10^{-3}$. In those models, Minimum Mass Solar Nebula disks produce Kuiper belts, and it is not possible to produce disks with $\sim 10^3 \times$ the mass of the Kuiper belt. We constructed a code to simulate the growth of planetesimals (chapter 3). We used that code to confirm the previous result that growth in inefficient.

The standard model begins with all the mass in kilometer size objects. We propose a new model, where most of the mass begins in centimeter sized grains. In this model, collisional cooling reduces encounter velocities to sub-Hill velocities, and accretion takes on a different form. Rather than the runaway accretion that sees a few bodies grow rapidly and dynamically heat all the small bodies before very many can grow, our model produces orderly growth at high speeds, and many bodies grow. This produces a high efficiency. This high efficiency model can produce the Cold Classical Kuiper Belt from $\sim 10^{-1} M_\oplus$ in its current position, eliminating the conflict between the amount of primordial mass needed to form it and models of Neptune's migration, and conflict between the amount of primordial mass needed to form the CCKB and the observed survival of binary KBOs. We also show that the same model can produce the parent planetesimal population needed to explain our results on extrasolar debris disks, from Minimum Mass Solar Nebula-like starting conditions.

6.2 The Road Ahead

We have shown that the current model of planetesimal growth, which begins with most of the solid mass in kilometer sized bodies, is untenable in light of the observed properties of extrasolar debris disks. We have proposed a new model of planetesimal growth, where most of the mass begins in centimeter sized grains, with a seed population of kilometer

sized bodies, and show that this model can produce debris disks in rough agreement with both the solar system's Kuiper Belt, and extrasolar debris disks.

This model would benefit from several improvements. The neglect of gas physics is reasonable in the collisionally undamped case, as kilometer and larger bodies are not strongly affected by gas, and gas clears out quickly relative to the $10^7 \sim 10^8$ years it takes to form the large bodies. In the collisionallay damped case, centimeter grains would be strongly affected by gas, and the timescale of 10^6 years means gas should be present during the whole evolution. Gas is a particularly pernicious theoretical problem, as the gas disk provides itself pressure support, and rotates more slowly than the circular Keplerian velocity. Dust grains of centimeter sizes are too large to be completely coupled to the gas, but too small to ignore the gas drag from the gas disk, thus their orbits quickly decay is a smooth disk (Weidenschilling, 1977a). This migration may be mitigated if the centimeter grains rain out to the midplane layer (Brauer et al., 2007), or collect in local pressure maxima (Whipple, 1972; Klahr & Henning, 1997). The grains may also be continuously produced by collisional destruction of larger bodies (Dullemond & Dominik, 2005), or by the growth of smaller grains (Alexander & Armitage, 2007). Whether such mechanisms can retain the centimeter grains for the $10^6 \sim 10^7$ years necessary for planetesimal growth remains the subject of investigation (Brauer et al., 2007; Pinilla et al., 2012). Despite the theoretical misgivings, the observational evidence suggests that the bulk of the grain mass can be found in millimeter or centimeter sized grains in protoplanetary disks at a few million years of age, which has been interpreted to mean that the small grains must persist for millions of years, despite the prediction they should quickly migrate inwards (Natta & Testi, 2004; Rodmann et al., 2006; Natta et al., 2007). Thus, although we cannot properly account for the influence of a massive gas disk (which may cause dust migration, create spatial inhomogeneities, provide turbulent stirring, etc.), the existence of a massive disk of centimeter sized particles which persists for $10^6 \sim 10^7$ years should be regarded as not only plausible, but a feature of the model which increases its congruence

150

with observations of disks with growing planetesimals. Our inability to explain how they persist must be taken to mean that we lack a crucial piece of physics governing the dynamics of the centimeter sized grains. As such, this model must be regarded as preliminary.

The issue of when large bodies become superthin remains outstanding. The significance of this effect is minimal for the collisionless case, but it is not negligible for the collisional case, and a proper treatment must correctly account for this phenomenon. A basic treatment might be attempted by tracking an i for our m, e bins, as full m, e, i tracking is computationally prohibitive. Superthinning is predicted based on the two groups treatment, which is not always applicable to full size distributions, thus a solution must be derived for a general case. Previous works (e.g., Ida & Makino, 1992; Rafikov, 2003) have considered conditions appropriate to the collisionless case, so the problem is one of interest in its own right for the collisional case.

Improved dust physics is also highly desirable. In the collisional evolution case, shadowing should prevent removal of small grains by radiation pressure, and significantly reduce the effectiveness of Poynting-Robertson drag. At early times in the simulation, centimeter size grains collide every 10^3 years and dissipate $\lesssim 10^{-4}$ of their energy, and the assumption of constant semimajor axis is reasonable. At late times μm grains collide every $\sim 10^{-1}$ years and dissipate $\sim 10^{-3}$ of their total energy - energy loss is probably important.

Binary Kuiper Belt Objects are providing strong constraints on the region's evolution, and our code is unable to address binaries at all. Binary formation, destruction, and evolution would allow us to make much stronger statements about the properties this model predicts for binary objects. This includes both long period binaries formed by dynamical processes, but also short period binaries formed in giant impacts (e.g., Canup, 2005).

If the kilometer plus centimeter model applies to debris disk formation, it should also

apply to the growth of planetesimals in the case where planets successfully form. The core accretion model of giant planet formation has difficulties producing the necessary cores before dissipation of the gas disk (Kobayashi et al., 2011), and the kilometer plus centimeter case should form the needed $\sim 10M_\oplus$ cores much faster than the kilometer case. However, the model has not been shown to work in the presence of gas, which must be addressed going forward. The shorter formation times and higher formation efficiencies may also explain the presence of planets at large distances from their host stars (Marois et al., 2008; Kalas et al., 2008), which are difficult to produce in the standard conglomeration case (Goldreich et al., 2004a).

The solar system provides the best data for comparison. We chose to model the formation of the Cold Classical Kuiper Belt because it is the cleanest of the small body populations - it has a more certain dynamical history. However, other small body populations in the Asteroids, Jupiter Trojans, and Neptune Trojans all show similar trends to the CCKB - a steep sloper ($q > 4$) at large sizes, then a turnover to a shallow $q < 4$ slope at an intermediate size $10 - 100$ km (Jewitt et al., 2000; Jedicke et al., 2002; Sheppard & Trujillo, 2010). As with the CCKB, the belief had been that the turnover was the result of collisional evolution. That story has been challenged (Bottke et al., 2005; Morbidelli et al., 2009), and must be revisited in light of this new model. In these cases, however, interactions with the giant planets probably cannot be ignored.

The model we propose explains naturally how bright debris disks form. To form the Kuiper Belt, we appeal to a variant of the popular model where Neptune's outward migration sets many of the properties of the Kuiper Belt region. The remaining $\sim 85\%$ of debris disks remain unexplained. An explanation may lie in a generalised version of the story we tell about the solar system. With a model that can produce the bright disks, asking "Why are there so many dim disks?" is the next logical step.

Chapter 7

Appendix

7.1 Evolution of Debris Disk Properties: Analytical Model

In the following, we present a simple analytical model that describes the time evolution of dust luminosity and size distribution in debris disks. This model is very similar to that described in Löhne et al. (2008), except for our choice for the size of the largest planetesimals. In the following, we present results with arbitrary strength law and initial size distribution, followed by numerical evaluations using the hard strength law and for $q_3 = 4$.

We approximate the body strength (eq. 2.5) by two broken power-laws,

$$
\bar{Q}_D = \begin{cases} A \left(\frac{s}{1\text{cm}} \right)^{\alpha} & s < s_1 \\ B\rho \left(\frac{s}{1\text{cm}} \right)^{\beta} & s > s_1 \end{cases} \tag{7.1}
$$

where s_1 is the size at which the two expressions meet. The body strength is dominated by material strength below s_1 and by self-gravity above s_1. For the hard strength law that we adopt, $\alpha = -0.3, \beta = 1.5$ and $s_1 = \left(\frac{B}{A}\rho \right)^{\frac{1}{\alpha-\beta}}$ cm ≈ 300 meters.

Combined with equation 2.4, the minimum size of an impactor that causes catas-

trophic disruption is

$$
s_{\text{impactor}} = \begin{cases} \left(\frac{2A}{1.75e^2 v_{\text{kep}}^2}\right)^{\frac{1}{3}} \left(\frac{s}{1 \text{ cm}}\right)^{1+\frac{\alpha}{3}} = k_1 s^{\kappa_1} & s < s_1 \\[2ex] \left(\frac{2B\rho}{1.75e^2 v_{\text{kep}}^2}\right)^{\frac{1}{3}} \left(\frac{s}{1 \text{ cm}}\right)^{1+\frac{\beta}{3}} = k_2 s^{\kappa_2} & s > s_1 \end{cases}
\tag{7.2}
$$

Here, $\kappa_1 = 0.9$ and $\kappa_2 = 1.5$ for our adopted strength law.

We define a break-size, $s_2 = s_2(t)$, to be the size at which the time-integrated chance of destruction per body is unity, or the optical depth for size s_2 to be hit is,

$$
\tau(s_2) = \frac{t_{\text{orb}}}{t}.
\tag{7.3}
$$

Bodies larger than s_2 have hardly collided and they retain their primordial size distribution, while bodies smaller than s_2 have collided many times, and they satisfy the size distribution for collisional equilibrium. If $s_2 > s_1$, we adopt a size distribution that is piece-wise continuous,

$$
\frac{dn}{ds} = \begin{cases} n_1 s^{-q_1} = n_3 s_1^{q_1-q_2} s_2^{q_2-q_3} s^{-q_1} & s < s_1 \\[2ex] n_2 s^{-q_2} = n_3 s_2^{q_2-q_3} s^{-q_2} & s_1 < s < s_2 \\[2ex] n_3 s^{-q_3} & s > s_2 \end{cases}
\tag{7.4}
$$

where q_1 and q_2 are the power indexes at collisional equilibrium.[1] They are 3.5 (Dohnanyi, 1969) if the size ratio between the impactor and the target is constant. Given equation 2.6, we have $q_1 = 3.6$ and $q_2 = 3.0$ for the hard strength law. This piece-wise size distribution breaks down near the blow-out size due to an abrupt deficit of small bullets. A more accurate derivation for the size distribution can be obtained by assuming that the mass loss rate is constant with size, as is carried out in Strubbe & Chiang (2006). The size distribution shows a flare-up toward the blow-out size, and the magnitude of the flare-up depends on, among other things, the value of eccentricity. Our analytical results obtained based on equation 7.4 should be regarded as illustrative.

---

[1] Numerical simulations (Thébault et al., 2003; Krivov et al., 2006; Thébault & Augereau, 2007) indicate that the collisional distribution is likely wavy and deviates from a simple power-law, due to the steep fall-off in particle number below the blow-out size. We ignore this complication in the analysis here. But it is included in our numerical results.

We first obtain the evolution of s_2 with time. When $s_2 < s_1$, i.e., collisions involve only bodies bound by the material strength, optical depth for destruction at s_2 is determined by integrating over all its possible bullets,

$$\tau(s_2) = \frac{n_3 s_2^{q_1-q_3}}{2\pi a \Delta a} \int_{k_1 s_2^{\kappa_1}}^{s_2} \pi \left(s_2 + s\right)^2 s^{-q_1} ds = \frac{n_3}{2a\Delta a} \frac{1}{q_1 - 1} k_1^{1-q_1} s_2^{q_1-q_3+2+\kappa_1-\kappa_1 q_1}. \quad (7.5)$$

Substituting this into the definition for s_2 (eq. 7.3), we obtain

$$s_2 \propto t^{\frac{1}{-q_1+q_3-2-\kappa_1+\kappa_1 q_1}} \quad (7.6)$$

This yields $s_2 \propto t^{1.4}$ for our parameters.

Once $s_2 > s_1$, we perform the same exercise and obtain,

$$s_2 \propto t^{\frac{1}{-q_2+q_3-2-\kappa_2+\kappa_2 q_2}} \quad (7.7)$$

or $s_2 \propto t^{0.5}$ for our parameters. So at early times, the break size rises steeply with time, due to an abundance of small bullets; while at late times, the break size rises with time more gradually due to the relative paucity of bullets. These two scaling relations are observed in our numerical results (Figure 2.2).

Now we proceed to derive the scaling of disk luminosity with system age. We let the infrared luminosity to be that portion of the starlight that is intercepted by debris particles. This is directly related to the total surface area of all particles, which is mostly contributed by particles around $s_{\min}$.[2] The fractional luminosity is therefore,

$$\frac{L_{\mathrm{IR}}}{L_*} \approx \frac{\int_{s_{\min}}^{s_2} \pi s^2 n_1 s^{-q_1} ds}{4\pi a^2} \approx \begin{cases} \frac{n_3}{4a^2(q_1-3)} s_2^{q_1-q_3} s_{\min}^{3-q_1} & s_2 < s_1 \\ \frac{n_3}{4a^2(q_1-3)} s_1^{q_1-q_2} s_2^{q_2-q_3} s_{\min}^{3-q_1} & s_2 > s_1 \end{cases} \quad (7.8)$$

So the evolution of luminosity is dictated by the evolution of s_2 with time. In particular, at late times (when $s_2 > s_1$), the fractional luminosity decays with time gradually,

$$\frac{L_{\mathrm{IR}}}{L_*} \propto s_2^{q_2-q_3} \propto t^{\frac{q_2-q_3}{q_2-q_3+2+\kappa_2-\kappa_2 q_2}}. \quad (7.9)$$

---

[2] The upper bound of the integration is chosen to be s_2 but it is of no importance.

Again, for our set of parameters, $L_{IR}/L_* \propto t^{-0.5}$. When q_3 takes different values, $L_{IR}/L_* \propto t^{(q_3-3)/(2-q_3)}$ and scales as $t^{-1/3}, t^{-1/2}$ and $t^{-2/3}$ for $q_3 = 3.5, 4$, and 5 respectively.[3] This forms the basis on which we decipher the primordial distribution of planetesimals.

To understand the dependence of the fractional luminosity on a range of parameters, we return to equations 7.8, 7.7 and 7.5, retaining all the neglected constants and obtaining the following expression,

$$\frac{L_{IR}}{L_*} \approx \begin{cases} \frac{n_3}{4a^2(q_1-3)} \left[\frac{2a\Delta a}{n_3} (q_1-1) \frac{t_{orb}}{t} \left(\frac{2A}{1.75e^2 v_{kep}^2} \right)^{\frac{1}{3}(q_1-1)} \right]^{\frac{q_1-q_3}{2+\kappa_1-\kappa_1 q_1+q_1-q_3}} s_{min}^{3-q_1} & s_2 < s_1 \\ \frac{n_3}{4a^2(q_1-3)} s_1^{q_1-q_2} \left[\frac{2a\Delta a}{n_3} (q_2-1) \frac{t_{orb}}{t} \left(\frac{2B\rho}{1.75e^2 v_{kep}^2} \right)^{\frac{1}{3}(q_2-1)} \right]^{\frac{q_2-q_3}{2+q_2-q_3+\kappa_2-\kappa_2 q_2}} s_{min}^{3-q_1} & s_2 > s_1 \end{cases}$$
(7.10)

Substituting our nominal values for the indexes ($\kappa_1 = 0.9$, $\kappa_2 = 1.5$, $q_1 = 3.6$, $q_2 = 3.0$, $q_3 = 4.0$), we simplify the dependency for luminosity into (for at late times when $s_2 > s_1$),

$$\frac{L_{IR}}{L_*} \propto t^{-0.5} M_0^{0.5} a^{-3.6} \left(\frac{\Delta a}{a} \right)^{0.5} e^{-\frac{2}{3}} M_*^{\frac{5}{6}} B^{\frac{1}{3}} A^{-\frac{5}{6}} s_{min}^{-0.6},$$
(7.11)

where M_0 is the total mass of the disk, a its radius, $\Delta a/a$ its fractional width, e the eccentricity of particles, M_* the central stellar mass, s_{min} the blow-out size, and A, B the strengths. This relation illuminates how our procedure, using luminosity to infer M_0, can be affected by various parameters. For example, the actual position of the belt is a piece of essential information, while other values should be known roughly to within a factor of a few to avoid gross mis-estimate.

Equation 7.10 can also be used to illustrate the effect of a time-varying eccentricity on our estimate for q_3. At a given dust luminosity, the inferred initial mass scales with the system age and the eccentricity as

$$M_0 \propto t^{q_3-3} e^{\frac{4}{3}(q_3-3)}.$$
(7.12)

---

[3] Note that in the case of $q_3 = 3$, the luminosity decreases with time logarithmically. For algebraic simplicity, we exclude this case from the following discussion.

We now consider the effect of a time-varying e. Let the plantesimals be stirred with a time-dependence of $e \propto t^\gamma$. We define a $\bar{q}_3$ as the value of q_3 one obtains by taking a constant eccentricity (in which case $M_0 \propto t^{\bar{q}_3 - 3}$). The true q_3 is related to it as

$$q_3 = 3 + (\bar{q}_3 - 3)\left(1 + \frac{4}{3}\gamma\right)^{-1}. \tag{7.13}$$

So for $\gamma = 1/4$, $\bar{q}_3 = 4$, we get the true $q_3 = 3.75$.

Numerically we find a weaker dependency on γ. This is related to the afore-mentioned flare-up near the blow-out size. If instead of equation 7.4, we make the simplifying assumption that the mass loss rate is the same at blow-out size as at other sizes, but that the micron grains are destroyed by similar grains (as opposed to smaller ones), we find that the dust luminosity is proportional to the total number of blow-out grains, while the mass loss rate is proportional to the square of this number. As a result, we write

$$\frac{L_{IR}}{L_*} \propto \dot{M}^{1/2}. \tag{7.14}$$

From this, we derive the dependence of dust luminosity on time and on eccentricity that are slightly different from those presented in equations 7.9, 7.11, 7.12 and 7.13. For instance, in contrast to equation 7.13, the dependence of q_3 on γ is logarithmic.

7.2 The Insignificance of Assuming Superthinness or Not in the Collisionless Case

In chapter 3, we assume that large bodies accrete have inclinations that are comparable to their eccentricities. It is known that in some limits, this is untrue for large bodies with subhill velocities dispersions. In that case, it may be more accurate to assume $i \approx 0°$ Ida & Makino (1992); Rafikov (2003). To test the significant of this, we modify our code to use the $i = 0$ cross section for large bodies if they meet two conditions:

- Their velocity dispersions are less than the hill velocity of the size of body which provides the most viscous stirring

- Their velocity dispersions are less than their own hill velocities

Encounters which meet these two conditions are treated as superthin, rather than thin. We perform two simulations using the standard parameters for our simulation in chapter 3. Each simulation begins with a disk of 10^{13} bodies with radius $s = 1$ km, density $\rho = 1.5$ g cm^{-3}, at semimajor axis $a = 45$ AU, with a semimajor axis spread $\Delta a = 6$ AU, and starting eccentricity $e_0 = 10^{-7}$. The results are plotted in figure 7.1. The two simulations are nearly identical.

Why are the results so similar? The enhancement in collisional cross section is $\frac{v_{\mathrm{H}}}{v}$, which can be as much as 10^2, but is often much less. With a surface density in large bodies of $10^{-3} \sim 10^{-4}$, accretion of other large bodies is still insignificant when enhanced by a typical factor of ~ 10 (compare to figure 3.12).

7.3 Two Groups From One?

We assume a two starting size condition. To justify this, we suggest that the efficiency for planetesimal formation may be low. Of course, our understanding of planetesimal formation is limited, and this assumption may not hold. As a possible alternative, we consider whether two populations could arise from a single population.

Previous work on the growth of planetesimals finds the growth is highly inefficient. Most of the mass remains in the starting size bodies. Once large bodies are produced, the starting size bodies break down. If the conditions during breakdown are favourable, this might produce small grains which collisionally cool.

As a test case, we begin with meter sized bodies. To facilitate collisional cooling of products, bodies that undergo catastrophic disruption are broken into two equal mass pieces, rather than a full size distribution. Otherwise, the initial conditions are the same as other simulations presented here, $10 M_\oplus$ between 42 and 48 AU, with $e = 10^{-6}$.

Early time growth proceeds similarly to the collisionless case, as described in chapter
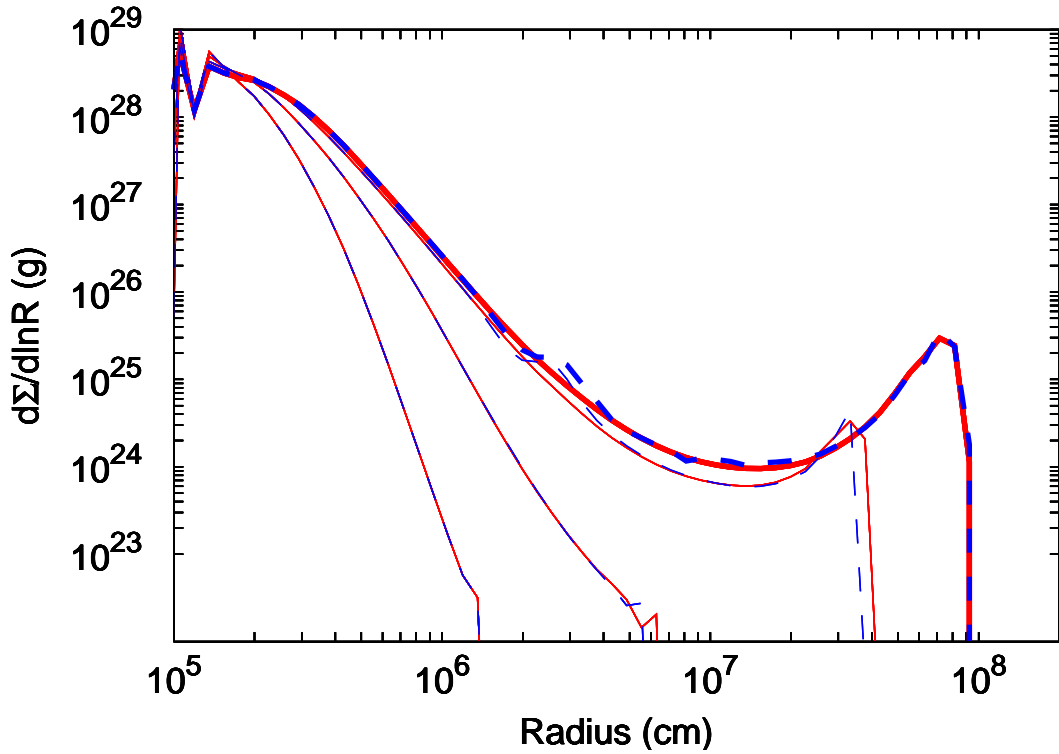
Figure 7.1: Comparison of two simulations with begin with $10 M_{\oplus}$ in kilometer sized bodies, with $a = 45$ AU, $\Delta a = 6$ AU, and initial eccentricity $e_0 = 10^{-7}$. We plot the size mass distributions at 5, 10, 15 Myrs (thin lines), and 20 Myrs (thick lines). Two cases are plotted. In the first, we assume that large bodies maintain isotropic velocity dispersions (solid red lines), in the second we assume that large bodies have $i \approx 0°$ when $v < v_{\mathrm{H}}$. The mass evolution is not significantly impacted by this choice. The lines may be difficult to distinguish because they lie atop one another.

3. Once the largest bodies are $\sim 10^3$ km in size, viscous stirring is sufficient to heat the primordial $\sim$ m bodies such that their collisions become erosive. The size of small bodies decreases, and their collisional cooling increases. The growth of the large bodies increases. When the largest body is 1000 km, $\sim 0.25\%$ of the total mass is in bodies > 10 km. By the time the largest body is 3000 km, $\sim 2.5\%$ of the total mass is in bodies > 10 km. This fraction continues to rise as R increases, until the small bodies are lost.

This mechanism is difficult to apply to the solar system small body populations, or extrasolar debris disks, however. The growth all occurs at the largest sizes - intermediate sized bodies were dynamically heated during the collisionless phase, and remain hot throughout the subsequent evolution. All of the growth subsequent to the onset of collisional breakdown occurs at the largest sizes ($\gtrsim 10^3$ km) (figure 7.2).
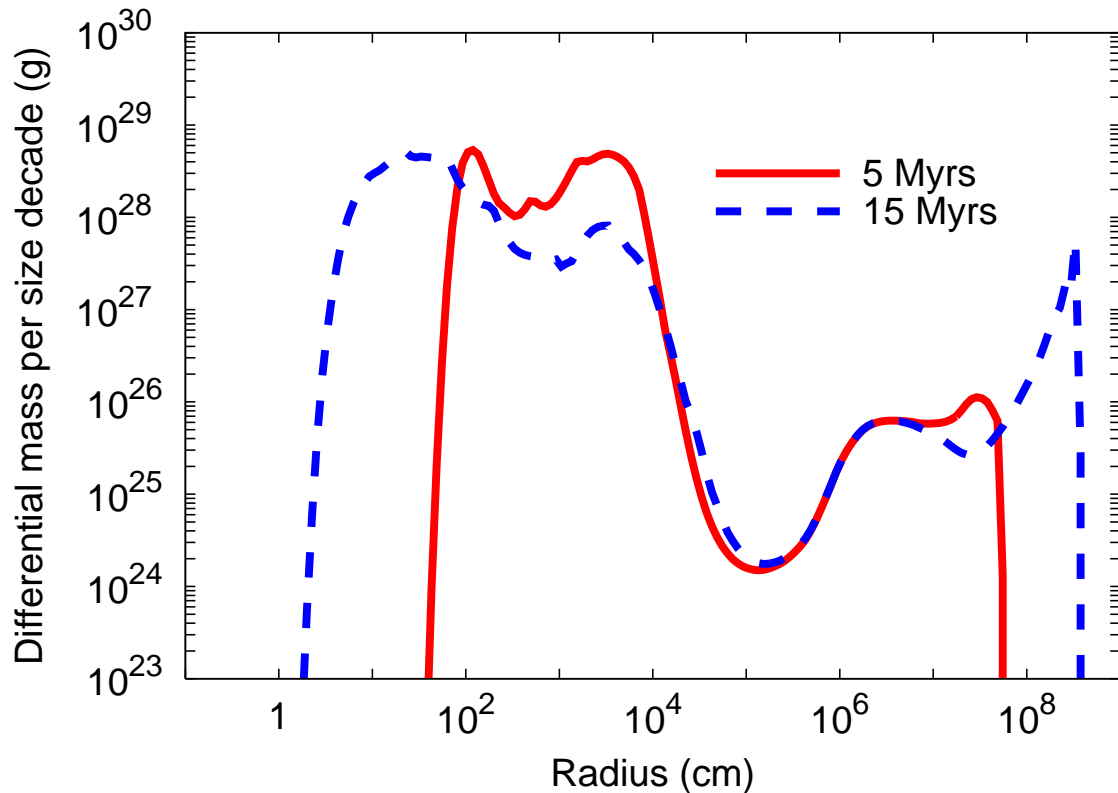

Figure 7.2: Differential mass per size decade for a simulation which begins with only meter sized bodies. Growth proceeds similar to collisionless simulations, until the largest body is ~ 1000 km, and the primordial meter sized bodies begin to breakdown. This onsets at about 5 myrs, the solid red line distribution. After 15 myrs (dashed blue line), the mass fraction in 10+ km bodies has increased from $\sim 10^{-3}$ to $\sim 10^{-2}$. But the growth is concentrated at the largest sizes. High surface densities at 10-100 km cannot be created this way.

The onset of the collisional cascade is set by the material strength of the meter sized boulders. If they were much softer, the cascade would onset earlier, and high surface densities at ~ 1 km could be obtained. With $q \sim 4$ in the collisionless case, $u \propto R^{\frac{3}{4}}$. Catastrophic disruption requires $u^2 \propto Q^*$. Thus to obtain the onset of the cascade when $R \sim 1$ km, Q^* must be reduced by $10^4 \times \sim 10^5 \times$. Such a soft strength law cannot extend to very small sizes, or dust grains will be lost before growth occurs. Similarly, it cannot extend to large sizes, or debris disk evolution will not fit the observed patterns[4] Very judicious choice of Q^* may allow for the recreation of kilometer plus centimeter conditions, but must be regarded as highly contrived.

7.4 Alternate Derivation of the Isotropic Solution to the Collisional Case

The small grains no longer obey equation 5.11. Rather than superhill stirring, they are stirred in the subhill regime, and they obey:

$$v_{\text{cm}} \sim \frac{\Sigma_{R_{\max}}}{\Sigma_{\text{cm}}} \frac{R_{\text{cm}}}{R_{\max}} \alpha^{-2} v_{\text{H,max}} \tag{7.15}$$

We observed this relation obeyed in our simulation when the largest body is $\sim 10^6 \sim 10^8$ cm. The largest bodies are cooled by dynamical friction from the small grains. The smallest large bodies for which this is possible are small enough that the small grains are superhill to them. Consequently, the subhill stirring by the largest body is balanced against the superhill cooling by the small grains, and the large bodies remain cold as long as they obey

$$R_{\text{cold}} \gtrsim \left(\frac{\Sigma_{\max}}{\Sigma_{\text{cm}}} \right)^{\frac{4}{3}} \alpha^{-2} R_{\text{cm}} \tag{7.16}$$

---

[4]With the reduced strength law, 1000 km bodies are catastrophically disrupted by 10 km objects. For the massive debris disks with MMSN-eque surface densities, their primordial collision time is $\sim 10^6$ years. With the largest bodies in collision equilibrium, the luminosity drops off linearly in time, with a 1 Myrs timescale (Wyatt et al., 2007b). Bright disks at late times would be impossible.

The cold bodies growing at superhill accretion rates grow very slowly compared to the largest bodies. Instead, what matters is which bodies grow at subhill rates. These bodies grow together uniformly. They obey

$$R_1 \geq \frac{\Sigma_{R_{\max}}}{\Sigma_{cm}} \alpha^{-2} R_{cm} \tag{7.17}$$

Bodies then stop growing once they are smaller than $R_1 \propto R_{\max}^{\gamma}$ will fall out of the growing population with a shallower (more top heavy) size number distribution than that of the growing bodies. Consider that $R_{\max}$ grows to $(1+\epsilon) R_{\max}$, then $(1+\epsilon)^2 R_{\max}$, and so on. During the nth such growth, bodies that were originally between $(1+\epsilon)^{n-1} R_1$ and $(1+\epsilon)^n R_1$ are deposited between $(1+\epsilon)^{\gamma(n-1)} R_1$ and $(1+\epsilon)^{\gamma n} R_1$. Here R_1 denotes the smallest size of body that was cold at $n=0$. The bodies grow in a uniform way, so the size distribution is preserved with respect to their original size. Thus the number of bodies deposited is

$$\Delta n = \frac{n_0}{1-q} R^{1-q} \Big|_{(1+\epsilon)^{n-1} R_1}^{(1+\epsilon)^n R_1} \tag{7.18}$$

These bodies are deposited over a size range

$$\Delta s = \left((1+\epsilon)^{\gamma n} - (1+\epsilon)^{\gamma(n-1)} \right) R_1 \tag{7.19}$$

Substitute in $s = \sqrt{(1+\epsilon)^{\gamma n} (1+\epsilon)^{\gamma(n-1)}} R_1$ (or rather, $(1+\epsilon)^n = s^{\frac{1}{\gamma}} R_1^{-\frac{1}{\gamma}} \sqrt{1+\epsilon}$), and solve for the new size number distribution:

$$\frac{dn}{ds} = \frac{\frac{n_0}{1-q} \left(1 - (1+\epsilon^{-1})\right)^{1-q} R_1^{(1-q)\left(1-\gamma^{-1}\right)}}{(1+\epsilon)^{\frac{\gamma}{2}} - (1+\epsilon)^{-\frac{\gamma}{2}}} s^{\frac{1-q}{\gamma}-1} \tag{7.20}$$

And thus an original size distribution with power law index q_0 is transformed to a power law index of

$$q = (q_0 + \gamma - 1)\gamma^{-1} \tag{7.21}$$

We can combine this result with equation 7.17. If $q < 4$, $\Sigma_{R_{\max}} \propto R_{\max}^{4-q}$, in which case equation 7.16 gives $\gamma = 4 - q$. This has a scale-free equilibrium, $q_0 = q$, which allows us to solve equation 7.21 to get $q = 3$. We observe $q \sim 3$ in simulations at the subhill growth

162

sizes (figure 7.3). If we imagine instead that equation 7.16 applies at the minimum size that grows, we instead get $q = \frac{13}{4}$. So the uncertainty here is small.
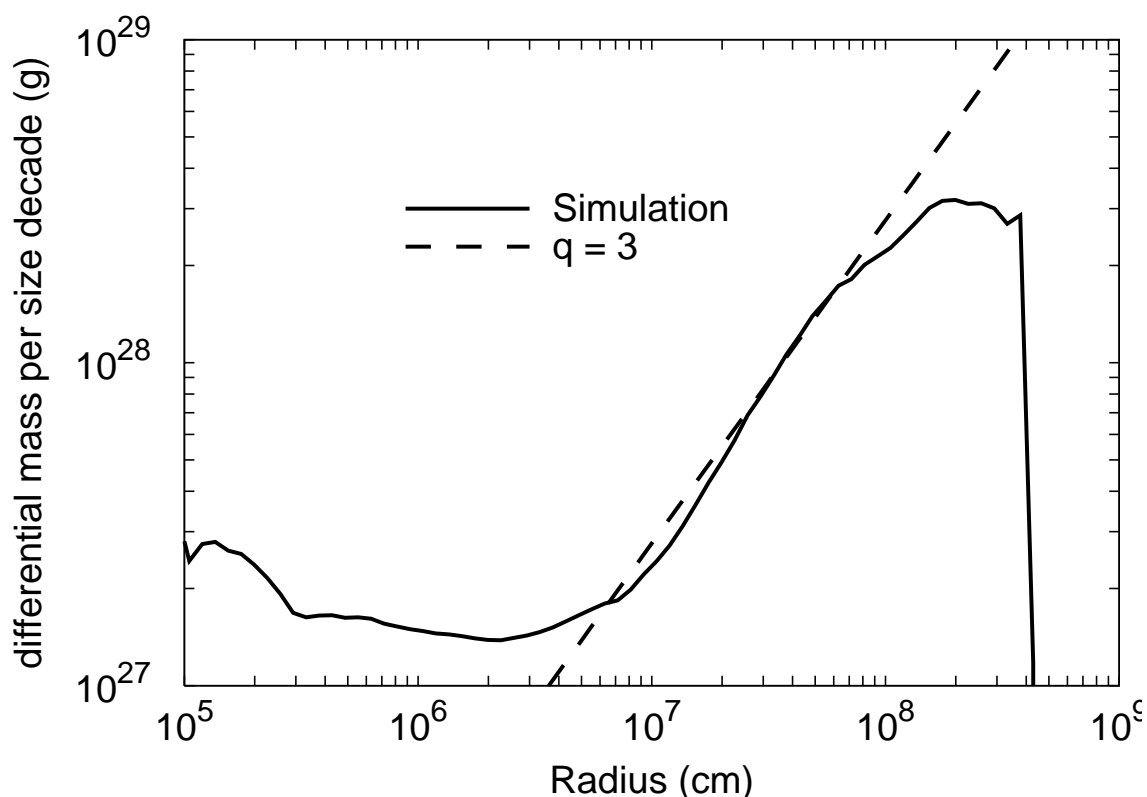

Figure 7.3: Differential size mass distribution of the "km + cm" case after 10 Myrs. Growth has essentially finished, as the small grains have been removed by radiation pressure. Bodies in the ~ 30 km to ~ 2000 km size range obey a power law size number law with index $q \sim 3$, the scale free solution to equation 7.21.

This argument may be more simply qualified as such: In the subhill case, equation 7.15 gives $v_{cm} \propto \Sigma_{R_{max}} \propto R_{max}^{4-q}$. Then the smallest body which accretes cm grains at subhill velocities has a size $R_d \propto R_{max}^{4-q}$. Bodies smaller than this drop out of the growing population. If $q > 3$, then R_d approaches R_{max} as R_{max} increases. The bodies which were just larger than R_d transition to being just smaller than R_d, and stop growing. With the loss of small bodies between R_d and R_{max}, the size number distribution decreases (i.e.,

q decreases). This continues until $q = 3$, at which point $R_d \propto R_{\mathrm{max}}$, and the bodies grow together in equilibrium.

Bibliography

Adachi, I., Hayashi, C., & Nakazawa, K. 1976, Progress of Theoretical Physics, 56, 1756

Alexander, R. D. & Armitage, P. J. 2007, MNRAS, 375, 500

Andrews, S. M. & Williams, J. P. 2005, ApJ, 631, 1134

Artymowicz, P. & Clampin, M. 1997, ApJ, 490, 863

Aumann, H. H., Beichman, C. A., Gillett, F. C., de Jong, T., Houck, J. R., Low, F. J.,
 Neugebauer, G., Walker, R. G., & Wesselius, P. R. 1984, ApJL, 278, L23

Barucci, M. A., Boehnhardt, H., Cruikshank, D. P., & Morbidelli, A. The Solar System
 Beyond Neptune: Overview and Perspectives, ed. Barucci, M. A., Boehnhardt, H.,
 Cruikshank, D. P., Morbidelli, A., & Dotson, R., 3–10

Batygin, K., Brown, M. E., & Fraser, W. C. 2011, ApJ, 738, 13

Benz, W. & Asphaug, E. 1999, Icarus, 142, 5

Bernstein, G. M., Trilling, D. E., Allen, R. L., Brown, M. E., Holman, M., & Malhotra,
 R. 2004, AJ, 128, 1364

Bianco, F. B., Zhang, Z., Lehner, M. J., Mondal, S., King, S., Giammarco, J., Holman,
 M. J., Coehlo, N. K., Wang, J., Alcock, C., Axelrod, T., Byun, Y., Chen, W. P., Cook,
 K. H., Dave, R., de Pater, I., Kim, D., Lee, T., Lin, H., Lissauer, J. J., Marshall, S. L.,
 Protopapas, P., Rice, J. A., Schwamb, M. E., Wang, S., & Wen, C. 2010, AJ, 139, 1499

Binney, J. & Tremaine, S. 1987, Galactic dynamics (Princeton, NJ, Princeton University Press, 1987, 747 p.)

Blum, J. 2010, Research in Astronomy and Astrophysics, 10, 1199

Booth, M., Wyatt, M. C., Morbidelli, A., Moro-Martín, A., & Levison, H. F. 2009, MNRAS, 399, 385

Bottke, W. F., Durda, D. D., Nesvorný, D., Jedicke, R., Morbidelli, A., Vokrouhlický, D., & Levison, H. 2005, Icarus, 175, 111

Brauer, F., Dullemond, C. P., & Henning, T. 2008, A&A, 480, 859

Brauer, F., Dullemond, C. P., Johansen, A., Henning, T., Klahr, H., & Natta, A. 2007, A&A, 469, 1169

Bromley, B. C. & Kenyon, S. J. 2006, AJ, 131, 2737

Brown, M. E. 2001, AJ, 121, 2804

—. The Largest Kuiper Belt Objects, ed. Barucci, M. A., Boehnhardt, H., Cruikshank, D. P., Morbidelli, A., & Dotson, R., 335–344

Brown, M. E., Burgasser, A. J., & Fraser, W. C. 2011a, ApJL, 738, L26

Brown, M. E., Schaller, E. L., & Fraser, W. C. 2011b, ApJL, 739, L60

Brown, M. E., Schaller, E. L., Roe, H. G., Rabinowitz, D. L., & Trujillo, C. A. 2006, ApJL, 643, L61

Brown, M. E., Trujillo, C., & Rabinowitz, D. 2004, ApJ, 617, 645

Brucker, M. J., Grundy, W. M., Stansberry, J. A., Spencer, J. R., Sheppard, S. S., Chiang, E. I., & Buie, M. W. 2009, Icarus, 201, 284

Bryden, G., Beichman, C. A., Trilling, D. E., Rieke, G. H., Holmes, E. K., Lawler, S. M., Stapelfeldt, K. R., Werner, M. W., Gautier, T. N., Blaylock, M., Gordon, K. D., Stansberry, J. A., & Su, K. Y. L. 2006, ApJ, 636, 1098

Burns, J. A., Lamy, P. L., & Soter, S. 1979, Icarus, 40, 1

Canup, R. M. 2005, Science, 307, 546

Carpenter, J. M., Bouwman, J., Mamajek, E. E., Meyer, M. R., Hillenbrand, L. A., Backman, D. E., Henning, T., Hines, D. C., Hollenbach, D., Kim, J. S., Moro-Martin, A., Pascucci, I., Silverstone, M. D., Stauffer, J. R., & Wolf, S. 2009, ApJS, 181, 197

Carry, B., Hestroffer, D., DeMeo, F. E., Thirouin, A., Berthier, J., Lacerda, P., Sicardy, B., Doressoundiram, A., Dumas, C., Farrelly, D., & Müller, T. G. 2011, A&A, 534, A115

Chambers, J. E. 2001, Icarus, 152, 205

Chambers, J. E. & Wetherill, G. W. 1998, Icarus, 136, 304

Chandrasekhar, S. 1943, ApJ, 97, 255

Charnoz, S. & Morbidelli, A. 2006, in AAS/Division for Planetary Sciences Meeting Abstracts, 34.04–+

Charnoz, S. & Morbidelli, A. 2007, Icarus, 188, 468

Collins, B. F. & Sari, R. 2006, AJ, 132, 1316

Collins, B. F., Schlichting, H. E., & Sari, R. 2007, AJ, 133, 2389

Currie, T., Kenyon, S. J., Balog, Z., Rieke, G., Bragg, A., & Bromley, B. 2008, ApJ, 672, 558

Cuzzi, J. N., Hogan, R. C., & Shariff, K. 2008, ApJ, 687, 1432

167

Davis, D. R. & Farinella, P. 1997, Icarus, 125, 50

Delsanti, A., Hainaut, O., Jourdeuil, E., Meech, K. J., Boehnhardt, H., & Barrera, L. 2004, A&A, 417, 1145

Dent, W. R. F., Walker, H. J., Holland, W. S., & Greaves, J. S. 2000, MNRAS, 314, 702

Desch, S. J. 2007, ApJ, 671, 878

Dohnanyi, J. W. 1969, J. Geophys. Res., 74, 2531

Dominik, C., Blum, J., Cuzzi, J. N., & Wurm, G. 2007, in Protostars and Planets V, ed. B. Reipurth, D. Jewitt, & K. Keil, 783–800

Dominik, C. & Decin, G. 2003, ApJ, 598, 626

Dones, L. 1997, in Astronomical Society of the Pacific Conference Series, Vol. 122, From Stardust to Planetesimals, ed. Y. J. Pendleton, 347–+

Dones, L. & Tremaine, S. 1993, Icarus, 103, 67

Donnison, J. R. 2006, Planet. Space. Sci., 54, 243

Doressoundiram, A., Boehnhardt, H., Tegler, S. C., & Trujillo, C. Color Properties and Trends of the Transneptunian Objects, ed. Barucci, M. A., Boehnhardt, H., Cruikshank, D. P., Morbidelli, A., & Dotson, R., 91–104

Dullemond, C. P. & Dominik, C. 2005, A&A, 434, 971

Duncan, M. J. & Levison, H. F. 1997, Science, 276, 1670

Duncan, M. J., Levison, H. F., & Budd, S. M. 1995, AJ, 110, 3073

Durda, D. D. & Dermott, S. F. 1997, Icarus, 130, 140

Dutrey, A. 2007, Comptes Rendus Geoscience, 339, 862

Edgeworth, K. E. 1949, MNRAS, 109, 600

Eiroa, C., Fedele, D., Maldonado, J., González-García, B. M., Rodmann, J., Heras, A. M., Pilbratt, G. L., Augereau, J.-C., Mora, A., Montesinos, B., Ardila, D., Bryden, G., Liseau, R., Stapelfeldt, K., Launhardt, R., Solano, E., Bayo, A., Absil, O., Arévalo, M., Barrado, D., Beichmann, C., Danchi, W., Del Burgo, C., Ertel, S., Fridlund, M., Fukagawa, M., Gutiérrez, R., Grün, E., Kamp, I., Krivov, A., Lebreton, J., Löhne, T., Lorente, R., Marshall, J., Martínez-Arnáiz, R., Meeus, G., Montes, D., Morbidelli, A., Müller, S., Mutschke, H., Nakagawa, T., Olofsson, G., Ribas, I., Roberge, A., Sanz-Forcada, J., Thébault, P., Walker, H., White, G. J., & Wolf, S. 2010, A&A, 518, L131+

Elliot, J. L., Person, M. J., Zuluaga, C. A., Bosh, A. S., Adams, E. R., Brothers, T. C., Gulbis, A. A. S., Levine, S. E., Lockhart, M., Zangari, A. M., Babcock, B. A., Dupré, K., Pasachoff, J. M., Souza, S. P., Rosing, W., Secrest, N., Bright, L., Dunham, E. W., Sheppard, S. S., Kakkala, M., Tilleman, T., Berger, B., Briggs, J. W., Jacobson, G., Valleli, P., Volz, B., Rapoport, S., Hart, R., Brucker, M., Michel, R., Mattingly, A., Zambrano-Marin, L., Meyer, A. W., Wolf, J., Ryan, E. V., Ryan, W. H., Morzinski, K., Grigsby, B., Brimacombe, J., Ragozzine, D., Montano, H. G., & Gilmore, A. 2010, Nature, 465, 897

Farinella, P., Paolicchi, P., & Zappala, V. 1982, Icarus, 52, 409

Fernandez, J. A. & Ip, W.-H. 1984, Icarus, 58, 109

Fitzgerald, M. P., Kalas, P. G., Duchêne, G., Pinte, C., & Graham, J. R. 2007, ApJ, 670, 536

Fraser, W. & Brown, M. E. 2011, in Bulletin of the American Astronomical Society, Vol. 43, American Astronomical Society Meeting Abstracts #217, #306.04–+

Fraser, W. C., Brown, M. E., & Schwamb, M. E. 2010, Icarus, 210, 944

Fraser, W. C. & Kavelaars, J. J. 2009, AJ, 137, 72

Fraser, W. C., Kavelaars, J. J., Holman, M. J., Pritchet, C. J., Gladman, B. J., Grav, T., Jones, R. L., Macwilliams, J., & Petit, J.-M. 2008, Icarus, 195, 827

Fromang, S. & Nelson, R. P. 2005, MNRAS, 364, L81

Fuentes, C. I. & Holman, M. J. 2008, AJ, 136, 83

Fuentes, C. I., Holman, M. J., Trilling, D. E., & Protopapas, P. 2010, ApJ, 722, 1290

Fuentes, C. I., Trilling, D. E., & Holman, M. J. 2011, ApJ, 742, 118

Galle, J. G. 1846, MNRAS, 7, 153

Garaud, P. 2007, ApJ, 671, 2091

Gladman, B., Holman, M., Grav, T., Kavelaars, J., Nicholson, P., Aksnes, K., & Petit, J.-M. 2002, Icarus, 157, 269

Gladman, B., Kavelaars, J. J., Petit, J., Morbidelli, A., Holman, M. J., & Loredo, T. 2001, AJ, 122, 1051

Glaschke, P. 2006, PhD thesis, PhD Thesis, Combined Faculties for the Natural Sciences and for Mathematics of the University of Heidelberg, Germany. XIV+134 pp. (2006)

Goldreich, P., Lithwick, Y., & Sari, R. 2004a, ApJ, 614, 497

—. 2004b, ARA&A, 42, 549

Goldreich, P. & Ward, W. R. 1973, ApJ, 183, 1051

Golimowski, D., John Krist, J., Chen, C., Stapelfeldt, K., Ardila, D., Clampin, M., Schneider, G., Silverstone, M., Ford, H., & Illingworth, G. 2007, in In the Spirit of Bernard Lyot: The Direct Detection of Planets and Circumstellar Disks in the 21st Century

Gomes, R. S., Morbidelli, A., & Levison, H. F. 2004, Icarus, 170, 492

Gradie, J. & Veverka, J. 1980, Nature, 283, 840

Greaves, J. S. & Wyatt, M. C. 2010, MNRAS, 404, 1944

Greenberg, R., Bottke, W. F., Carusi, A., & Valsecchi, G. B. 1991, Icarus, 94, 98

Greenberg, R., Hartmann, W. K., Chapman, C. R., & Wacker, J. F. 1978, Icarus, 35, 1

Grigorieva, A., Artymowicz, P., & Thébault, P. 2007, A&A, 461, 537

Gulbis, A. A. S., Elliot, J. L., Adams, E. R., Benecchi, S. D., Buie, M. W., Trilling, D. E., & Wasserman, L. H. 2010, AJ, 140, 350

Gurnett, D. A., Ansher, J. A., Kurth, W. S., & Granroth, L. J. 1997, Geophys. Res. Lett., 24, 3125

Habing, H. J., Dominik, C., Jourdain de Muizon, M., Kessler, M. F., Laureijs, R. J., Leech, K., Metcalfe, L., Salama, A., Siebenmorgen, R., & Trams, N. 1999, Nature, 401, 456

Hahn, J. M. & Malhotra, R. 1999, AJ, 117, 3041

—. 2005, AJ, 130, 2392

Hahn, J. M., Zook, H. A., Cooper, B., & Sunkara, B. 2002, Icarus, 158, 360

Haisch, Jr., K. E., Lada, E. A., & Lada, C. J. 2001, ApJL, 553, L153

Hayashi, C. 1981, Progress of Theoretical Physics Supplement, 70, 35

Hernández, J., Briceño, C., Calvet, N., Hartmann, L., Muzerolle, J., & Quintero, A. 2006, ApJ, 652, 472

Herschel, M. & Watson, D. 1781, Royal Society of London Philosophical Transactions Series I, 71, 492

Hillenbrand, L. A., Carpenter, J. M., Kim, J. S., Meyer, M. R., Backman, D. E., Moro-Martín, A., Hollenbach, D. J., Hines, D. C., Pascucci, I., & Bouwman, J. 2008, ApJ, 677, 630

Hornung, P., Pellat, R., & Barge, P. 1985, Icarus, 64, 295

Housen, K. R. & Holsapple, K. A. 1990, Icarus, 84, 226

Ichikawa, K. & Fukugita, M. 2011, ApJ, 736, 122

Ida, S., Kokubo, E., & Makino, J. 1993, MNRAS, 263, 875

Ida, S. & Makino, J. 1992, Icarus, 96, 107

—. 1993, Icarus, 106, 210

Jedicke, R., Larsen, J., & Spahr, T. 2002, Asteroids III, 71

Jewitt, D. & Luu, J. 1993, Nature, 362, 730

Jewitt, D. C. & Luu, J. X. 1995, AJ, 109, 1867

Jewitt, D. C., Trujillo, C. A., & Luu, J. X. 2000, AJ, 120, 1140

Johansen, A., Klahr, H., & Henning, T. 2011, A&A, 529, A62+

Johansen, A., Oishi, J. S., Low, M.-M. M., Klahr, H., Henning, T., & Youdin, A. 2007, Nature, 448, 1022

Johansen, A., Youdin, A., & Mac Low, M.-M. 2009, ApJL, 704, L75

Juric, M., Ivezic, Z., Lupton, R., & SDSS Collaboration. 2007, in Bulletin of the American Astronomical Society, Vol. 38, Bulletin of the American Astronomical Society, 828–+

Jutzi, M., Benz, W., & Michel, P. 2008, Icarus, 198, 242

Kalas, P., Graham, J. R., Chiang, E., Fitzgerald, M. P., Clampin, M., Kite, E. S., Stapelfeldt, K., Marois, C., & Krist, J. 2008, Science, 322, 1345

Kalas, P., Graham, J. R., & Clampin, M. 2005, Nature, 435, 1067

Kalas, P., Graham, J. R., Clampin, M. C., & Fitzgerald, M. P. 2006, ApJL, 637, L57

Kant, I. 1755, Allgemeine Naturgeschichte und Theorie des Himmels, ed. Kant, I.

Kavelaars, J., Jones, L., Gladman, B., Parker, J. W., & Petit, J.-M. The Orbital and Spatial Distribution of the Kuiper Belt, ed. Barucci, M. A., Boehnhardt, H., Cruikshank, D. P., Morbidelli, A., & Dotson, R., 59–69

Kavelaars, J. J., Jones, R. L., Gladman, B. J., Petit, J.-M., Parker, J. W., Van Laerhoven, C., Nicholson, P., Rousselot, P., Scholl, H., Mousis, O., Marsden, B., Benavidez, P., Bieryla, A., Campo Bagatin, A., Doressoundiram, A., Margot, J. L., Murray, I., & Veillet, C. 2009, AJ, 137, 4917

Kenyon, S. J. & Bromley, B. C. 2001, AJ, 121, 538

—. 2004a, AJ, 127, 513

—. 2004b, AJ, 128, 1916

—. 2008, ApJS, 179, 451

Kenyon, S. J. & Luu, J. X. 1998, AJ, 115, 2136

—. 1999a, AJ, 118, 1101

—. 1999b, ApJ, 526, 465

Kepler, J. 1619, Harmonices mvndi libri v. qvorvm primus geometricvs, de figurarum regularium, quae proportiones harmonicas constituunt, ortu & demonstrationibus, secundus architectonicvs, SEU EX geometria figvrata, de figurarum regularium congru-

entia in plano vel solido: tertius proprie harmonicvs, de proportionum harmonicarum ortu EX figuris, ed. Kepler, J.

Klahr, H. & Bodenheimer, P. 2006, ApJ, 639, 432

Klahr, H. H. & Henning, T. 1997, Icarus, 128, 213

Knezevic, Z., Milani, A., Farinella, P., Froeschle, C., & Froeschle, C. 1991, Icarus, 93, 316

Kobayashi, H., Tanaka, H., & Krivov, A. V. 2011, ApJ, 738, 35

Kokubo, E. & Ida, S. 1995, Icarus, 114, 247

—. 1996, Icarus, 123, 180

—. 1998, Icarus, 131, 171

Kratter, K. M., Murray-Clay, R. A., & Youdin, A. N. 2010, ApJ, 710, 1375

Krist, J. E., Stapelfeldt, K. R., Bryden, G., Rieke, G. H., Su, K. Y. L., Chen, C. C., Beichman, C. A., Hines, D. C., Rebull, L. M., Tanner, A., Trilling, D. E., Clampin, M., & Gáspár, A. 2010, AJ, 140, 1051

Krivov, A. V., Löhne, T., & Sremčević, M. 2006, A&A, 455, 509

Krivov, A. V., Sremčević, M., & Spahn, F. 2005, Icarus, 174, 105

Kuiper, G. P. 1951, in 50th Anniversary of the Yerkes Observatory and Half a Century of Progress in Astrophysics, ed. J. A. Hynek, 357–+

Landgraf, M., Liou, J.-C., Zook, H. A., & Grün, E. 2002, AJ, 123, 2857

Laplace, P. 1796, Impr. du Cercle-Social, 1

Lawler, S. M., Beichman, C. A., Bryden, G., Ciardi, D. R., Tanner, A. M., Su, K. Y. L., Stapelfeldt, K. R., Lisse, C. M., & Harker, D. E. 2009, ApJ, 705, 89

Lebedev, P. 1901, Annalen der Physik, 311, 433

Lecar, M. & Aarseth, S. J. 1986, ApJ, 305, 564

Lestrade, J.-F., Wyatt, M. C., Bertoldi, F., Menten, K. M., & Labaigt, G. 2009, A&A, 506, 1455

Levison, H. F. & Morbidelli, A. 2003, Nature, 426, 419

Levison, H. F., Morbidelli, A., Vanlaerhoven, C., Gomes, R., & Tsiganis, K. 2008, Icarus, 196, 258

Levison, H. F. & Stern, S. A. 2001, AJ, 121, 1730

Liou, J. C. & Malhotra, R. 1997, Science, 275, 375

Liseau, R., Eiroa, C., Fedele, D., Augereau, J., Olofsson, G., González, B., Maldonado, J., Montesinos, B., Mora, A., Absil, O., Ardila, D., Barrado, D., Bayo, A., Beichman, C. A., Bryden, G., Danchi, W. C., Del Burgo, C., Ertel, S., Fridlund, C. W. M., Heras, A. M., Krivov, A. V., Launhardt, R., Lebreton, J., Löhne, T., Marshall, J. P., Meeus, G., Müller, S., Pilbratt, G. L., Roberge, A., Rodmann, J., Solano, E., Stapelfeldt, K. R., Thébault, P., White, G. J., & Wolf, S. 2010, A&A, 518, L132+

Lissauer, J. J. 1987, Icarus, 69, 249

Löhne, T., Krivov, A. V., & Rodmann, J. 2008, ApJ, 673, 1123

Luu, J. & Jewitt, D. 1996, AJ, 112, 2310

Luu, J., Marsden, B. G., Jewitt, D., Trujillo, C. A., Hergenrother, C. W., Chen, J., & Offutt, W. B. 1997, Nature, 387, 573

Lykawka, P. S. & Mukai, T. 2005, Earth Moon and Planets, 97, 107

Makino, J., Fukushige, T., Funato, Y., & Kokubo, E. 1998, New Astronomy, 3, 411

Malhotra, R. 1993, Nature, 365, 819

—. 1995, AJ, 110, 420

Malhotra, R., Duncan, M. J., & Levison, H. F. 2000, Protostars and Planets IV, 1231

Marois, C., Macintosh, B., Barman, T., Zuckerman, B., Song, I., Patience, J., Lafrenière, D., & Doyon, R. 2008, Science, 322, 1348

Mason, B. 1960, Nature, 186, 230

Matthews, B. C., Sibthorpe, B., Kennedy, G., Phillips, N., Churcher, L., Duchêne, G., Greaves, J. S., Lestrade, J.-F., Moro-Martin, A., Wyatt, M. C., Bastien, P., Biggs, A., Bouvier, J., Butner, H. M., Dent, W. R. F., di Francesco, J., Eislöffel, J., Graham, J., Harvey, P., Hauschildt, P., Holland, W. S., Horner, J., Ibar, E., Ivison, R. J., Johnstone, D., Kalas, P., Kavelaars, J., Rodriguez, D., Udry, S., van der Werf, P., Wilner, D., & Zuckerman, B. 2010, A&A, 518, L135+

Maxwell, J. C. 1873, A treatise on electricity and magnetism, ed. Maxwell, J. C. (Clarendon Press)

McCaughrean, M. J. & O'Dell, C. R. 1996, AJ, 111, 1977

Meyer, M. R., Backman, D. E., Weinberger, A. J., & Wyatt, M. C. 2007, in Protostars and Planets V, ed. B. Reipurth, D. Jewitt, & K. Keil, 573–588

Meyer, M. R., Carpenter, J. M., Mamajek, E. E., Hillenbrand, L. A., Hollenbach, D., Moro-Martin, A., Kim, J. S., Silverstone, M. D., Najita, J., Hines, D. C., Pascucci, I., Stauffer, J. R., Bouwman, J., & Backman, D. E. 2008, ApJL, 673, L181

Minor Planet Center. 2012, Minor Planet Database

Moór, A., Ábrahám, P., Derekas, A., Kiss, C., Kiss, L. L., Apai, D., Grady, C., & Henning, T. 2006, ApJ, 644, 525

Moór, A., Apai, D., Pascucci, I., Ábrahám, P., Grady, C., Henning, T., Juhász, A., Kiss, C., & Kóspál, Á. 2009, ApJL, 700, L25

Moór, A., Pascucci, I., Kóspál, Á., Ábrahám, P., Csengeri, T., Kiss, L. L., Apai, D., Grady, C., Henning, T., Kiss, C., Bayliss, D., Juhász, A., Kovács, J., & Szalai, T. 2011, ApJS, 193, 4

Morbidelli, A., Bottke, W. F., Nesvorný, D., & Levison, H. F. 2009, Icarus, 204, 558

Morbidelli, A. & Brown, M. E. The kuiper belt and the primordial evolution of the solar system, ed. Festou, M. C., Keller, H. U., & Weaver, H. A., 175–191

Morishima, R., Schmidt, M. W., Stadel, J., & Moore, B. 2008, ApJ, 685, 1247

Morishima, R., Stadel, J., & Moore, B. 2010, Icarus, 207, 517

Müller, T. G., Lellouch, E., Stansberry, J., Kiss, C., Santos-Sanz, P., Vilenius, E., Protopapa, S., Moreno, R., Mueller, M., Delsanti, A., Duffard, R., Fornasier, S., Groussin, O., Harris, A. W., Henry, F., Horner, J., Lacerda, P., Lim, T., Mommert, M., Ortiz, J. L., Rengel, M., Thirouin, A., Trilling, D., Barucci, A., Crovisier, J., Doressoundiram, A., Dotto, E., Gutiérrez, P. J., Hainaut, O. R., Hartogh, P., Hestroffer, D., Kidger, M., Lara, L., Swinyard, B., & Thomas, N. 2010, A&A, 518, L146

Mustill, A. J. & Wyatt, M. C. 2009, MNRAS, 399, 1403

Natta, A. & Testi, L. 2004, in Astronomical Society of the Pacific Conference Series, Vol. 323, Star Formation in the Interstellar Medium: In Honor of David Hollenbach, ed. D. Johnstone, F. C. Adams, D. N. C. Lin, D. A. Neufeeld, & E. C. Ostriker , 279

Natta, A., Testi, L., Calvet, N., Henning, T., Waters, R., & Wilner, D. 2007, Protostars and Planets V, 767

Nilsson, R., Liseau, R., Brandeker, A., Olofsson, G., Pilbratt, G. L., Risacher, C., Rod-mann, J., Augereau, J., Bergman, P., Eiroa, C., Fridlund, M., Thébault, P., & White, G. J. 2010, A&A, 518, A40+

Nishida, S. 1983, Progress of Theoretical Physics, 70, 93

Noll, K. S., Grundy, W. M., Stephens, D. C., Levison, H. F., & Kern, S. D. 2008, Icarus, 194, 758

O'Brien, D. P., Morbidelli, A., & Bottke, W. F. 2007, Icarus, 191, 434

Ogihara, M. & Ida, S. 2009, ApJ, 699, 824

Ohtsuki, K., Stewart, G. R., & Ida, S. 2002, Icarus, 155, 436

Ormel, C. W., Dullemond, C. P., & Spaans, M. 2010, Icarus, 210, 507

Oudmaijer, R. D., van der Veen, W. E. C. J., Waters, L. B. F. M., Trams, N. R., Waelkens, C., & Engelsman, E. 1992, A&AS, 96, 625

Pan, M. & Sari, R. 2005, Icarus, 173, 342

Pan, M. & Schlichting, H. E. 2012, ApJ, 747, 113

Parker, A. H. & Kavelaars, J. J. 2010a, ApJL, 722, L204

—. 2010b, Icarus, 209, 766

—. 2012, ApJ, 744, 139

Parker, A. H., Kavelaars, J. J., Petit, J.-M., Jones, L., Gladman, B., & Parker, J. 2011, ApJ, 743, 1

Peixinho, N., Lacerda, P., & Jewitt, D. 2008, AJ, 136, 1837

Perna, D., Barucci, M. A., Fornasier, S., DeMeo, F. E., Alvarez-Candal, A., Merlin, F., Dotto, E., Doressoundiram, A., & de Bergh, C. 2010, A&A, 510, A53+

Petit, J.-M., Chambers, J., Franklin, F., & Nagasawa, M. 2002, Asteroids III, 711

Petit, J.-M., Kavelaars, J. J., Gladman, B. J., Jones, R. L., Parker, J. W., Van Laerhoven, C., Nicholson, P., Mars, G., Rousselot, P., Mousis, O., Marsden, B., Bieryla, A., Taylor, M., Ashby, M. L. N., Benavidez, P., Campo Bagatin, A., & Bernabeu, G. 2011, AJ, 142, 131

Pinilla, P., Birnstiel, T., Ricci, L., Dullemond, C. P., Uribe, A. L., Testi, L., & Natta, A. 2012, A&A, 538, A114

Poppe, A., James, D., Jacobsmeyer, B., & Horányi, M. 2010, Geophys. Res. Lett., 37, L11101

Poynting, J. H. 1904, Royal Society of London Philosophical Transactions Series A, 202, 525

Pyo, J., Ueno, M., Kwon, S. M., Hong, S. S., Ishihara, D., Ishiguro, M., Usui, F., Ootsubo, T., & Mukai, T. 2010, A&A, 523, A53+

Rafikov, R. R. 2003, AJ, 126, 2529

Raymond, S. N., Armitage, P. J., Moro-Martín, A., Booth, M., Wyatt, M. C., Armstrong, J. C., Mandell, A. M., Selsis, F., & West, A. A. 2011, A&A, 530, A62+

Robertson, H. P. 1937, MNRAS, 97, 423

Rodmann, J., Henning, T., Chandler, C. J., Mundy, L. G., & Wilner, D. J. 2006, A&A, 446, 211

Safronov, V. S. 1969, Evoliutsiia doplanetnogo oblaka., ed. Safronov, V. S.

Schlichting, H. E., Ofek, E. O., Wenz, M., Sari, R., Gal-Yam, A., Livio, M., Nelan, E., & Zucker, S. 2009, Nature, 462, 895

Schlichting, H. E. & Sari, R. 2007, ApJ, 658, 593

—. 2011, ApJ, 728, 68

Sheppard, S. S., Ragozzine, D., & Trujillo, C. 2011, ArXiv e-prints

Sheppard, S. S. & Trujillo, C. A. 2010, ApJL, 723, L233

Sicardy, B., Ortiz, J. L., Assafin, M., Jehin, E., Maury, A., Lellouch, E., Hutton, R. G., Braga-Ribas, F., Colas, F., Hestroffer, D., Lecacheux, J., Roques, F., Santos-Sanz, P., Widemann, T., Morales, N., Duffard, R., Thirouin, A., Castro-Tirado, A. J., Jelínek, M., Kubánek, P., Sota, A., Sánchez-Ramírez, R., Andrei, A. H., Camargo, J. I. B., da Silva Neto, D. N., Gomes, A. R., Martins, R. V., Gillon, M., Manfroid, J., Tozzi, G. P., Harlingten, C., Saravia, S., Behrend, R., Mottola, S., Melendo, E. G., Peris, V., Fabregat, J., Madiedo, J. M., Cuesta, L., Eibe, M. T., Ullán, A., Organero, F., Pastor, S., de Los Reyes, J. A., Pedraz, S., Castro, A., de La Cueva, I., Muler, G., Steele, I. A., Cebrián, M., Montañés-Rodríguez, P., Oscoz, A., Weaver, D., Jacques, C., Corradi, W. J. B., Santos, F. P., Reis, W., Milone, A., Emilio, M., Gutiérrez, L., Vázquez, R., & Hernández-Toledo, H. 2011, Nature, 478, 493

Slipher, V. M. & Tombaugh, C. W. 1930, The Science News-Letter, 17, 179

Smith, B. A. & Terrile, R. J. 1984, Science, 226, 1421

Smith, R., Wyatt, M. C., & Dent, W. R. F. 2008, A&A, 485, 897

Spaute, D., Weidenschilling, S. J., Davis, D. R., & Marzari, F. 1991, Icarus, 92, 147

Stansberry, J., Grundy, W., Brown, M., Cruikshank, D., Spencer, J., Trilling, D., & Margot, J.-L. Physical Properties of Kuiper Belt and Centaur Objects: Constraints from the Spitzer Space Telescope, ed. Barucci, M. A., Boehnhardt, H., Cruikshank, D. P., Morbidelli, A., & Dotson, R., 161–179

Stern, S. A. 1991, Icarus, 90, 271

Stern, S. A. & Colwell, J. E. 1997, ApJ, 490, 879

Stewart, G. R. & Ida, S. 2000, Icarus, 143, 28

Stewart, G. R. & Kaula, W. M. 1980, Icarus, 44, 154

Stewart, G. R. & Wetherill, G. W. 1988, Icarus, 74, 542

Stewart, S. T. & Leinhardt, Z. M. 2009, ApJL, 691, L133

Strubbe, L. E. & Chiang, E. I. 2006, ApJ, 648, 652

Su, K. Y. L., Rieke, G. H., Misselt, K. A., Stansberry, J. A., Moro-Martin, A., Stapelfeldt, K. R., Werner, M. W., Trilling, D. E., Bendo, G. J., Gordon, K. D., Hines, D. C., Wyatt, M. C., Holland, W. S., Marengo, M., Megeath, S. T., & Fazio, G. G. 2005, ApJ, 628, 487

Su, K. Y. L., Rieke, G. H., Stansberry, J. A., Bryden, G., Stapelfeldt, K. R., Trilling, D. E., Muzerolle, J., Beichman, C. A., Moro-Martin, A., Hines, D. C., & Werner, M. W. 2006, ApJ, 653, 675

Tegler, S. C. & Romanishin, W. 2000, Nature, 407, 979

Teplitz, V. L., Stern, S. A., Anderson, J. D., Rosenbaum, D., Scalise, R. J., & Wentzler, P. 1999, ApJ, 516, 425

Thébault, P. 2009, A&A, 505, 1269

Thébault, P. & Augereau, J.-C. 2007, A&A, 472, 169

Thébault, P., Augereau, J. C., & Beust, H. 2003, A&A, 408, 775

Thébault, P. & Wu, Y. 2008, A&A, 481, 713

181

Thommes, E. W., Duncan, M. J., & Levison, H. F. 1999, Nature, 402, 635

Trilling, D. E., Bryden, G., Beichman, C. A., Rieke, G. H., Su, K. Y. L., Stansberry, J. A., Blaylock, M., Stapelfeldt, K. R., Beeman, J. W., & Haller, E. E. 2008, ApJ, 674, 1086

Trujillo, C. A. & Brown, M. E. 2001, ApJL, 554, L95

Trujillo, C. A., Jewitt, D. C., & Luu, J. X. 2001, AJ, 122, 457

Vitense, C., Krivov, A. V., & Löhne, T. 2010, A&A, 520, A32+

Walker, H. J. & Wolstencroft, R. D. 1988, PASP, 100, 1509

Weidenschilling, S. J. 1977a, MNRAS, 180, 57

—. 1977b, Ap&SS, 51, 153

—. 1980, Icarus, 44, 172

—. 1995, Icarus, 116, 433

Weidenschilling, S. J., Spaute, D., Davis, D. R., Marzari, F., & Ohtsuki, K. 1997, Icarus, 128, 429

Weisberg, M. K., McCoy, T. J., & Krot, A. N. Systematics and Evaluation of Meteorite Classification, ed. Lauretta, D. S. & McSween, H. Y., 19–52

Wetherill, G. W. 1992, Icarus, 100, 307

Wetherill, G. W. & Stewart, G. R. 1989, Icarus, 77, 330

—. 1993, Icarus, 106, 190

Whipple, F. L. 1972, in From Plasma to Planet, ed. A. Elvius, 211

Williams, I. & Bell, J. 2006, Astronomy and Geophysics, 47, 050000

Wyatt, M. C. 2005, A&A, 433, 1007

—. 2008, ARA&A, 46, 339

Wyatt, M. C., Clarke, C. J., & Booth, M. 2011, Celestial Mechanics and Dynamical Astronomy, 111, 1

Wyatt, M. C., Smith, R., Greaves, J. S., Beichman, C. A., Bryden, G., & Lisse, C. M. 2007a, ApJ, 658, 569

Wyatt, M. C., Smith, R., Su, K. Y. L., Rieke, G. H., Greaves, J. S., Beichman, C. A., & Bryden, G. 2007b, ApJ, 663, 365

Yamamoto, S. & Mukai, T. 1998, A&A, 329, 785

Youdin, A. N. & Shu, F. H. 2002, ApJ, 580, 494

Young, E. F., Young, L. A., & Buie, M. 2007, in Bulletin of the American Astronomical Society, Vol. 38, AAS/Division for Planetary Sciences Meeting Abstracts #39, 541

Zalucha, A. M., Zhu, X., Gulbis, A. A. S., Strobel, D. F., & Elliot, J. L. 2011, Icarus, 214, 685

Zuckerman, B., Forveille, T., & Kastner, J. H. 1995, Nature, 373, 494